A mechanical and microstructural study of corrosion resistant alloys produced using wire arc additive manufacturing

PhD Thesis

J. lain Sword

Mechanics of Materials Research group

Department of Mechanical and Aerospace Engineering

University of Strathclyde, Glasgow

25/09/2025

This thesis is the result of the author's original research. It has been composed by the author and has not been previously submitted for examination which has led to the award of a degree. The copyright of this thesis belongs to the author under the terms of the United Kingdom Copyright Acts as qualified by University of Strathclyde Regulation 3.50. Due acknowledgement must always be made of the use of any material contained in, or derived from, this thesis.

Signed: J. lain Sword

Date: 07/06/2025

Abstract

This thesis investigates the production of corrosion resistant alloys (CRA) through wire arc additive manufacturing (WAAM). This work has analysed the properties of three (3) alloys when this method is used for manufacture. Furthermore, the environmental impact of adopting WAAM has been considered. The development of these alloys was quantified through microstructural analysis and mechanical testing. Methods for the analysis of mechanical properties included hardness, impact, fatigue and tensile testing.

Changes in process parameters employed for the production of precipitation-hardening stainless steel 15-5PH were investigated. This investigation observed that the heat input during deposition had a significant impact on the mechanical properties of this alloy. In addition, post weld heat treatment can be used to control the resulting properties. Of those investigated in this study, the most effective process relied on a heat input of 0.565kJ/mm followed by the standard H1150 aging heat treatment. This combination of process parameters achieved partial compliance with the requirements of ASTM standard A693. It was identified that this high heat input during deposition led to in-situ heating causing the matrix to be solutionised. This improved its response to the following aging treatment, resulting in superior properties as strengthening phases had been able to develop.

Furthermore, the nickel-based superalloys; Inconel 625 and 718 were also studied. The mechanical properties of these alloys were compared against the results from previous literature. In addition, the results of fatigue testing were compared against alloys produced by other manufacturing processes. It was identified that Inconel 625 produced through this process achieved the performance required by standard ASTM B443 with fatigue performance exceeding that of conventional processing for this alloy. WAAM produced Inconel 718 did not achieve the required mechanical properties as defined by standard ASTM B637. This difference was due to the formation of the weakening δ phase caused by precipitating elements not being returned to solution following segregation during solidification. However, the fatigue performance was found to be comparable with existing literature. The columnar grains and δ made the material more sensitive to crack growth at

lower stress ranges, leading to reduced fatigue performance compared with the literature.

It was found that the strengthening mechanism of the alloy plays a major role in the sensitivity of its mechanical properties to process parameters and post weld heat treatment when produced using WAAM. This is most significant for precipitation hardening alloys such as 15-5PH stainless steel and Inconel 718. 15-5PH stainless steel showed up to a 5x increase in Charpy impact energy following heat treatment and up to a 25% reduction in yield strength depending on the process parameters. Hardness was shown to vary up to 20% between all cases of process parameters and heat treatment. Inconel 718 was shown to exhibit a 72% increase in hardness with proper heat treatment. Solid solution strengthening alloys such as Inconel 625 were less sensitive as they are not dependent on the development of precipitates within the matrix, for strengthening. Hardness was shown to reduce by 16% following heat treatment. These differences account for improvements in the fatigue strength of WAAM Inconel 625 when compared to the wrought alloy, while the results for Inconel 718 showed a slight reduction in fatigue strength.

A methodology for the comparison of the environmental impact of manufacturing methods was applied to the production of CRA components through WAAM. It was identified through a case study of an Inconel 625 impeller that significant reductions in the primary energy consumption and carbon dioxide emissions can be achieved. In addition, the calculated carbon dioxide emissions were found to be sensitive to the carbon emission signature of the energy supply used during manufacture due to the significant contribution of electrical energy in deposition and heat treatment.

Table of Contents

Abs	tract	t	2
Tab	le of	f Contents	4
Ack	nowl	rledgements	8
N	ome	enclature	9
1.	Intro	oduction	12
1.	.1.	Aim and objectives	15
1.	.2.	Thesis structure	15
1.	.3.	References	16
2.	Lite	erature review	19
2	.1.	Arc cladding	19
2	.2.	Effect of shielding gasses	20
2	.3.	WAAM of stainless steels	21
2	.4.	WAAM of nickel-based corrosion resistant alloys	23
2	.5.	References	28
3.	Ехр	perimental apparatus and methods	33
3	.1.	Additive manufacturing cell setup	33
	3.1.	.1. Welding system	34
	3.1.	.2. Robotics system	35
	3.1.	.3. Pre-heating	36
3.	.2.	Materials	37
	3.2.	.1. Bulk materials	37
	3.2.	.2. Shielding gas	37
3.	.3.	Heat treatment	37
3.	.4.	Metallographic analysis	37
	3.4.	.1. Sample preparation	37

	3.4.2.	Optical microscopy	41
	3.4.3.	Hardness testing	41
	3.4.4.	Scanning electron microscopy (SEM)	42
	3.4.5.	Glow discharge analysis	44
	3.5. Me	chanical analysis	44
	3.5.1.	Tensile testing	46
	3.5.2.	Fatigue testing	46
	3.5.3.	Charpy impact toughness testing	47
	3.6. Ref	erences	47
4	. 15-5PH	precipitation-hardening stainless steel	49
	4.1. Mic	rostructure	49
	4.1.1.	Wrought 15-5PH	52
	4.1.2.	WAAM 15-5PH: high heat input (HH)	55
	4.1.3.	WAAM 15-5PH: low heat input (LH)	60
	4.2. Har	dness testing	63
	4.2.1.	Wrought 15-5PH	63
	4.2.2.	WAAM 15-5PH	64
	4.3. Ter	nsile testing	65
	4.3.1.	Wrought 15-5PH	66
	4.3.2.	WAAM 15-5PH: high heat input (HH)	67
	4.3.3.	WAAM 15-5PH: low heat input (LH)	72
	4.4. Cha	arpy Impact testing	74
	4.4.1.	WAAM 15-5PH: high heat input (HH)	75
	4.4.2.	WAAM 15-5PH: low heat input (LH)	77
	4.5. Fat	igue testing	81
	4.5.1.	Wrought 15-5PH	81
	4.5.2.	WAAM 15-5PH: high heat input (HH)	84

	4.5.	3.	WAAM 15-5PH: low heat input (LH)	. 89
4	.6.	Disc	ussion	. 94
4	.7.	Refe	rences	. 98
5.	Inco	onel 6	25 WAAM	100
5	5.1.	Micro	ostructure	100
5	5.2.	Hard	ness testing	105
5	5.3.	Tens	sile testing	106
5	5.4.	Fatig	gue Testing	109
5	5.5.	Disc	ussion	112
5	5.6.	Refe	rences	113
6.	Inco	onel 7	18 WAAM	117
	6.1.	1.	Microstructure	117
6	5.2.	Hard	ness testing	123
6	5.3.	Tens	sile testing	124
6	5.4.	Fatig	jue testing	127
6	5.5.	Disc	ussion	131
6	5.6.	Refe	rences	131
7.	Env	rironm	nental impact analysis	134
7	'.1.	Meth	od	135
	7.1.	1.	Material production and pre-manufacturing	137
7	.2.	WAA	AM process model	138
	7.2.	1.	Machining process model	139
	7.2.	2.	Heat treatment model	140
	7.2.	3.	Data gathering	140
7	'.3.	Case	e study	141
7	'. 4 .	Resu	ults	141
7	· 5	Disc	ussion	147

	7.6.	References	148
8.	Con	cluding remarks	150
	8.1.	WAAM production of 15-5PH	151
	8.2.	WAAM production of Inconel 625	152
	8.3.	WAAM production of Inconel 718	153
	8.4.	Environmental impact analysis	153
	8.5.	Recommendations for future work	154
	8.6.	References	156
Α	. Histor	ical Context	158
	A.1. A	dditive manufacturing	158
	A.1.	1. Overview of AM processes	159
	A.1.	2. Methods of metal AM for high deposition rate	160
	A.2. W	/ire arc additive manufacturing	161
	A.2.	1. Arc sources	161
	A.2.	2. Cold metal transfer (CMT-WAAM)	163
	A.2.	3. Twin wire (T-WAAM)	163
	A.3. C	orrosion resistant alloys	163
	A.3.	1. Stainless Steels	164
	A.3.	2. Inconel 625	165
	A.3.	3. Inconel 718	166
	A.4. F	atigue testing	167
	A.5. E	nvironmental impact analysis	168
	A.6. R	eferences	169
R	Peer	Reviewed Journal Articles	177

Acknowledgements

The completion of this thesis would not have been possible without the support both professionally and emotionally of a great many people. Not least of all, my supervisors Prof. Alex Galloway and Dr Athanasios Toumpis. Their assistance in navigating the work of a postgraduate research project has been invaluable in addition to their patience when the going was difficult. My thanks also go to the University of Strathclyde for the awarding of a Research Excellence Award studentship to support the funding of this research.

Furthermore, I would like to recognise the contribution of the University of Strathclyde Mechanical Engineering workshop and Advanced Materials Research Laboratory (AMRL) for their support in completing the experimental aspects of this project. In particular, James Kelly for his advice and guidance with metallographic and fractographic study and James Gillespie for his assistance in mechanical testing.

My gratitude is also extended to my colleagues in the mechanics of materials research group at the University of Strathclyde. This community of fellow postgraduate researchers provided insightful suggestions throughout the research project.

Beyond the University of Strathclyde, I would like to thank Robert "Bud" Graham of Glenalmond Technologies for the use of their additive manufacture cell and materials. Over and above this, "Bud" and the other staff of Glenalmond Technologies provided excellent mentorship in the practical aspects of additive manufacturing.

I am grateful to my family and friends for their continuous support throughout my research, particularly my parents, Anne-Marie and Callum, my grandad, Barrie and sister, Rhona.

Nomenclature

Symbol	Definition	Unit
AM	Additive manufacturing	
BSE	Backscatter electron detector	
BTF	Buy to fly ratio	
CFD	Computational fluid dynamics	
CMT	Cold metal transfer	
CMT-WAAM	Cold metal transfer - wire arc additive	
	manufacturing	
CNC	Computer numerical control	
DED	Directed energy deposition	
DIC	Differential interference contrast	
EBM	Electron beam melting	
EDS	Energy dispersive spectroscopy	
FDM	Filament deposition modelling	
FGM	Functionally graded materials	
GMAW	Gas metal arc welding	
GTAW	Gas tungsten arc welding	
HIP	Hot isostatic pressing	
HV	Vickers hardness	
LCA	Life cycle analysis	
LENS	Laser engineered net shape	
LMD	Laser metal deposition	
LPBF	Laser powder bed fusion	
LRM	Laser rapid manufacture	
PBF	Powder bed fusion	
PPAD	Pulsed plasma arc deposition	
SE	Secondary electron detector	
SEM	Scanning electron microscopy	
SLM	Selective laser melting	
TEM	Transmission electron microscopy	

T-WAAM	Tandem - wire arc additive	
	manufacturing	
WAAM	Wire arc additive manufacturing	
CTE	Coefficient of Thermal Expansion	ε/°C
CES	Carbon emission signature	kgCO2eq/GJ
Ra	Surface roughness	μm
UTS	Ultimate tensile strength	MPa
15-5PH	Precipitation-hardening stainless steel,	
	approximately 15% Chromium, 5%	
	Nickel	
EN32B	European standard, low carbon, mild	
	steel 32B	
ERNiCrMo-3	Electrode, rod containing nickel,	
	chromium, molybdenum composition no.	
	3	
Al ₂ O ₃	Alumina	
CO ₂	Carbon dioxide	
CrO	Chromium oxide	
Fe ₃ C	Cementite	
H ₂ S	Hydrogen sulphide (sour gas)	
MC	Metal carbide	
NbC	Niobium carbide	
NOx	Oxides of nitrogen	
SiC	Silicon carbide	
TiCN	Titanium carbonitride	
M ₂₃ C ₆	Grain boundary carbide (Inconel 718),	
	typically Cr ₂₃ C ₆	
NbN	Niobium nitride	
TiN	Titanium nitride	
γ	FCC Matrix (Inconel 625 and 718)	
γ'	Ni ₃ (Al,Ti) strengthening phase (Inconel	
	625)	

γ"	Ni₃Nb strengthening phase (Inconel 625	
	and 718)	
δ	Ni₃Nb (Inconel 718)	
δ - ferrite	BCC phase of iron (15-5PH)	
A1	Intermediate aging (Inconel 718)	
AD	As-deposited	
H1025	Heat treatment for 15-5PH (550°C, 4hr,	
	air cool)	
H1150	Heat treatment for 15-5PH (620°C, 4hr,	
	air cool)	
H900	Heat treatment for 15-5PH (480°C, 1hr,	
	air cool)	
HH	High heat input process parameters	
LH	Low heat input process parameters	
ST	Solution treatment	
STA	Solution treated and aged (Inconel 718)	

1. Introduction

Additive manufacturing (AM) is a broad term used to describe the fabrication of components by the addition of material [1-1,1-2]. This description is in contrast to "subtractive manufacturing" such as milling and turning [1-3,1-4]. AM has seen an increase in popularity in recent decades, transitioning from a means of rapid prototyping to widespread use producing operational components for a range of industries [1-5,1-6].

As a discipline, the roots of AM can be traced to the early 1980s with Chuck Hull's development of stereolithography [1-7,1-8]. The last 30 years have seen an acceleration in the pace of development with desktop 3D printers. Both stereolithography and filament deposition modelling have become commonplace with hobbyists to produce plastic and resin components [1-2]. Industrial users have developed and adopted novel methods to produce metal components over the last decade.

The primary advantage of AM is the production of complex geometries without expensive tooling such as moulds or dies required by forging, casting or moulding processes. Indeed, AM techniques can be used to manufacture geometries which were previously impossible to produce through conventional manufacturing techniques. Further advantages include a reduction in the "buy to fly ratio" (BTF) which is particularly valuable when manufacturing components from high-cost materials such as Inconel or titanium alloys [1-9,1-10]. In addition, lead times can also be reduced [1-11,1-12]. For example, the design of components in the aerospace industry typically results in a high BTF for structural components [1-5]. This waste is caused by designs being optimised to reduce weight while maintaining structural stiffness. This weight reduction can be achieved while reducing the BTF ratio by utilising AM to deposit material only where it is needed [1-10,1-13].

The key components of an AM system are: a build area, method of depositing feedstock and a binding method [1-14] as shown in Figure 1-1. The build area typically takes the form of a build plate or a build volume for methods employing a powder bed. The form the feedstock takes is important in determining the method of deposition. For example, common forms of AM

processes use wire and powder for solid feedstocks while liquids are used in some polymer deposition processes. Wire feed is widely used and easy to implement. In contrast, powder methods can utilise a filled bed or deposit a stream of feedstock through a nozzle to reduce waste [1-15].

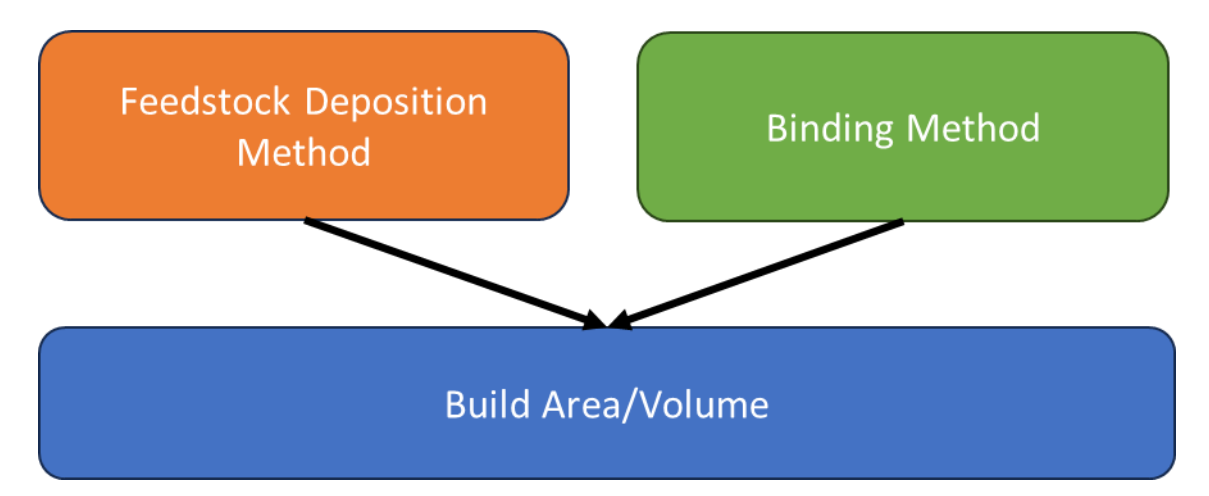


Figure 1-1 General schematic for AM processes.

An energy source is typically used to bond the feedstock in most AM methods. This energy is used to melt or sinter the feedstock to the build plate or to previous layers of deposited material [1-16,1-17]. The source of energy can take many forms, with examples being an electrical heater, laser beam, or an electrical arc.

Wire arc additive manufacturing (WAAM) makes use of a solid build plate, wire feedstock and an electrical or plasma arc to melt and fuse the material [1-11,1-18]. The lack of a restrictive build volume and use of well understood, mature equipment such as welding power sources allow the production of large components at a low cost and high production rate [1-10,1-19,1-20]. The benefits of WAAM come at the cost of reduced dimensional accuracy, in addition, the high heat input can have a negative impact on the material properties of some alloys [1-16,1-21,1-22].

The way industry has adopted WAAM is derived from surface cladding techniques which use fusion welding. A layer of a corrosion resistant alloy is used to clad a lower cost bulk material [1-23,1-24] for industries such as energy and chemical processing. This process typically extends the lifespan of such components or allows them to operate in harsh environments.

This thesis will consider the use of corrosion resistant alloys (CRA) as a feedstock for the WAAM process. These alloys are primarily formed by alloying chromium and other elements with a base of iron, nickel or cobalt [1-25,1-26]. Those with an iron base are referred to as stainless steels, while the others are commonly known by trade names such as Inconel, Hastelloy and Stellite [1-27 - 1-29]. CRAs are predominantly used by industries requiring high performance materials such as aerospace, defence, marine and energy [1-30]. These alloys are valuable to these industries due to their corrosion resistance, high strength at both low and high temperatures, in addition to their creep resistance [1-31].

In this thesis, a range of techniques are used to examine the microstructure and mechanical properties of material produced by WAAM. Analysis of the chemical composition is also performed using glow discharge and electron dispersive spectroscopy (EDS). To assess the microstructure and fracture surfaces, optical and electron microscopy are used. In addition, mechanical properties such as hardness, yield strength, impact toughness and fatigue life are tested. Supplementally, the environmental impact of this process will also be compared against conventional manufacturing techniques. This analysis enables the reduction of environmental impact factors associated with transitioning to WAAM from machining to be determined.

The alloys considered in this research will be a selection of CRAs commonly used in the oil and gas industries. These alloys are the precipitation hardening stainless steel 15-5PH and nickel-based superalloys Inconel 625 and 718.

Variations in process parameters are investigated for the deposition of 15-5PH as the use of this alloy for WAAM is less well established. The parameters which will be modified include the weld heat input and post weld heat treatment (PWHT). The results will be compared to determine how improvements can be made to the mechanical properties.

The production of some alloys using WAAM does not yet have mature processing parameters due to different strengthening mechanisms, such as solid solution strengthening in the case of Inconel 625, and precipitation hardening for Inconel 718 and 15-5PH stainless steel. These precipitation

hardening alloys are more sensitive to in situ heating during deposition, and the effect of post weld heat treatment to develop their mechanical properties. The solidification process and in situ heating can lead to elemental segregation and the formation of low angle grain boundaries within columnar grain structures. This can reduce the strength of the material and produce anisotropic material properties.

1.1. Aim and objectives

The aim of this research is to determine the suitability of WAAM to manufacture components with CRAs. This will involve categorising the microstructure and mechanical properties of alloys produced through this method.

The main objectives will therefore be to:

- Develop an understanding of the microstructure and mechanical properties of CRAs produced through WAAM and the relationship between them.
- Demonstrate production parameters which result in material with mechanical properties meeting existing material standards.
- Determine the improvement in environmental impact of manufacturing
 CRA components through the adoption of WAAM.

1.2. Thesis structure

The following chapter details a survey of the existing literature in the field of additive manufacturing, with a focus on WAAM methods and corrosion resistant alloys. Chapter 3 describes the additive manufacturing cell used to produce material for analysis. In addition, details are provided on the feedstocks and substrates used to manufacture sample material. Supplementing this is a description of laboratory equipment and processes used to investigate the mechanical properties and microstructure of the produced material.

Chapter 4 discusses the microstructure and mechanical properties of precipitation hardening stainless steel 15-5PH. These results are used to develop a comparison between the wrought alloy and WAAM production with different process parameters.

Chapters 5 and 6 expand this to the nickel-based corrosion resistant alloys: Inconel 625 and Inconel 718. Microstructural evaluation and mechanical testing are again performed, and these results are compared against the existing literature and material standards.

In chapter 7, a study of the environmental impact of manufacturing a corrosion resistant alloy component is performed. The relative impact of WAAM and machining are compared.

A summary of the results obtained through this thesis and their applications to industry are presented in chapter 8. In addition, this also discusses suggestions for future work identified through this study.

1.3. References

- [1-1] H. Lee, C. H. J. Lim, M. J. Low, N. Tham, V. M. Murukeshan, and Y.-J. Kim, "Lasers in additive manufacturing: A review," *Int. J. of Precis. Eng. and Manuf.-Green Tech,* vol. 4, no. 3, pp. 307-322, 2017, doi: 10.1007/s40684-017-0037-7.
- [1-2] T. D. Ngo, A. Kashani, G. Imbalzano, K. T. Q. Nguyen, and D. Hui, "Additive manufacturing (3D printing): A review of materials, methods, applications and challenges," *Composites. Part B, Engineering*, vol. 143, pp. 172-196, 2018, doi: 10.1016/j.compositesb.2018.02.012.
- [1-3] S. Qu and Y. Gong, "Effect of heat treatment on microstructure and mechanical characteristics of 316L stainless steel parts fabricated by hybrid additive and subtractive process," *The International Journal of Advanced Manufacturing Technology*, vol. 117, no. 11, pp. 3465-3475, 2021/12/01 2021, doi: 10.1007/s00170-021-07786-w.
- [1-4] D. Ding, Z. Pan, D. Cuiuri, and H. Li, "Wire-feed additive manufacturing of metal components: technologies, developments and future interests," *Int J Adv Manuf Technol*, vol. 81, no. 1-4, pp. 465-481, 2015, doi: 10.1007/s00170-015-7077-3.
- [1-5] F. Martina and S. Williams, "Wire + arc additive manufacturing vs. traditional machining from solid a cost comparison.," Cranfield University, 2015.
- [1-6] Orbex. "Orbex Commissions Largest Industrial 3D Printer in Europe for Rapid Rocket-Building." https://orbex.space/news/orbex-commissionslargest-industrial-3d-printer-in-europe-for-rapid-rocket-building (accessed 03/09/2021.
- [1-7] C. W. Hull, "On Stereolithography," *Virtual and Physical Prototyping,* vol. 7, no. 3, pp. 177-177, 2012/09/01 2012, doi: 10.1080/17452759.2012.723409.
- [1-8] C. W. Hull, "Apparatus for production of three-dimensional objects by stereolithography," United States, 1984.
- [1-9] D. Clark, M. R. Bache, and M. T. Whittaker, "Shaped metal deposition of a nickel alloy for aero engine applications," *Journal of materials*

- *processing technology,* vol. 203, no. 1, pp. 439-448, 2008, doi: 10.1016/j.jmatprotec.2007.10.051.
- [1-10] B. Wu, D. Ding, Z. Pan, D. Cuiuri, H. Li, J. Han, and Z. Fei, "Effects of heat accumulation on the arc characteristics and metal transfer behavior in Wire Arc Additive Manufacturing of Ti6Al4V," *Journal of materials processing technology*, vol. 250, pp. 304-312, 2017, doi: 10.1016/j.jmatprotec.2017.07.037.
- [1-11] Z. Pan, D. Ding, B. Wu, D. Cuiuri, H. Li, and J. Norrish, "Arc Welding Processes for Additive Manufacturing: A Review," in *Transactions on Intelligent Welding Manufacturing*, Singapore, 2018, Pan18: Springer Singapore, in Transactions on Intelligent Welding Manufacturing, pp. 3-24, doi: 10.1007/978-981-10-5355-9 1.
- [1-12] F. Martina, J. Ding, S. Williams, A. Caballero, G. Pardal, and L. Quintino, "Tandem metal inert gas process for high productivity wire arc additive manufacturing in stainless steel," *Additive Manufacturing*, vol. 25, pp. 545-550, 2019/01/01/ 2019, doi: 10.1016/j.addma.2018.11.022.
- [1-13] E. Atzeni and A. Salmi, "Economics of additive manufacturing for endusable metal parts," *International journal of advanced manufacturing technology,* vol. 62, no. 9-12, pp. 1147-1155, 2012, doi: 10.1007/s00170-011-3878-1.
- [1-14] BS EN ISO/ASTM 52900:2017 Additive manufacturing General principles Terminology, BSI, 2017.
- [1-15] A. Busachi, J. Erkoyuncu, P. Colegrove, F. Martina, C. Watts, and R. Drake, "A review of Additive Manufacturing technology and Cost Estimation techniques for the defence sector," CIRP journal of manufacturing science and technology, vol. 19, pp. 117-128, 2017, doi: 10.1016/j.cirpj.2017.07.001.
- [1-16] G. Xu, M. Kutsuna, Z. Liu, and K. Yamada, "Comparison between diode laser and TIG cladding of Co-based alloys on the SUS403 stainless steel," *Surface & coatings technology*, vol. 201, no. 3, pp. 1138-1144, 2006, doi: 10.1016/j.surfcoat.2006.01.040.
- [1-17] J. P. Kelly, J. W. Elmer, F. J. Ryerson, J. R. I. Lee, and J. J. Haslam, "Directed Energy Deposition Additive Manufacturing of Functionally Graded Al-W Composites," *Additive Manufacturing*, p. 101845, 2021/01/22/ 2021, doi: https://doi.org/10.1016/j.addma.2021.101845.
- [1-18] J. Liu, Y. Xu, Y. Ge, Z. Hou, and S. Chen, "Wire and arc additive manufacturing of metal components: a review of recent research developments," *The International Journal of Advanced Manufacturing Technology*, vol. 111, no. 1, pp. 149-198, 2020/11/01 2020, doi: 10.1007/s00170-020-05966-8.
- [1-19] L. Love, B. Post, M. Noakes, A. Nycz, and V. Kunc, "There's Plenty of Room at the Top," *Additive manufacturing*, 2020, doi: 10.1016/j.addma.2020.101727.
- [1-20] S. I. Evans, J. Wang, J. Qin, Y. He, P. Shepherd, and J. Ding, "A review of WAAM for steel construction Manufacturing, material and geometric properties, design, and future directions," *Structures* (Oxford), vol. 44, pp. 1506-1522, 2022, doi: 10.1016/j.istruc.2022.08.084.
- [1-21] F. J. Xu, Y. H. Lv, B. S. Xu, Y. X. Liu, F. Y. Shu, and P. He, "Effect of deposition strategy on the microstructure and mechanical properties of

- Inconel 625 superalloy fabricated by pulsed plasma arc deposition," *Materials in engineering,* vol. 45, pp. 446-455, 2013, doi: 10.1016/j.matdes.2012.07.013.
- [1-22] B. Wu, Z. Pan, D. Ding, D. Cuiuri, H. Li, J. Xu, and J. Norrish, "A review of the wire arc additive manufacturing of metals: properties, defects and quality improvement," *Journal of Manufacturing Processes*, vol. 35, pp. 127-139, 2018/10/01/ 2018, doi: 10.1016/j.jmapro.2018.08.001.
- [1-23] T. E. Abioye, D. G. McCartney, and A. T. Clare, "Laser cladding of Inconel 625 wire for corrosion protection," *Journal of materials* processing technology, vol. 217, pp. 232-240, 2015, doi: 10.1016/j.jmatprotec.2014.10.024.
- [1-24] B. Silwal, J. Walker, and D. West, "Hot-wire GTAW cladding: Inconel 625 on 347 stainless steel," *International journal of advanced manufacturing technology,* vol. 102, no. 9-12, pp. 3839-3848, 2019, doi: 10.1007/s00170-019-03448-0.
- [1-25] T. P. Hoar, "Corrosion-resistant alloys in chloride solutions: materials for surgical implants," *Proceedings of the Royal Society of London.,* vol. 294, no. 1439, pp. 486-510, 1966, doi: 10.1098/rspa.1966.0220.
- [1-26] BS EN ISO 15156-3:2020: Petroleum and natural gas industries. Materials for use in H2S-containing environments in oil and gas production: Cracking-resistant CRAs (corrosion-resistant alloys) and other alloys, BSI, 2020.
- [1-27] E. P. Cardozo, S. Ríos, S. Ganguly, and A. S. C. M. D'Oliveira, "Assessment of the effect of different forms of Inconel 625 alloy feedstock in Plasma Transferred Arc (PTA) additive manufacturing," *Int J Adv Manuf Technol*, vol. 98, no. 5, pp. 1695-1705, 2018, doi: 10.1007/s00170-018-2340-z.
- [1-28] Haynes-International, "Hastelloy C-276 alloy datasheet," 2002.
- [1-29] Deloro, "Stellite 6 Datasheet," 2008.
- [1-30] E. Hosseini and V. A. Popovich, "A review of mechanical properties of additively manufactured Inconel 718," *Additive manufacturing*, vol. 30, p. 100877, 2019, doi: 10.1016/j.addma.2019.100877.
- [1-31] V. Shankar, K. B. S. Rao, and S. L. Mannan, "Microstructure and mechanical properties of Inconel 625 superalloy," *Journal of nuclear materials*, vol. 288, no. 2-3, pp. 222-232, 2001, doi: 10.1016/s0022-3115(00)00723-6.

2. Literature review

This chapter will discuss the current state of wire arc additive manufacturing (WAAM) and its use with corrosion resistant alloys (CRAs). This will begin with a discussion of results from the precursor technology: arc cladding. In addition, the effect of different shielding gasses on welding will be evaluated. Following this, a review is performed on the results of WAAM on CRAs.

2.1. Arc cladding

Cladding can be viewed as a limited additive manufacturing process, where only a few layers are deposited onto the substrate [2-1]. This can be used to improve surface properties such as hardness and corrosion resistance [2-2] by applying hard facing or corrosion resistant alloys to bulk materials such as mild steel [2-3]. The deposition of these materials can be achieved with a laser [2-4] or welding arc (GTAW [2-5] or GMAW [2-1]) which produces different surface properties in addition to varying complexity and cost.

A comparison of these methods has been made by Xu et al. [2-6] with laser and GTAW cladding of the cobalt alloy Stellite 6. This study found that the lower heat input of laser cladding reduced the dilution of the cobalt alloy resulting in a higher hardness of the coating and a reduction in wear rate.

Laser cladding has been further demonstrated with other alloys such as Inconel 625, a nickel-chromium alloy [2-7] and Triballoy T-800, a cobalt-chromium alloy [2-8]. The optimisation of parameters displayed with the T-800 alloy achieved a 33% increase in Vickers hardness. The study of Inconel 625 laser cladding showed a low dilution of 4.5% and very high corrosion resistance, protecting the substrate from attack.

Early literature for arc cladding of Inconel alloys details the manual welding of a pad onto the base metal. As is expected from the results of Xu et al. [6], heat input should be minimised to reduce dilution. Overall, these basic coatings provide a significant improvement in wear and corrosion resistance over their substrate material [2-9]. Bansal et al. [2-10] determined that heat treatment could further improve the effectiveness of Inconel claddings by as much as 15% as well as improving the microstructure through the precipitation of

strengthening particles. Further developments include the use of hot wire GTAW and CMT processes to decrease the heat input, resulting in reduced dilution [2-11,2-12].

WAAM techniques can also be used to deposit structural steel which can then be protected by the deposition of stainless steel as an outer skin, improving the lifespan and reducing cost for maritime applications. For example, in a study by Chandresakeren et al. [2-13] using this method, a small diffusion region was observed; however the improvement in corrosion resistance of deposited stainless steel was shown to be 12 times higher than the base material.

Multiple studies have also described the process of depositing nickel alloys on additively manufactured stainless steel structures which found a bond strength between the materials comparable to that of the base material [2-14]. This process was also conducted with Hastelloy C-276 for tensile and fatigue strength. The samples showed a reduced fatigue life compared to the wrought stainless steel substrate. Failure was noted to initiate in the weaker stainless steel region due to reduced ductility, and a dendritic microstructure. [2-15]. A study with alloy Stellite 6 demonstrated that a minimum energy input is required for a continuous weld bead. However, as discussed previously, an increase in heat input increases the dilution and reduces material hardness, negating the primary advantage of hardfacing with Stellite 6 [2-16].

2.2. Effect of shielding gasses

The primary purpose of shielding gases is to protect the weld pool from oxidizing agents during solidification. In addition, arc stabilization and weld penetration can be controlled using the composition of the shielding gas [2-17]. The parameters which can be modified are gas flow rate, composition and pulsing frequency [2-18].

Argon, helium and carbon dioxide (CO₂) are the gases most commonly used to shield the arc. In certain applications, oxygen, nitrogen and hydrogen are also used in small proportions [2-19]. Used alone, the inert gases (argon and helium) can generate an unstable arc, so are often combined with oxygen or hydrogen to improve the stability. CO₂ and helium are both used to increase

weld penetration, though this is combined with an increase in heat input into the weld which may not be desired [2-20]. For the welding of nickel alloys and stainless steels, gas mixes low in CO₂ are recommended, and helium is typically included to improve the wetting of the melt pool [2-21].

Using schlieren imaging and a high-speed camera, it has been possible to examine the distribution of gases when the gas flow is pulsed at different frequencies. In research published by Bitharas et al. [2-18,2-22] this has been explored with helium and argon. In addition, the gas flows have been examined in a CFD simulation (computational fluid dynamics). Higher frequencies of 8 Hz have been shown to produce premixing while 2 Hz pulsing frequencies produced a transient effect of increased intensity as helium was deposited into the weld area [2-22]. Sufficiently low flow rates have also been shown to allow dangerous concentrations of oxygen into the weld pool, this minimum flow rate varies depending on external conditions [2-18].

2.3. WAAM of stainless steels

One of the most common austenitic stainless steel alloys, SS304 was examined for use with the WAAM process by Sarathchandra et al. [2-23]. This study considered the deposition of single beads on plate using CMT welding and developed an empirical model to optimise the dilution, height, and width of the bead. Other related papers research WAAM of martensitic [2-24,2-25] or duplex [2-13,2-26] stainless steels.

The work of Roy et al. [2-25] on ER410 focussed on different shielding gasses to improve layer height. The mechanical properties of the stainless steel are altered by the shielding gas, with 97% Ar -3% N₂ providing improved hardness and tensile strength. Carbon dioxide was found to cause porosity due to the inclusion of oxygen and moisture in the weld pool. A study by Salahi et al. [2-24] of ER420 investigated the changes in microstructure and properties caused by different inter-pass temperatures of 25°C and 200°C. The results were focussed on corrosion performance and found that a lower interlayer temperature resulted in a greater susceptibility to localised corrosion. This was caused by increased chromium sensitization at the interfaces between δ -ferrite and martensite, while a more isotropic microstructure was observed. At higher

interlayer temperatures, early stages of intergranular corrosion were observed, but the microstructure was highly anisotropic.

Similarly, Zhang et al. [2-27] also studied the corrosion resistance and texture of duplex stainless steel ER2205 produced by WAAM. The samples underwent a post-manufacturing heat treatment at a range of temperatures. This was found to improve corrosion resistance when processed at 1300°C for 1 hour followed by water quenching. Chandrasekaran et al. [2-13] investigated the production of structures containing both duplex stainless steel ER2209 and X-52 carbon manganese steel. It was found that some elemental diffusion took place between the alloys and the strength was comparable to the X-52. In addition, failure occurred away from the transition region due to the formation of high strength martensite [2-13].

Several papers have detailed WAAM and welding procedures for precipitation-hardening (PH) stainless steels. Caballero et al. [2-28], Martina et al. [2-29], and Guo et al. [2-30] have produced WAAM samples using wire of composition ER630. Guo used composition ER631 which better matches the composition of 15-5PH but is not commercially available [2-30].

The research of Caballero et al. [2-28] investigates the importance of weldpath on mechanical properties and microstructure. In addition, the effect of different heat treatments and shielding gases was considered on the mechanical properties in the vertical and transverse directions. Martina et al. [2-29] conducts a study of parameters used in the deposition of ER630 stainless steel including wire feed and travel speeds using a tandem wire feed to increase deposition rate. The work of Guo et al. [2-30] expands on this, considering the effect of heat treatment on ER631, a similar alloy with reduced chromium content. It was found that heat treatment resulted in improved strength while making the alloy less susceptible to brittle fracture.

Other research has investigated the failure modes of welded PH stainless steels. Ziewiec et al. [2-31] detailed a possible mechanism for the formation of hot cracking in ER630 welds. In this case, the vaporisation of copper from the weld pool leads the formation of pure copper deposits within the weld metal, resulting in hot cracking in the heat affected zone (HAZ) while the welds are in

service. The same study suggests that these cracks can be eliminated through remelting which can be achieved through the WAAM process for interior layers but may require post-processing for the upper layers of the sample.

Thomas et al. [2-32] investigated the welding of 15-5PH to a cobalt superalloy (Haynes 25) with filler wires matching the composition of each (ER630 and KC20WN). The results for welds with ER630 filler metal showed a significant decrease in hardness in the weld bead compared to the wrought 15-5PH plate.

2.4. WAAM of nickel-based corrosion resistant alloys

One common problem with the deposition of nickel alloys is the formation of the Laves phase. This can increase brittleness and reduce corrosion resistance [2-33]. Some techniques such as post weld heat treatment or current pulsed welding can be used to reduce the Laves phase and improve mechanical properties [2-34].

A study by Bansal et al. [2-10] confirmed that a heat treatment at 850°C for Inconel 625 produces the highest hardness while partially dissolving the Laves phase. In comparison, 950°C resulted in complete dissolution of Laves and promoted homogenisation of the material, while 650°C resulted in no dissolution.

In general, it has been found that reduction of the arc energy is required to minimise the dilution of the clad layers, however a compromise must be found between dilution and forming a successful weld between the substrate and clad layer. However, despite the presence of iron dilution as high as 7%, Inconel cladding was found to produce a 50 times reduction in corrosion rate compared to structural steel substrates [2-9]. A hot-wire system (passing current through the feedstock wire when performing GTAW) can also be used to reduce the arc energy required, further reducing the dilution [2-12]. Many oil and gas industry specifications require that Inconel cladding achieves dilution of less than 5-7% within the clad layer [2-9].

A range of WAAM strategies have been investigated with nickel alloys these include plasma arc welding, GMAW and GTAW. Plasma arc welding is

complex but can achieve a lower thermal input into the deposit. Early research into the process used alloy GH163 powder and demonstrated a good microstructure and the precipitation of γ and carbides following solution and aging heat treatment [2-35]. This demonstrated the advantages of power deposition for additive manufacturing. As each particle is a single grain, these processes result in a microstructure displaying smaller dendrites.

A series of studies were conducted by Xu et al. [2-36 - 2-38] on the pulsed plasma arc deposition (PPAD) of Inconel 625. These studies evaluated the heat treatment and deposition strategies by examining the microstructure and mechanical properties through the cross section of the samples [2-36]. Hardness was found to increase at the interface between layers due to a refined microstructure while strength decreases gradually with height.

The optimal heat treatment to dissolve the brittle Laves phase, while allowing the precipitation of strengthening phases, was found to be solution treatment followed by aging (STA). Homogenisation followed by STA treatment was found to completely eliminate the Laves phase, but resulted in reduced mechanical properties due to grain growth [2-38].

Another factor which can influence material properties is the deposition strategy. In this case, an interpass cooling strategy was compared to continuous deposition [2-37]. Overall, the sample incorporating interpass cooling was found to display better mechanical properties but lower hardness in the as-deposited condition. Following heat treatment, the sample displayed the highest hardness. In comparison, the continuous deposition strategy leads to a loss of accuracy, high heat buildup, poor surface finish and lowered mechanical properties.

The GTAW and GMAW forms of WAAM process are well developed. While the two most common nickel alloys researched are Inconel 625 and 718, other alloys such as Inconel 600 [2-14], ATI718+ [2-39] and Hastelloy C-276 [2-40] have been investigated.

The most significant difference between Inconel 625 and 718 is in the iron content, with 625 containing a maximum of 5% iron while 718 typically contains 18% [2-41]. 625 also typically contains greater levels of nickel, chromium and

molybdenum while 718 has a greater niobium content [2-42]. ATI718+ is a further development of Inconel 718 with half of the iron content replaced with cobalt and tungsten, improving thermal stability [2-39].

Investigations into WAAM of Inconel 625 have investigated heat treatment [2-42], microstructure, corrosion [2-43] and wear resistance [2-11]. The most common process used is CMT, while early work by Wang used the GTAW process [2-44]. This work found an increase in segregation and a decrease in hardness with increasing build height. These variations were found to be linked to the thermal gradient and cooling rate solidification.

Research by Tanvir et al. [2-42,2-45] and Wang et al. [2-43,2-46] in 2019 and 2020 look closely at the development of the microstructure with different process parameters. The impact of heat treatment was investigated by Tanvir et al. [2-42,2-45], while corrosion processes were researched by Wang et al. [2-43,2-46]. The results following heat treatment confirmed the strengthening effect of precipitates such as metal carbides and δ phase after annealing for 2 hours at 980°C [2-45].

Wang et al. [2-46] also tested the mechanical properties and determined that CMT-WAAM produced Inconel 625 displayed better yield strength than the cast alloy. It was also found that a higher travel speed resulted in superior mechanical properties due to enhanced precipitation. Corrosion performance was found to be non-uniform, with superior corrosion resistance present in the upper region of the sample [2-43].

The earliest example of WAAM using Inconel 718 was by Clark et al. [2-33] in 2008. His work demonstrated the practicality of this process and material combination and identified the risks caused a low cooling rate and the formation of the Laves phase.

Further research by Xu et al. [2-41] identified that the as deposited microstructure was primarily formed of large columnar grains and was poorly suited to form precipitates. This resulted in a reduced improvement in strength through heat treatment compared to the wrought alloy.

A summary of literature by Hosseini et al. [2-47] on the additive manufacture of 718 alloy suggests that a solution and double aging heat treatment should be performed to maximise the γ ' and γ '' phases while dissolving the Laves phase.

An investigation of the variant alloy ATI718+ has only investigated the microstructure, however it detected η phase in place of the typical δ phase following heat treatment. The study also showed niobium segregation similar to other alloys studied [2-39].

Inconel 600 is similar to Inconel 625, however, it has increased Mn and Fe content while retaining the nickel-chromium matrix and niobium content [2-14]. Meanwhile Hastelloy C-276 is a high molybdenum nickel-chromium alloy used in steam equipment in the energy sector due to its corrosion resistance [2-48].

Studies utilising Inconel 600 deposited a bead of the alloy on a previous bead of 308 stainless steel. This determined the compatibility of the two alloys and identified a diffusion region thickness of 0.19mm [2-14]. A study of Hastelloy C-276 investigated the fatigue life of the alloy deposited as a functionally graded material with stainless steel SS904L. The samples produced by WAAM were found to have lower fatigue strength when compared to the wrought alloy [2-15].

Table 2-1 Typical elemental composition of nickel-based corrosion resistant alloys. [2-49]

Alloy	Ni	Cr	Мо	Nb	Fe	Со	W	С
Inconel	67	20	-	2.5	3.0	-	-	0.1
600								
Inconel	64	21.7	8.5	3.8	0.4	-	-	0.02
625								
Inconel	52.3	18.8	3.2	5.3	18.41	0.35	-	-
718								
ATI 718+	52.1	17.6	3.1	5.5	9.1	9.2	1.0	0.004
Hastelloy	57.2	16.2	16.2	-	5.7	0.1	3.6	0.01
C-276								
Alloy	Mn	Р	S	Cu	Ti	Si	V	Al
Inconel	2.0	0.02	0.0015	0.5	0.7	0.5	-	-
600								
Inconel	0.1	0.005	0.001	0.01	0.17	0.14	-	0.1
625								
Inconel	0.15	-	-	-	0.96	-	-	0.53
718								
ATI 718+	-	-	-	-	0.85	-	-	1.5
Hastelloy	0.61	-	0.002	0.03	-	0.08	0.16	-
C-276								

2.5. References

- [2-1] M. K. Saha and S. Das, "Gas Metal Arc Weld Cladding and its Anti-Corrosive Performance- A Brief Review," *Athens Journal of Technology* and Engineering, vol. 5, no. 2, pp. 155-174, 2018, doi: 10.30958/ajte.5-2-4.
- [2-2] N. Murugan, "Stainless steel cladding deposited by automatic gas metal arc welding," *Welding journal*, vol. 76, no. 10, p. 391s, 1997.
- [2-3] M. P. Raj, M. Kumar, and A. K. Pramanick, "Microstructure and hardness evaluation of Stellite 6 coating developed on hot forging die steel using gas tungsten arc cladding process," *Materials Today: Proceedings*, vol. 66, pp. 3718-3722, 2022, doi: 10.1016/j.matpr.2022.05.337.
- [2-4] R. Vilar, "Laser cladding," *Journal of laser applications,* vol. 11, no. 2, pp. 64-79, 1999, doi: 10.2351/1.521888.
- [2-5] Q. Fan, C. Chen, C. Fan, Z. Liu, X. Cai, S. Lin, and C. Yang, "Effect of high Fe content on the microstructure, mechanical and corrosion properties of AlCoCrFeNi high-entropy alloy coatings prepared by gas tungsten arc cladding," *Surface & coatings technology*, vol. 418, p. 127242, 2021, doi: 10.1016/j.surfcoat.2021.127242.
- [2-6] G. Xu, M. Kutsuna, Z. Liu, and K. Yamada, "Comparison between diode laser and TIG cladding of Co-based alloys on the SUS403 stainless steel," *Surface & coatings technology,* vol. 201, no. 3, pp. 1138-1144, 2006, doi: 10.1016/j.surfcoat.2006.01.040.
- [2-7] T. E. Abioye, D. G. McCartney, and A. T. Clare, "Laser cladding of Inconel 625 wire for corrosion protection," *Journal of materials* processing technology, vol. 217, pp. 232-240, 2015, doi: 10.1016/j.jmatprotec.2014.10.024.
- [2-8] K. Malikongwa, M. Tlotleng, and E. O. Olakanmi, "Optimisation of the wear resistance properties of laser cladded T-800 coatings," *The International Journal of Advanced Manufacturing Technology*, vol. 114, no. 1, pp. 481-496, 2021/05/01 2021, doi: 10.1007/s00170-021-06718v.
- [2-9] J. Adamiec, "High temperature corrosion of power boiler components cladded with nickel alloys," *Materials characterization*, vol. 60, no. 10, pp. 1093-1099, 2009, doi: 10.1016/j.matchar.2009.03.017.
- [2-10] A. Bansal, S. Zafar, and Suneet, "Influence of heat treatment on microstructure and mechanical properties of Inconel 625 clad deposited on mild steel," *Indian Journal of Engineering and Materials Sciences*, vol. 24, no. 6, pp. 477-483, 2017.
- [2-11] A. Evangeline and P. Sathiya, "Cold metal arc transfer (CMT) metal deposition of Inconel 625 superalloy on 316L austenitic stainless steel: microstructural evaluation, corrosion and wear resistance properties," *Materials Research Express*, vol. 6, no. 6, p. 066516, 2019, doi: 10.1088/2053-1591/ab0a10.
- [2-12] B. Silwal, J. Walker, and D. West, "Hot-wire GTAW cladding: Inconel 625 on 347 stainless steel," *International journal of advanced*

- *manufacturing technology,* vol. 102, no. 9-12, pp. 3839-3848, 2019, doi: 10.1007/s00170-019-03448-0.
- [2-13] S. Chandrasekaran, S. Hari, and M. Amirthalingam, "Wire arc additive manufacturing of functionally graded material for marine risers," *Materials science & engineering. A, Structural materials: properties, microstructure and processing,* vol. 792, p. 139530, 2020, doi: 10.1016/j.msea.2020.139530.
- [2-14] T. Abe and H. Sasahara, "Dissimilar metal deposition with a stainless steel and nickel-based alloy using wire and arc-based additive manufacturing," *Precision engineering*, vol. 45, pp. 387-395, 2016, doi: 10.1016/j.precisioneng.2016.03.016.
- [2-15] R. A. Kannan, M. S. Kumar, P. N. Kumar, S. N. Shanmugam, A. S. Vishnu, and Y. Palguna, "Process-microstructural features for tailoring fatigue strength of wire arc additive manufactured functionally graded material of SS904L and Hastelloy C-276," *Materials letters*, vol. 274, p. 127968, 2020, doi: 10.1016/j.matlet.2020.127968.
- [2-16] Z. Lin, W. Ya, V. V. Subramanian, C. Goulas, B. di Castri, M. J. M. Hermans, and B. Pathiraj, "Deposition of Stellite 6 alloy on steel substrates using wire and arc additive manufacturing," *The International Journal of Advanced Manufacturing Technology*, vol. 111, no. 1, pp. 411-426, 2020/11/01 2020, doi: 10.1007/s00170-020-06116-w.
- [2-17] M. Tanaka, S. Tashiro, T. Satoh, A. B. Murphy, and J. J. Lowke, "Influence of shielding gas composition on arc properties in TIG welding," *Science and technology of welding and joining*, vol. 13, no. 3, pp. 225-231, 2008, doi: 10.1179/174329308X283929.
- [2-18] I. Bitharas, N. A. McPherson, W. McGhie, D. Roy, and A. J. Moore, "Visualisation and optimisation of shielding gas coverage during gas metal arc welding," *Journal of materials processing technology.*, vol. 255, pp. 451-462, 2018, doi: 10.1016/j.jmatprotec.2017.11.048.
- [2-19] P. Kah and J. Martikainen, "Influence of shielding gases in the welding of metals," *The international journal of advanced manufacturing technology*, vol. 64, no. 9, pp. 1411-1421, 2013, doi: 10.1007/s00170-012-4111-6.
- [2-20] B. Mvola and P. Kah, "Effects of shielding gas control: welded joint properties in GMAW process optimization," *The international journal of advanced manufacturing technology*, vol. 88, no. 9, pp. 2369-2387, 2017, doi: 10.1007/s00170-016-8936-2.
- [2-21] A. S. M. I. H. Committee, ASM handbook. Volume 6, Welding, brazing, and soldering (Welding, brazing, and soldering). Materials Park, OH: Materials Park, OH: ASM International, 1993.
- [2-22] I. Bitharas, S. W. Campbell, A. M. Galloway, N. A. McPherson, and A. J. Moore, "Visualisation of alternating shielding gas flow in GTAW," *Materials & design*, vol. 91, pp. 424-431, 2016, doi: 10.1016/j.matdes.2015.11.085.
- [2-23] D. T. Sarathchandra, M. J. Davidson, and G. Visvanathan, "Parameters effect on SS304 beads deposited by wire arc additive manufacturing," *Materials and manufacturing processes*, vol. 35, no. 7, pp. 852-858, 2020, doi: 10.1080/10426914.2020.1743852.
- [2-24] S. Salahi, A. V. Nemani, M. Ghaffari, J. Lunde, and A. Nasiri, "On Microstructure, Crystallographic Orientation, and Corrosion Properties

- of Wire Arc Additive Manufactured 420 Martensitic Stainless Steel: Effect of the Inter-layer Temperature," *Additive Manufacturing*, p. 102157, 2021/07/02/ 2021, doi: 10.1016/j.addma.2021.102157.
- [2-25] S. Roy, B. Silwal, A. Nycz, M. Noakes, E. Cakmak, P. Nandwana, and Y. Yamamoto, "Investigating the effect of different shielding gas mixtures on microstructure and mechanical properties of 410 stainless steel fabricated via large scale additive manufacturing," *Additive Manufacturing*, vol. 38, p. 101821, 2021/02/01/ 2021, doi: 10.1016/j.addma.2020.101821.
- [2-26] Y. Zhang, F. Cheng, and S. Wu, "Improvement of pitting corrosion resistance of wire arc additive manufactured duplex stainless steel through post-manufacturing heat-treatment," *Materials Characterization*, vol. 171, p. 110743, 2021/01/01/ 2021, doi: 10.1016/j.matchar.2020.110743.
- [2-27] L. Zhang, L. Qi, S. Deng, O. Oguntuase, T. Deng, H. Wang, and O. A. Ojo, "Analyses of Anodically Formed Passive Film and Corrosion Behavior of Wire-arc Additive Manufactured ATI 718Plus® Superalloy," *Additive Manufacturing*, vol. 48, p. 102443, 2021/12/01/ 2021, doi: 10.1016/j.addma.2021.102443.
- [2-28] A. Caballero, J. Ding, S. Ganguly, and S. Williams, "Wire + Arc Additive Manufacture of 17-4 PH stainless steel: Effect of different processing conditions on microstructure, hardness, and tensile strength," *Journal* of materials processing technology, vol. 268, pp. 54-62, 2019, doi: 10.1016/j.jmatprotec.2019.01.007.
- [2-29] F. Martina, J. Ding, S. Williams, A. Caballero, G. Pardal, and L. Quintino, "Tandem metal inert gas process for high productivity wire arc additive manufacturing in stainless steel," *Additive Manufacturing*, vol. 25, pp. 545-550, 2019/01/01/ 2019, doi: 10.1016/j.addma.2018.11.022.
- [2-30] C. Guo, R. Hu, and F. Chen, "Microstructure and performances for 15-5 PH stainless steel fabricated through the wire-arc additive manufacturing technology," *Materials technology*, pp. 1-12, 2020, doi: 10.1080/10667857.2020.1800296.
- [2-31] A. Ziewiec, J. Czech, and E. Tasak, "Welded Joint Cracking in Martensitic Stainless Steel Precipitation-Strengthened with Copper," Archives of metallurgy and materials., vol. 57, no. 4, pp. 1055-1061, 2012, doi: 10.2478/v10172-012-0117-1.
- [2-32] J. V. Thomas, T. K. Thomas, C. R. Anoop, and P. Chakravarthy, "Influence of Filler Wire Material on Dissimilar Welding of 15-5PH to KC20WN (Haynes 25)," *Materials science forum.*, vol. 830, pp. 298-301, 2015, doi: 10.4028/www.scientific.net/MSF.830-831.298.
- [2-33] D. Clark, M. R. Bache, and M. T. Whittaker, "Shaped metal deposition of a nickel alloy for aero engine applications," *Journal of materials processing technology,* vol. 203, no. 1, pp. 439-448, 2008, doi: 10.1016/j.jmatprotec.2007.10.051.
- [2-34] G. D. J. Ram, A. V. Reddy, K. P. Rao, and G. M. Reddy, "Control of Laves phase in Inconel 718 GTA welds with current pulsing," *Science* and *Technology of Welding and Joining*, vol. 9, no. 5, pp. 390-398, 2004, doi: 10.1179/136217104225021788.
- [2-35] W. Zhao and L. Liu, "Structural characterization of Ni-based superalloy manufactured by plasma transferred arc-assisted deposition," *Surface*

- & coatings technology, vol. 201, no. 3, pp. 1783-1787, 2006, doi: 10.1016/j.surfcoat.2006.03.004.
- [2-36] F. Xu, Y. Lv, Y. Liu, P. He, B. Xu, and F. Shu, "Microstructural Evolution and Mechanical Properties of Inconel 625 Alloy during Pulsed Plasma Arc Deposition Process," *Journal of Materials Science & Technology*, vol. 29, no. 5, pp. 480-488, 2013, doi: 10.1016/j.jmst.2013.02.010.
- [2-37] F. J. Xu, Y. H. Lv, B. S. Xu, Y. X. Liu, F. Y. Shu, and P. He, "Effect of deposition strategy on the microstructure and mechanical properties of Inconel 625 superalloy fabricated by pulsed plasma arc deposition," *Materials in engineering*, vol. 45, pp. 446-455, 2013, doi: 10.1016/j.matdes.2012.07.013.
- [2-38] F. Xu, Y. Lv, Y. Liu, B. Xu, and P. He, "Effect of Heat Treatment on Microstructure and Mechanical Properties of Inconel 625 Alloy Fabricated by Pulsed Plasma Arc Deposition," *Physics procedia*, vol. 50, pp. 48-54, 2013, doi: 10.1016/j.phpro.2013.11.010.
- [2-39] G. Asala, A. K. Khan, J. Andersson, and O. A. Ojo, "Microstructural Analyses of ATI 718Plus® Produced by Wire-ARC Additive Manufacturing Process," *Metall and Mat Trans A*, vol. 48, no. 9, pp. 4211-4228, 2017, doi: 10.1007/s11661-017-4162-2.
- [2-40] Z. Qiu, B. Wu, H. Zhu, Z. Wang, A. Hellier, Y. Ma, H. Li, O. Muransky, and D. Wexler, "Microstructure and mechanical properties of wire arc additively manufactured Hastelloy C276 alloy," *Materials & design*, vol. 195, p. 109007, 2020, doi: 10.1016/j.matdes.2020.109007.
- [2-41] X. Xu, J. Ding, S. Ganguly, and S. Williams, "Investigation of process factors affecting mechanical properties of Inconel 718 superalloy in wire + arc additive manufacture process," *Journal of materials processing* technology, vol. 265, pp. 201-209, 2019, doi: 10.1016/j.jmatprotec.2018.10.023.
- [2-42] A. N. M. Tanvir, M. R. U. Ahsan, C. Ji, W. Hawkins, B. Bates, and D. B. Kim, "Heat treatment effects on Inconel 625 components fabricated by wire + arc additive manufacturing (WAAM)—part 1: microstructural characterization," *International journal of advanced manufacturing technology*, vol. 103, no. 9, pp. 3785-3798, 2019, doi: 10.1007/s00170-019-03828-6.
- [2-43] Y. Wang, C. Xizhang, and S. Chuanchu, "Microstructure and mechanical properties of Inconel 625 fabricated by wire-arc additive manufacturing," *Surface & coatings technology*, vol. 374, pp. 116-123, 2019, doi: 10.1016/j.surfcoat.2019.05.079.
- [2-44] J. F. Wang, Q. J. Sun, H. Wang, J. P. Liu, and J. C. Feng, "Effect of location on microstructure and mechanical properties of additive layer manufactured Inconel 625 using gas tungsten arc welding," *Materials* science & engineering. A, Structural materials: properties, microstructure and processing, vol. 676, pp. 395-405, 2016, doi: 10.1016/j.msea.2016.09.015.
- [2-45] A. N. M. Tanvir, M. R. U. Ahsan, G. Seo, J.-d. Kim, C. Ji, B. Bates, Y. Lee, and D. B. Kim, "Heat treatment effects on Inconel 625 components fabricated by wire + arc additively manufacturing (WAAM)—part 2: mechanical properties," *International journal of advanced manufacturing technology*, vol. 110, no. 7-8, pp. 1709-1721, 2020, doi: 10.1007/s00170-020-05980-w.

- [2-46] Y. Wang and X. Chen, "Investigation on the microstructure and corrosion properties of Inconel 625 alloy fabricated by wire arc additive manufacturing," *Materials Research Express*, vol. 6, no. 10, p. 106568, 2019, doi: 10.1088/2053-1591/ab39f6.
- [2-47] E. Hosseini and V. A. Popovich, "A review of mechanical properties of additively manufactured Inconel 718," *Additive manufacturing*, vol. 30, p. 100877, 2019, doi: 10.1016/j.addma.2019.100877.
- [2-48] Q. Guo, Y. Li, J. Qian, H. Yu, and C. Chen, "Study of the pitting corrosion at welding joints of Inconel 625 alloy under high temperature and high H2S, CO2 partial pressure," *International Journal of Electrochemical Science*, vol. 12, pp. 8929-8943, 2017, doi: 10.20964/2017.10.46.
- [2-49] ASM handbook. Volume 2, Properties and selection: nonferrous alloys and special-purpose materials, 10th edition. ed. Materials Park, OH: Materials Park, OH: ASM International, 1990.

3. Experimental apparatus and methods

3.1. Additive manufacturing cell setup

The production of bulk material by wire arc additive manufacturing (WAAM) was performed on a robotic welding cell shown in Figure 3-1. The material produced on this cell provides samples for metallographic analysis and mechanical testing to assess the micro and macroscopic properties of corrosion resistant alloys produced by WAAM.

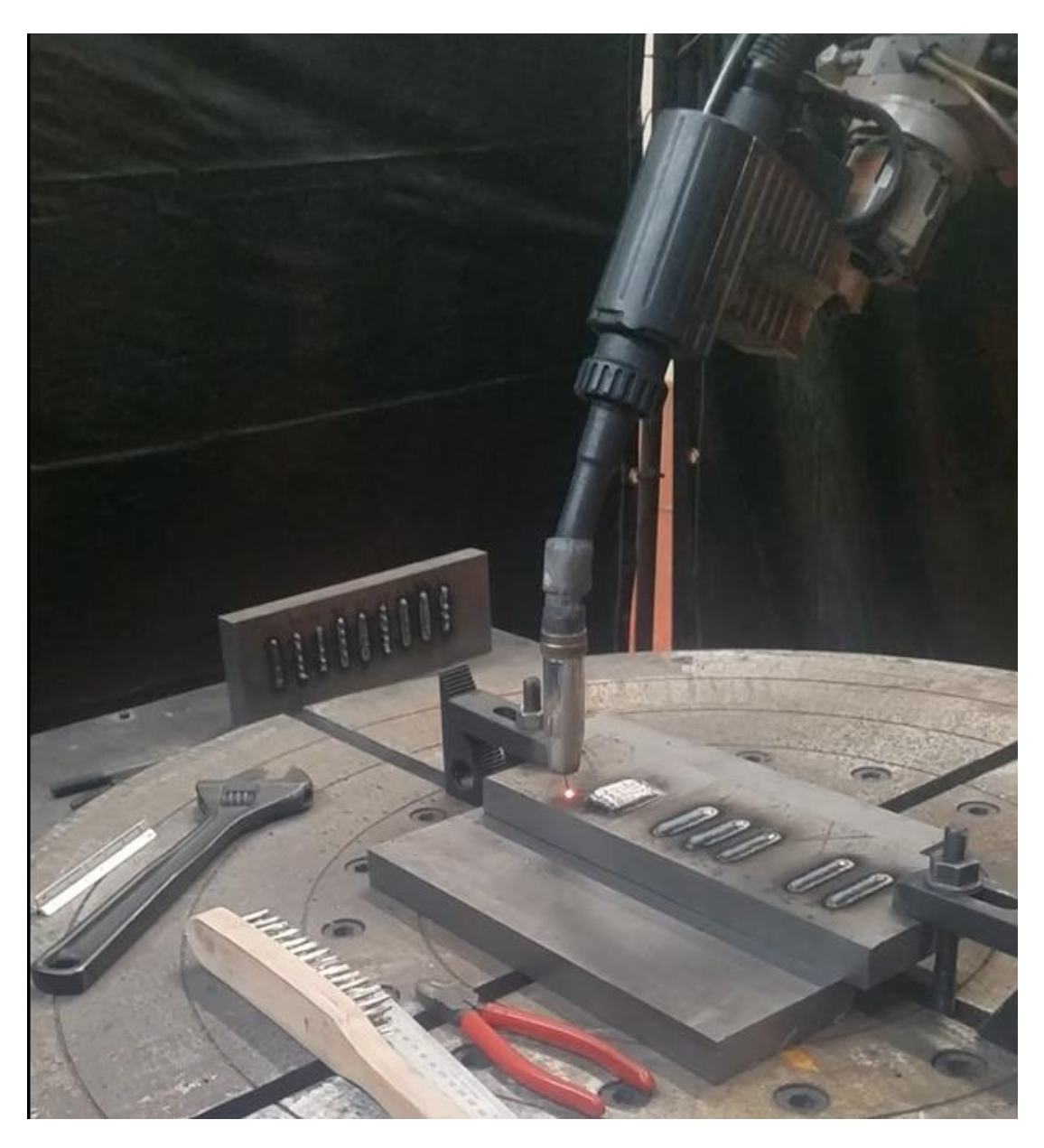


Figure 3-1 An additive manufacturing and robotic welding cell in operation.

3.1.1. Welding system

WAAM deposition typically uses a commercial arc welding system such as gas metal arc welding (GMAW) or gas tungsten arc welding (GTAW) to deposit material. In this case, the cold metal transfer (CMT) process, a variant of GMAW was used. This process forms an electrical arc pulsing at a known frequency to deposit droplets of molten metal from a consumable electrode wire onto the parent material. The stages of this process are shown in Figure 3-2. This process was performed using a Fronius CMT welding system, this includes VR 7000 CMT power supply and torch with push-pull wire feed and RCU 5000i control unit. As the voltage and current vary throughout the process, and are controlled by a synergic curve, the heat input is controlled by varying the wire feed speed and travel speed.

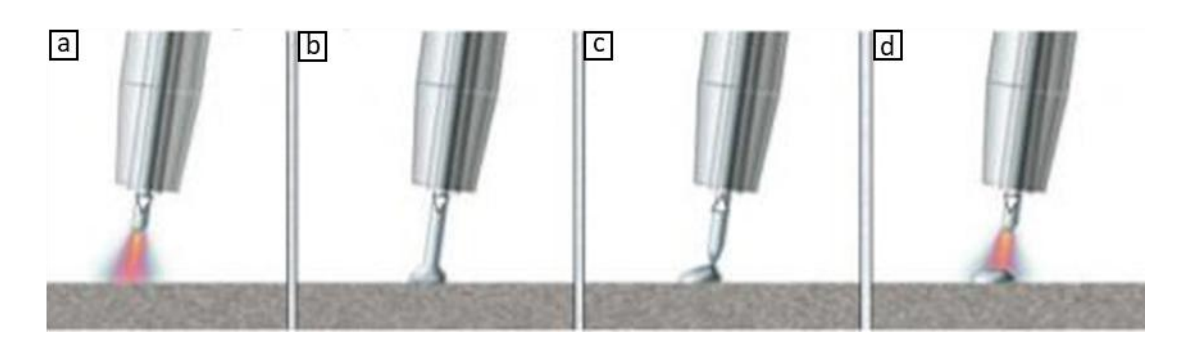


Figure 3-2 Principal phases of the CMT process: a) the arc is ignited and the filler wire is advanced into the weld pool b) when filler metal contacts the weld pool, a short circuit extinguishes the arc c) the filler wire is retracted to detach the droplet d) the wire motion is reversed and the process begins again [3-1].

In GMAW welding processes, of which CMT is a derivative, a shielding gas is used to protect the weld pool from oxidation as it solidifies and cools. This gas is selected depending on the material to be welded. In the case of stainless steel (15-5PH), pure argon is used, while for nickel-based alloys such as Inconel 625 and 718, the shielding gas is 70% argon – 30% helium.

The consumable electrode was selected based on the composition of material to be deposited. To produce material of 15-5PH stainless steel and Inconel 718, a commercial filler wire of matching composition was used, while for the production of Inconel 625, filler wire ERNiCrMo-3 was used. These wires had a diameter of 1.2mm and the feed rate was controlled at the welding control unit, while other welding parameters were determined using the synergic curve

and vary throughout the CMT process. The filler wire was deposited onto 25mm thickness EN32B low-carbon mild steel.

3.1.2. Robotics system

To automate the deposition process, the welding torch must be directed to the appropriate location by means of an automated and precise positioning system. This precise positioning can be achieved using a gantry similar to a CNC machining centre, or a robotic arm. In the production of material for the following studies, a 6 axis ABB 2400L robot arm was utilised. This robot was controlled by an IRC5 control cabinet and teach pendant, with programs created and tested within ABB's RAPID programming environment. The interactions between each component and the welding system is shown in Figure 3-3.



Figure 3-3 A schematic of the components of the additive manufacturing and robotic welding cell.

3.1.3. Pre-heating

To achieve the best deposition, the workpiece is preheated to reduce cooling rate, leading to a reduction in cracking and residual stresses. Therefore, when re-starting production after a long shutdown or depositing directly onto the substrate, the workpiece must be raised to the interpass temperature. This is achieved using a propane torch directed at the workpiece, with the temperature measured periodically with a digital thermocouple probe to ensure the correct temperature is achieved.

3.2. Materials

3.2.1. Bulk materials

All samples were deposited on a substrate of 080A15 mild steel, while a range of filler materials were used. The mechanical properties and chemical composition of these alloys are shown in Table 3-1 and Table 3-2.

3.2.2. Shielding gas

Two shielding gas mixtures were used in the course of these studies. Pure argon was used in the deposition of stainless steel 15-5PH, while the deposition of ERNiCrMo-3 and Inconel 718 was shielded with 70% argon - 30% helium gas.

3.3. Heat treatment

Where components required heat treatment [3-2], a Carbolite RHF1500 resistive furnace capable of 1500°C with Eurotherm digital set point control was used. To reduce the development of an oxidative skin, 321 stainless steel heat treatment foil was used to approach the effect of heat treating in a vacuum furnace.

3.4. Metallographic analysis

To better understand the effect of the wire arc deposition process on materials, metallographic samples have been prepared to analyse micro and macroscopic features.

3.4.1. Sample preparation

3.4.1.1. Cutting

Many methods for extracting samples from a workpiece can influence the microstructure or chemical composition, including through thermal input. As such, silicon carbide abrasive cutting disks were used with coolant to extract metallographic samples while a water-jet cutter was used to produce the shape of testing coupons.

Table 3-1 Chemical composition range of materials. TYPO FOR EN32B, had UTS and YS mixed round

Chemical		<u>Z.</u>	Cr	Fe	S S	Mo	∄	≥	Cu	M o	<u>S</u>	ဂ	ס	တ
element %														
Filler wire	15-5PH	3.50-	14.00-	Bal.	0.15-	1	•	•	2.50-	1.00	1.00	0.07	0.040 0.030	0.030
	[3-3]	5.50	15.50		0.45				4.50					
	ERNiCrMo- 64.33 22.32 0.3	64.33	22.32		3.44	9.10	0.018 0.12	0.12	0.01	0.01	0.07	0.01	0.003 0.001	0.001
	3 [3-4]													
	Inconel 718 50-55 17-21	50-55		Bal.	4.75- 2.80-	2.80-	0.65-	•	0.20-	0.20- 0.30 0.35	0.35		0.08 0.015 0.015	0.015
	[3-4]				5.50	3.30	1.15		0.80					
Substrate	080A15	'	•	Bal.	•	'	1	'	'	0.70	0.22		0.15 0.016 0.010	0.010
	[3-5]													
Table 3 0 Manhanisal proportion of matarials		,												

lable 3-2 Mechanical properties of materials.

Mechanical property	Material	Yield strength	strength Tensile strength	Elongation
(as deposited)		(MPa)	(MPa)	(%)
Filler wire	15-5PH [3-3]	740	930	10
	ERNiCrMo-3 [3-4] 470	470	750	42
	Inconel 718 [3-4]	567.4	832.5	28
Substrate	080A15 [3-5]	357	467	23

3.4.1.2. Sample Mounting

Mounting samples in a phenolic resin allows samples to be easily manipulated and reduce damage in the lab environment.

This was performed with an ATM Opal 410 mounting press and MetPrep Bakelite phenolic resin, with Conducto-mount conductive resin used to provide a conductive surface for electron microscopy. This process of hot mounting provides good sample quality and short processing times. The edges of these samples were bevelled to eliminate any burrs which could impact the grinding plane.

3.4.1.3. Grinding

A grinding process is used to produce a consistent surface, free of damage and residual stress caused by cutting. This is achieved with a progression of silicon carbide (SiC) abrasives of progressiveness fineness. A Struers Rotopol-21 automated grinding and polishing machine is used with water both as a coolant and to eliminate detached abrasive particles and removed material. The grade of abrasive paper is defined by the number of SiC grains per square inch. Papers of grade 120, 220, 500, 800, 1200 and 2400 were used for 2 minutes each under a force of 110N per sample at 300rpm.

3.4.1.4. Polishing

The same grinding-polishing machine was used with polishing pads to produce a fine high surface finish. Polishing pads are covered in soft cloth where abrasive particles are suspended in a lubricant allowing them to roll or slide. Two "coarse stages" are used, with 6µm and 3µm diamond particles lubricated by an alcohol-based coolant on a DP-MOL pad while the final stage of polishing is achieved with an aqueous suspension of 0.05µm colloidal silica on an OP-CHEM pad.

Each polishing stage is performed for 2 minutes each under a force of 90N per sample at 150rpm with corotation enabled for the final polishing stage.

3.4.1.5. Etching

After polishing to a mirror finish for metallographic analysis, the sample will appear as a white image with little detail under the microscope. Chemical or electrolytic etching can be used to reveal microscopic features such as grain boundaries and precipitates. This is achieved through preferential reaction by the etchant. The etchant used in these studies was Kalling's No.2 reagent to reveal ferrite grains in stainless steel (12g cupric chloride, 20ml hydrochloric acid, 225ml ethanol).

A stronger etching process is required to reveal the microstructure of nickel-based corrosion resistant alloys. In this case, 10% oxalic acid solution was used for electrolytic etching at 2 volts. This creates an electrochemical reaction, where electrochemically reactive elements of the sample (the cathode) are dissolved, and electroplate an electrode also immersed in the electrolyte (the anode).

These processes result in microstructural detail being revealed as shown in Figure 3-4, with different responses noted for i) deposited 15-5PH, ii) dilution zone between 15-5PH and mild steel substrate, iii) Inconel 625.

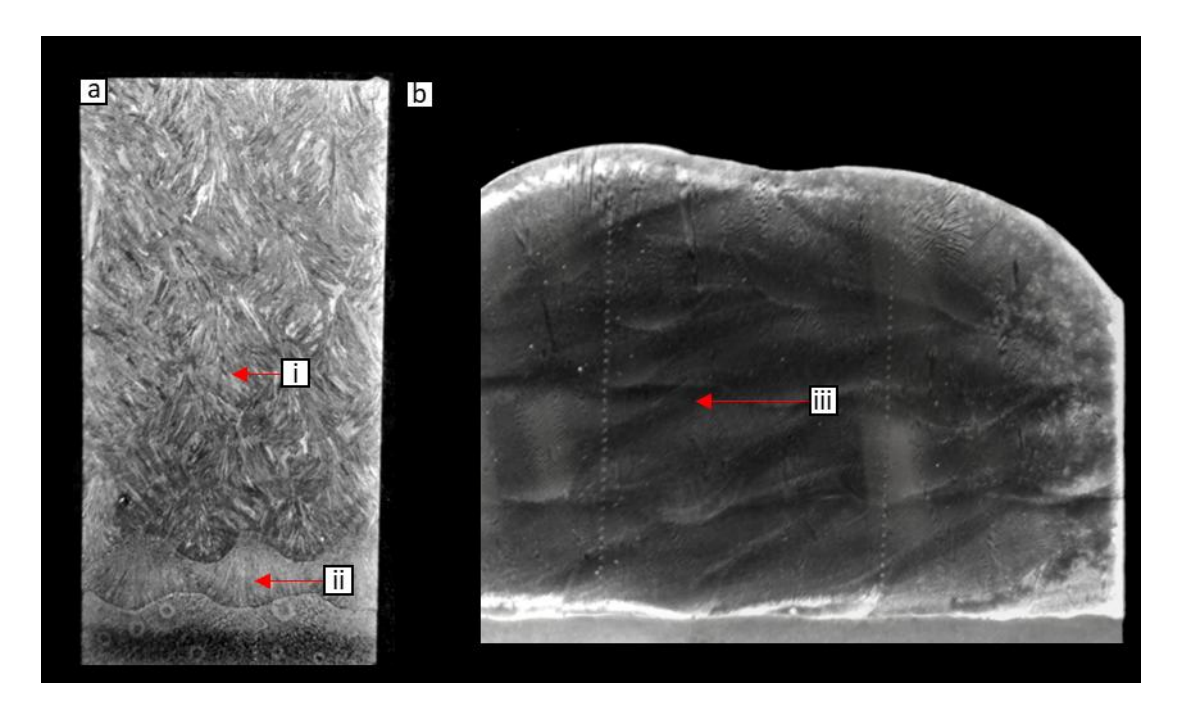


Figure 3-4 Micrographs showing the results of (a) chemical etching of WAAM 15-5PH and (b) electrolytic etching of Inconel 625 and 718.

3.4.2. Optical microscopy

An Olympus GX51 inverted microscope is used to image the samples at magnifications up to 1000 times. Through the use of a UIS2 optics system and depolariser a high contrast and clarity image can be achieved.

A differential interference contrast (DIC) system is also used to enhance contrast which can be used to observe 3D formations in the sample surface. However, due to the inclusion of additional prisms in the light path, resolution is reduced. The DIC was only used for identifying features for closer examination under optical microscopy and has not been used for imaging or analysis in this thesis.

3.4.3. Hardness testing

3.4.3.1. Macrohardness

For assessing the hardness of a material in preliminary testing, a macro hardness tester is used. The machine is a manually operated Vickers hardness tester with a load of 5kg. The sample is positioned using a low power optical microscope before preparing the load and engaging the diamond indenter. The resulting indent is measured using optical shutters; with hardness being found by comparing the indent size to a data table.

3.4.3.2. Microhardness

Microhardness was performed on samples prepared for metallographic analysis using a Q-ness 60A+ evo automated microhardness tester shown in Figure 3-5. The load and dwell time was determined by the indent spacing, with these spacings kept large enough to eliminate the effect of work hardening on subsequent indents. The optical instruments contained within the equipment determined the hardness from indent size, with measurements bring verified manually.



Figure 3-5 Qness 60A+ automated hardness tester.

3.4.4. Scanning electron microscopy (SEM)

To resolve smaller details than are possible through optical microscopy, a scanning electron microscope (SEM) can be used. This is due to the de Brogli wavelength of electrons being less than that of visible light. The spectrum of electrons emitted and then detected by the SEM can also be used to determine the elements present under the electron beam. A combination of three (3) sensors are primarily used in SEM analysis of a sample. Analysis was performed using an electron acceleration voltage of 15.0kV and a working distance of 10mm.

1. A secondary electron (SE) detector which detects electrons ejected directly from the atoms struck by the electron beam.

- 2. A backscatter electron detector (BSE) which detects electrons reflected or which approach and escape the nuclei of an atom in the sample.
- 3. The electron dispersive spectroscopy (EDS) sensor analyses the release of characteristic x-rays caused by the interaction of the electron beam with the sample. This can be used to identify the elements present and their proportions.

For these observations, a Hitachi S3700-N W-SEM was used with an Oxford Instruments X-Max 80mm² SDD EDS detector.

3.4.4.1. Secondary electron detector (SE)

The secondary electron detector is primarily used to observe the topology of samples. Due to their low energy, only secondary electrons originating from within a few nanometers of the surface of the sample are detected. Topology can be mapped because as the angle of incidence relative to the electron beam increases, the number of secondary electrons which escape also increases, leading to a brighter region in the image.

3.4.4.2. Backscatter electron detector (BSE)

In contrast to the secondary electron detector, the backscatter electron detector is used to identify the average atomic mass in a region. This phenomenon is caused by the high energy electrons of the beam being backscattered by high atomic mass nuclei. Thus, heavier elements appear brighter, while lighter elements, darker.

3.4.4.3. Electron dispersive spectroscopy (EDS)

When atoms are excited by the electron beam then return to their ground state, X-rays are released. The energy of these X-rays corresponds to a spectrum for each given atom; this allows the elements present to be identified. The observational capability of this sensor is limited in its analysis of elements of low atomic mass (lighter than sodium) and present in low quantities, such as trace alloying elements.

3.4.5. Glow discharge analysis

To make up for the limitations of EDS for chemical analysis, glow discharge optical emission spectroscopy (GD-OES) was performed using a Horiba GD-Profiler 2. This apparatus creates a plasma which sputters atoms from the sample surface. Now in the gaseous state, optical emissions from these atoms can be measured to determine the elemental composition in relation to reference samples. This is a quantitative method and is calibrated using certified reference materials.

3.5. Mechanical analysis

The bulk mechanical properties of a material are influenced by the microstructure but are also affected by macroscopic properties such as porosity. As such, a range of mechanical testing techniques were used to assess the mechanical properties of material produced by WAAM. This included tensile, fatigue and impact testing.

Samples of Inconel 625 and 718 were extracted in the horizontal orientation due to the material's low susceptibility to build direction as shown by Xu et al. [3-6].

The samples for mechanical testing were extracted from walls of deposited material with the following dimensions: 235mm x 30mm x 110mm. The nesting diagram for these walls are shown in Figure 3-6, while an example of a completed wall is shown in Figure 3-7. These samples were extracted through waterjet cutting followed CNC milling to reach the final dimensions shown in Figure 3-8.

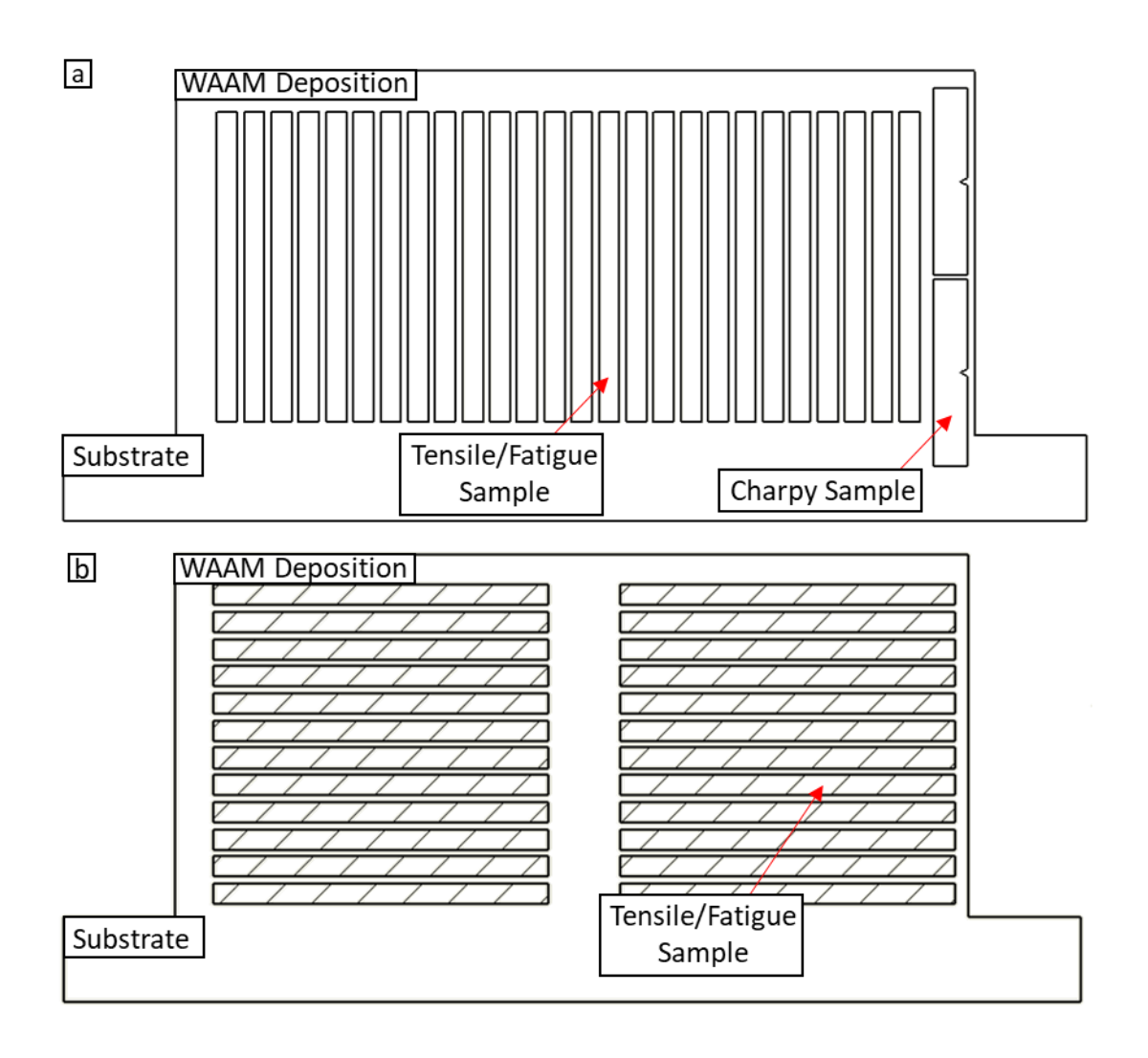


Figure 3-6 Nesting diagrams for walls deposited of a) 15-5PH Stainless Steel and b) Inconel 625 and 718 showing the locations of extracted samples.



Figure 3-7 A completed example of a deposited wall.

3.5.1. Tensile testing

To assess the elastic modulus, elastic limit, ultimate tensile stress (UTS) and elongation of material produced by WAAM, samples were tested in an Instron 8802 250kN servo-hydraulic universal testing machine. This apparatus uses precisely controlled hydraulics to apply axial load to a specimen held between its grips. Load was applied at a rate of 1mm extension per minute, with the elastic limit determined by the 0.2% offset strain. The dimensions of these samples are shown in Figure 3-9a and b. Testing was performed in accordance with standard ASTM E8 [3-7].

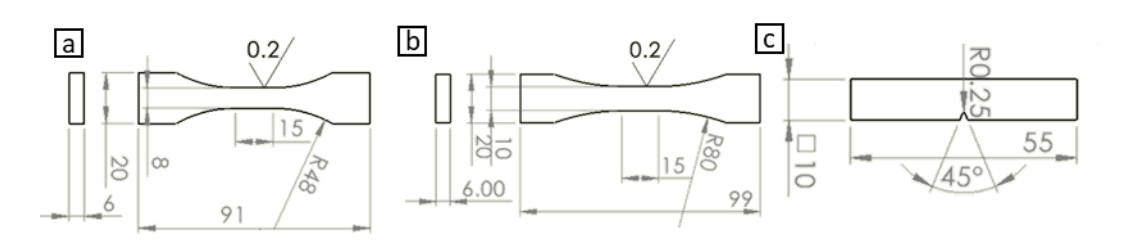


Figure 3-8 Dimensioning and tolerances of a) tensile and fatigue testing samples of 15-5PH Stainless steel b) tensile and fatigue testing samples of Inconel 625 and 718 c) Charpy impact samples of 15-5PH Stainless steel. Tensile and fatigue samples were produced to standard ASTM E8 [3-7] while Charpy impact samples were produced to standard BS EN 148 [3-9].

3.5.2. Fatigue testing

To assess the strength of material over repeated loading cycles below failure throughout its life, fatigue testing is required [3-8]. For a direct comparison, all tests were performed on the Instron 8802 with a loading ratio of 0.1 and cycle frequency of 10Hz. The maximum stress during testing was defined as a percentage of the yield stress or 0.2% proof stress identified during tensile testing.

The same sample design used in tensile testing was used. This incorporated a surface finish of Ra<0.2µm and a large radius of transition between the grips and reduced area. This improved surface finish was achieved through manual polishing with silicon carbide papers up to grade 2400, similar to metallographic grinding.

3.5.3. Charpy impact toughness testing

Impact toughness testing was performed using a Losenhausenwerk 14590 Charpy impact apparatus with a capacity of 290J shown in Figure 3-9. These tests were conducted using samples which met standard BS EN 148 [3-9] with dimensions shown in Figure 3-8c. This test involves striking a notched square cross section sample with mass at the end of a pendulum. The energy required to fracture the sample is determined from the height the pendulum rises to following contact with the sample [3-9].



Figure 3-9 Losenhausenwerk 14590 Charpy impact apparatus with sample capturing enclosure.

3.6. References

- [3-1] A. Evangeline and P. Sathiya, "Cold metal arc transfer (CMT) metal deposition of Inconel 625 superalloy on 316L austenitic stainless steel: microstructural evaluation, corrosion and wear resistance properties", *Materials Research Express*, vol. 6, no. 6, p. 066516, 2019, doi: 10.1088/2053-1591/ab0a10.
- [3-2] ASM handbook: Induction Heating and Heat Treatment (no. 30). Beaverton: Beaverton: Ringgold, Inc, 2014.
- [3-3] A693-16 Standard Specification for Precipitation-Hardening Stainless and Heat-Resisting Steel Plate, Sheet, and Strip, ASTM-A693, 2016.

- [3-4] ASM handbook. Volume 2, Properties and selection: nonferrous alloys and special-purpose materials, 10th edition. ed. Materials Park, OH: Materials Park, OH: ASM International, 1990.
- [3-5] ASM handbook. Volume 1, Properties and selection: irons, steels, and high-performance alloys, 10th edition. ed. Materials Park, OH: Materials Park, OH: ASM International, 1990.
- [3-6] F. J. Xu, Y. H. Lv, B. S. Xu, Y. X. Liu, F. Y. Shu, and P. He, "Effect of deposition strategy on the microstructure and mechanical properties of Inconel 625 superalloy fabricated by pulsed plasma arc deposition," *Materials in engineering*, vol. 45, pp. 446-455, 2013, doi: 10.1016/j.matdes.2012.07.013.
- [3-7] E8-21 Standard Test Methods for Tension Testing of Metallic Materials, ASTM-E8, 2021.
- [3-8] E466-21 Standard Practice for Conducting Force Controlled Constant Amplitude Axial Fatigue Tests of Metallic Materials, ASTM-E466, 2021.
- [3-9] BS EN ISO 148-1:2016: Metallic materials. Charpy pendulum impact test. Test method, BS148-1, 2016.

4. 15-5PH precipitation-hardening stainless steel

Precipitation-hardening stainless steels such as 15-5PH rely on the precipitation of alloyed elements such as copper to increase strength and hardness through heat treatment [4-1].

The alloy 15-5PH has a predominantly martensitic structure in addition to precipitates, primarily copper nanoparticles, though carbides and other phases can also be present depending on the thermal history [4-2]. A high temperature solutionising treatment is important as a means of returning the elements required for precipitation hardening back into solution within the matrix. Following this, a precipitation hardening or aging treatment leads to the development of copper and carbide precipitates, increasing strength.

The primary means of modifying the microstructure is solution treatment followed by aging heat treatments. Solution treatment is conducted at 1040°C for 1 hour with aging performed between 482°C (H900) and 621°C (H1150) for 4 hours. Reverted austenite forms during heat treatment over 550°C which softens the alloy, while the precipitation of copper hardens the alloy. Note that the designations (H900, H1025 and H1150) reference the aging temperature in °F by convention. This effect is reduced with increasing temperature as the precipitates coarsen [4-3]. A summary of the most common heat treatments is shown in Table 4-1.

4.1. Microstructure

This section will detail the microstructure found in 15-5PH alloy produced both from wrought plate and by wire arc additive manufacturing (WAAM). These microstructures will be compared to determine the differences between these production methods. The samples produced using WAAM used 2 different sets of process parameters, designed to investigate the effect of changing the thermal input of the process by varying the travel speed. These are subsequently referred to as high heat (HH) and low heat (LH). Details of the process parameters are shown in Table 4-3. Due to the complex waveform of CMT, only an indicative voltage and current was collected from the welding control unit, which are presented in the table.

Table 4-1 Heat treatments for 15-5PH alloy. Visualised in Figure 4-1.

Heat treatment	Temperature °C	Time
Condition A	1040	1 hr
H900	482	4 hr
H1025	555	4 hr
H1150	621	4 hr

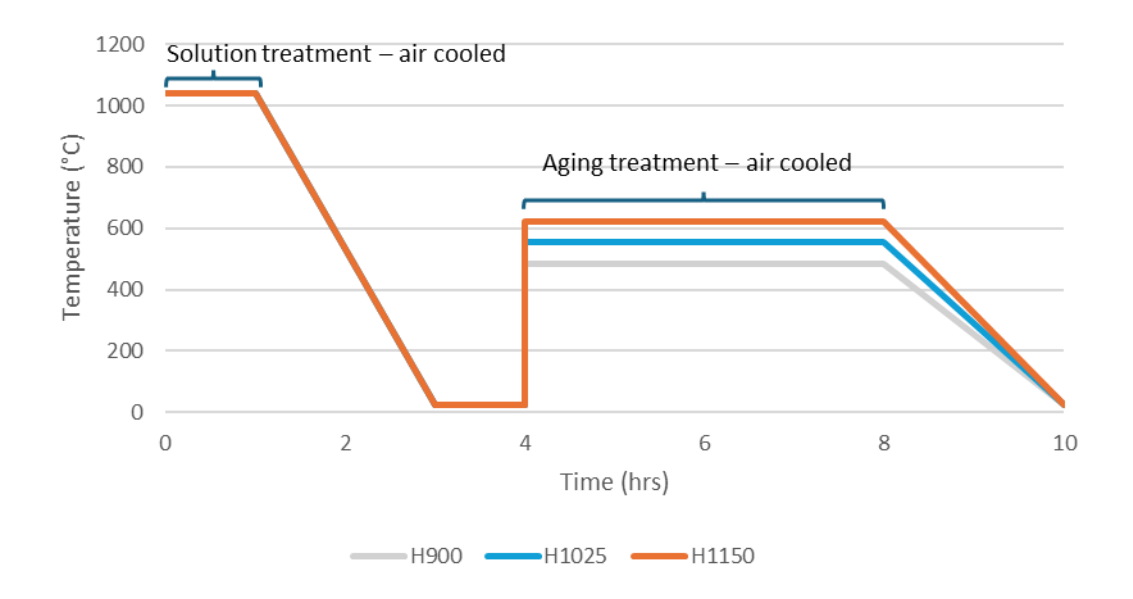


Figure 4-1 Time – temperature chart for heat treatment.

Table 4-2 Composition of 15-5PH from glow discharge measurement.

Element	Fe	Cr	Ni	Cu	Nb
Composition %	Bal.	14.5	4.89	2.94	0.14
Element	Si	С	Mn	P	
			14111	•	

Table 4-3 Process parameters for WAAM deposition of 15-5PH.

Process parameter	CMT program	Travel speed	Wire feed speed	Standoff distance	Weave
P	program.	(mm/s)	(m/min)	(mm)	
High heat	CuNi30Fe	4	6.5	15	2mm
(HH)					circular
Low heat	CuNi30Fe	10	6.5	15	none
(LH)					
Process	Interpass	Step	Indicated	Indicated	Heat
parameter	temperature	width	Current (A)	Voltage (V)	input
	(°C)	(mm)			(kJ/mm)
High heat	200	6	157	18.0	0.565
(HH)					
Low heat	200	4	173	16.1	0.223
(LH)					

4.1.1.Wrought 15-5PH

The alloy 15-5PH is typically supplied in Condition A, the solution treated state. To tailor strength, ductility and toughness, aging heat treatments are then performed. The H1025 and H1150 conditions have been analysed to compare the effect of aging temperature. The composition of this alloy was determined using glow discharge analysis with the results shown in Table 4-2.

During an initial microstructural analysis of heat-treated material shown in Figure 4-2, a skin of chromium oxide (CrO) was discovered following heat treatment. To combat the formation of this surface layer, subsequent samples were sealed within stainless steel foil during heat treatment. The temperature of the foil raises more rapidly than the sample, causing rapid oxidation of the foil, absorbing oxygen within the sealed volume. This produces a similar effect to a vacuum furnace and reduces the production of an oxidative skin.

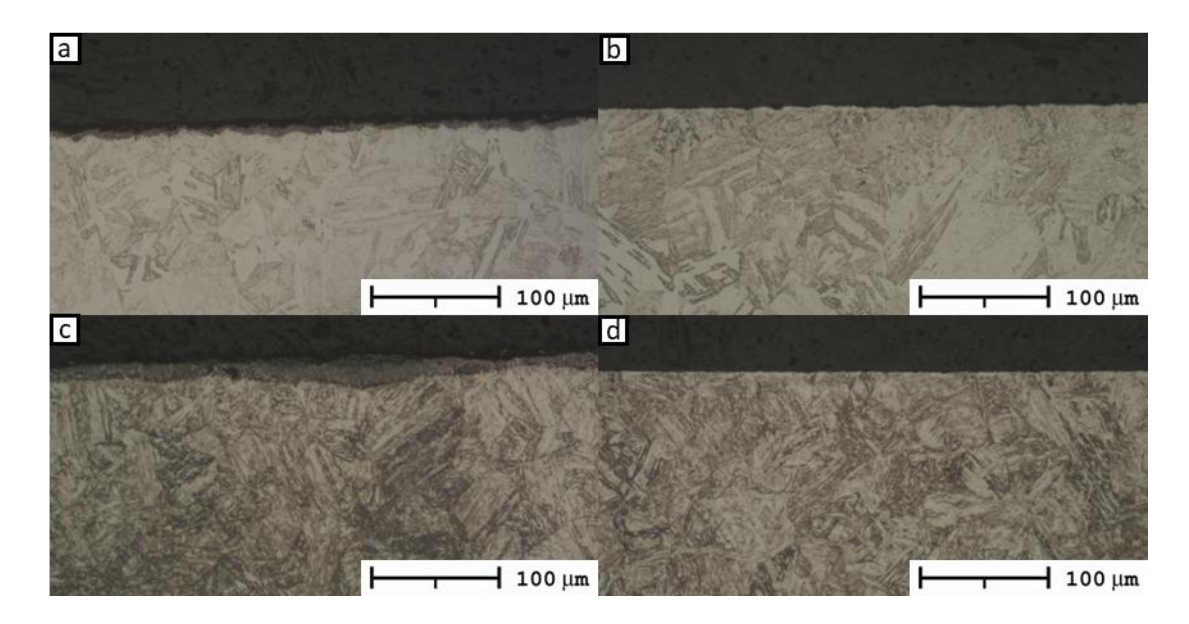


Figure 4-2 Comparison showing the effect of foil on skin oxidation. a) H1025 b) H1025 with foil c) H1150 d) H1150 with foil.

The microstructure is dominated by a martensitic matrix within which, other phases will precipitate. The largest of these are rectangular or angular regions with a golden colour. Also of note are smaller, round precipitates.

The composition of different precipitates was identified using scanning electron microscopy (SEM). The backscatter electron detector (BSE) was used to locate discontinuities in elemental composition. Finally, energy dispersive

spectroscopy (EDS) was then used to identify the elements contained within a precipitate and determine the composition.

The angular golden precipitates were identified to have a composition of TiCN (titanium carbonitride) while the small, round precipitates were found to predominantly have a composition of NbC (niobium carbide) and other metal carbides (MC).

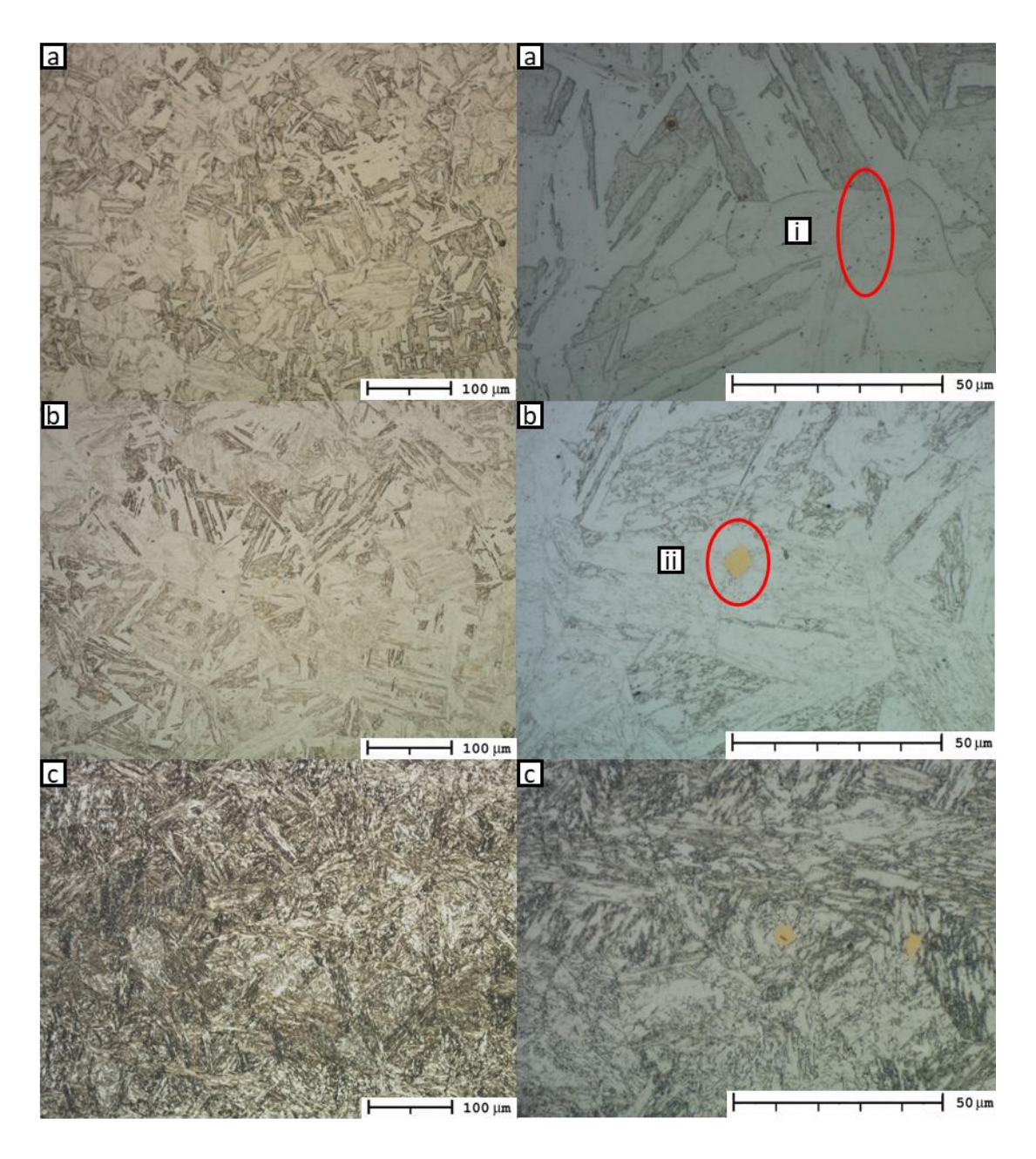


Figure 4-3 Micrographs of wrought 15-5PH of heat treatments a) Condition A b) Condition A + H1025 c) Condition A + H1150 i) small precipitates such as NbC ii) TiCN carbonitrides.

It can be seen in Figure 4-3 that the aging treatment causes the coarse martensitic laths produced by solution treatment (Figure 4-3a) to be refined, particularly in the case of over aging: Condition A + H1150 (Figure 4-3c). Aging treatment also causes the growth of carbonitride precipitates. These are present in small numbers following solution treatment, but following the H1025 and H1150 heat treatment, their size and quantity has increased.

Smaller, globular inclusions were also identified. These were determined to be NbC precipitates based on their size and shape compared to previous literature [4]. Increased aging temperature caused an increase in the quantity of these precipitates.

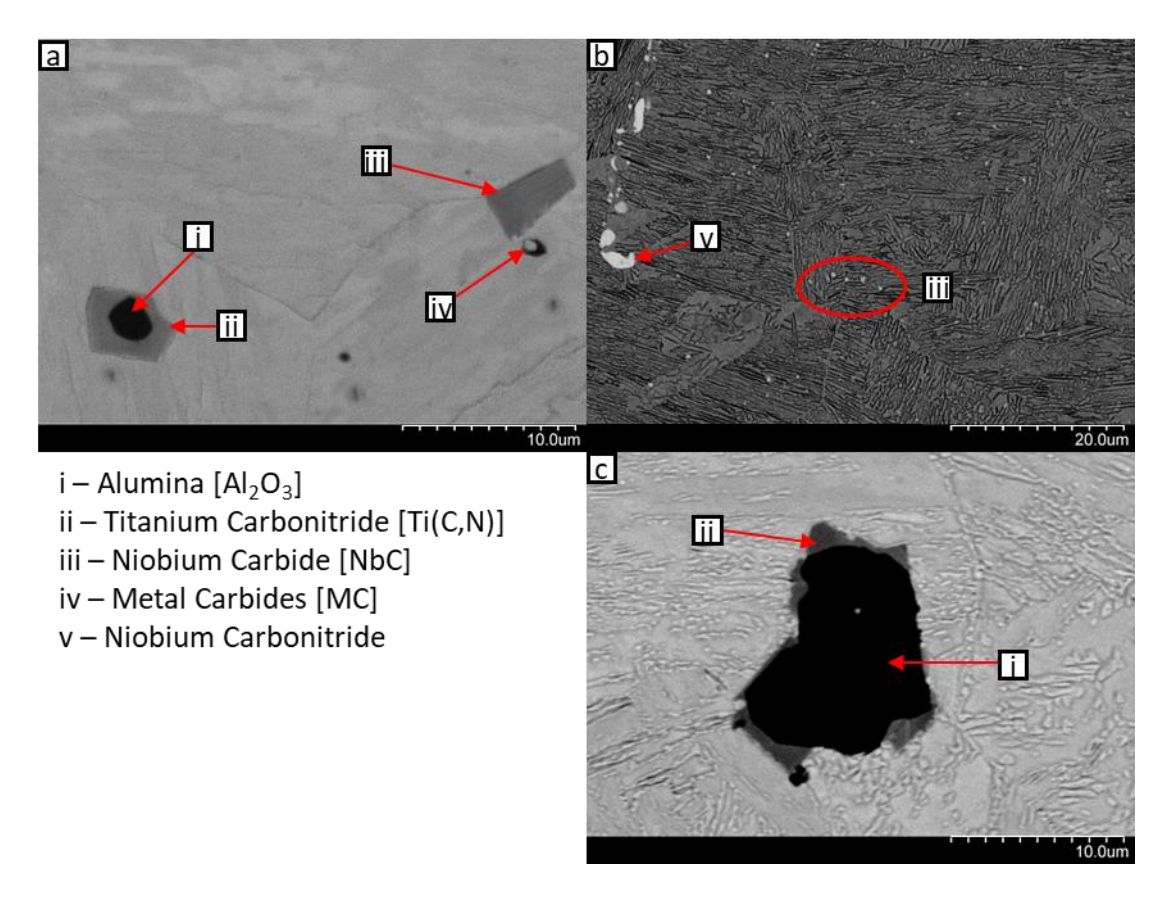


Figure 4-4 Backscatter electron (BSE) images of precipitates in 15-5PH alloy. a) a pair of angular precipitates in solution treated alloy. b) Niobium carbides (NbC) and carbonitrides (Nb(C,N)) and c) a large alumina and titanium carbonitride precipitate in solution treated and over-aged alloy.

In Figure 4-4, the large precipitates were identified by EDS to be a combination of an alumina seed [4-5], from which, titanium carbonitride grows (i and ii). The smaller precipitates were found to display a range of compositions, some metallic carbides (iv) primarily of iron (cementite, Fe₃C) while the majority were

identified as niobium carbide (iii). Stringers of globular precipitates in BSE imaging indicate the presence niobium carbonitride precipitates [4-6] which are not visible to optical or secondary electron imaging.

Copper precipitation is observed in the literature following aging, however these are observed using transmission electron microscopy (TEM) to have a precipitate size of 5nm [4-7], smaller than can be resolved with scanning electron microscopy (SEM).

4.1.2. WAAM 15-5PH: high heat input (HH)

Two sets of process parameter have been developed for comparison with the wrought alloy. The first of these results in a high heat input. This causes significant heat buildup, requiring cooling between passes to an interpass temperature of 200°C. Comparisons are made between samples in the asdeposited condition and following aging heat treatment H1150.



Figure 4-5 Schematic of microstructure locations within WAAM produced material.

It is expected that the varying thermal history in each section will lead to different microstructures [4-2, 4-4]. Close to the substrate (Figure 4-5-1a/b), the microstructure will experience thermal cycles from each subsequent welding pass in addition to iron dilution from the mild steel substrate on the initial layers. The highest point of the component (Figure 4-5-3a/b) will experience rapid cooling while the intermediate location (Figure 4-5-2a/b) is representative of bulk material. To examine this difference, micrographs from each region will be compared.

The alloy 15-5PH produces a martensitic matrix when welded; however, due to the rapid solidification during the cooling of the weld pool and steep thermal

gradients, a directional, dendritic microstructure is produced in the direction of the greatest thermal gradient.

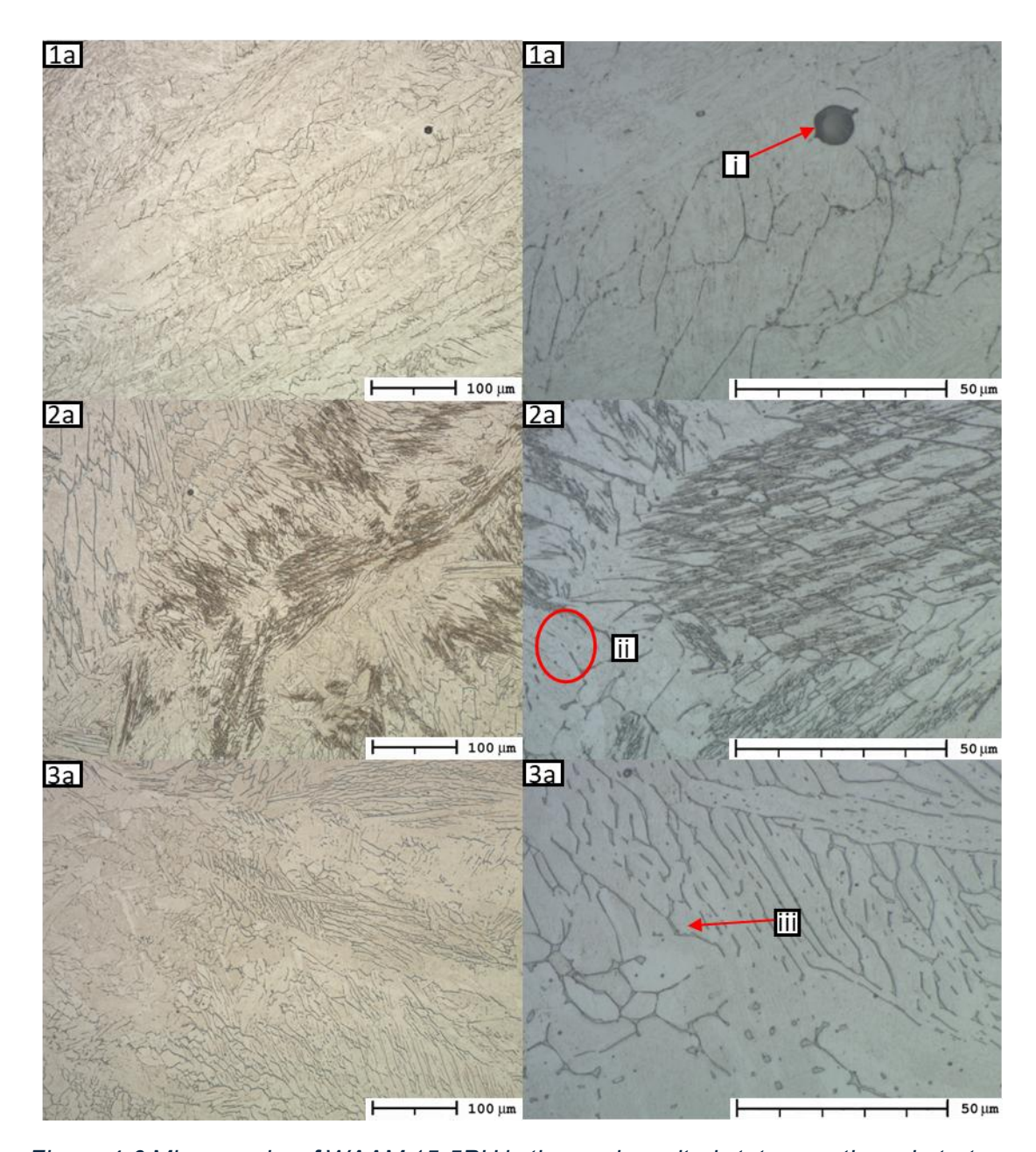


Figure 4-6 Micrographs of WAAM 15-5PH in the as-deposited state near the substrate (1a), middle (2a) and at the top (3a) of the sample.

A number of features are noted within the microstructure, these are similar to those found in the wrought material. In Figure 4-6 and Figure 4-7, these are identified as: i) gas pores within the deposition, ii) small carbide precipitates (such as MC), iii) δ -ferrite dendrites.

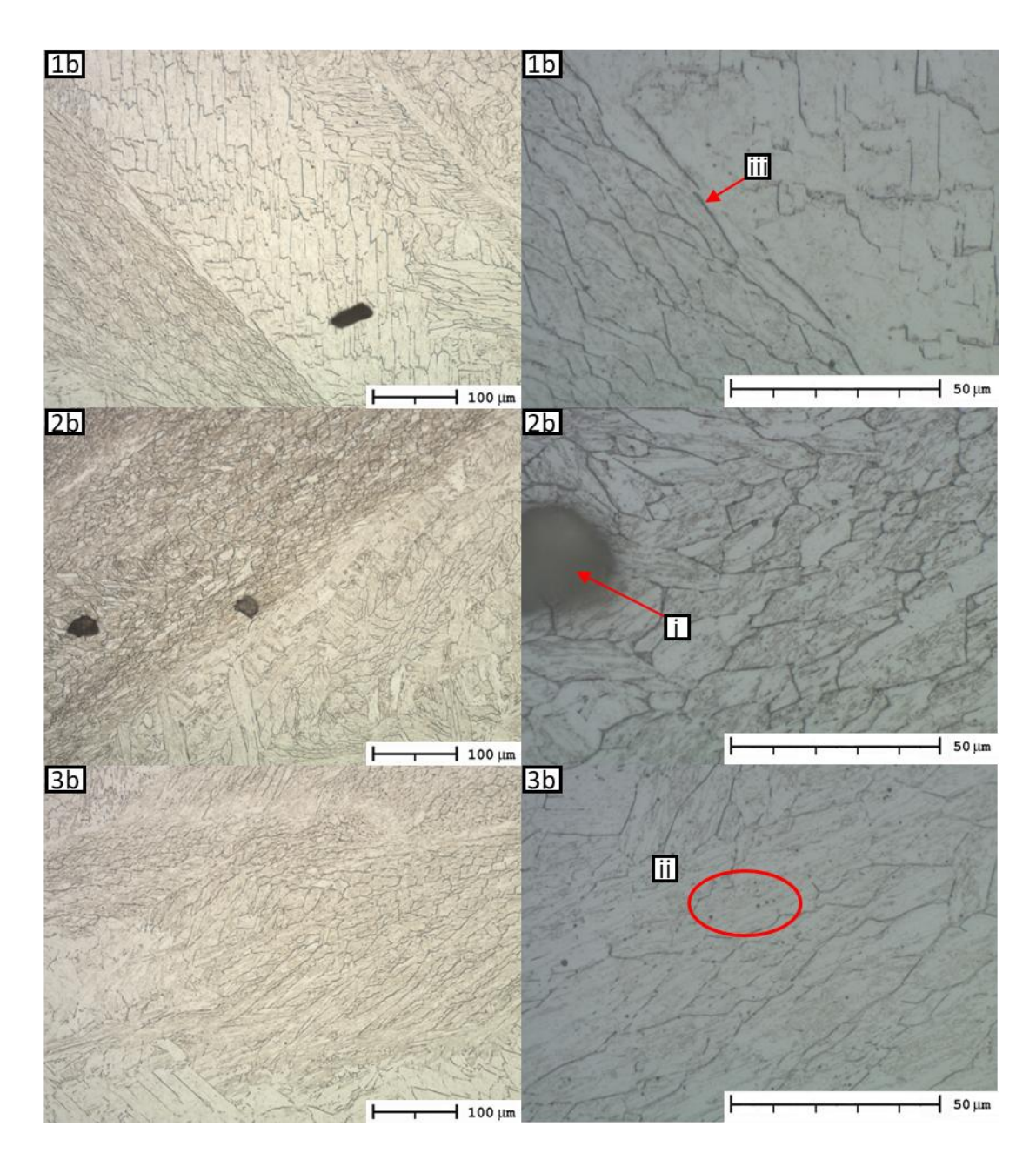


Figure 4-7 Micrographs of WAAM 15-5PH in the H1150 heat-treated state near the substrate (1b), middle (2b) and at the top (3b) of the sample.

Comparisons can be drawn between different regions of the sample and between the as-deposited and heat-treated conditions. Bands with fine and coarse dendritic structures can be seen, though the fine structure is more prevalent close to the substrate and in the final layers. The direction of solidification is expected to follow that of the maximum thermal gradient, which would be directed between that of the substrate and the previously deposited material in the same layer [4-8]. δ -ferrite is formed during rapid solidification, such as the cooling following WAAM deposition [4-9]. The thickness of these δ -ferrite stringers is maximised in the intermediate sections, while the first

deposited layers show very thin stringers. It can also be seen that the aging heat-treatment reduces the thickness of these stringers.

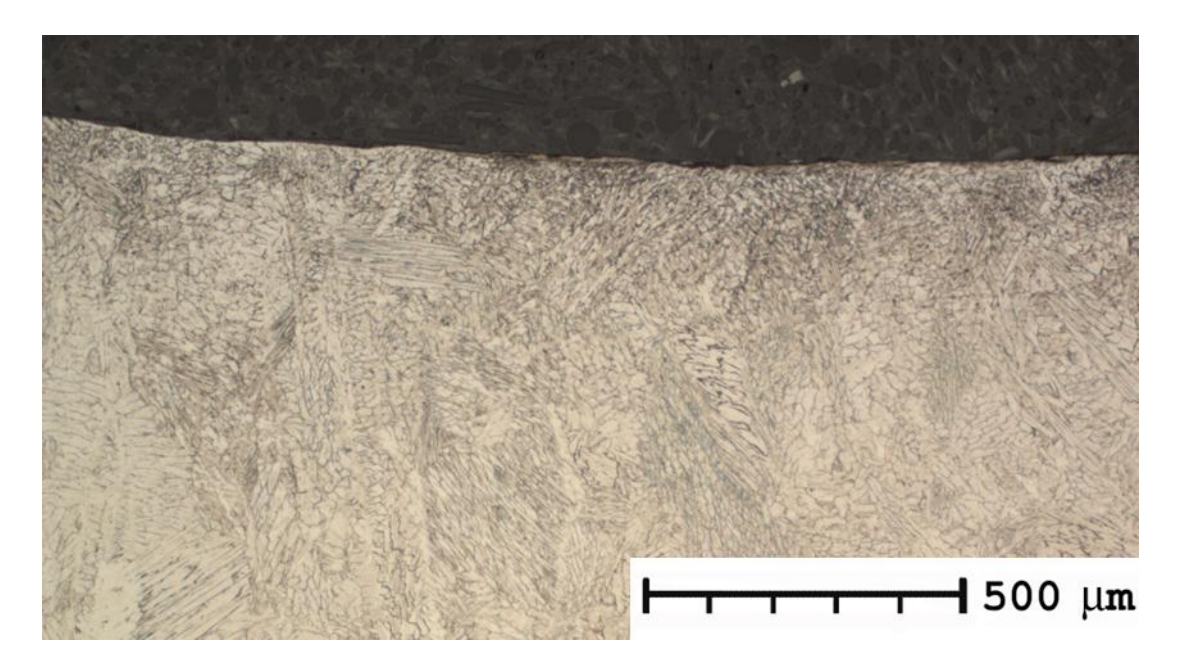


Figure 4-8 The edge of sample 3a, showing the transition in grain size and directionality in the final layer.

Looking at Figure 4-8, the grain structure can be clearly seen to transition from a highly directional series of dendrites to smaller, more equiaxed structures in the outer 100µm. This is expected as the direction of maximum thermal gradient shifts. In the interior of the sample, conductivity to the previously deposited alloy is dominant leading to directional solidification. At the surface, convection with the outside environment becomes an equally significant form of heat transfer, resulting in the loss of directionality.

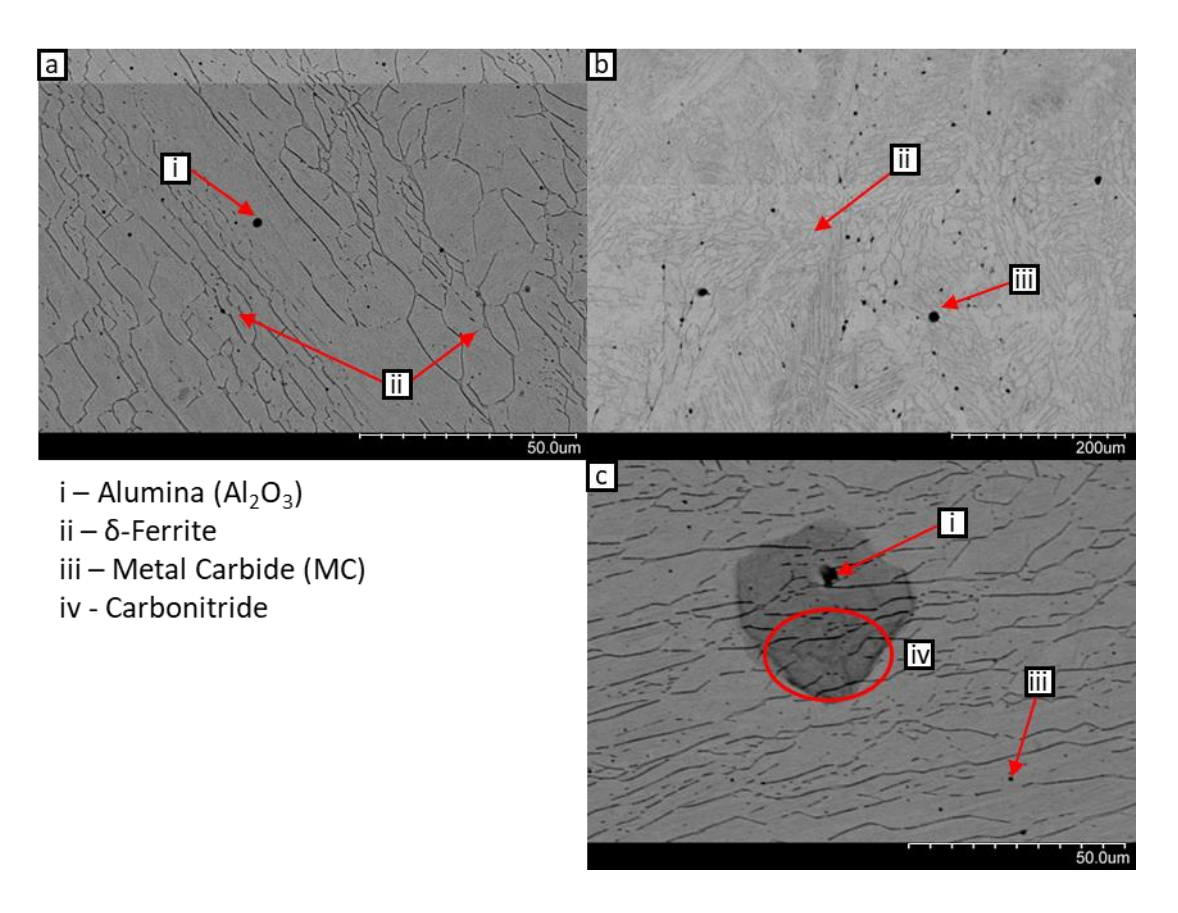


Figure 4-9 SEM images from WAAM produced 15-5PH alloy manufactured with process parameters HH showing alumina particles, metal carbide (MC) precipitates and a large carbonitride precipitate.

Using SEM imaging and testing sites of interest with EDS, the composition of features identified by optical microscopy could be confirmed and are shown in Figure 4-9. Some small circular precipitates were identified as alumina inclusions, while the stringers were found to match the composition of δ -ferrite.

Other small inclusions included high proportions of carbon, suggesting the presence of metal carbides. The irregular inclusions were found to contain a large quantity of impurities including sulphur, suggesting they were inclusions of slag within the alloy. Notably, niobium and titanium were not found to be present within the inclusions or matrix, therefore the presence of niobium carbides was not noted.

As the proportion of δ -ferrite and number of carbide particles are important for the understanding of the material, these have been presented in Figure 4-10. This shows that aging treatment results in a reduction in the proportion of δ -ferrite and an increase in the number of carbide particles. When these are

compared to the wrought material, it is noted that the δ -ferrite proportion is slightly reduced, while the number of carbides is dramatically lower.

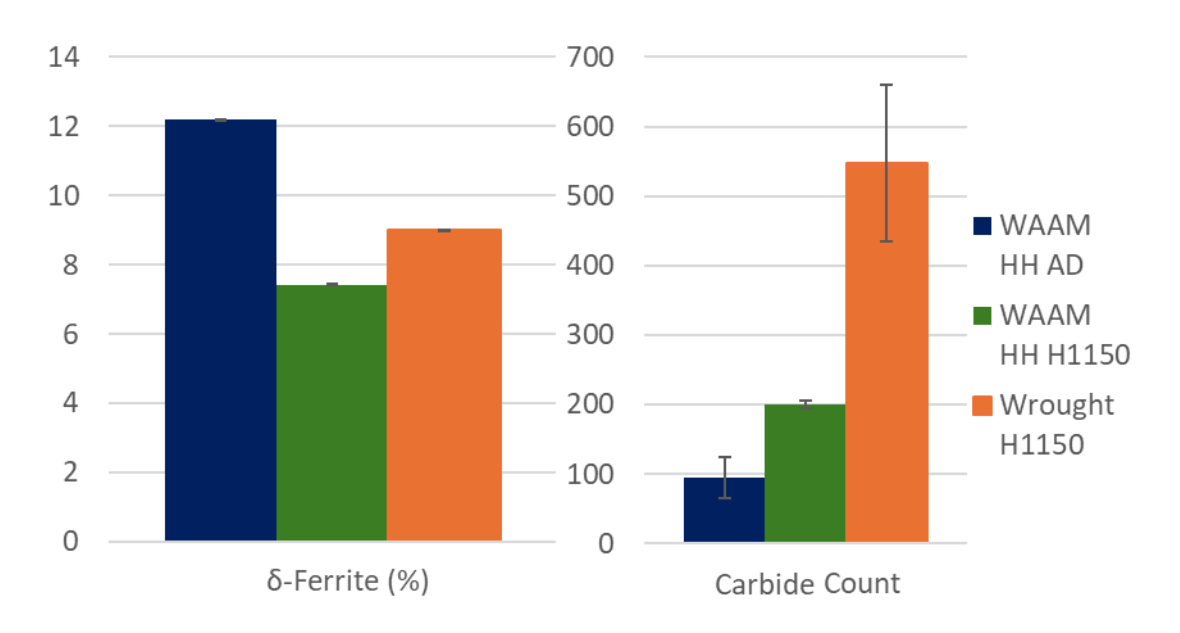


Figure 4-10 Proportion of δ -ferrite and carbide particle count in the microstructure for WAAM produced 15-5PH in the AD and H1150 conditions from mid height of the deposit (2a and 2b).

4.1.3. WAAM 15-5PH: low heat input (LH)

The second process parameter set (LH) reduces heat input in the interest of improving production rate by reducing the interpass cooling time and has the potential to improve mechanical properties [4-10]. This comes with the drawback of increasing the possibility of developing flaws within the microstructure such as porosity. Comparisons are made between samples in the as-deposited condition and following aging treatment H1150.

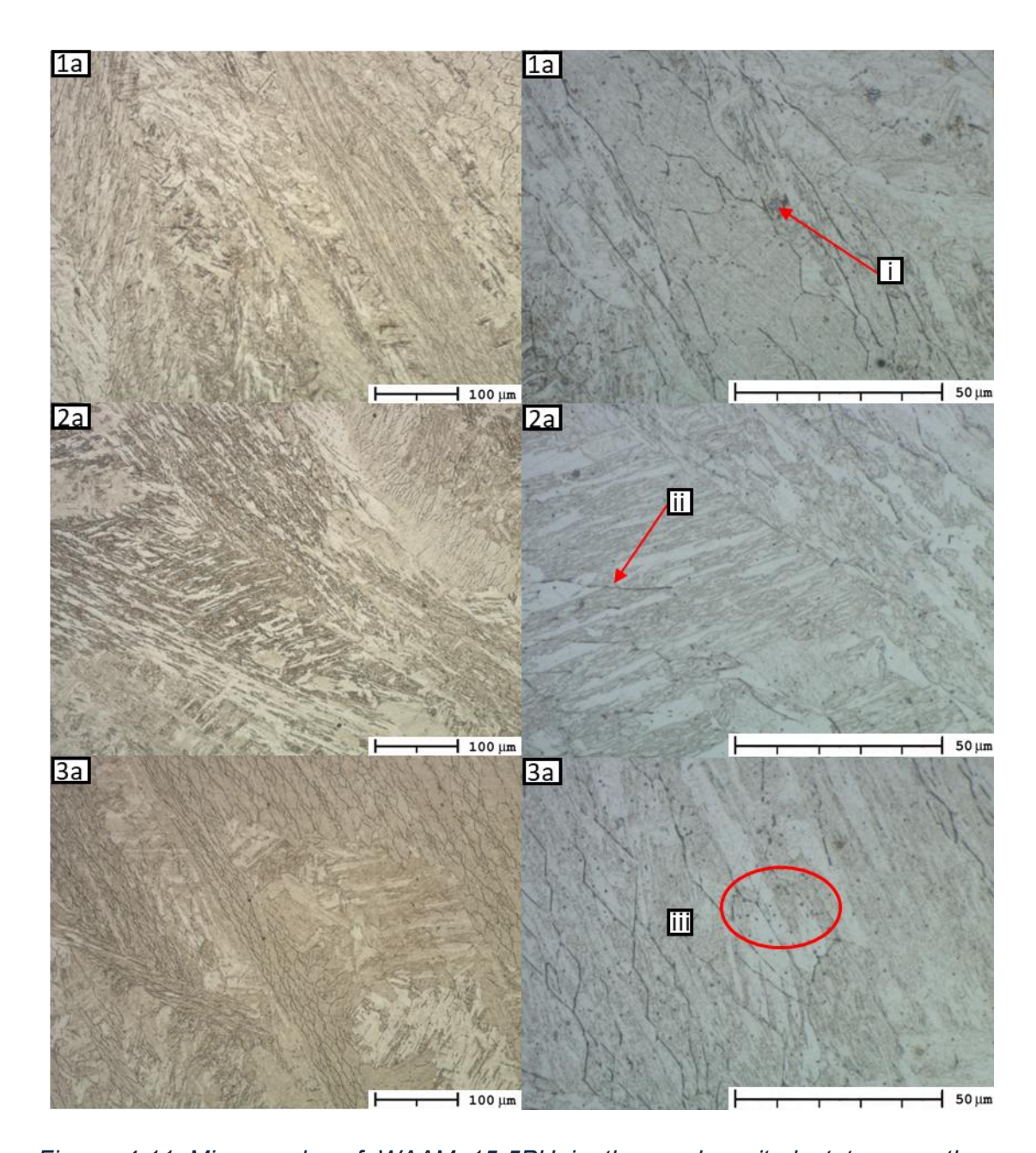


Figure 4-11 Micrographs of WAAM 15-5PH in the as-deposited state near the substrate (1a), middle (2a) and at the top (3a) of the sample.

The micrographs shown in Figure 4-11 shows the microstructure of 15-5PH alloy produced using the LH process parameters. A martensitic matrix can be seen, in addition to other notable features: i) and iii) show larger angular precipitates and clusters of small round precipitates. Finally, ii) indicates δ -ferrite stringers.

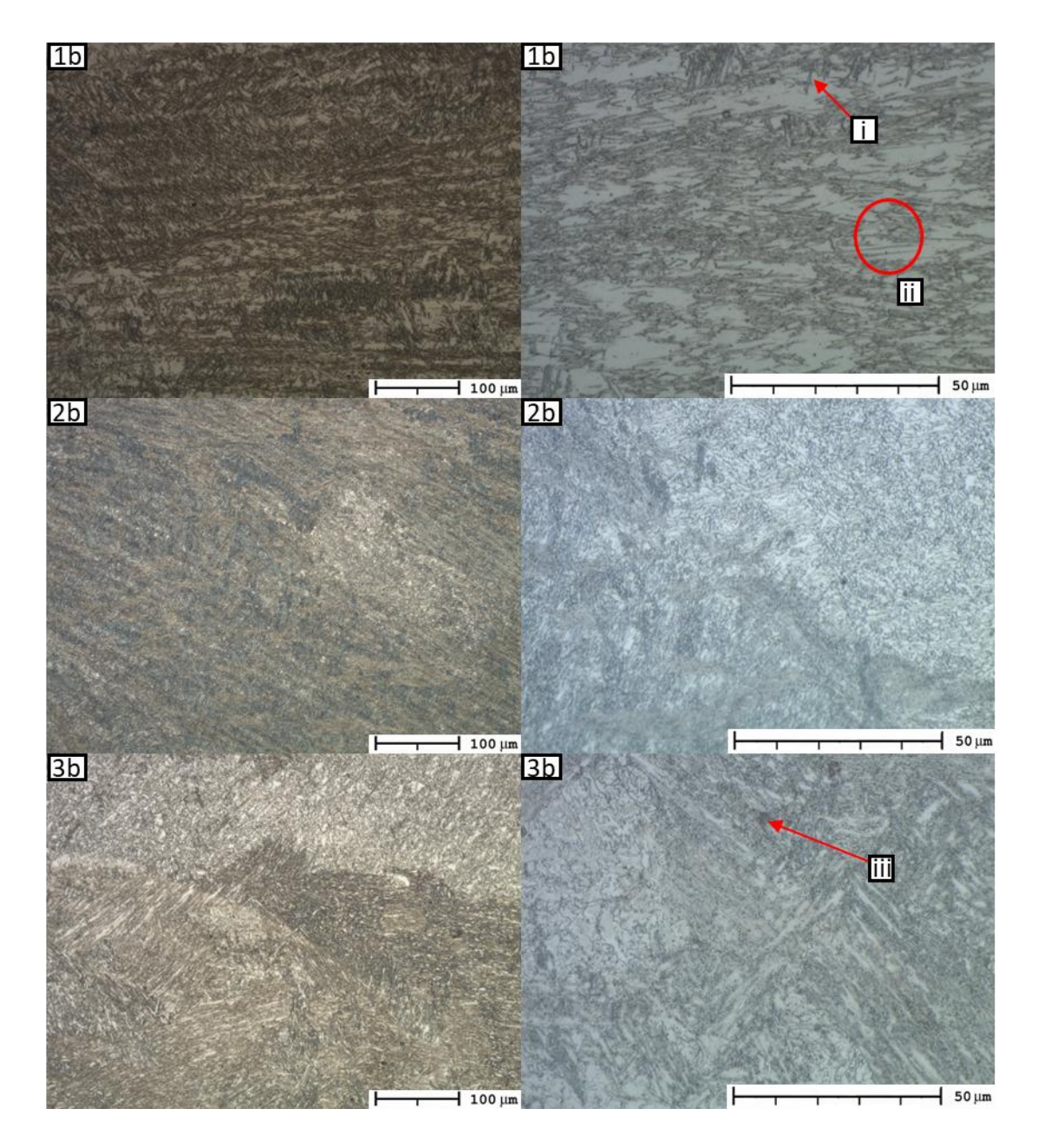


Figure 4-12 Micrographs of WAAM 15-5PH in the H1150 heat treated state near the substrate (1b), middle (2b) and at the top (3b) of the sample.

Figure 4-12 displays the microstructure in the H1150 aged state. A notable difference is the refinement of the martensitic microstructure through aging heat-treatment. Similar features to Figure 4-11 are identified which include i) δ -ferrite stringers ii) carbide precipitates and iii) instances of gas porosity.

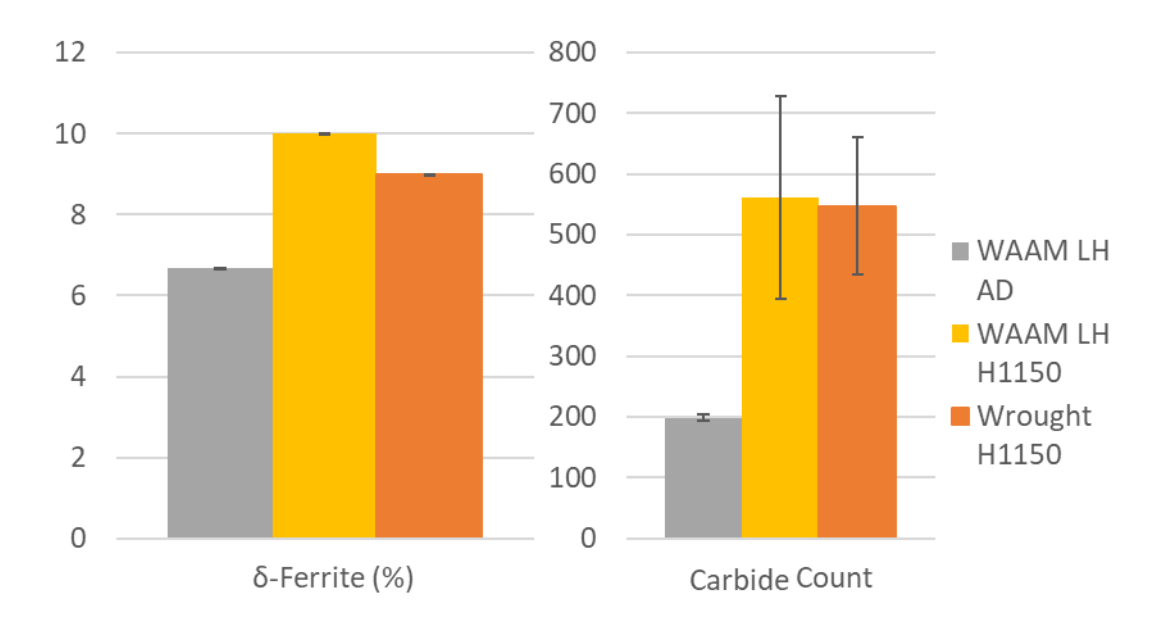


Figure 4-13 Proportion of δ -ferrite and carbide particle count in the microstructure for WAAM produced 15-5PH in the AD and H1150 conditions.

The proportion of δ -ferrite and the number of carbides in the material produced using LH process parameters are shown in Figure 4-13. In this case, the δ -ferrite proportion and quantity of carbides are shown to increase with aging heat treatment to match the composition seen in the wrought alloy.

4.2. Hardness testing

To relate the mechanical properties and microstructure of the 15-5PH alloy being investigated, hardness and microhardness measurements were taken in the different production parameters and heat-treatment states.

4.2.1. Wrought 15-5PH

The wrought alloy was tested in the following heat treatment states: Condition A (solution treated), H1025 (aged) and H1150 (over aged) with the results shown in Figure 4-14. These results show an increase in hardness with H1025, while H1150 reduces hardness to a value closer to the solution treated condition. These values are all within the ranges allowed by the standard ASTM A693 [4-11]. 250 microhardness indents were taken on each sample with a force of 0.05kgf. The spread of this data shows that H1025 results in an increase in segregation, leading to regions of high and low hardness, while H1150 reduces the segregation to a similar value to that seen in the solution

treated condition. While the H1150 condition is not the peak strength for this material, it is still valuable in some use cases due to enhanced fatigue life and improved ductility.

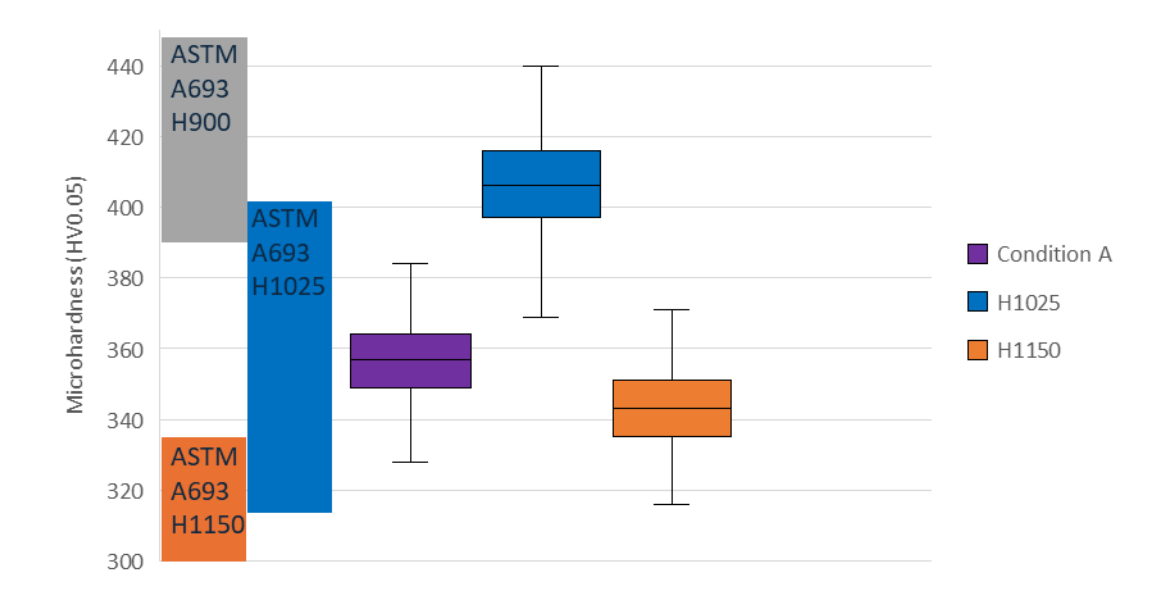


Figure 4-14 Microhardness results for wrought 15-5PH alloy.

4.2.2.WAAM 15-5PH

The samples produced by WAAM were also tested for their hardness to compare both heat treatment and thermal input during deposition. These results are averaged over each vertical location within the sample as shown in Figure 4-14.

As shown by the results, these process parameters experience opposite responses to heat treatment. For HH process parameters, aging results in an increase in hardness, corresponding to the development of precipitates. For LH process parameters, the hardness is reduced. This is likely due to reduced in situ heating during deposition leading to reduced response to aging treatment, as the strengthening elements had not been returned to solution within the matrix. As such, The results for LH material with the H1150 aging treatment most closely align with the properties specified by standard ASTM A693 [4-11].

The variation in microhardness results, captured with a load of 0.05kgf is shown in Figure 4-15. This confirms that heat treatment reduces the variation of hardness. This is likely due to diffusion and stress relief reducing residual

stresses and segregation of hardening phases. It is noted that the results for LH material in the as-deposited condition show the highest hardness.

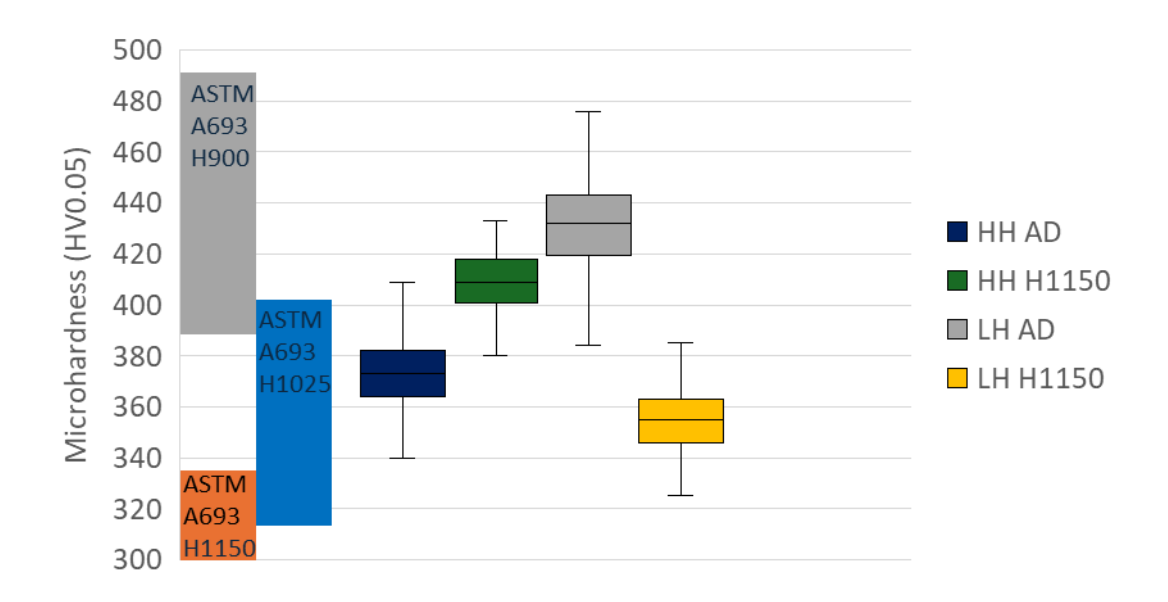


Figure 4-15 Microhardness plots for alloy 15-5PH produced using WAAM.

4.3. Tensile testing

To establish a comparison between the mechanical properties of wrought and WAAM produced 15-5PH stainless steel, tensile testing was performed on samples in a range of conditions. This testing allows the yield strength, elongation and UTS to be determined.

Following testing, the fracture surfaces were examined optically and with SEM to identify the failure mode and if aspects of the microstructure are correlated with the initiation of failure.

Existing literature details previous studies on the mechanical properties of wrought material and welds of 15-5PH in different heat-treatment conditions. In the case of wrought alloy, studies have been performed examining the hardness resulting from aging heat-treatments. Peak hardness is achieved for heat treatment at between 450°C and 480°C for 4 hours which corresponds to the standard aging treatment H900 [4-3]. It was found that this also resulted in a peak strength, as an increase in the aging temperature increases the size of needle-like precipitates and spherical precipitates become more common at higher temperature aging, resulting in a decrease in strength and increase in ductility [4-4].

Welded precipitation hardening alloys also show a response to post weld heat treatments. Aging treatments are performed directly upon the welded joints, resulting in an increase in yield strength with H900 aging, while H1025 and H1150 aging results in a lesser increase in strength [4-7]. The H1025 and H1150 treatments also result in an increase in ductility and impact toughness [4-12].

In a study of a sample produced by WAAM, solution treatment is applied. This results in lower strength in the as-deposited and heat-treated conditions compared to welded plates, while the solution treatment also increases the ductility as expected [4-13].

4.3.1. Wrought 15-5PH

Tensile testing was performed on wrought specimens of 15-5PH stainless steel in Condition A + H1025 and Condition A + H1150.

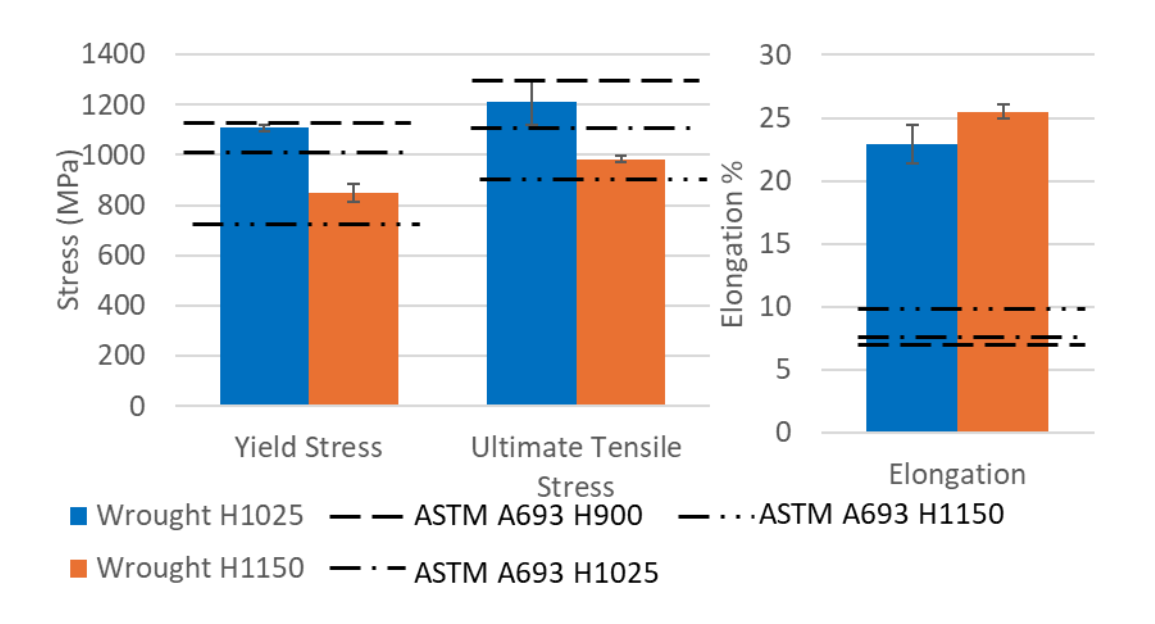


Figure 4-16 Results from tensile testing of wrought 15-5PH alloy in Condition A + H1025 and Condition A + H1150 conditions.

From the results shown in Figure 4-16, as indicated by the literature, the overaging heat treatment H1150 causes a decrease in strength but an increase in elongation.

These results are compared against the minimum specifications for 15-5PH in the standard ASTM A693-16 [4-11]. The comparison is shown in Table 4-4 (pg

95) shows that the results obtained from testing are in excess of those specified for all properties.

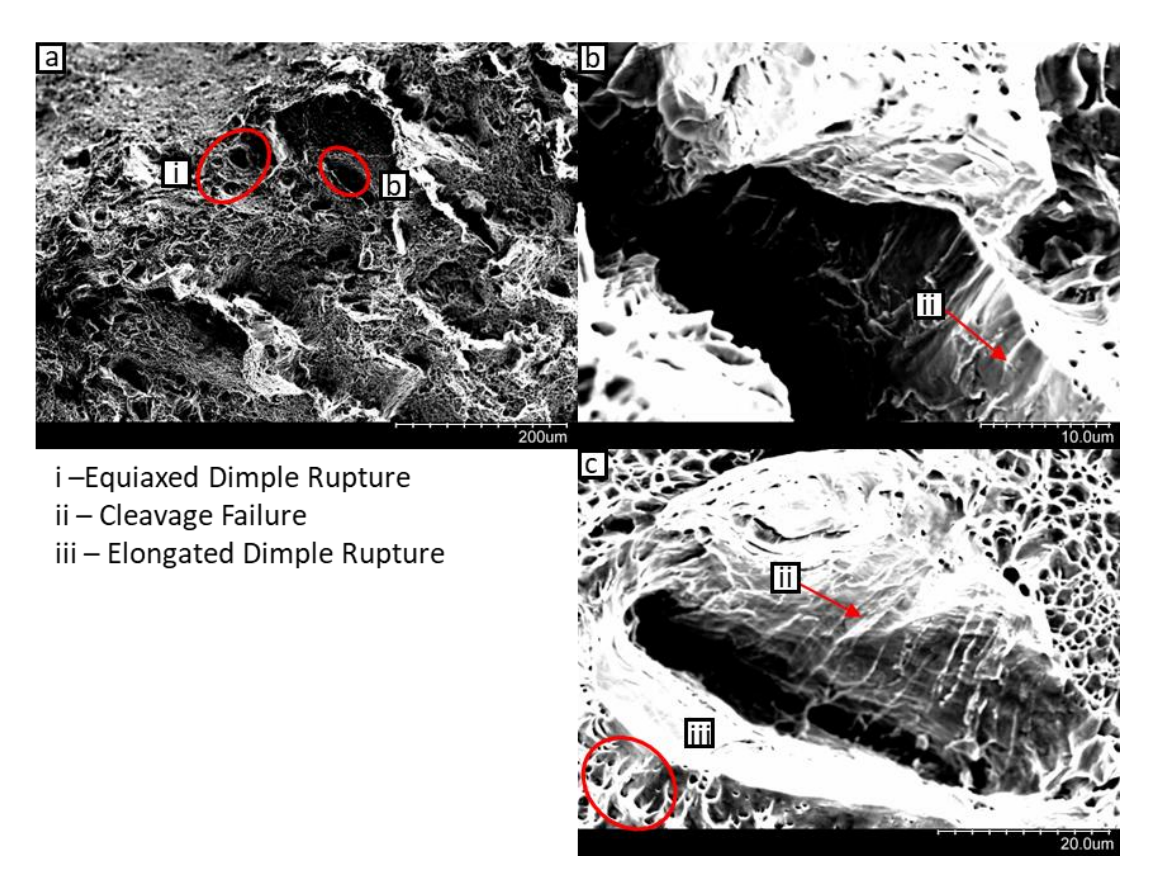


Figure 4-17 SEM fractographs of wrought 15-5PH following tensile testing.

The fractography of these tensile samples are shown in Figure 4-17. They predominantly show dimple rupture as the primary mode of failure. Regions b) and c) show localised regions of cleavage failure, with the characteristic river texture. Elongated dimples emanate from the cleavage failure in c) suggesting a tearing response [4-14].

4.3.2. WAAM 15-5PH: high heat input (HH)

In the first series of samples produced by WAAM, a low travel speed was used, resulting in a high heat input. The comparison is made between samples in the as-deposited (AD) and H1150 conditions. The results are shown in Figure 4-18 which agree with the pattern of H1150 heat treatment reducing ultimate strength, though yield strength remains constant.

There is no direct comparison for material properties for the as-deposited condition given in the material standard ASTM A693. However, when the

results for the as-deposited condition is assessed against the values specified for H1025, it was found that the yield stress is below this specification while when compared to H1150, the results were higher than both the value from the standard and those attained from the wrought material. The mechanical properties were also found to be higher than those attained in previous studies of this material and process [4-13].

A significant variation is noted in the elongation of the aged samples, indicating that samples displayed differing failure behaviour. This increased range of elongation results is accompanied by a similar increase in the variation in yield and ultimate tensile strength. The cause of this can be identified through examination of fracture surfaces to identify the failure modes of each sample. The fracture surfaces shown in Figure 4-19 and Figure 4-20 show similar features, such as large regions of quasi-cleavage fracture however the presence of defects such as gas pores lead to a reduction in ductility.

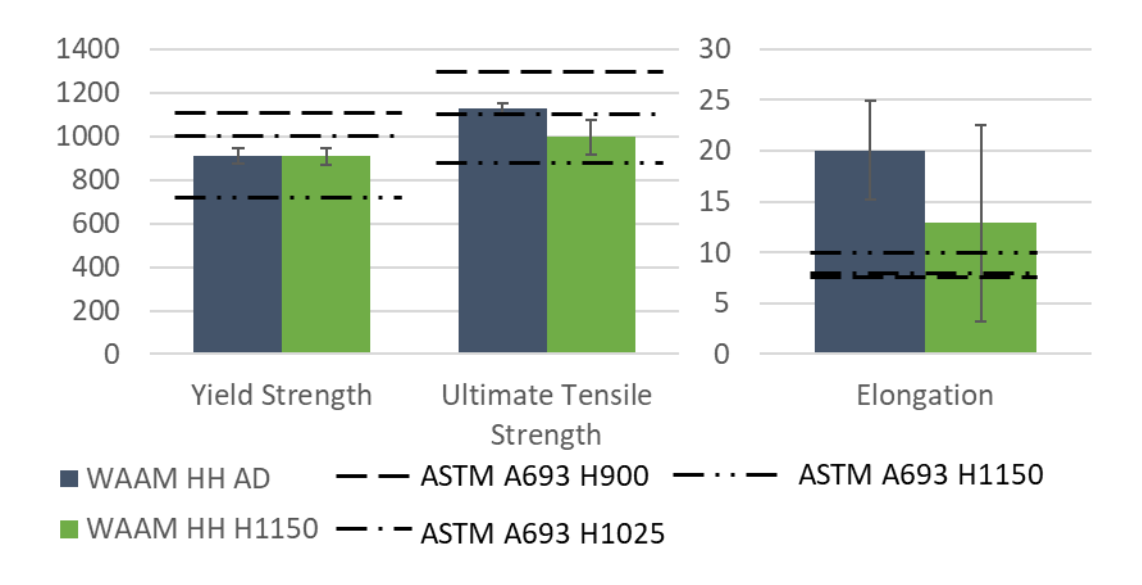


Figure 4-18 Results from tensile testing of WAAM 15-5PH alloy in the AD and H1150 conditions produced using high heat input.

Examining the fracture surfaces of the samples, certain features can be identified. For the as-deposited samples, fractographs are shown in Figure 4-19. Notable features are identified, with regions of cleavage fracture surrounding flaws such as gas porosity or a tearing feature such as Figure 4-19b initiated by a stringer defect. Large cleavage steps are noted around these

tearing features, and as these transition into dimple rupture, the features are typical of quasi-cleavage dominant fracture [4-14].

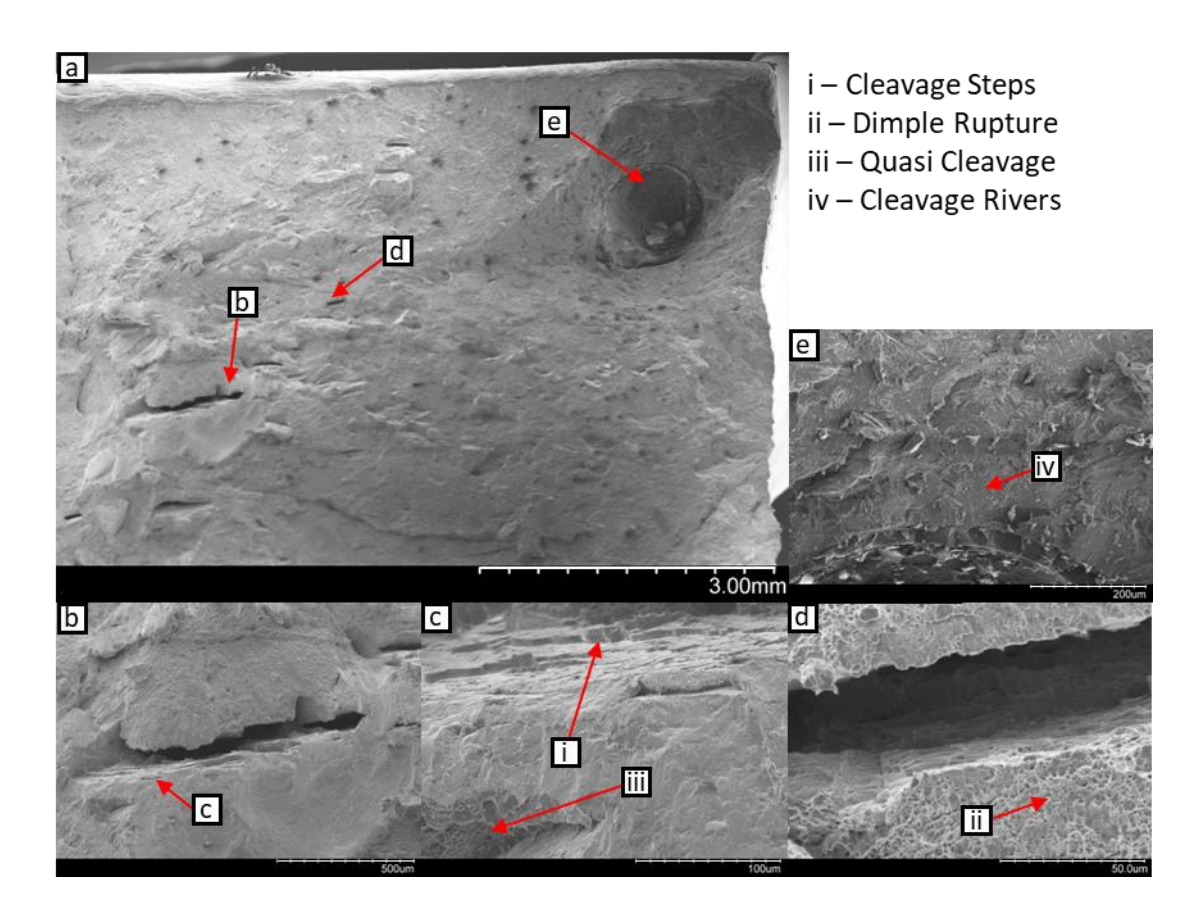


Figure 4-19 Fractographs of a tensile test on 15-5PH alloy produced using process parameters HH in the as-deposited condition showing a) the full fracture surface b) a cleavage crack c) detail of cleavage steps d) detail of ductile rupture around a cleavage feature e) cleavage features around a gas pore.

In the aged samples, there is a greater prevalence of these stringer tearing features surrounded by dimple rupture. The fracture surfaces also differences associated with high and low elongation recorded during testing. The sample exhibiting low elongation (8%) in Figure 4-20 shows predominantly quasicleavage fracture with limited regions of ductile rupture. Figure 4-21 shows the fracture surface of a sample displaying higher elongation (24%). Quasicleavage is also observed, but the ductile regions surrounding cleavage features are noted to be larger. This increased predominance of ductile failure accounts for the higher elongation of the sample. The cause of reduced ductility is related to the observation of gas porosity in some samples which accelerate failure.

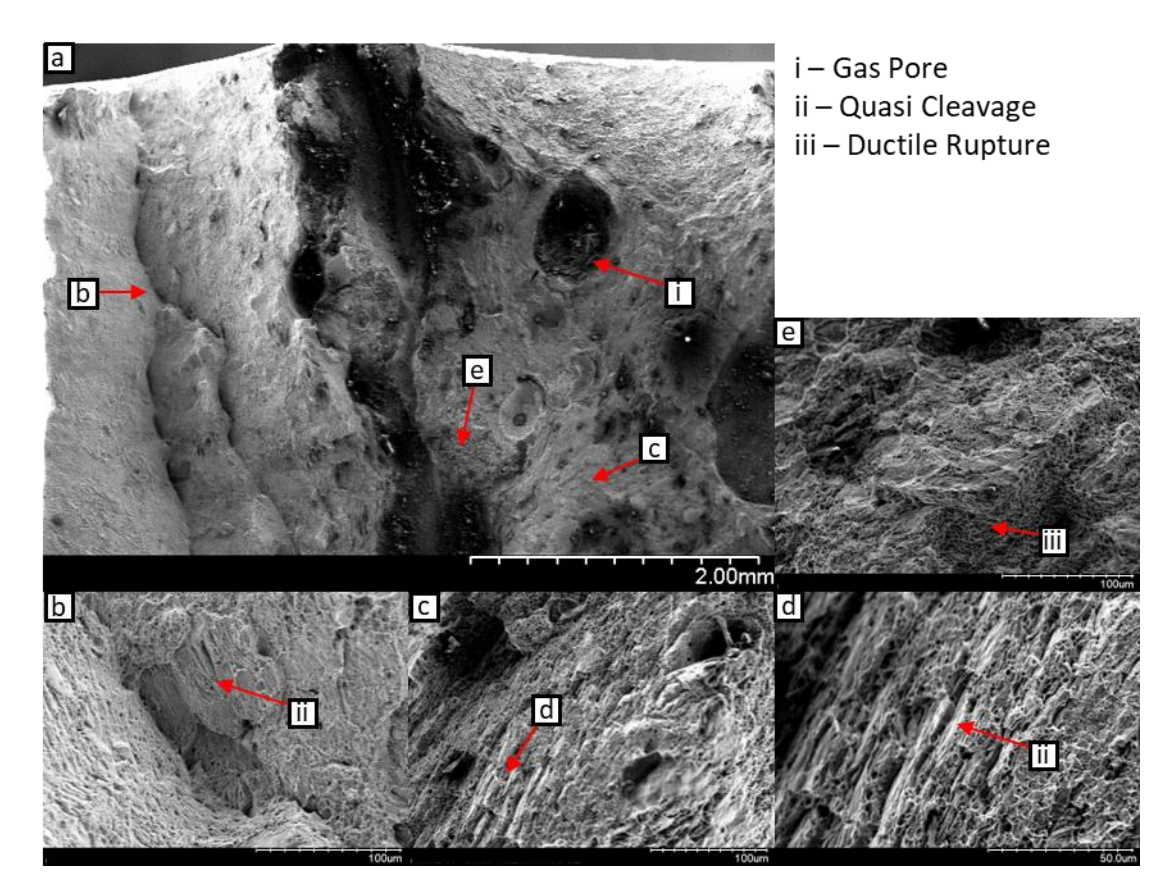


Figure 4-20 Fractographs of a tensile test on 15-5PH alloy produced using process parameters HH in the H1150 condition displaying low ductility showing a) an overview of the fracture surface b) quasi cleavage fracture in a fissure c) & d) detail of stepped quasi cleavage e) areas of ductile and cleavage fracture.

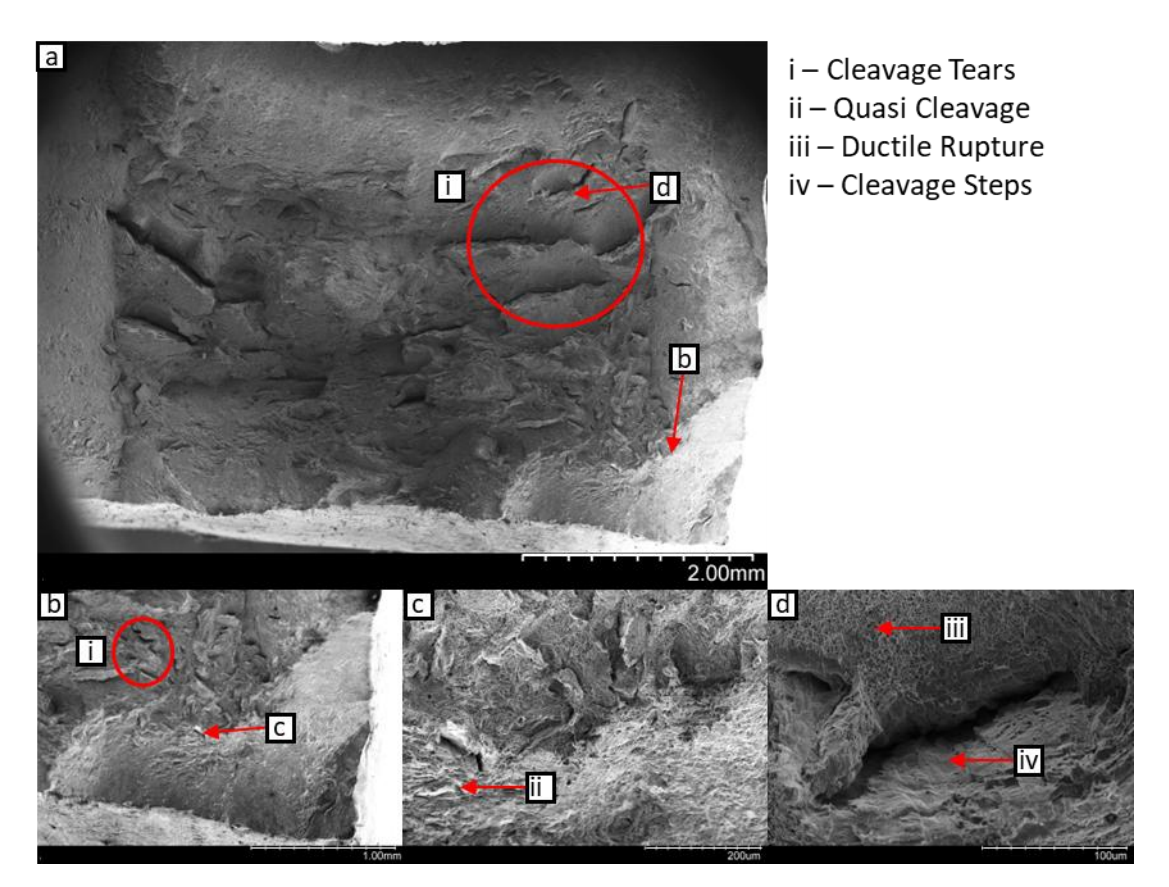


Figure 4-21 Fractographs of a tensile test on 15-5PH alloy produced using process parameters HH in the H1150 condition displaying high ductility showing a) an overview of the fracture surface b) & c) the transition from quasi-cleavage to cleavage tearing d) the transition to ductile rupture in the vicinity of ductile tear features.

4.3.3. WAAM 15-5PH: low heat input (LH)

In the second series of tensile results using WAAM produced 15-5PH, the heat input during deposition was reduced. Again, a comparison was made between samples in the as-deposited (AD) condition and those in the aged (H1150) condition with the results shown in Figure 4-22. The trends shown by these results broadly agree with those expected for the material and heat-treatment combination, with yield and ultimate tensile strength reducing following aging, while elongation significantly increases. As with the HH material, the asdeposited material has no direct comparison in ASTM A693 [4-11], however, it was also compared against the specifications for H1025. These results also showed that the yield and ultimate tensile strengths of the as-deposited material did not meet those specified for the H1025 condition. In the H1150 condition, the yield strength was also found to be lower than is required by the standard as seen in the comparison in Table 4-4. These results are noted to be superior to those produced by previous studies [4-13]. This is caused by the reduction in heat input during deposition, in addition, the increased wire feed speed increases the rate of deposition.

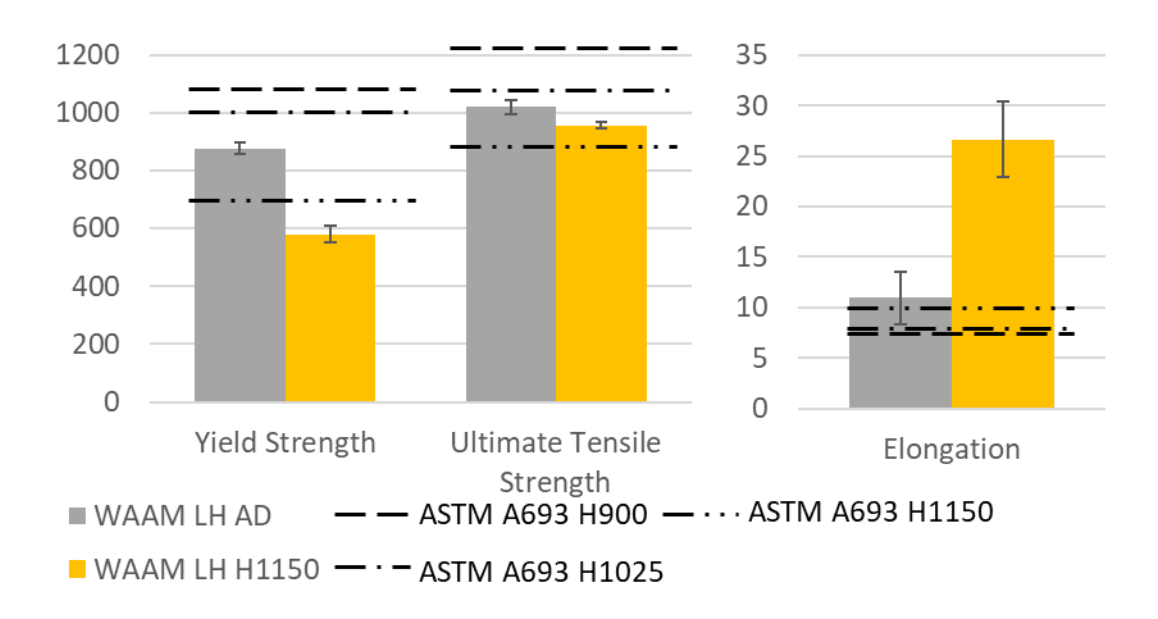


Figure 4-22 Results from tensile testing of WAAM 15-5PH alloy in the AD and H1150 conditions produced using LH process parameters.

An analysis of the fracture surfaces was performed to identify causes of the degradation of elongation and yield strength in the two prepared conditions. The fractographs of the as-deposited sample are shown in Figure 4-23, the

initiation of failure was identified as a series of gas pores between 0.5 and 0.7mm in size. This causes a region of cleavage and quasi-cleavage fracture to develop radially from the pore, followed by a transition to fine dimple rupture, this rapid, brittle failure explains the low elongation.

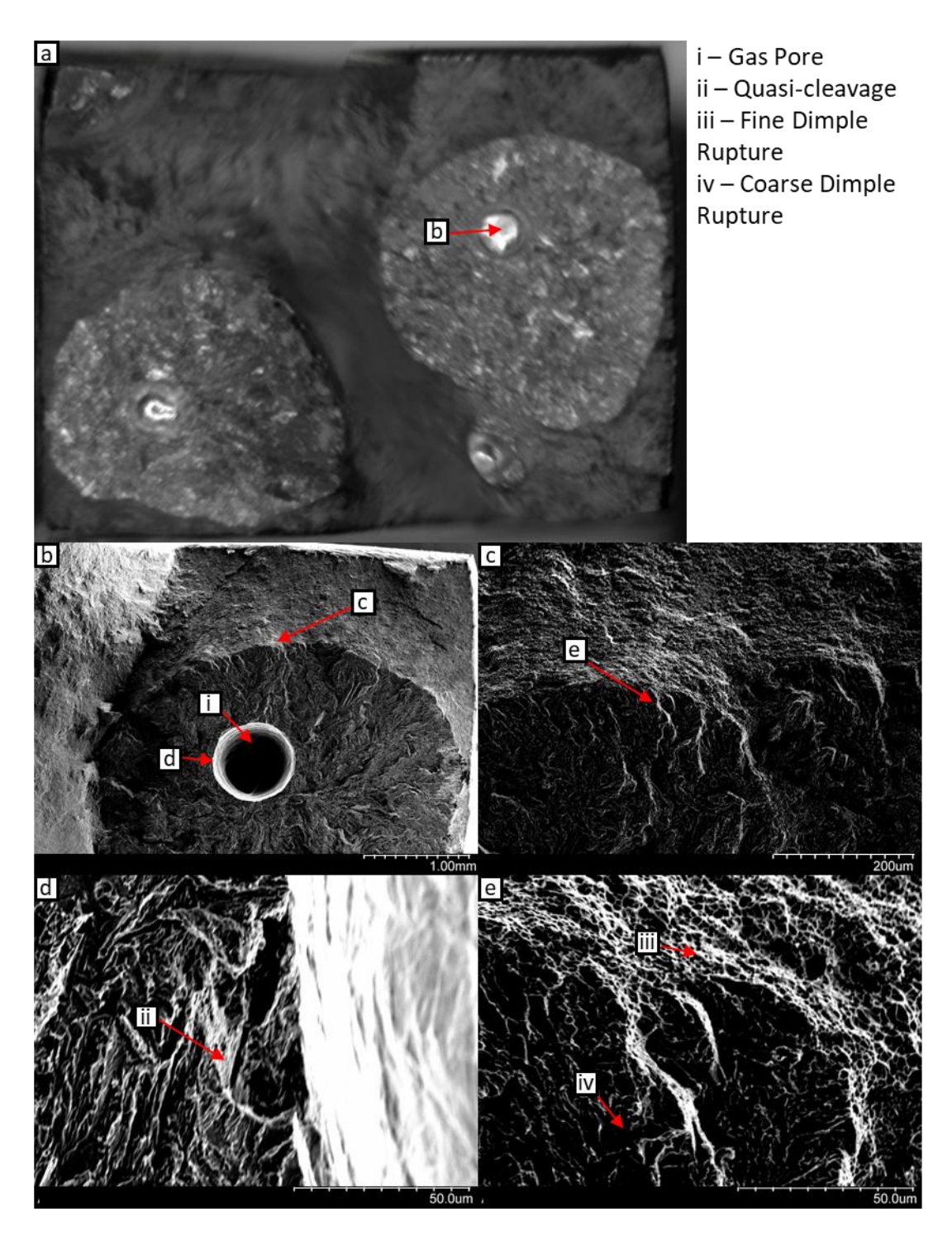


Figure 4-23 Fractographs of a tensile test on 15-5PH alloy produced using LH process parameters in the as-deposited condition showing a) the full fracture surface b) a gas pore c) transition to fully ductile fracture d) detail of the fracture at the gas pore e) detail of the ductile transition.

Figure 4-24 shows the fracture surface of the aged sample, this shows large regions of dimple rupture centred on cleavage features which is indicative of the quasi-cleavage mode of failure typical of this alloy [4-14]. The reduced hardness and increased elongation may reduce the sensitivity to fracture at the gas pores and promote ductile rupture [4-15].

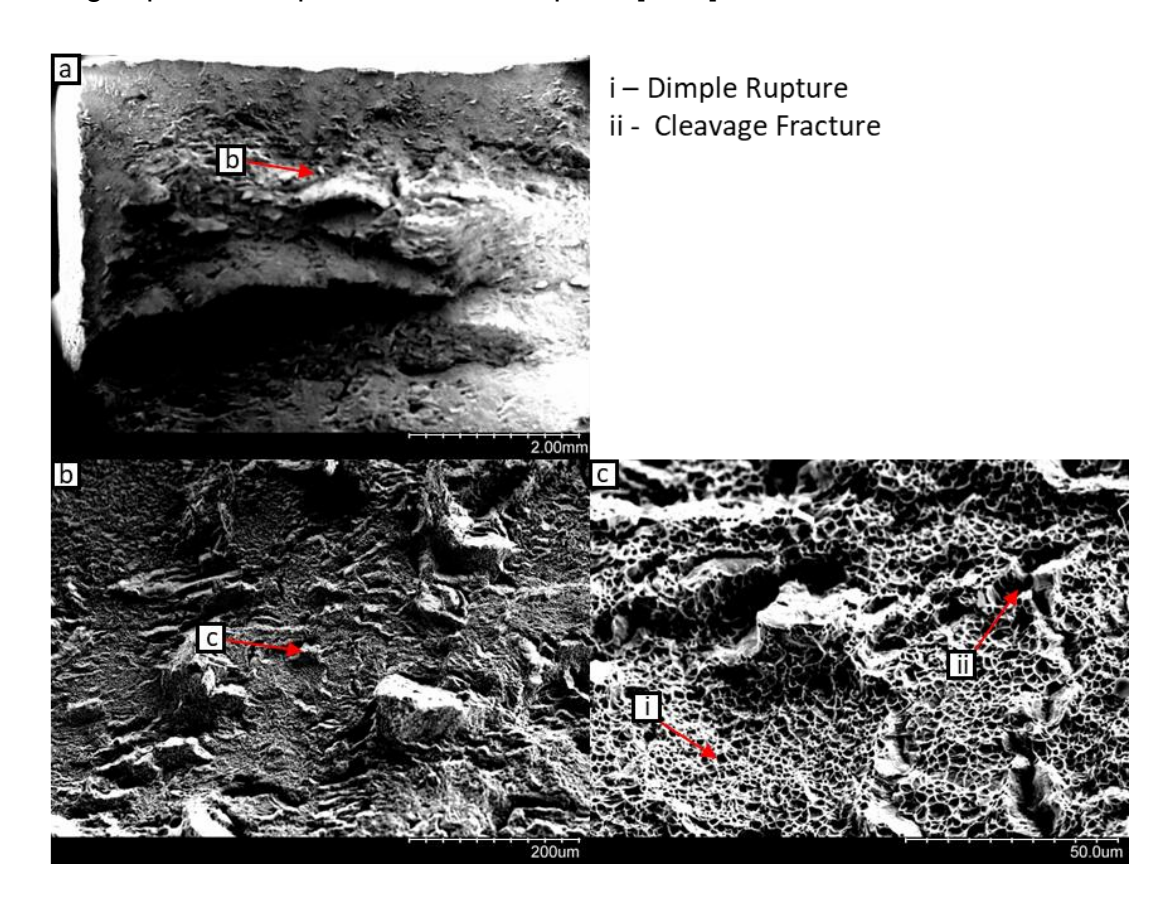


Figure 4-24 Fractographs of a tensile test on 15-5PH alloy produced using LH process parameters aged to H1150 showing a) the full fracture surface b) detail of the fracture modes.

4.4. Charpy Impact testing

Impact testing was performed on 15-5PH alloy produced using WAAM. It is expected that aging heat treatments will increase the impact toughness of the samples [4-5, 4-7]. The fractography of each sample is also important, with the width of the crack initiation zone typically increasing with the aging temperature [4-7]. It is identified that the over-aged condition displays quasi-cleavage and ductile fracture compared to cleavage fracture morphologies prevalent in the as-deposited condition. This results in increased impact toughness.

4.4.1.WAAM 15-5PH: high heat input (HH)

Charpy impact testing was performed on samples produced using HH process parameters. The results are shown in Figure 4-25, and show that the aging treatment causes a large increase in impact toughness. This indicates a greater effective ductility at the very high strain rates tested in impact testing. Only the results for the heat treated samples meet the minimum requirements for impact toughness specified by ASTM A693 [4-11].

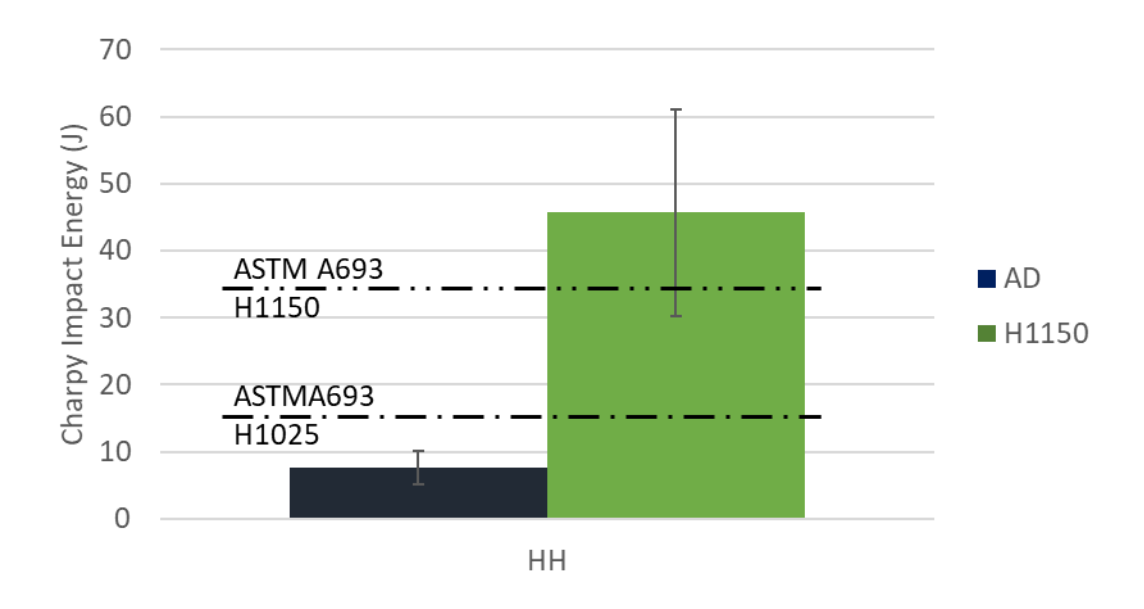


Figure 4-25 Results from impact testing of WAAM 15-5PH alloy in the AD and H1150 conditions produced using HH process parameters.

When the fracture surfaces were examined, the as-deposited samples in Figure 4-26 displayed predominantly cleavage fracture with small, dispersed regions of quasi-cleavage, typical for precipitation hardening stainless steels [4-14]. Only a very small region, opposite the notch shows dimple rupture. For comparison, the aged samples displayed in Figure 4-27 exhibited a higher impact energy. These samples showed predominantly quasi-cleavage failure, especially at the notch, with regions of cleavage showing a range of structures including rivers, feathers and very large cleavage steps. The large regions of dimple rupture and complex crack propagation features explain the high impact toughness of these samples.

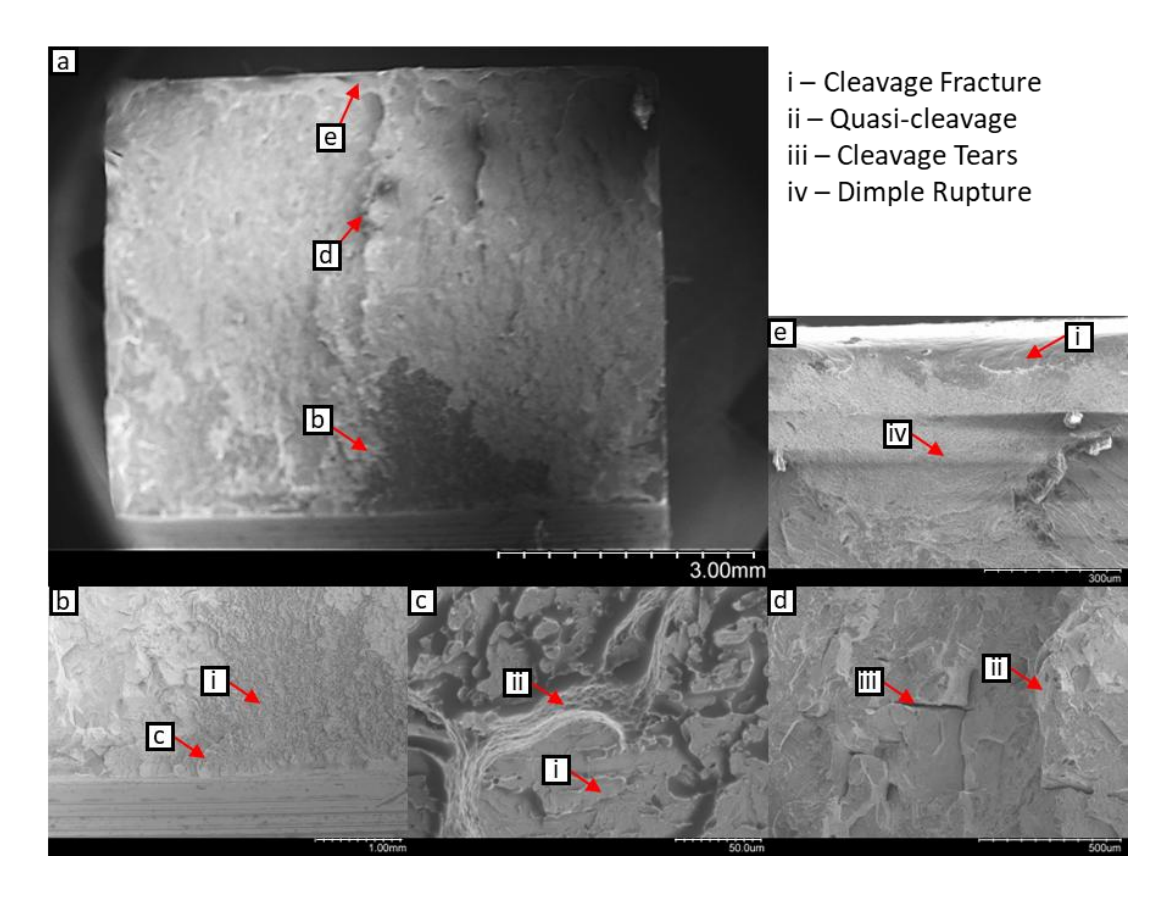


Figure 4-26 Fractographs of an impact test on 15-5PH alloy produced using HH process parameters in the as-deposited condition showing a) the full fracture surface b) a view close to the notch region, c) detail of b), d) the region in the middle of the sample, e) the region of final failure of the sample.

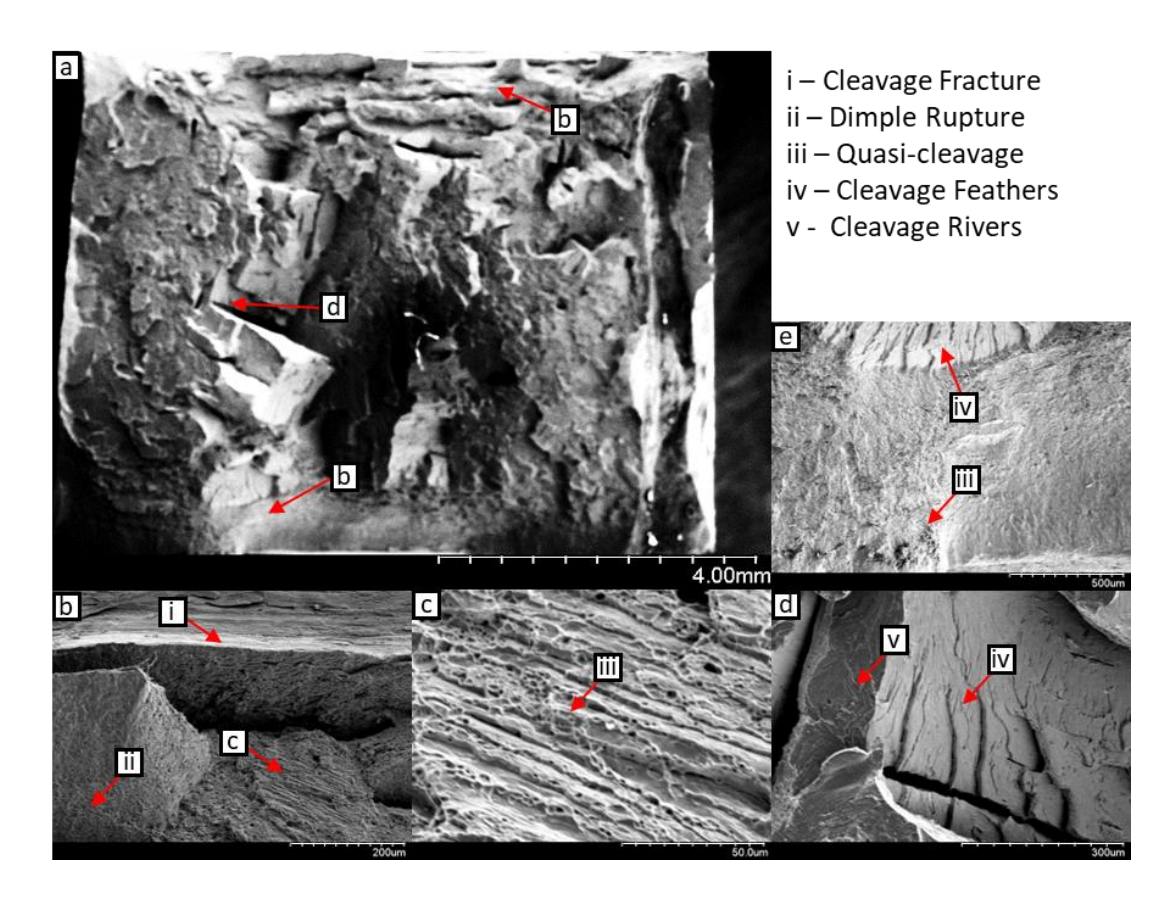


Figure 4-27 Fractographs of an impact test on 15-5PH alloy produced using HH process parameters aged in the H1150 condition showing a) the full fracture surface b) a view close to the notch region, c) detail of b), d) cleavage structures in the middle of the sample, e) the region of final failure of the sample.

4.4.2. WAAM 15-5PH: low heat input (LH)

For comparison, impact tests were also performed on samples produced using LH process parameters. The results in Figure 4-28 show an increase in impact toughness in both conditions compared to testing on material produced using higher thermal input. In this case, both conditions meet the requirements for impact toughness set by ASTM A693 [4-11]. In the as-deposited condition, however, this minimum requirement sits within 1 standard deviation of the mean, therefore further testing would be required to confirm that this material and process combination meets this standard.

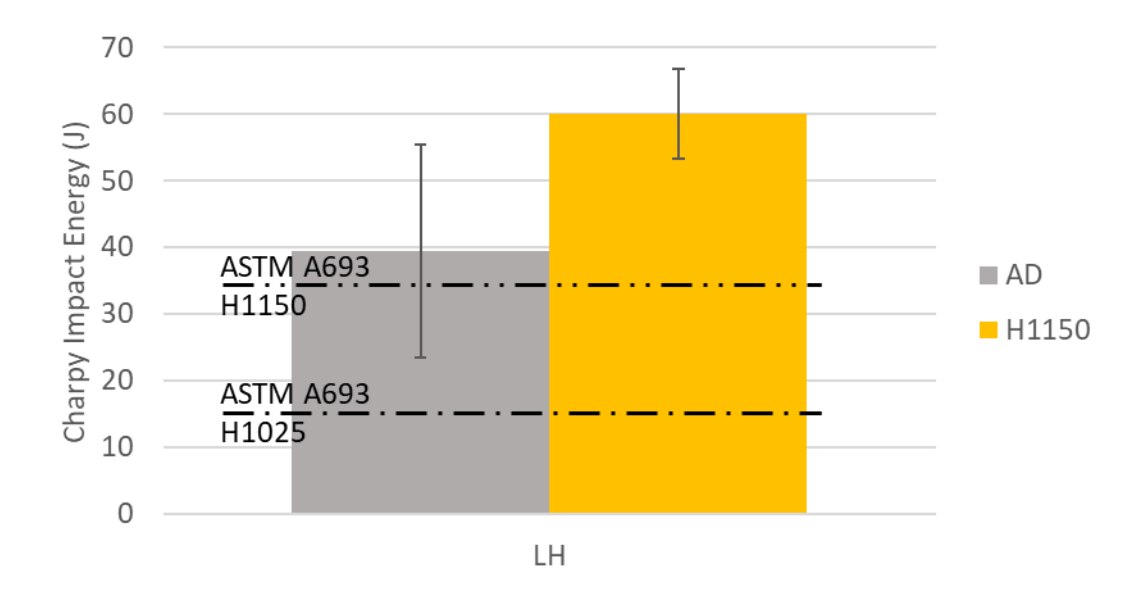


Figure 4-28 Results from impact testing of WAAM 15-5PH alloy in the AD and H1150 conditions produced using LH process parameters.

When the fracture surfaces are examined, the as-deposited samples showed quasi cleavage at the notch and other small, localised regions, while the bulk of the sample failed through dimple rupture as shown in Figure 4-29. The aged samples exhibited higher impact energy combined with larger shear wings and more extreme dimple rupture as seen in Figure 4-30. Cleavage failure was only noted at the notch, with quasi cleavage in very small regions on the surface and opposite the notch.

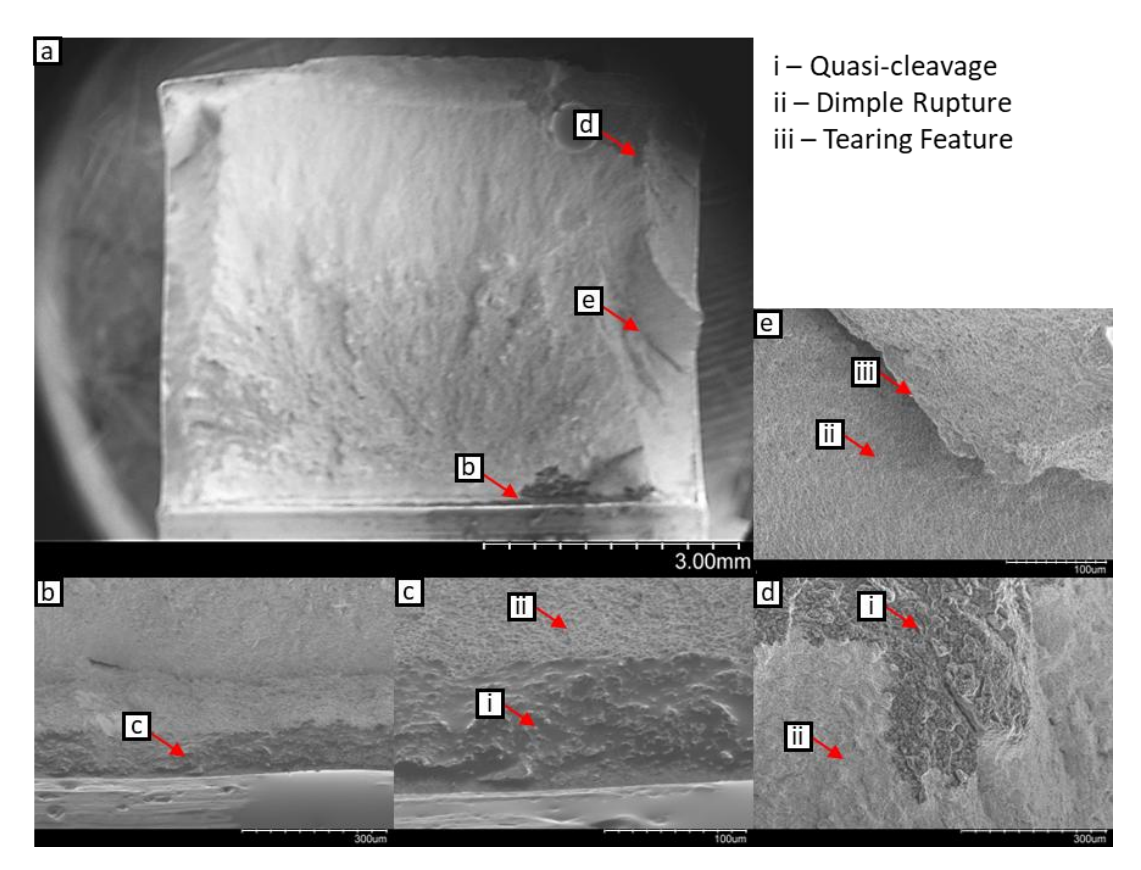


Figure 4-29 Fractographs of an impact test on 15-5PH alloy produced using LH process parameters in the as-deposited condition showing a) the full fracture surface b) a view of the notch region c) detail of the notch region d) a region of quasi cleavage opposite the notch e) the shear wings of the sample.

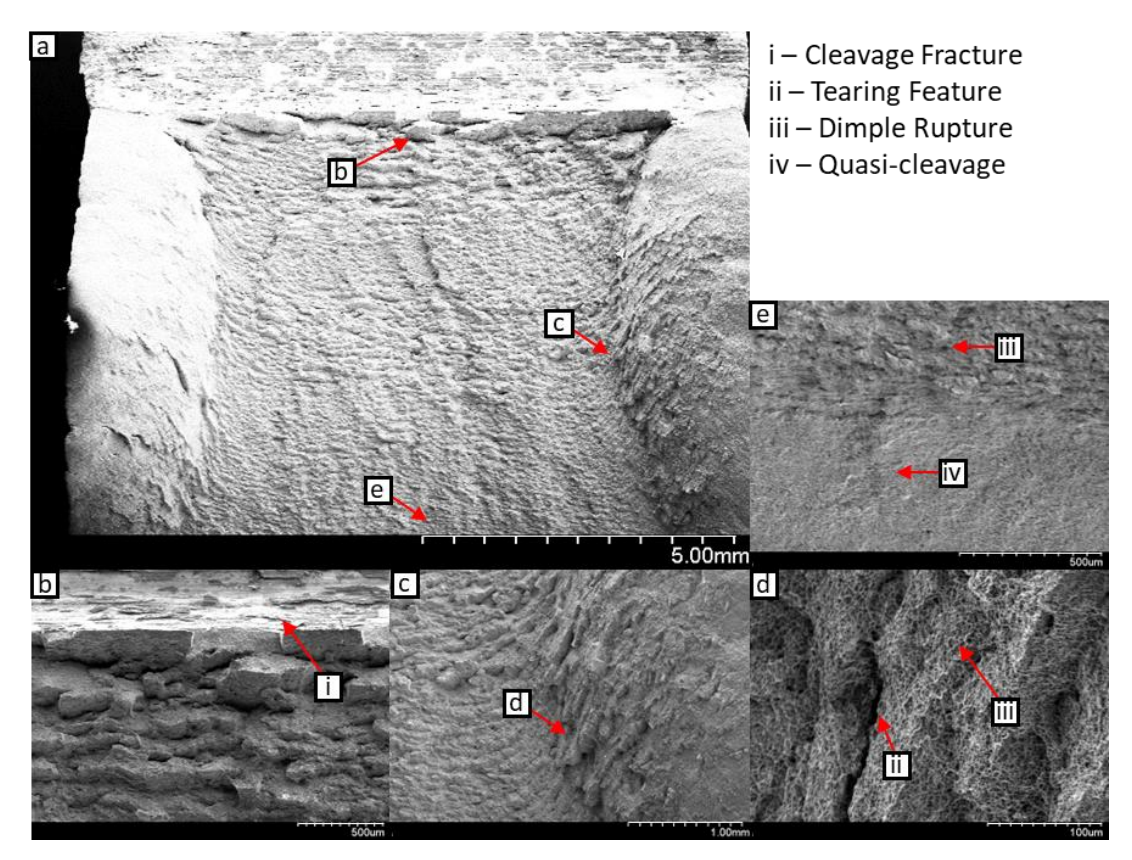


Figure 4-30 Fractographs of an impact test on 15-5PH alloy produced using LH process parameters aged in the H1150 condition showing a) the full fracture surface b) a view of the notch region c) the shear wings d) detail of the shear wings e) the region of final failure of the sample.

4.5. Fatigue testing

Fatigue properties are important for evaluating the use of materials for high performance engineering components. Precipitation hardening stainless steels are commonly used in environments where high strength and corrosion resistance is required and cycling loading is experienced [4-16]. These alloys typically display resistance to crack initiation through the development of precipitates, however the lower yield strength of the alloy in the over-aged condition reduces the absolute fatigue strength [4-17].

Validation can be performed by comparing this material in the H1025 condition against data published by Voorwald et al. [4-18]. This can then be used to confirm the results for the H1150 condition. This data will then be used to assess the fatigue performance of as-deposited material produced using the WAAM process.

4.5.1. Wrought 15-5PH

To better understand the fatigue response of 15-5PH produced by WAAM, a comparison is made against wrought alloy in the H1025 and H1150 conditions. The results of these tests are shown in Figure 4-31. It is observed that H1150 displays better fatigue resistance, while both conditions produce a similar gradient on the S-N curve. The results for H1025 shows a good agreement with the existing literature [4-18].

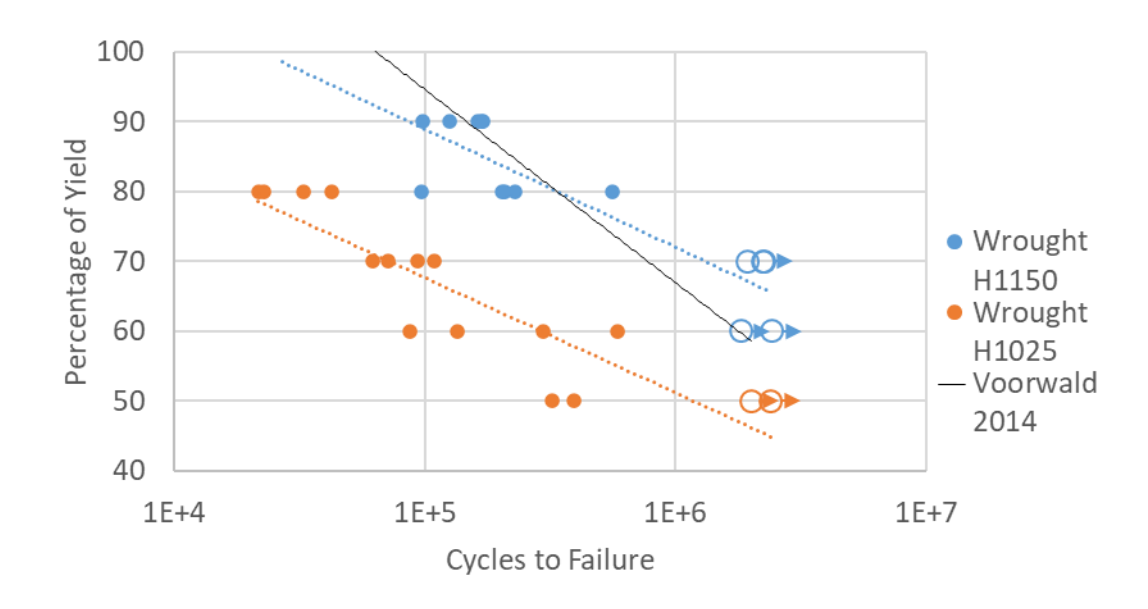


Figure 4-31 Fatigue results for wrought 15-5PH alloy in H1025 and H1150 aging heat treatments.

The fracture surface of a sample tested at 80% of yield stress shows that ductile tensile failure initiates (Figure 4-32d) after a period of fatigue crack growth encompassing 35% of the cross section. The tearing at the edge of the sample shows ductile failure with elongated dimples (Figure 4-32c). At a lower stress range of 50% of yield, the crack growth period is extended, while not exhibiting the tearing fractures at the initiation surface (Figure 4-33). Fracture is predominantly in shear [4-14], though some fatigue striations are noted. Dimple rupture becomes the dominant form of failure after a short transition region.

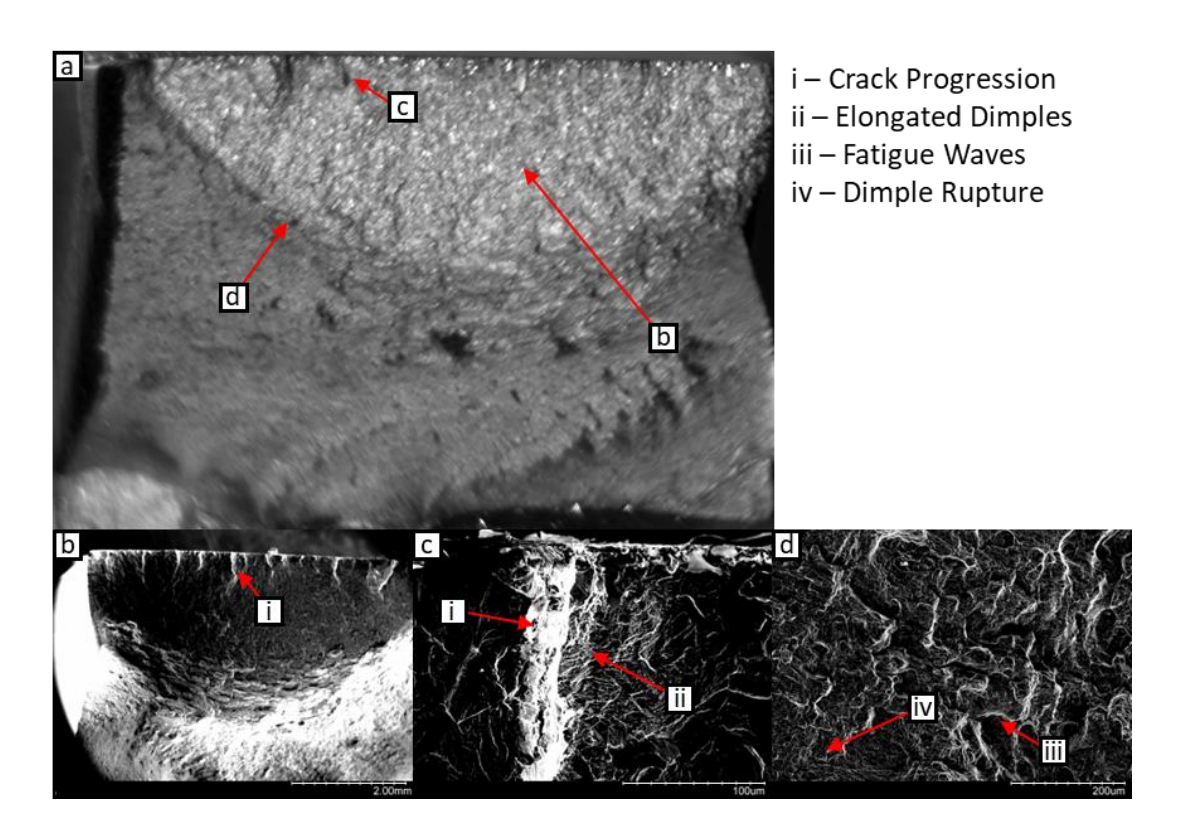


Figure 4-32 Fractographs of fatigue sample tested at 80% of yield stress for 21,622 cycles showing a) the complete fracture surface b) the initiation of failure from multiple cracks growing across a surface c) detail of an initiation crack d) the transition to ductile rupture.

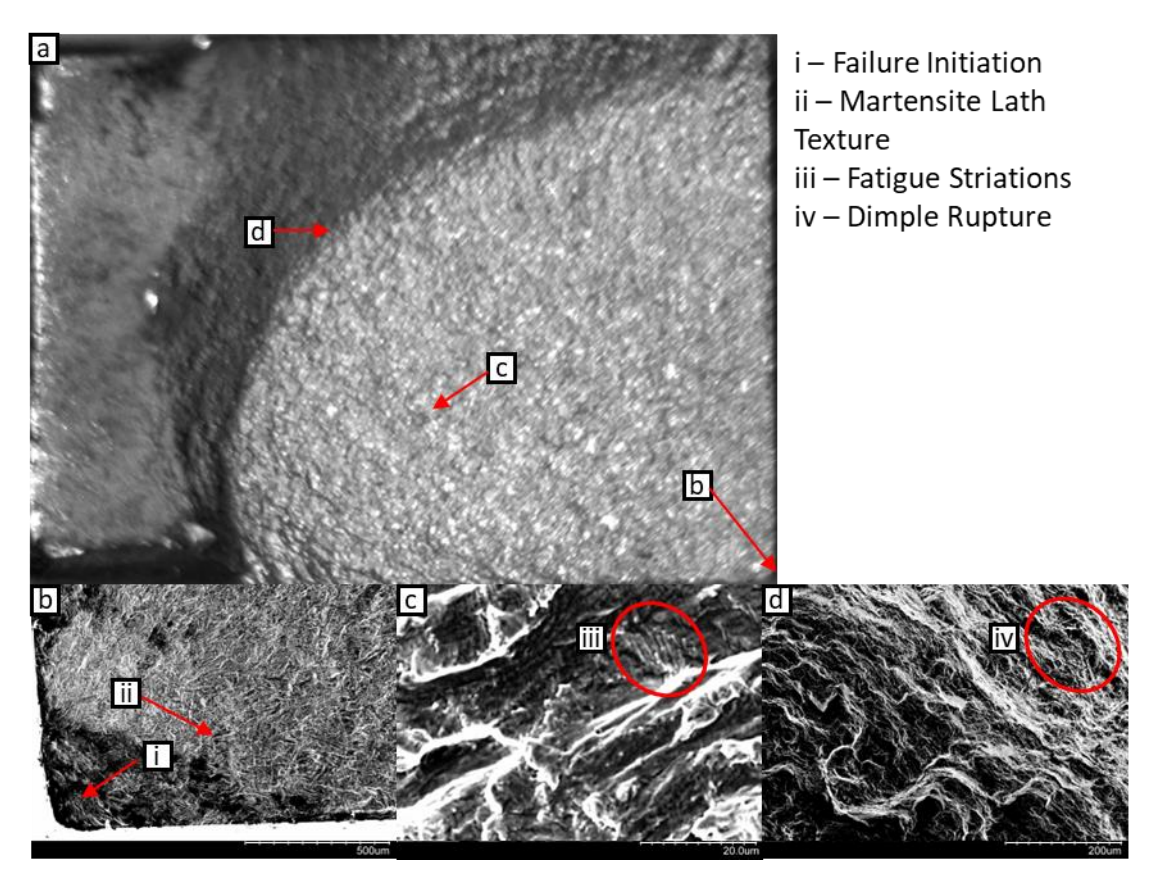


Figure 4-33 Fractographs of fatigue sample tested at 50% of yield stress for 319,395 cycles showing a) the complete fracture surface b) the initiation of fracture showing cleavage rivers c) fatigue striations within the fracture surface d) the transition from cleavage to ductile rupture.

4.5.2. WAAM 15-5PH: high heat input (HH)

Fatigue testing was performed to reveal the impact of the WAAM process on the fatigue life of 15-5PH in the as-deposited and aged conditions. The curve comparing cycles to failure and stress as a percentage of yield is given in Figure 4-34. It is noted that when produced using the HH process parameters, the fatigue performance is reduced by aging heat-treatment. It is suspected that this is related to the reduction in elongation and increased hardness produced by this treatment. The failure of these samples is further analysed through fractography of samples tested at 90% and 60% of yield stress.

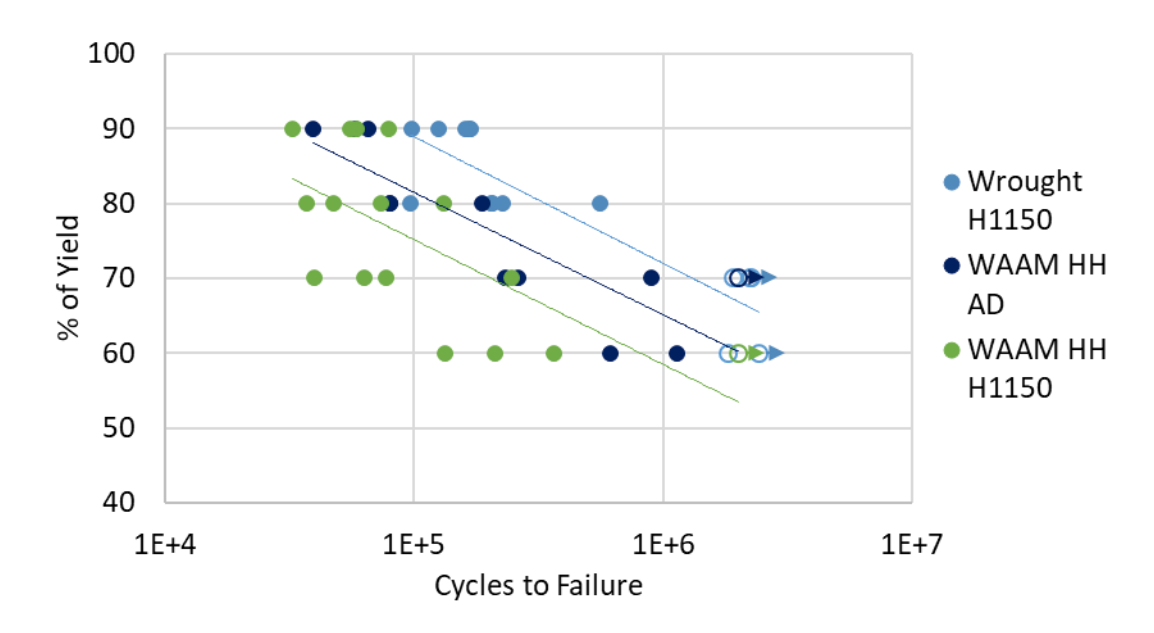


Figure 4-34 Results from fatigue testing of 15-5PH alloy produced using WAAM and HE process parameters.

The trend from the results shown in Figure 4-34 indicate that the fatigue curve shows higher performance in the as-deposited condition. H1150 aging heat-treatment is noted to reduce the fatigue life of samples relative to yield strength. Samples from each set were found to reach the run-out threshold of 2 million cycles and having results of a similar order to that of the wrought material shown in Figure 4-31.

The fracture surfaces of samples in each heat-treatment condition and at the extremes of stress ranges were tested. For the as-deposited samples, quasi-cleavage fracture is dominant across the sample combined with long river features indicative of cleavage fracture seen in Figure 4-35. At large stress ranges, the fracture follows similar trends to tensile failure, propagating along stringer defects. Large fatigue striations are visible at the transition from cleavage and quasi-cleavage to ductile rupture at low stress ranges as seen in Figure 4-36.

In the examples of the aged samples in Figure 4-37 and Figure 4-38, the increased prevalence of ductile behaviour leads to failure initiating at gas pores. The dominant mode of fracture was ductile rupture, with cleavage fracture surrounding the initiation site and some localised regions of quasicleavage.

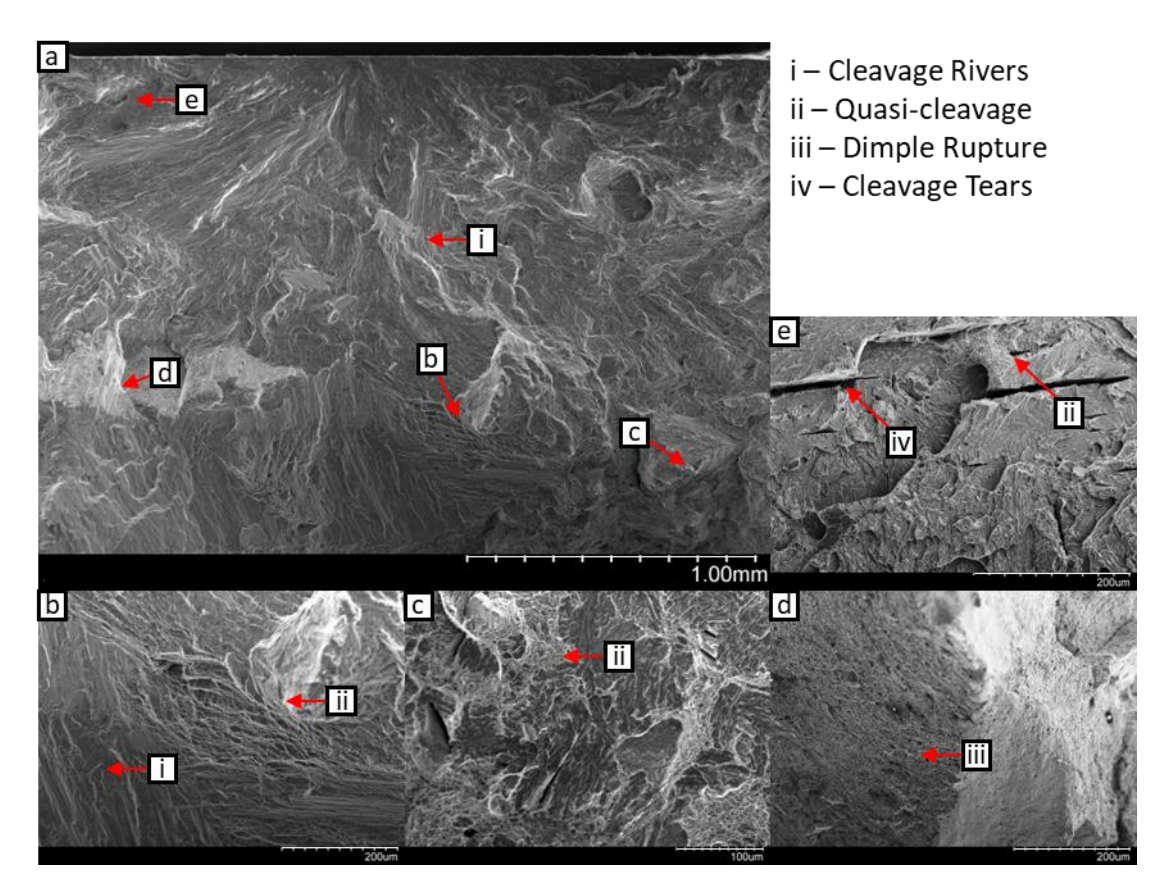


Figure 4-35 Fractographs of a sample tested at 90% of yield for 58,306 cycles in the as-deposited condition showing a) an overview of the fracture surface b) cleavage rivers spreading from the failure initiation c) regions of quasi-cleavage d) the transition to dimple rupture failure e) the growth of cleavage tear features.

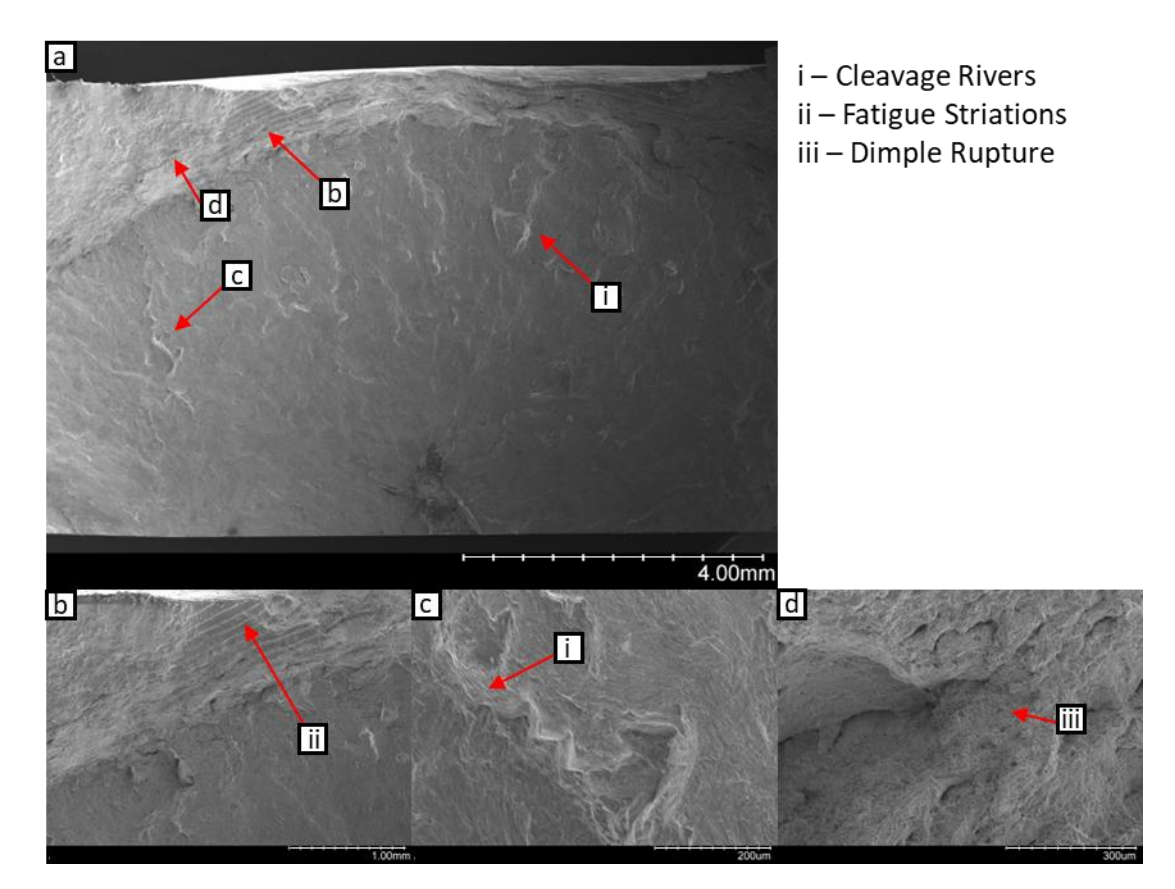


Figure 4-36 Fractographs of a sample tested at 60% of yield for 612,000 cycles in the as-deposited condition showing a) the full fracture surface b) the transition from cleavage failure to fatigue striations and dimple rupture c) the growth of cleavage rivers d) regions of dimple rupture before final failure.

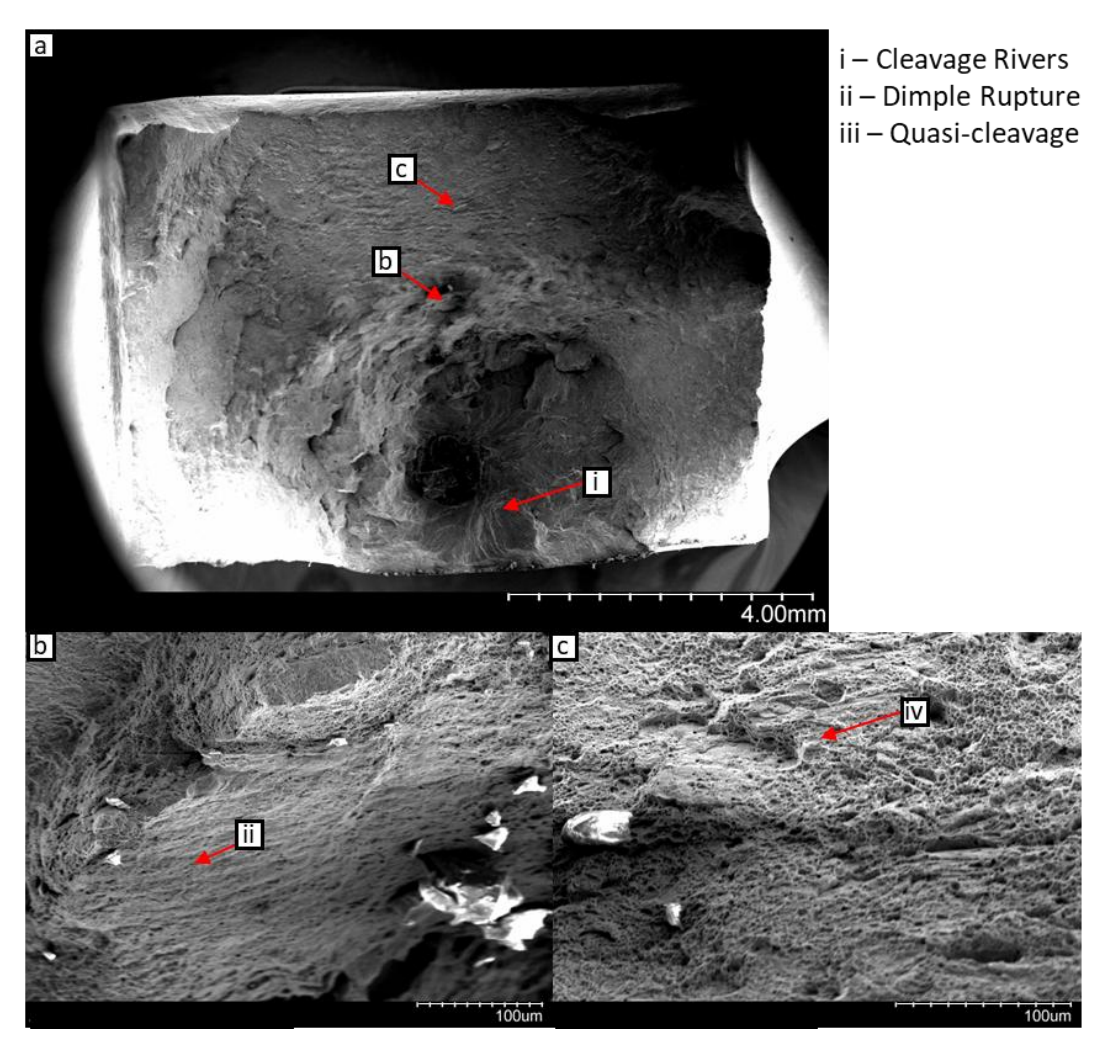


Figure 4-37 Fractographs of a sample tested at 90% of yield for 32,575 cycles in the aged condition showing a) the complete fracture surface b) the development of dimple rupture c) localised regions of quasi-cleavage as fracture progresses.

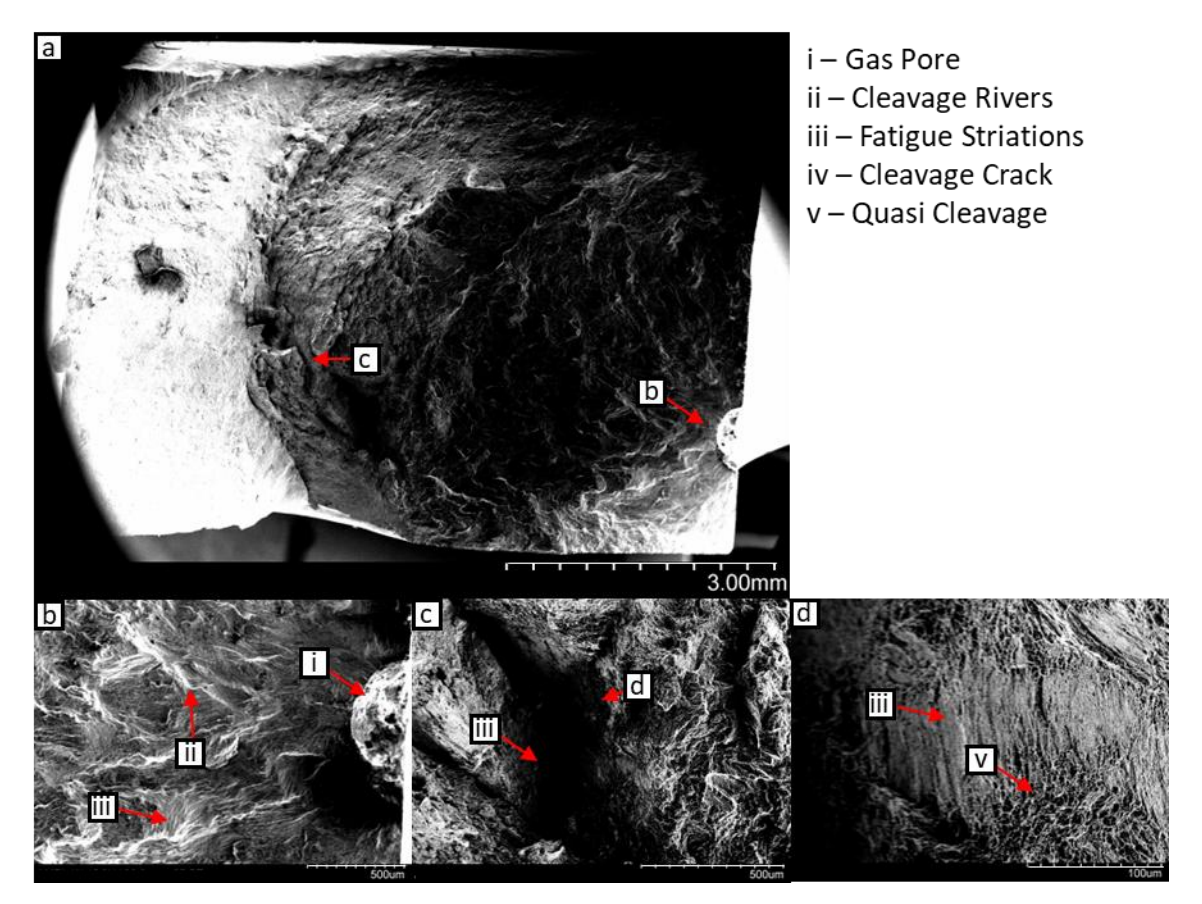


Figure 4-38 Fractographs of a sample tested at 60% of yield for 47,756 cycles in the aged condition showing a) the complete fracture surface b) the growth of cleavage rivers from a gas pore defect c) a tearing feature d) detail of a tearing feature.

4.5.3. WAAM 15-5PH: low heat input (LH)

Fatigue testing was also performed on samples produced using the LH process parameters. The results of this testing are shown in Figure 4-39. This shows that in contrast to the results in Figure 4-34, the aging heat treatment improves fatigue performance relative to yield stress. Overall, these results are substantially lower than those of the wrought material suggesting a significant flaw in the process leading to a reduction in performance.

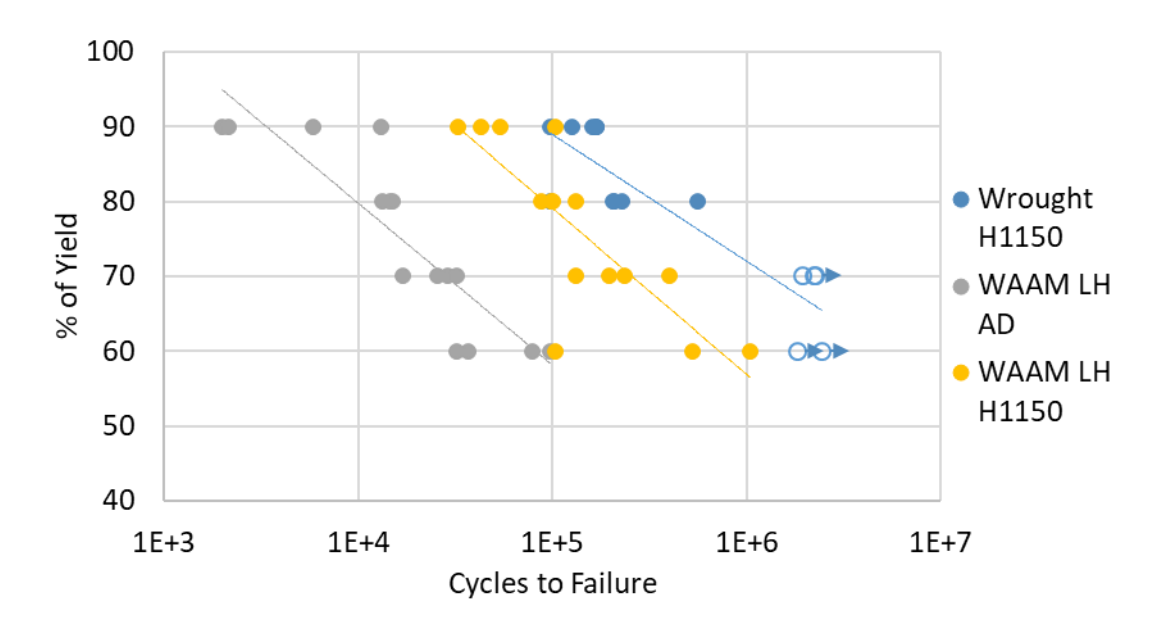


Figure 4-39 Results from fatigue testing of 15-5PH alloy produced using WAAM and LH process parameters.

All samples show gas porosity, identified as the initiation site for crack growth leading to rapid ductile fracture. Figure 4-40 and Figure 4-41 show the fracture surfaces of samples tested at 90% of yield, while Figure 4-42 and Figure 4-43 samples tested at 60% of yield. Comparing the area of cleavage to ductile fracture, the as-deposited samples experience a short growth of cleavage fracture before ductile rupture becomes dominant. The reduction of the stress range causes an extension of the growth of the cleavage fracture region. In the aged condition, the cleavage fracture surface is larger in proportion, while showing wider fatigue striations. The ductile rupture region shows greater elongation, with the fracture surface deviating significantly from the initial fracture plane. This improvement in fatigue strength with aging stands in contrast to the results from HH process parameters (Figure 4-34), but in agreement with the wrought alloy (Figure 4-31).

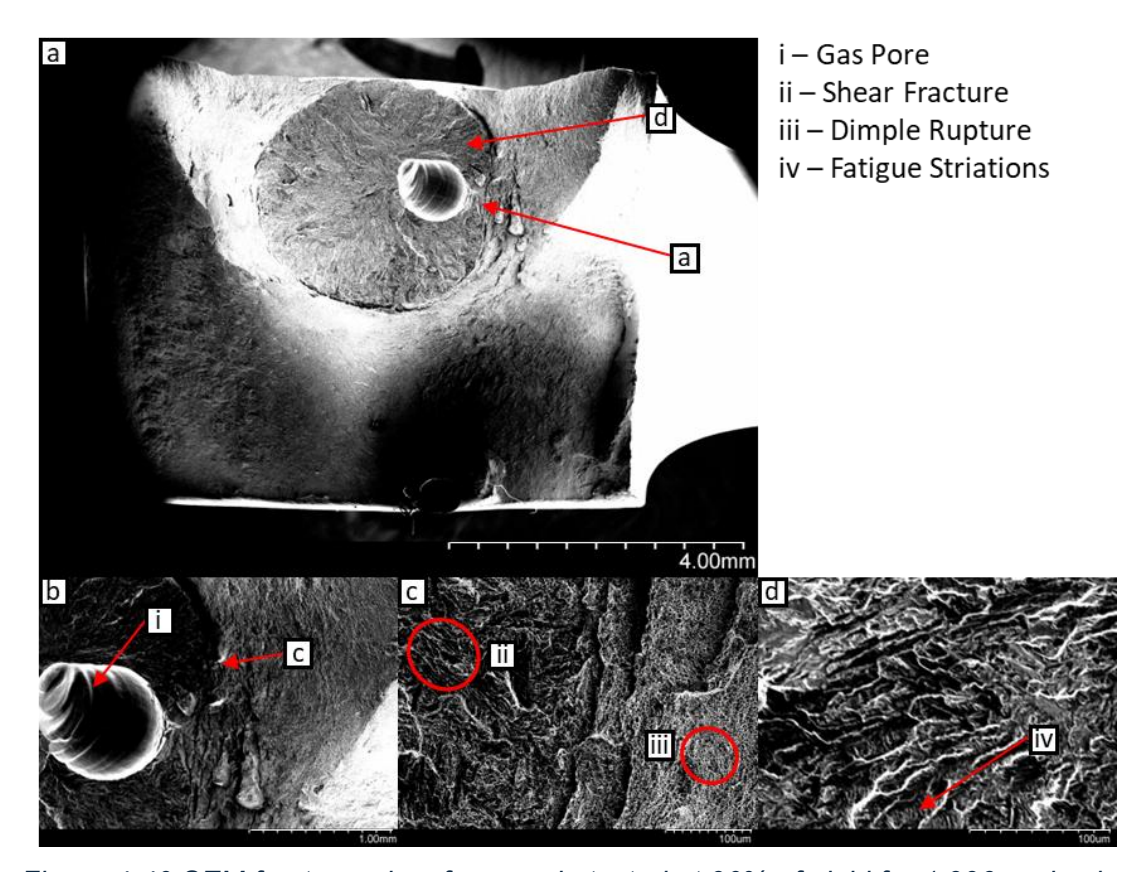


Figure 4-40 SEM fractographs of a sample tested at 90% of yield for 1,996 cycles in the as-deposited condition showing b) fracture initiating at a gas pore c) the transition to ductile rupture and d) the propagation of fatigue striations.

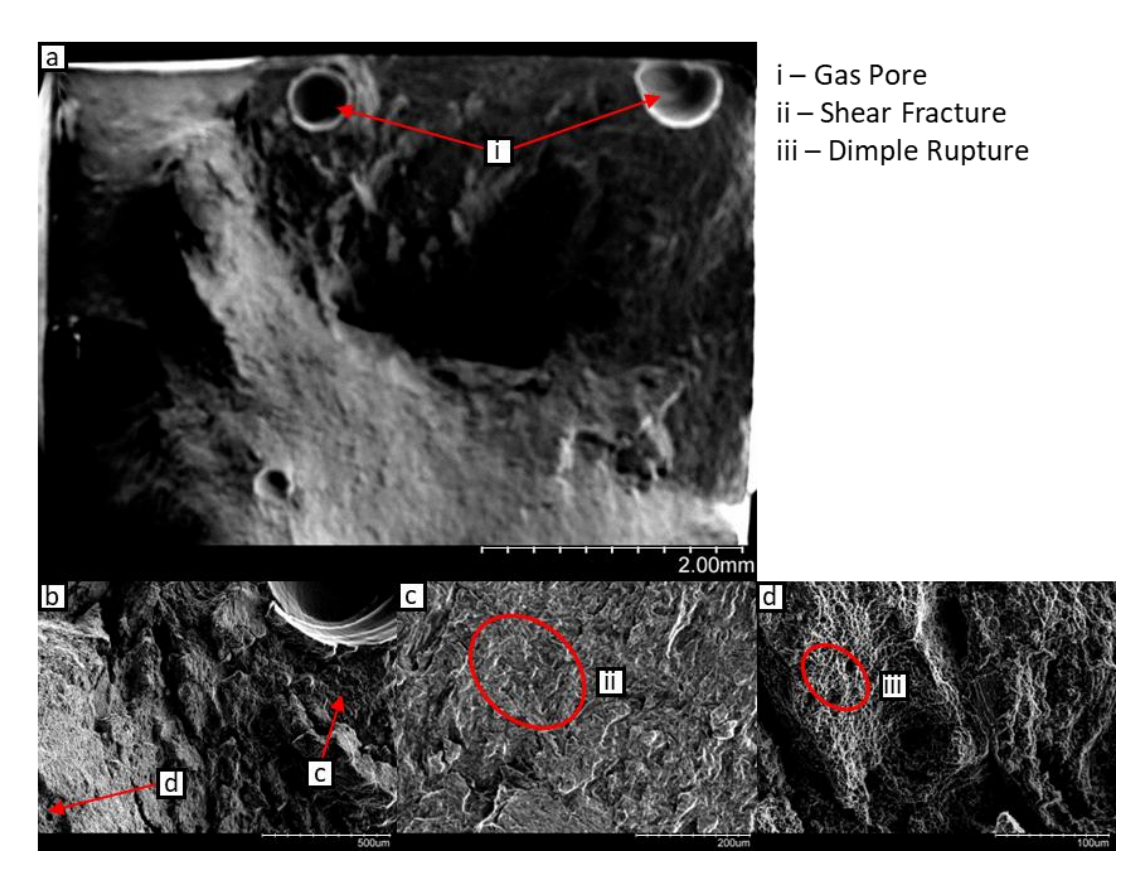


Figure 4-41 SEM fractographs of a sample tested at 60% of yield for 31,999 cycles in the as-deposited condition showing b) and c) the growth of shear failure from the gas pores and d) the development of ductile rupture.

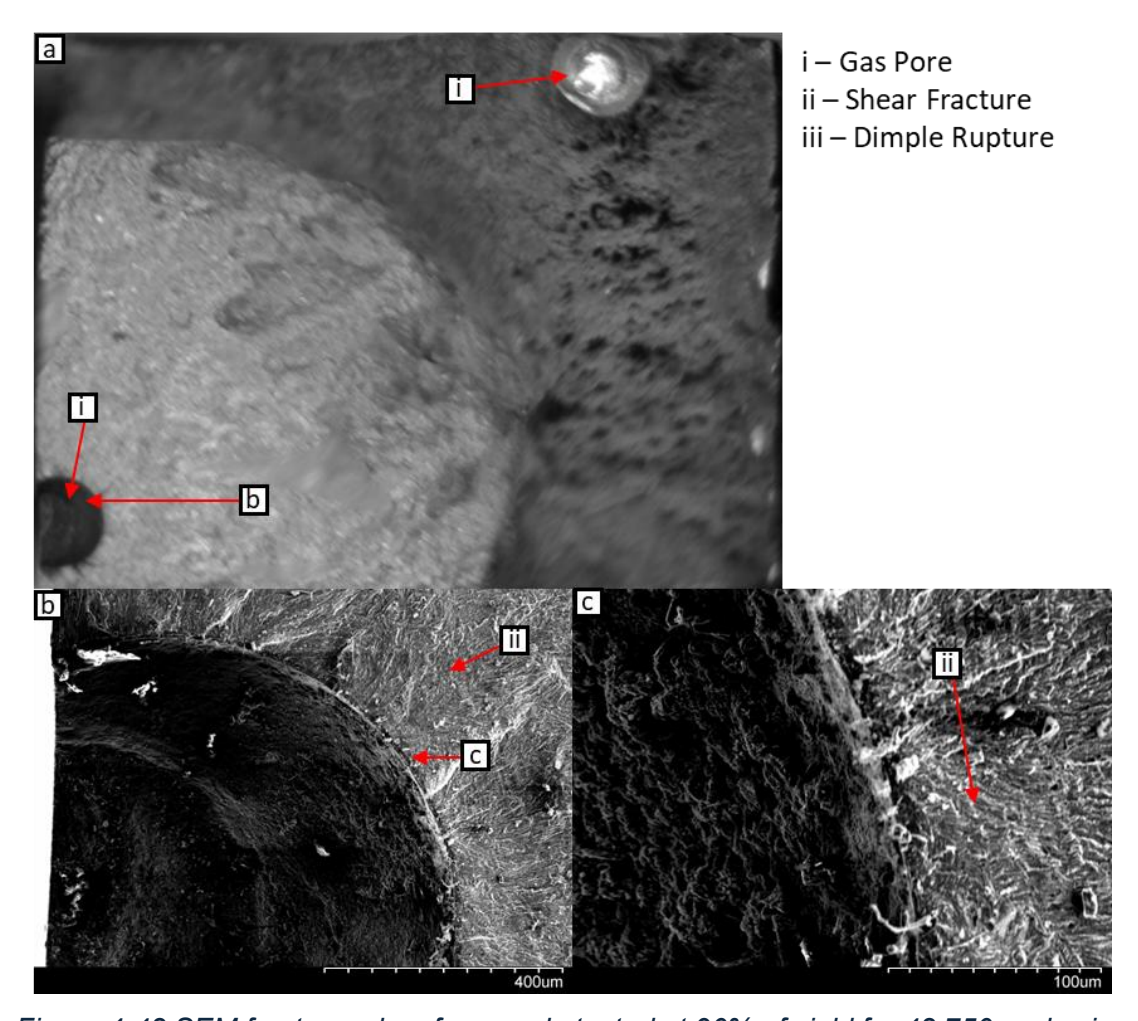


Figure 4-42 SEM fractographs of a sample tested at 90% of yield for 42,750 cycles in the aged condition showing b) and c) the development of shear failure from the gas pore and d) the interaction of impurities with ductile rupture.

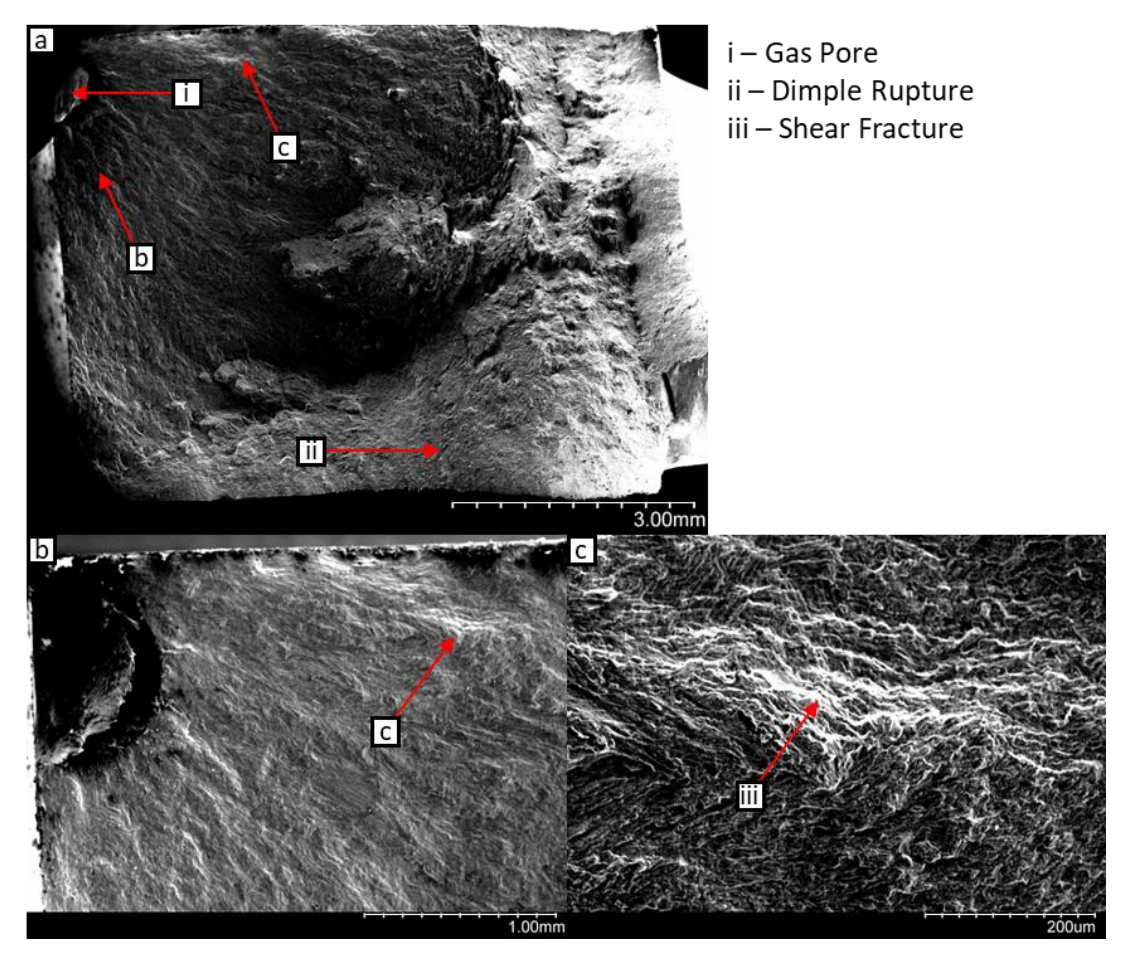


Figure 4-43 H1150 60% SEM fractographs of a sample tested at 60% of yield for 103,500 cycles in the aged condition showing b) and c) the growth of wave like shear fracture structures.

4.6. Discussion

The results from this experimental series can be compared to assess the value of using WAAM to fabricate 15-5PH stainless steel. While local assessments have been made throughout this chapter; this section will include comparisons between these data sets. As described previously, the as-deposited results are assessed relative to the specifications for H1025 in ASTM A693.

Table 4-4 Mechanical properties data from testing of 15-5PH alloy compared with standard ASTM A693-16 [4-11].

	Yield stress	UTS	Elongation	Hardness	Impact				
	(MPa)	(MPa)	(%)	(HV0.05)	toughness				
As-deposited results									
HH	910	1127	20.1	374	8				
LH	875	1020	10.9	432	40				
H1025 resul	H1025 results								
Wrought	1107	1210	22.9	405	120 [4-19]				
ASTM	1000	1070	8	311-406	14				
A693									
H1150 resul	H1150 results								
Wrought	849	984	25.3	343	145 [4-19]				
НН	908	996	12.9	408	46				
LH	580	956	26.7	354	60				
ASTM	725	930	10	258-342	34				
A693									

Comparing the results from tensile testing shows that in the as-deposited state, neither set of process parameters results in the yield stress meeting the values specified in standard ASTM A693 for H1025 condition, while they do greatly exceed the value specified for the H1150 condition.

Only in the case of process parameters HH and following aging treatment H1150, are all of the mechanical properties specified by ASTM A693 met. Even in this case, however, the hardness is observed to exceed those specified in the standard [4-11].

It is also noted that material produced using LH parameters consistently displays the lowest yield and ultimate tensile strengths compared to wrought and HH material. This extends to a comparison of fatigue results in Figure 4-44, where in the as-deposited state, HH material outperforms wrought material in the H1025 condition with similar mechanical properties, while LH material displays inferior performance.

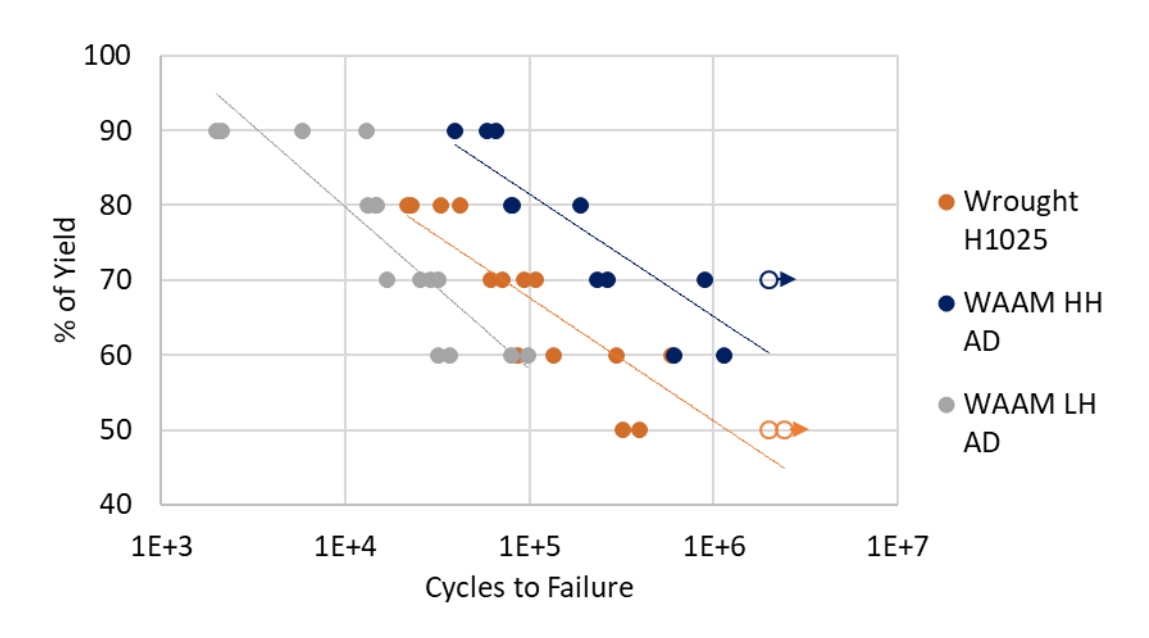


Figure 4-44 Fatigue data comparing wrought material aged to H1025 and WAAM material in the as-deposited condition.

In the case of samples in the H1150 condition, the fatigue data in Figure 4-45 shows that similar performance is obtained from WAAM produced using both sets of process parameters. There is a loss of performance compared to the wrought material which is associated with defects such as gas porosity.

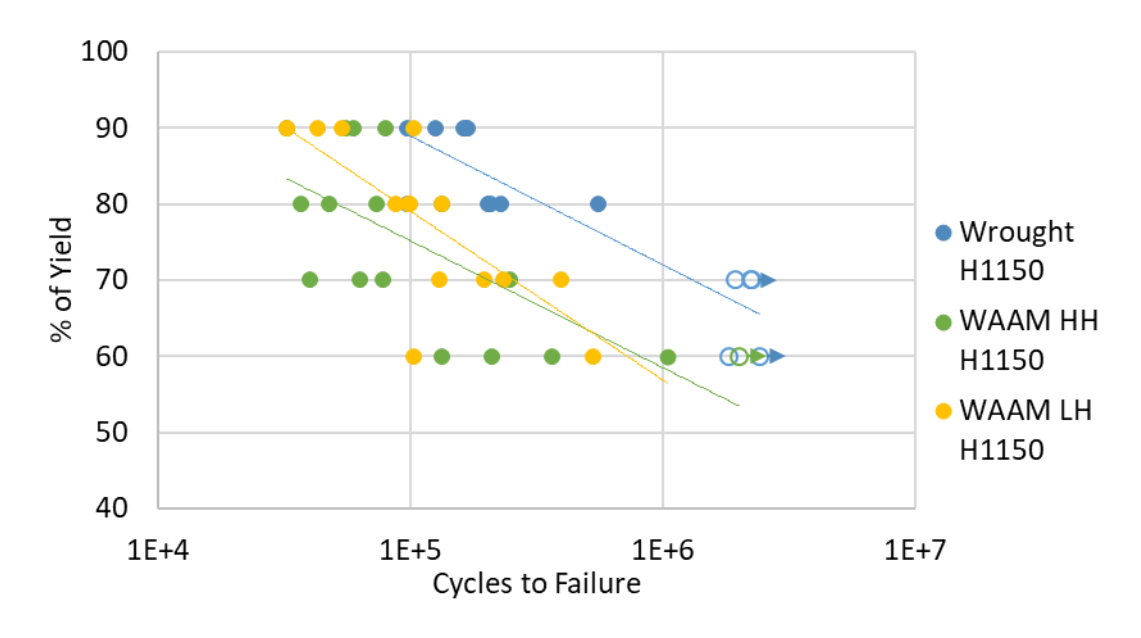


Figure 4-45 Fatigue data comparing wrought and WAAM material in the H1150 condition.

The overall inferior performance of material produced using LH parameters can be explained by the greater proportion of inclusions and gas pores in the samples compared to material produced using HH parameters. In addition, the significant growth of metal carbides in HH aged samples may contribute to the

increased strength and hardness compared to the same material in the asdeposited condition, and LH material in the same H1150 condition. This is noted to come at the cost of reduced elongation. In these samples, the proportion of δ -ferrite also decreased. This has been associated with a reduction in strength and hardness, however, the increase in MC mitigates this effect.

When impact testing was performed, it was found that the aged samples dramatically outperformed their as-deposited counterparts, with material manufactured using LH process parameters displaying the greatest impact toughness in the aged condition. Alongside this, a lower proportion of cleavage failure regions and a greater prevalence of dimple rupture are observed. The formation of shear wings was noted on all samples manufactured using LH process parameters. Large shear wings were also noted on the LH-H1150 samples, which correlates to the low hardness and yield stress displayed in addition to high ductility and impact toughness.

An overall analysis of this data suggests that the most promise is shown by modifying the HH process parameters and refining the post weld heat treatment. Downsides of this condition include the low ductility as well as yield stress and impact toughness below that required by standard ASTM A693 [4-11]. These downsides are likely to be mitigated by an aging or stress relief heat treatment regime with lower temperature or time than the H1150 heat treatment. This lower temperature heat treatment would likely relieve internal stresses caused by welding and improve the impact toughness of the material. These improvements would be achieved without causing a significant change in the strength of the material through changes to the microstructure.

An alternative to this would be to precede the aging treatment with a solution treatment, after which, the material could be processed in an equivalent manner to the wrought alloy. The biggest concern is that of defects such as gas porosity. Solving this problem requires further research to investigate the causes of porosity and would likely require further refinement of the process parameters.

4.7. References

- [4-1] ASM handbook. Volume 1, Properties and selection: irons, steels, and high-performance alloys, 10th edition. ed. Materials Park, OH: Materials Park, OH: ASM International, 1990.
- [4-2] L. Couturier et al., "Evolution of the microstructure of a 15-5PH martensitic stainless steel during precipitation hardening heat treatment", *Materials & Design*, vol. 107, pp. 416-425, 2016/10/05 2016, doi: 10.1016/j.matdes.2016.06.068.
- [4-3] X. Peng et al., "Effect of Aging on Hardening Behavior of 15-5 PH Stainless Steel", Journal of Iron and Steel Research, International, vol. 22, no. 7, pp. 607-614, 2015/07/01/ 2015, doi: 10.1016/S1006-706X(15)30047-9.
- [4-4] H. R. Habibi Bajguirani, "The effect of ageing upon the microstructure and mechanical properties of type 15-5 PH stainless steel", *Materials* science & engineering. A, Structural materials: properties, microstructure and processing, vol. 338, no. 1, pp. 142-159, 2002, doi: 10.1016/S0921-5093(02)00062-X.
- [4-5] B. J. A, "Weld microstructure development and properties of precipitation-strengthened martensitic stainless steels", Welding journal, vol. 78, no. 8, p. 280, 1999.
- [4-6] V. T. Ha and W. S. Jung, "Niobium carbo-nitride precipitation behavior in a high nitrogen 15Cr-15Ni heat resistant austenitic stainless steel", *Met. Mater. Int*, vol. 17, no. 5, pp. 713-720, 2011, doi: 10.1007/s12540-011-1003-5.
- [4-7] J. Niu *et al.*, "Effect of Post-Weld Aging Temperature on Microstructure and Mechanical Properties of Weld Metal of 15-5 PH Stainless Steel", *Journal of materials engineering and performance,* vol. 29, no. 11, pp. 7026-7033, 2020, doi: 10.1007/s11665-020-05193-y.
- [4-8] J. F. Wang et al., "Effect of location on microstructure and mechanical properties of additive layer manufactured Inconel 625 using gas tungsten arc welding", Materials science & engineering. A, Structural materials: properties, microstructure and processing, vol. 676, pp. 395-405, 2016, doi: 10.1016/j.msea.2016.09.015.
- [4-9] M. Ghaffari, A. V. Nemani, and A. Nasiri, "Microstructure and mechanical behavior of PH 13–8Mo martensitic stainless steel fabricated by wire arc additive manufacturing", *Additive Manufacturing*, vol. 49, p. 102374, 2022/01/01/ 2022, doi: 10.1016/j.addma.2021.102374.
- [4-10] J. González *et al.*, "Additive manufacturing with GMAW welding and CMT technology", *Procedia manufacturing*, vol. 13, pp. 840-847, 2017, doi: 10.1016/j.promfg.2017.09.189.
- [4-11] A693-16 Standard Specification for Precipitation-Hardening Stainless and Heat-Resisting Steel Plate, Sheet, and Strip, 2016.
- [4-12] A. S. Prabhakar et al., "Effect of Post Weld Heat Treatment on Mechanical Properties of 17-4-PH Stainless Steel Welds", *Materials science forum.*, vol. 830, pp. 181-184, 2015, doi: 10.4028/www.scientific.net/MSF.830-831.181.
- [4-13] C. Guo, R. Hu, and F. Chen, "Microstructure and performances for 15-5 PH stainless steel fabricated through the wire-arc additive

- manufacturing technology", *Materials technology*, pp. 1-12, 2020, doi: 10.1080/10667857.2020.1800296.
- [4-14] ASM handbook. Volume 12, Fractography. Metals Park, Ohio : American Society for Metals., 1987.
- [4-15] S. Vantadori et al., "Effect of the porosity on the fatigue strength of metals", Fatigue & fracture of engineering materials & structures, vol. 45, pp. 2734-2747, 2022, doi: 10.1111/ffe.13783.
- [4-16] B. M. Schönbauer, K. Yanase, and M. Endo, "VHCF properties and fatigue limit prediction of precipitation hardened 17-4PH stainless steel", *International journal of fatigue*, vol. 88, pp. 205-216, 2016, doi: 10.1016/j.ijfatigue.2016.03.034.
- [4-17] J.-H. Wu and C.-K. Lin, "Tensile and fatigue properties of 17-4 PH stainless steel at high temperatures", *Metallurgical and Materials Transactions A*, vol. 33, no. 6, pp. 1715-1724, 2002, doi: 10.1007/s11661-002-0180-8.
- [4-18] H. J. C. Voorwald, M. O. H. Cioffi, and G. S. Júnior, "Influence of HVOF Coating on the Fatigue Strength of 15-5 PH Stainless Steel", *Advanced materials research.*, vol. 891, pp. 843-847, 2014, doi: 10.4028/www.scientific.net/AMR.891-892.843.
- [4-19] G. R. Ebrahimi, H. Keshmiri, and A. Momeni, "Effect of heat treatment variables on microstructure and mechanical properties of 15Cr–4Ni–0.08C martensitic stainless steel", *Ironmaking & steelmaking*, vol. 38, pp. 123-128, 2011, doi: 10.1179/030192310X12816231892468.

5. Inconel 625 WAAM

Inconel 625 is a widely used nickel-based corrosion resistant alloy [5-1]. Due to its combination of high corrosion resistance with high strength and performance at high temperatures [5-2], it is commonly used in adverse conditions experienced by oil and gas, defence, and energy equipment [5-3 - 5-5]. Inconel 625 is widely used as a clad coating to provide high levels of corrosion resistance in pipelines [5-6]. This is typically performed using arc cladding and a wire feedstock with good results [5-4, 5-7]. As such, this material is well suited to the WAAM process [5-8].

The composition of alloy 625 is specified in standard ASTM B443 [5-9]. These are compared with data obtained through EDS analysis of the microstructure in Table 5-1. This chapter will characterise the microstructure in addition to determining the mechanical and fatigue properties of this material.

Table 5-1 Composition of Inconel 625.

Element	Ni	Cr	Fe	Мо	Nb
Wrought Inconel 625	58 min	20-23	5 max	8-10	3.15-4.15
[5-1, 5-9]					
WAAM deposited Inconel	62.7	23	0	10.3	4.0
625					
Element	Ti	Al	С	Mn	Si
Wrought Inconel 625	0.4	0.4	0.1	0.5	0.5
[5-1, 5-9]					
WAAM deposited Inconel	trace	0	trace	trace	trace
625					

5.1. Microstructure

This section will detail the microstructure found in Inconel 625 manufactured using WAAM with the composition and process parameters shown in Table 5-3 and Table 5-4. The alloys will be examined both in the as-deposited (AD) condition and following solution treatment (ST). The heat treatment performed is shown in Table 5-2.

Table 5-2 Heat treatment of Inconel 625 [5-10]. Visualised in Figure 5-1

Alloy	Solution treatment (ST)				
	Temperature	Cooling			
	(°C)	(hr)			
Inconel	1150	1	Air cool		
625					

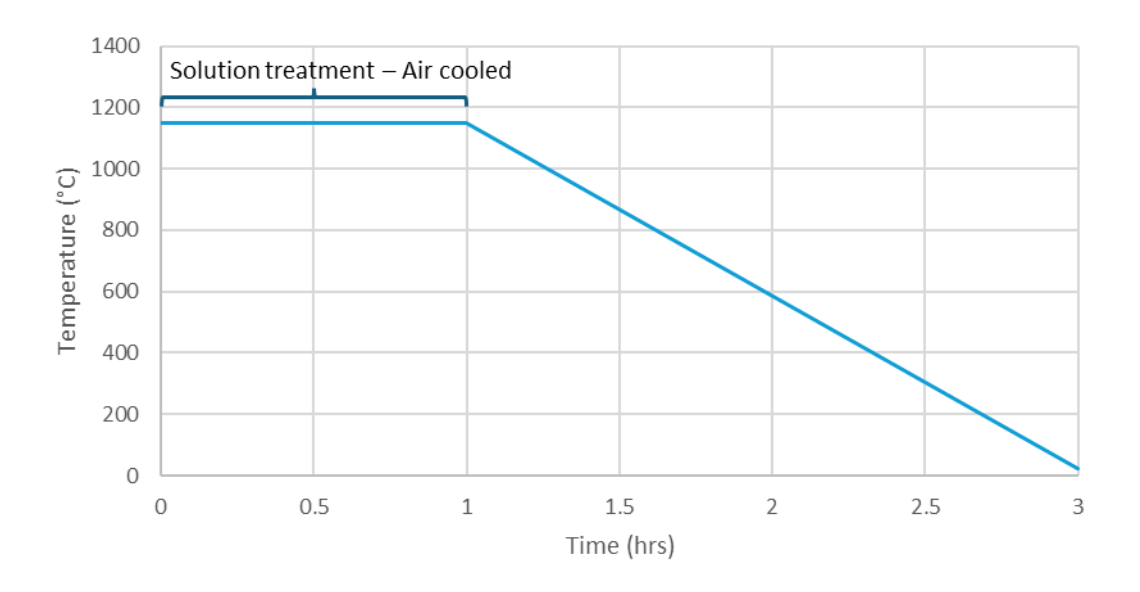


Figure 5-1 Time – temperature chart for heat treatment.

Table 5-3 WAAM process parameters for Inconel 625.

Alloy	CMT	Travel	Wire feed	Standoff	Interpass
	program	speed	speed	distance	temperature
		(mm/s)	(m/min)	(mm)	(°C)
Inconel	CrNi 19 9	13	6.5	8	60
625	CMT928				
Alloy	Step	Indicated	Indicated	Heat	
	width	Current (A)	Voltage (V)	input	
	(mm)			(kJ/mm)	
Inconel	4	178	17.4	0.191	
625					

Table 5-4 Composition of Inconel 625 filler wire.

Alloy	С	Si	Ni	Cr	Мо	Fe	Ti	Al	Nb
Inconel	0.01	0.07	Bal	22.32	9.10	0.3	0.018	0.12	3.44
625									

Inconel 625 is widely used in high temperature environments and in contact with corrosive agents such as hydrogen sulphide (H₂S) [5-11]. It is primarily alloyed with chromium and molybdenum which provide resistance to oxidation and promote solid solution strengthening [5-12]. It is further alloyed with niobium, aluminium and titanium which form strengthening phases such as carbides, as well as y' and y" precipitates [5-13]. As the alloy is commonly used in high temperature environments such as energy equipment or jet engines, the evolution of the microstructure during extended exposure to high temperatures has been investigated. Typical service exposed material will show carbides on the grain boundaries [M₂₃C₆] in addition to the γ" and [Ni₂(Cr,Mo)] (Laves) phases which increase matrix strain [5-13]. The precipitate phases and carbides which form are described in a timetemperature-transformation (TTT) diagram as shown in Figure 5-2; this diagram shows that primary carbides develop after less than an hour at temperatures above 700°C, while the γ", Laves and δ phases form after 10 to 100 hours, with extended exposure to temperatures of 650°C converting y" to the Laves and δ phases [5-14, 5-15].

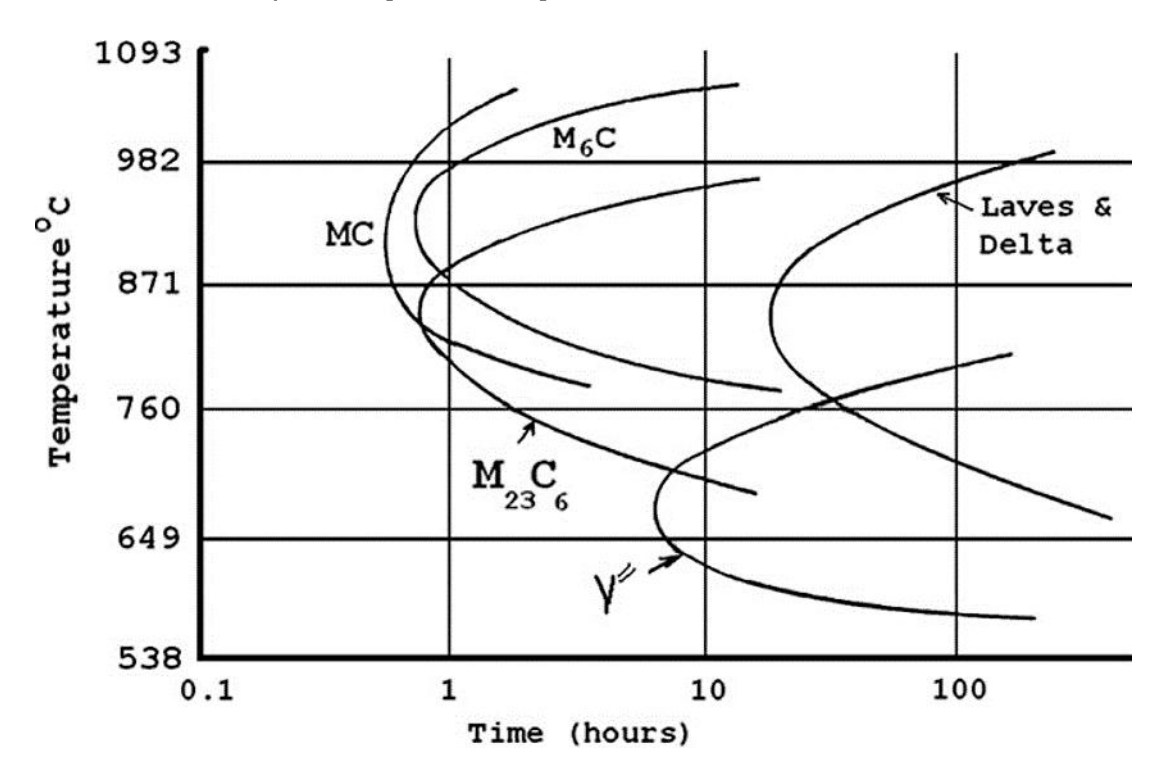


Figure 5-2 Time-Temperature-Transition (TTT) diagram for Inconel 625 [5-12].

This alloy is typically solution treated to improve strength at high temperature by dissolving the detrimental Laves phase while retaining the primary carbides (NbC and TiC) [5-12].

As for the investigation of 15-5PH in chapter 4, the effect of heat treatment on the surface of the alloy is characterised. As shown in Figure 5-3, a surface skin of chromium oxide forms with a thickness of $3.5\mu m$, while a change in the microstructure caused by mechanical treatment of the sample is observed to a depth of 22 μm .

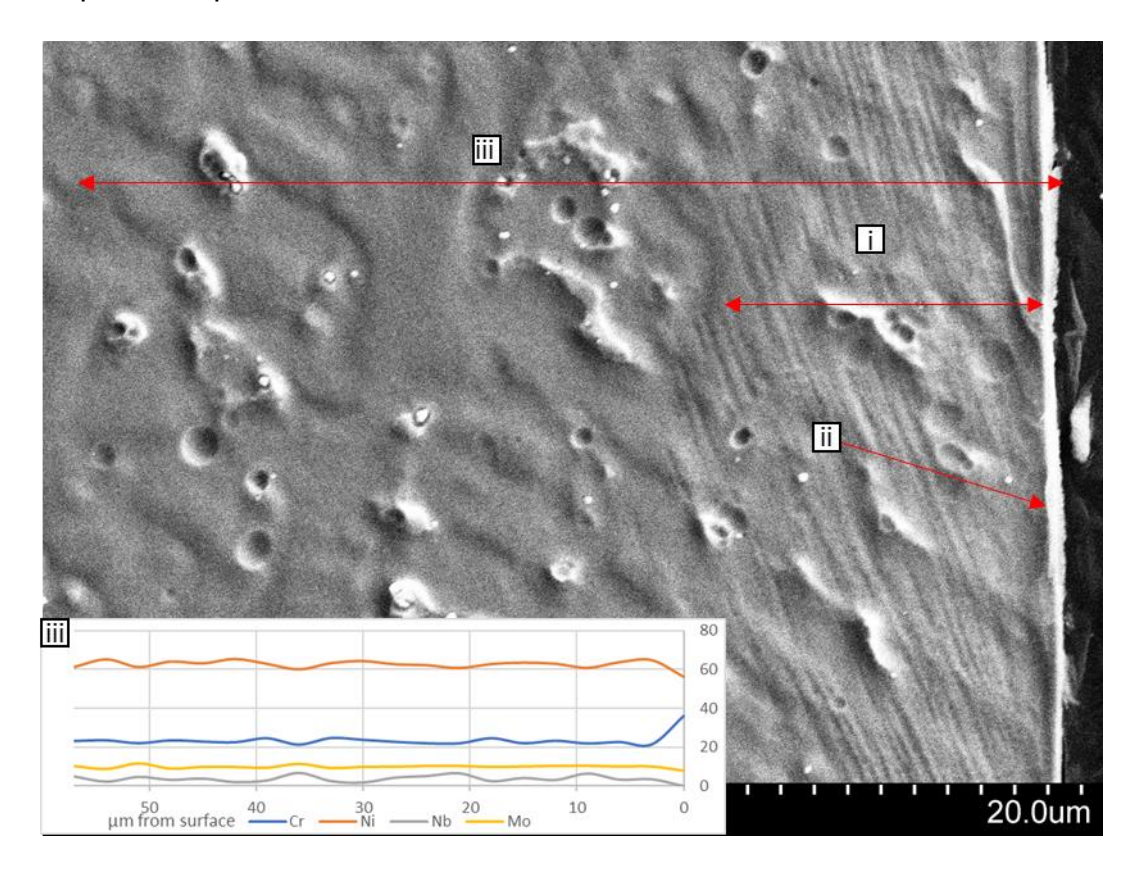


Figure 5-3 SEM imaging of the chromium oxide skin formed through heat treatment of Inconel 625 i) recrystalised region ii) CrO skin iii) EDS scan path.

Under optical microscopy, the microstructure produced through WAAM deposition can be characterised, as well as its development following solution treatment as displayed in Figure 5-4. In the as-deposited condition, a columnar dendritic structure is observed [5-16]. Through electron microscopy, the Laves phase and carbides of Nb and Ti are observed as irregular structures. The Laves phase is identified as small stringers [5-17] and the precipitated carbides have an irregular, globular morphology [5-4]. Using EDS analysis, it is noted that the interdendritic spaces display a segregation of Nb and Mo [5-17].

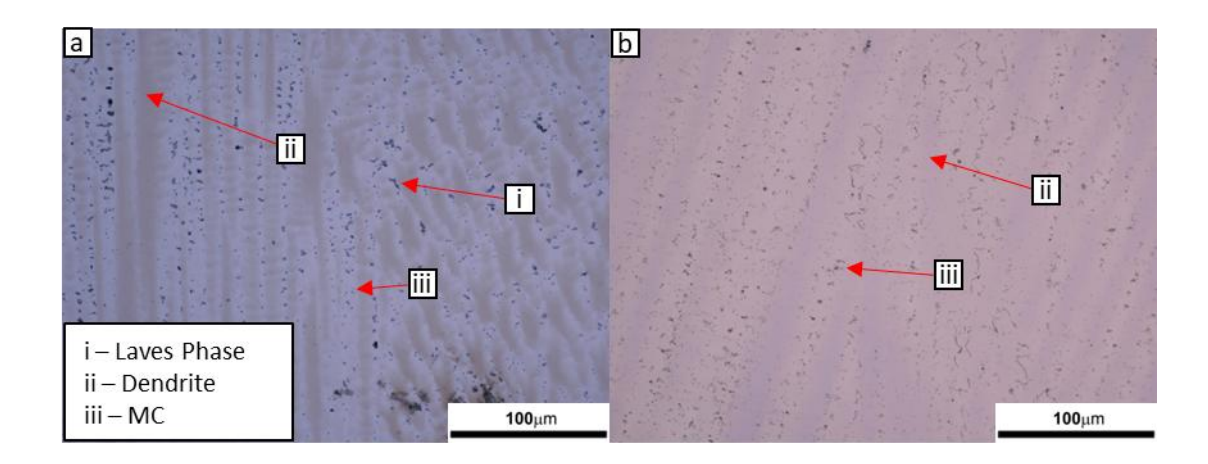


Figure 5-4 Optical microscopy of WAAM produced Inconel 625 in as-deposited (a) and solution treated (b) conditions.

When the WAAM deposited alloy undergoes solution treatment, the distinction between columnar dendrites is reduced, the Laves phase is dissolved while the number of carbides increases.

The most common form of carbides in Inconel 625 is of composition MC (TiC and NbC) [5-13] which are widely observed in the microstructure (Figure 5-4). In addition, Cr₂₃C₆ carbides can be observed on grain boundaries following solution treatment [5-2, 5-17] (Figure 5-5).

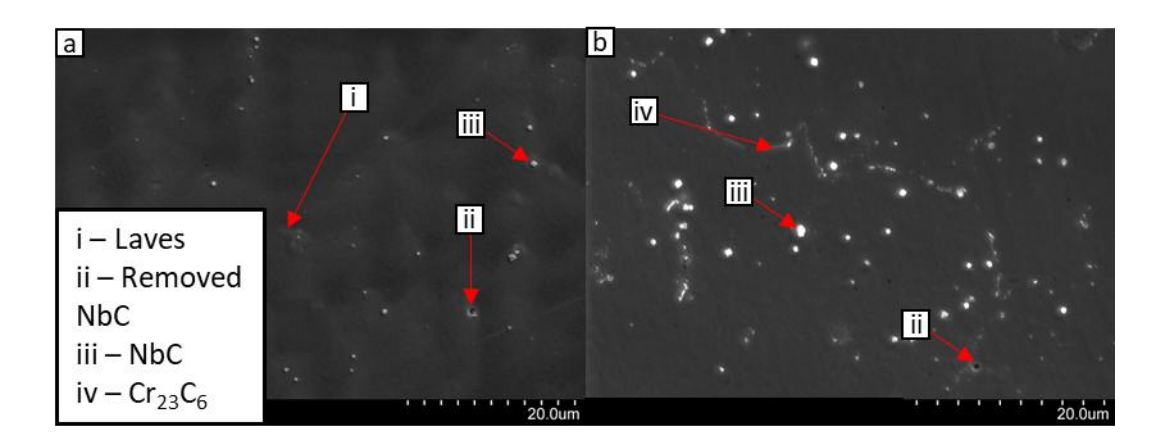


Figure 5-5 SEM micrographs of alloy 625 following each stage of heat treatment: a) as-deposited b) solution treated.

5.2. Hardness testing

Inconel 625 produced using WAAM in the as-deposited (AD) and solution treated (ST) conditions were subject to microhardness testing. The results are presented in Figure 5-6.

Solution treatment is identified to reduce the hardness of Inconel 625 compared to the as-deposited condition. This is combined with a reduction in the spread of values indicating a homogenisation of the microstructure.

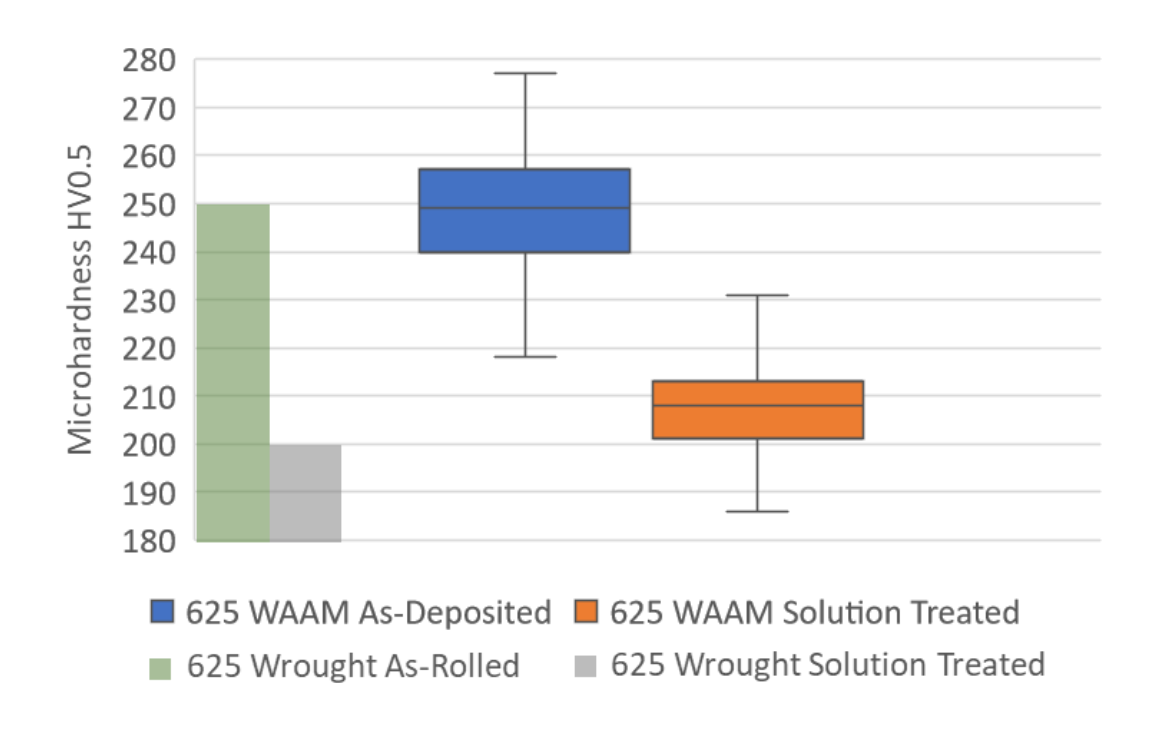


Figure 5-6 Microhardness data for WAAM produced Inconel 625 in as-deposited and solution treated conditions compared against data from the manufacturer [5-18].

These results confirm observations from the microstructure that the brittle Laves phase was dissolved during solution treatment resulting in the softening of the material [5-17, 5-19]. In addition, the reduction in the variation of the data indicates that solution treatment promotes homogenisation of the material [5-20].

5.3. Tensile testing

To establish the mechanical properties of Inconel 625, tensile testing was performed on samples in the typical service condition (ST). This testing allows the yield strength, elongation and ultimate tensile strength to be determined.

Following testing, the fracture surfaces were examined optically and by SEM to identify the failure mode. This investigation will also identify if aspects of the microstructure are correlated with the initiation of failure.

Previous literature has investigated the tensile strength of this alloy produced using a range of production methods. These are detailed in Figure 5-7 and

show that overall, WAAM methods produce lower strength material when compared to laser and powder methods such LMD (laser metal deposition), however, these methods result in a reduced elongation due to high lattice distortion and small grain size [5-21, 5-22].

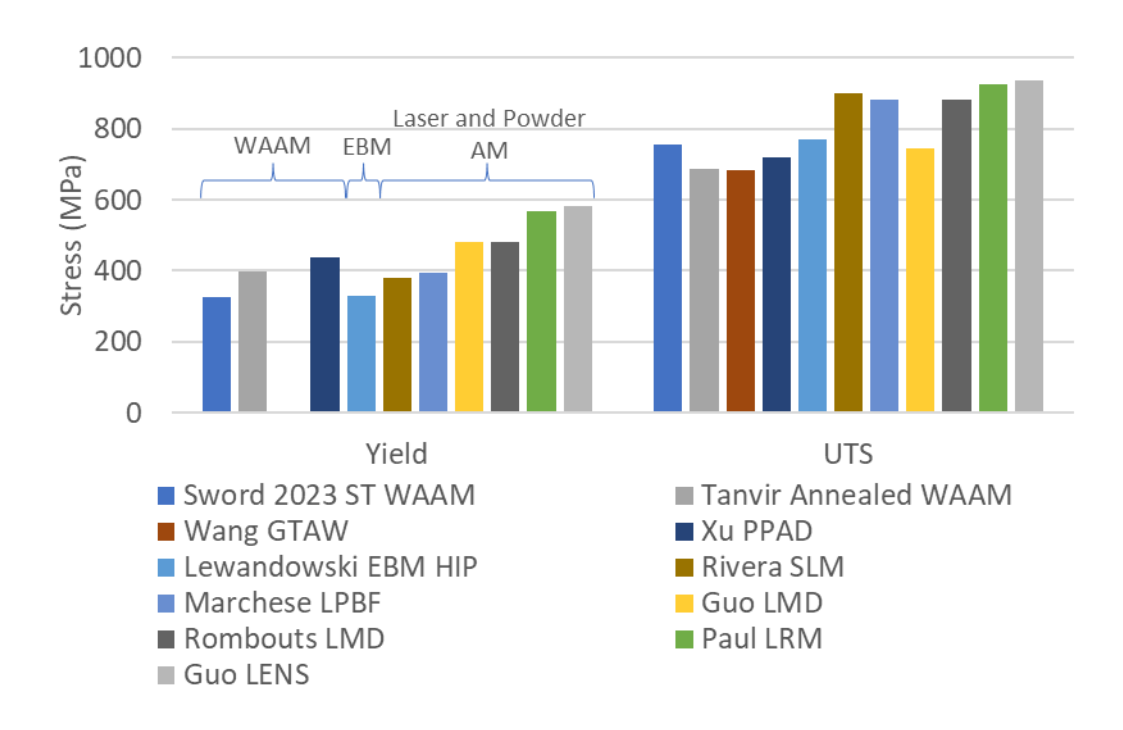


Figure 5-7 Comparison of mechanical properties for the additive manufacturing of Inconel 625 by various methods [5-19, 5-23 - 5-29].

When samples of Inconel 625 in the solution treated state were subject to tensile testing, a yield strength of 324MPa and UTS of 756MPa with an elongation of 55.7%. These results are very consistent, with a standard deviation of 1.2%, 1.4% and 8.7% respectively. Figure 5-8 presents a comparison between this data and that produced by Tanvir et al. [5-19] and Wang et al. [5-23]. In these cases, solution treated, WAAM produced Inconel 625 is considered. The differences in these results reveals that the material produced exceed all the requirements presented in standard ASTM B443 [9] in addition to surpassing previously published results for UTS and elongation [19, 23].

The difference between the results presented here and those from Tanvir et al. [17] and Wang et al. [23] can be explained through the observation of differences in the microstructure. The material presented by Tanvir et al. demonstrates the presence of δ phase in the solution treated condition,

suggesting that γ" strengthening phases have been reduced leading to a reduction in UTS. The material produced by Wang et al. was tested in the asdeposited condition, therefore still retaining the Laves phase, resulting in reduced elongation.

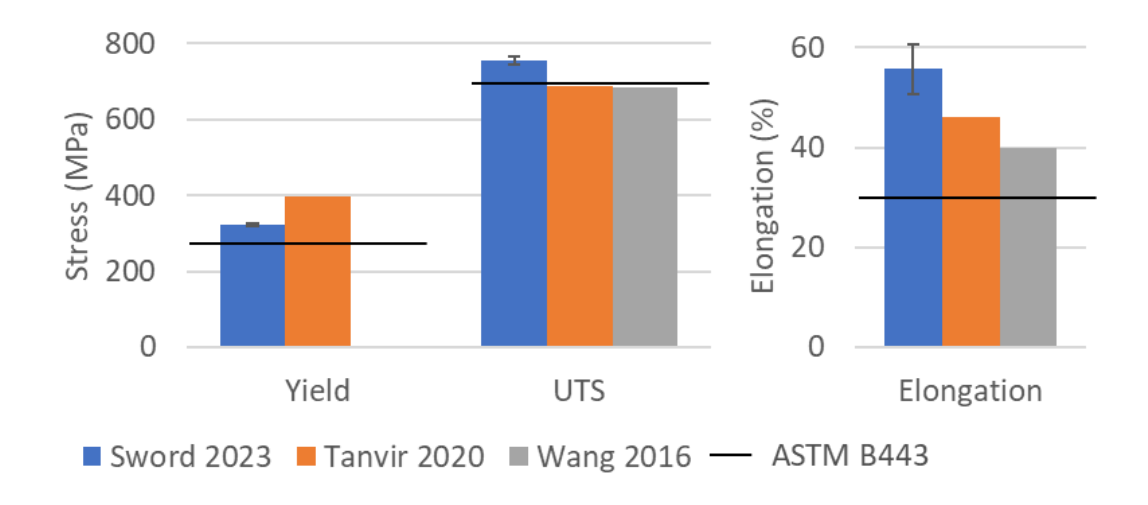


Figure 5-8 Results of tensile testing for WAAM produced, solution treated Inconel 625 compared to results from Tanvir et al. [19] and Wang et al. [23].

When the fracture surfaces are investigated, further information about the material can be determined. As noted in Figure 5-9, the fracture surface is primarily made up of equiaxed dimples, typical of tensile ductile rupture [5-19]. Under tensile tearing, as noted near the edges in Figure 5-9c, elongated dimples are observed.

Due to the significant plastic deformation observed by this alloy during tensile testing, slip planes are observed in Figure 5-9i [5-30]. Carbide particles have also been identified as nucleating sites for microvoids, while intergranular cracking has been observed, in line with previous literature on this material [5-14].

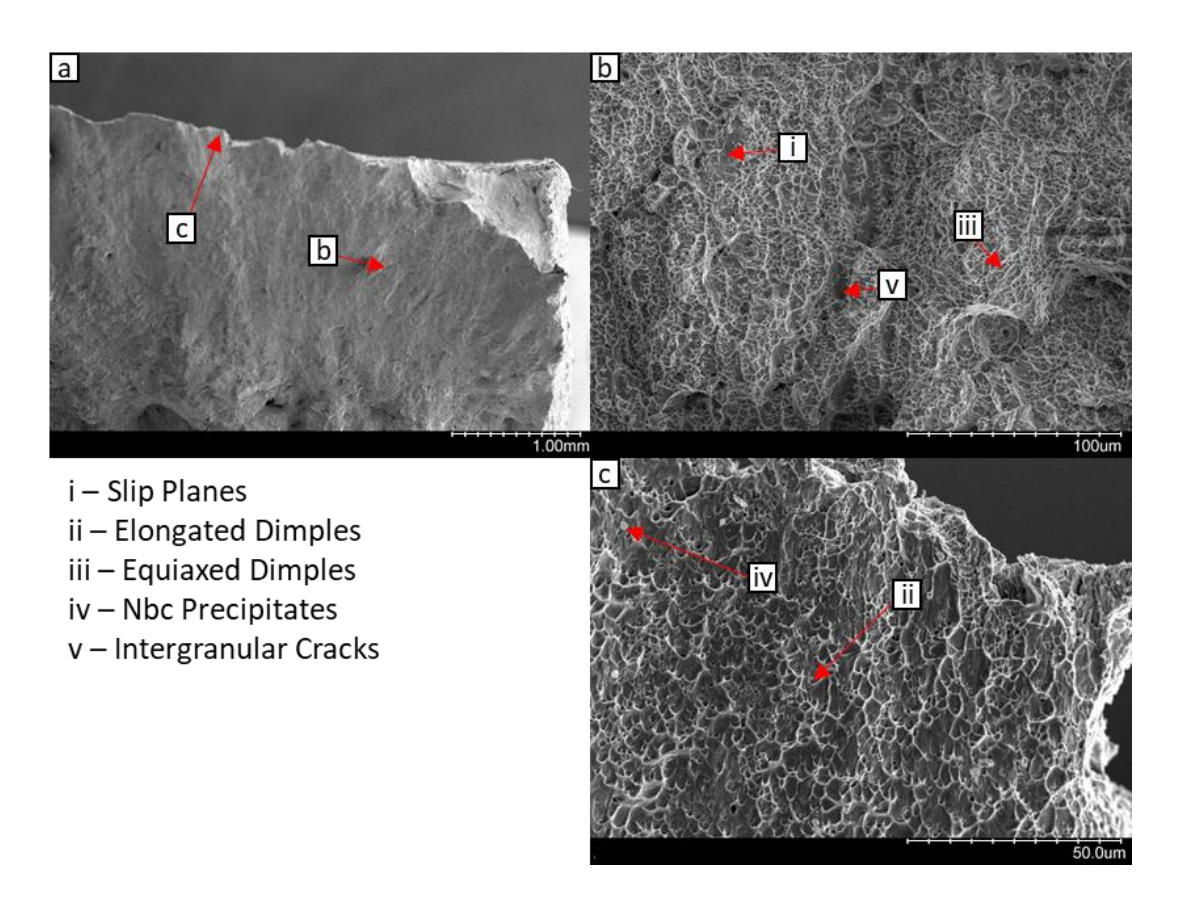


Figure 5-9 Fractography of Inconel 625 tested in tension. a) overview b) detail of inner region showing pure tension c) detail of edge fracture showing tensile tearing.

5.4. Fatigue Testing

To assess the response of this material to cyclic loading, a series of fatigue tests have been performed on WAAM produced, solution treated Inconel 625.

To develop an understanding of the fatigue response, 15 samples were tested at a range of maximum stresses between 100% and 160% of the yield strength of the material with the results are plotted in Figure 5-10. These results show that the material begins to experience run-out at 100% of yield, and remains in the high cycle regime at 160% of yield. These results exceed the performance of previously published wrought and welded material [5-31 - 5-33], while closely matching the results found for material produced through powder metallurgy (PM) and hot isostatic pressing (HIP) [34].

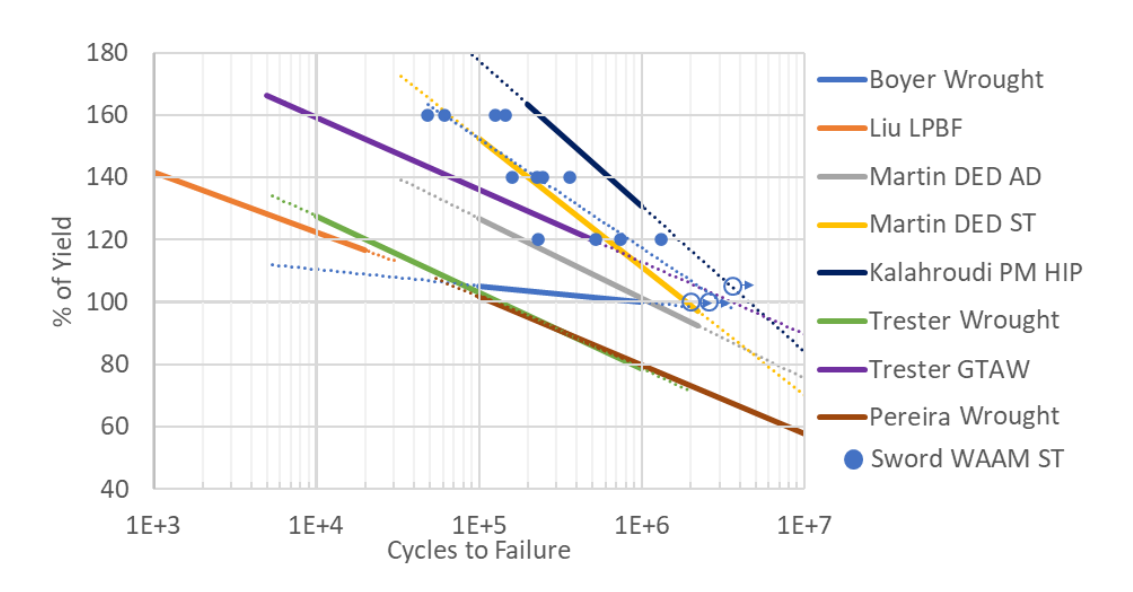


Figure 5-10 Results of fatigue testing of Inconel 625 produced using WAAM compared against existing literature for different manufacturing methods [5-31 - 5-36].

The fracture surface of samples tested at both extremes of stress range have been investigated. The sample examined in Figure 5-11 was tested at a maximum stress of 105% of yield and failed at 3.6 million cycles. On this sample, it is observed that regions of fine striations divided by cleavage river features appear in proximity to the initiation site [5-33], while a final, fast fracture is similar to tensile fracture noted in Figure 5-9 with slip planes and elongated dimples being observed.

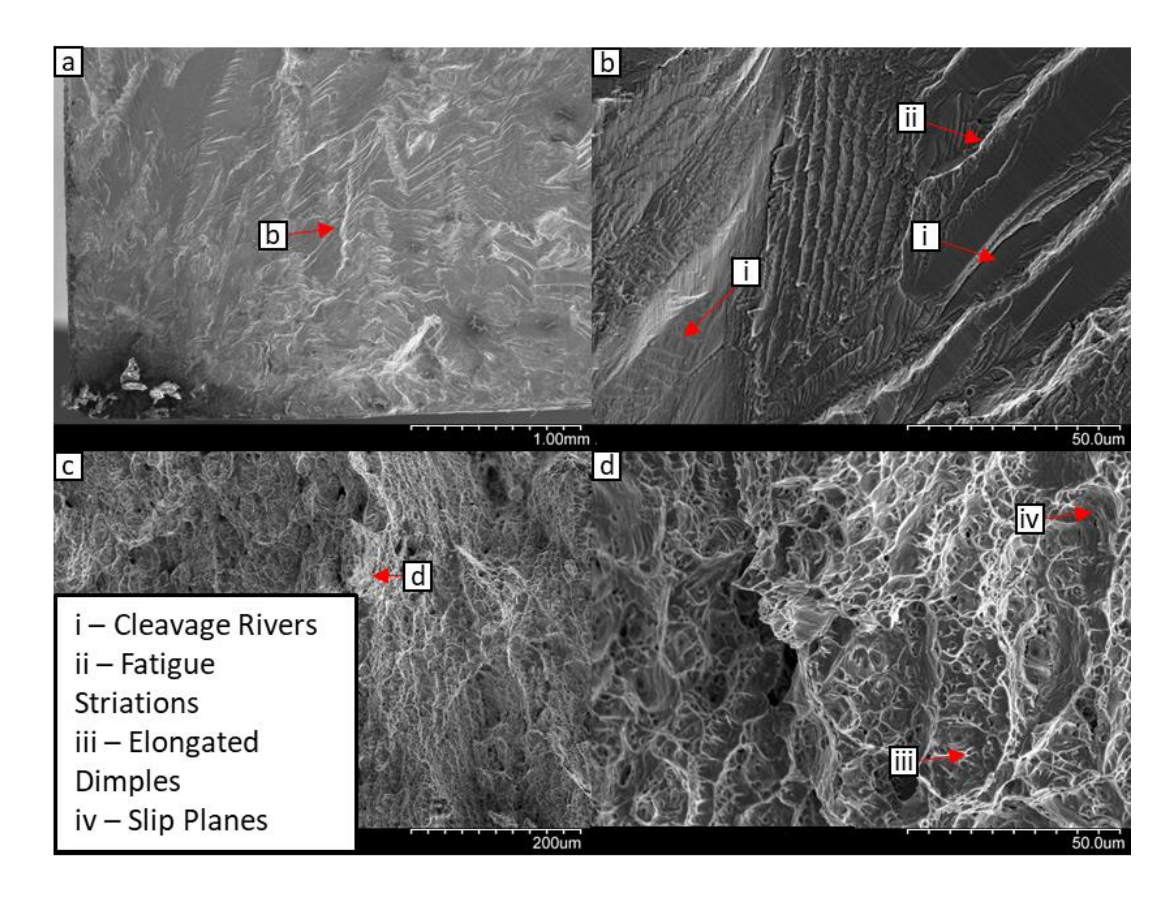


Figure 5-11 Fracture surface of Inconel 625 tested in fatigue at 105% of yield for 3.6M cycles. Regions shown include a) initiation region b) detail of fatigue striations in a c) fast fracture region d) detail of c.

In Figure 5-12, the sample was tested at a maximum stress of 160% of yield and failed at 47,883 cycles. The crack growth region is much smaller in this sample, transitioning to fast fracture and elongated dimple rupture after less than 2mm. In the crack growth region, cleavage rivers and fatigue striations are observed. The observation of the fracture surfaces suggest that the produced material has few defects and a high resistance to crack growth.

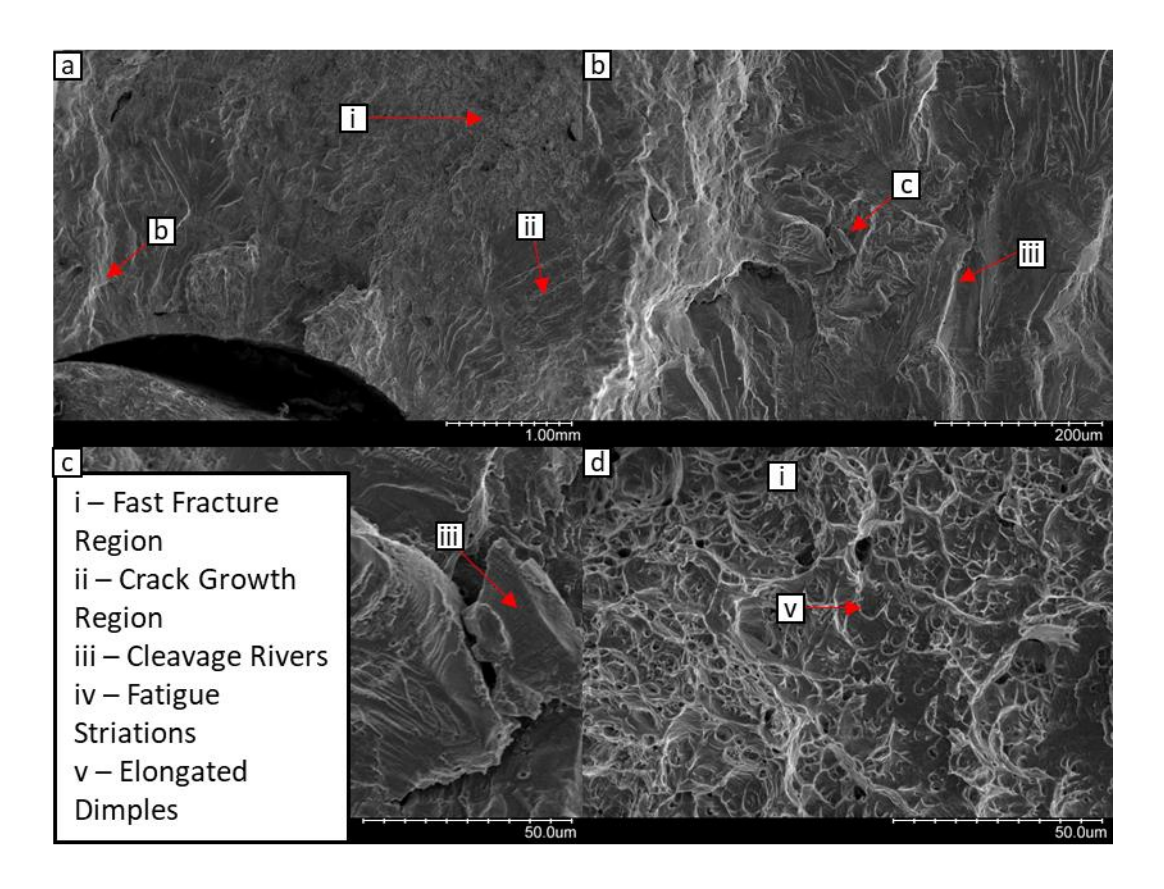


Figure 5-12 Fracture surface of Inconel 625 tested in fatigue at 160% of yield for 47,883 cycles. Regions shown include a) initiation region b) detail of fatigue striations in a c) detail of b d) detail of fast fracture.

5.5. Discussion

In this chapter, Inconel 625 produced through WAAM was studied through microscopy, hardness, tensile and fatigue testing. The results of these tests indicate that the material exhibits a higher hardness than is specified [18] in both the as-deposited and solution treated conditions. In the as-deposited condition, this is caused by the development of the Laves phase during WAAM deposition [5-23]. Following solution treatment, this is caused by the development of grain boundary carbides [5-28].

The results of tensile testing display results exceeding the requirements of standard ASTM B443 [5-9]. When these are compared to existing results for WAAM produced by Tanvir et al. [5-19] and Wang et al. [5-23], the yield strength is found to be slightly lower than obtained by Tanvir, while UTS and elongation are greater than both Tanvir and Wang. The reduced UTS and elongation observed by Tanvir can be explained by retained Laves phase following heat treatment at a lower temperature, while no heat treatment was

performed by Wang, resulting in the retained Laves phase leading to reduced UTS and elongation. It is also noted that following extended high temperature service, the δ phase develops which can also reduce elongation [5-2].

The comparison of fatigue results shows equivalent performance to DED produced and welded material [5-32, 5-36], and superior performance compared to the wrought alloy [5-32, 5-33, 5-35]. Only material produced through powder metallurgy (PM) and post processed with hot isostatic pressing (HIP) has demonstrated improved performance over WAAM.

The wrought alloys were tested following a 900°C heat treatment [35-3]. This is associated with the precipitation of the δ phase and retention of the Laves phase [5-14, 5-20]. The presence of $Cr_{23}C_6$ noted in WAAM deposited and solution treated material has also been noted to reduce crack growth due to their discontinuous formation and high hardness [5-33].

5.6. References

- [5-1] ASM handbook. Volume 2, Properties and selection: nonferrous alloys and special-purpose materials, 10th edition. ed. Materials Park, OH: Materials Park, OH: ASM International, 1990.
- [5-2] V. Shankar, K. B. S. Rao, and S. L. Mannan, "Microstructure and mechanical properties of Inconel 625 superalloy", *Journal of nuclear materials*, vol. 288, no. 2-3, pp. 222-232, 2001, doi: 10.1016/s0022-3115(00)00723-6.
- [5-3] J. Adamiec, "High temperature corrosion of power boiler components cladded with nickel alloys", *Materials characterization*, vol. 60, no. 10, pp. 1093-1099, 2009, doi: 10.1016/j.matchar.2009.03.017.
- [5-4] A. Bansal, S. Zafar, and Suneet, "Influence of heat treatment on microstructure and mechanical properties of Inconel 625 clad deposited on mild steel", *Indian Journal of Engineering and Materials Sciences*, vol. 24, no. 6, pp. 477-483, 2017.
- [5-5] P. R. Gradl *et al.*, "Additive Manufacturing of Liquid Rocket Engine Combustion Devices: A Summary of Process Developments and Hot-Fire Testing Results", presented at the American Institute of Aeronautics and Astronautics, 2018. doi: 10.2514/6.2018-4625.
- [5-6] T. E. Abioye, D. G. McCartney, and A. T. Clare, "Laser cladding of Inconel 625 wire for corrosion protection", *Journal of materials* processing technology, vol. 217, pp. 232-240, 2015, doi: 10.1016/j.jmatprotec.2014.10.024.
- [5-7] B. Silwal, J. Walker, and D. West, "Hot-wire GTAW cladding: Inconel 625 on 347 stainless steel", *International journal of advanced* manufacturing technology, vol. 102, no. 9-12, pp. 3839-3848, 2019, doi: 10.1007/s00170-019-03448-0.

- [5-8] A. Evangeline and P. Sathiya, "Cold metal arc transfer (CMT) metal deposition of Inconel 625 superalloy on 316L austenitic stainless steel: microstructural evaluation, corrosion and wear resistance properties", *Materials Research Express*, vol. 6, no. 6, p. 066516, 2019, doi: 10.1088/2053-1591/ab0a10.
- [5-9] ASTM-B443 Standard Specification for Nickel-Chromium-Molybdenum-Columbium Alloy (UNS N06625) and Nickel-Chromium-Molybdenum-Silicon Alloy (UNS N06219) Plate, Sheet, and Strip, ASTM, 2014.
- [5-10] ASM handbook. Volume 4E, Heat treating of nonferrous alloys. Materials Park, OH: ASM International, 2016.
- [5-11] Q. Guo *et al.*, "Study of the pitting corrosion at welding joints of Inconel 625 alloy under high temperature and high H2S, CO2 partial pressure", *International Journal of Electrochemical Science*, vol. 12, pp. 8929-8943, 2017, doi: 10.20964/2017.10.46.
- [5-12] S. Floreen, "Metallurgy of alloy 625", presented at the International Symposium on Superalloys 718, 625, 706 and Various Derivatives, 1994.
- [5-13] S. K. Rai *et al.*, "Characterization of microstructures in Inconel 625 using X-ray diffraction peak broadening and lattice parameter measurements", *Scripta materialia*, vol. 51, no. 1, pp. 59-63, 2004, doi: 10.1016/j.scriptamat.2004.03.017.
- [5-14] J. Mittra *et al.*, "Fracture behavior of Alloy 625 with different precipitate microstructures", *Materials science & engineering. A, Structural materials : properties, microstructure and processing,* vol. 574, pp. 86-93, 2013, doi: 10.1016/j.msea.2013.03.021.
- [5-15] G. P. Dinda, A. K. Dasgupta, and J. Mazumder, "Laser aided direct metal deposition of Inconel 625 superalloy: Microstructural evolution and thermal stability", *Materials science & engineering. A, Structural* materials: properties, microstructure and processing, vol. 509, no. 1-2, pp. 98-104, 2009, doi: 10.1016/j.msea.2009.01.009.
- [5-16] Y. Wang and X. Chen, "Investigation on the microstructure and corrosion properties of Inconel 625 alloy fabricated by wire arc additive manufacturing", *Materials Research Express*, vol. 6, no. 10, p. 106568, 2019, doi: 10.1088/2053-1591/ab39f6.
- [5-17] A. N. M. Tanvir et al., "Heat treatment effects on Inconel 625 components fabricated by wire + arc additive manufacturing (WAAM)—part 1: microstructural characterization", International journal of advanced manufacturing technology, vol. 103, no. 9, pp. 3785-3798, 2019, doi: 10.1007/s00170-019-03828-6.
- [5-18] Special-Metals, "Inconel 625 Datasheet", 2013.
- [5-19] A. N. M. Tanvir *et al.*, "Heat treatment effects on Inconel 625 components fabricated by wire + arc additively manufacturing (WAAM)—part 2: mechanical properties", *International journal of advanced manufacturing technology*, vol. 110, no. 7-8, pp. 1709-1721, 2020, doi: 10.1007/s00170-020-05980-w.
- [5-20] G. Marchese et al., "Influence of heat treatments on microstructure evolution and mechanical properties of Inconel 625 processed by laser powder bed fusion", Materials science & engineering. A, Structural materials: properties, microstructure and processing, vol. 729, pp. 64-75, 2018, doi: 10.1016/j.msea.2018.05.044.

- [5-21] L. Xue and C. Purcell, "Laser consolidation of net-shape shells for flextensional sonar projectors", presented at the International Congress on Applications of Lasers & Electro-Optics, 2006. doi: 10.2351/1.5060761.
- [5-22] S. Li et al., "Microstructure Characteristics of Inconel 625 Superalloy Manufactured by Selective Laser Melting", Journal of Materials Science & Technology, vol. 31, no. 9, pp. 946-952, 2015, doi: 10.1016/j.jmst.2014.09.020.
- [5-23] J. F. Wang et al., "Effect of location on microstructure and mechanical properties of additive layer manufactured Inconel 625 using gas tungsten arc welding", Materials science & engineering. A, Structural materials: properties, microstructure and processing, vol. 676, pp. 395-405, 2016, doi: 10.1016/j.msea.2016.09.015.
- [5-24] F. Xu et al., "Microstructural Evolution and Mechanical Properties of Inconel 625 Alloy during Pulsed Plasma Arc Deposition Process", Journal of Materials Science & Technology, vol. 29, no. 5, pp. 480-488, 2013, doi: 10.1016/j.jmst.2013.02.010.
- [5-25] J. J. Lewandowski and M. Seifi, "Metal Additive Manufacturing: A Review of Mechanical Properties", *Annual Review of Materials Research*, vol. 46, no. 1, pp. 151-186, 2016, doi: 10.1146/annurev-matsci-070115-032024.
- [5-26] O. G. Rivera et al., "Microstructures and mechanical behavior of Inconel 625 fabricated by solid-state additive manufacturing", Materials science & engineering. A, Structural materials: properties, microstructure and processing, vol. 694, pp. 1-9, 2017, doi: 10.1016/j.msea.2017.03.105.
- [5-27] N. Guo and M. C. Leu, "Additive manufacturing: technology, applications and research needs", *Front. Mech. Eng,* vol. 8, no. 3, pp. 215-243, 2013, doi: 10.1007/s11465-013-0248-8.
- [5-28] M. Rombouts et al., "Laser metal deposition of Inconel 625: Microstructure and mechanical properties", Journal of Laser Applications, vol. 24, no. 5, p. 052007, 2012/11/01 2012, doi: 10.2351/1.4757717.
- [5-29] C. P. Paul *et al.*, "Investigating laser rapid manufacturing for Inconel-625 components", *Optics and laser technology*, vol. 39, no. 4, pp. 800-805, 2007, doi: 10.1016/j.optlastec.2006.01.008.
- [5-30] ASM handbook. Volume 12, Fractography. Metals Park, Ohio : American Society for Metals., 1987.
- [5-31] M. Liu *et al.*, "The low cycle fatigue property, damage mechanism, and life prediction of additively manufactured Inconel 625: Influence of temperature", *Fatigue & fracture of engineering materials & structures*, vol. 46, pp. 3829-3845, 2023, doi: 10.1111/ffe.14106.
- [5-32] P. W. Trester, J. L. Kaae, and R. Gallix, "Fatigue strength of inconel 625 plate and weldments used in the DIII-D configuration vacuum vessel", Journal of nuclear materials, vol. 133, p. 347, 1985, doi: 10.1016/0022-3115(85)90165-5.
- [5-33] F. G. L. Pereira *et al.*, "Fracture Behavior and Fatigue Performance of Inconel 625", *Materials research*, vol. 21, no. 4, 2018, doi: 10.1590/1980-5373-MR-2017-1089.
- [5-34] F. Javadzadeh Kalahroudi *et al.*, "On the microstructure and high cycle fatigue of near-net shape PM-HIPed Inconel 625", *Materials Science*

- *and Engineering A,* vol. 886, p. 145671, 2023, doi: 10.1016/j.msea.2023.145671.
- [5-35] H. E. Boyer, *Atlas of fatigue curves*. Metals Park, Ohio: Metals Park, Ohio: American Society for Metals, 1986.
- [5-36] N. Martin *et al.*, "Fatigue properties of as-built and heat-treated Inconel 625 obtained by the hybridization of two laser-powder based additive processes", *International journal of fatigue*, vol. 172, p. 107650, 2023, doi: 10.1016/j.ijfatigue.2023.107650.

Inconel 718 WAAM

Inconel 718 is a nickel-iron-chromium superalloy [6-1]. Due to its combination of corrosion resistance with high strength and performance at high temperature [6-2], it is commonly used in adverse conditions experienced by equipment in the oil and gas, defence and energy sectors [6-3 - 6-5]. In contrast to Inconel 625, Inconel 718 incorporates iron within its matrix to improve mechanical properties [6-6] at the cost of corrosion resistance [6-7]. This modified composition allows the material to undergo aging heat treatment to enhance strength [6-8].

The composition of Inconel 718 is specified in standard ASTM B670 [6-9]. These are compared with data obtained through EDS of the microstructure in Table 6-1. This chapter will characterise the microstructure in addition to determining the mechanical and fatigue properties of this material.

Table 6-2 Composition of Inconel 718.

Element	Ni	Cr	Fe	Мо	Nb
Wrought Inconel 718	50.55	17-21	Bal.	2.8-3.3	4.75-5.5
[6-1, 6-9]					
WAAM Inconel 718	49.2	17.3	Bal.	3.66	7.43
Element	Ti	Al	С	Mn	Si
Wrought Inconel 718	0.65-1.15	0.2-0.8	0.08	0.35	0.35
[6-1, 6-9]					
WAAM Inconel 718	1.07	0.47	trace	trace	trace

6.1. Microstructure

This section will detail the microstructure found in Inconel alloy 718 manufactured using WAAM with the composition and process parameters shown in Table 6-3 and Table 6-4. The alloy will be examined in the asdeposited (AD) condition and following solution (ST) and aging (A1 & STA) heat treatments. A table of the heat treatments performed is shown in Table 6-2.

Table 6-2 Heat treatment of Inconel 718 [6-10]. Visualised in Figure 6-1.

Alloy	Solution treatment (ST)			Aging (A1)		
	Temperature	Time	Cooling	Temperature	Time	Cooling
	(°C)	(hr)		(°C)	(hr)	
Inconel	920	0.5	Air cool	720	8	Furnace
718						cool to
						620°C
Alloy	Double aging (STA)					
	Temperature	Time	Cooling			
	(°C)	(hr)				
Inconel	620	8	Air cool			
718						

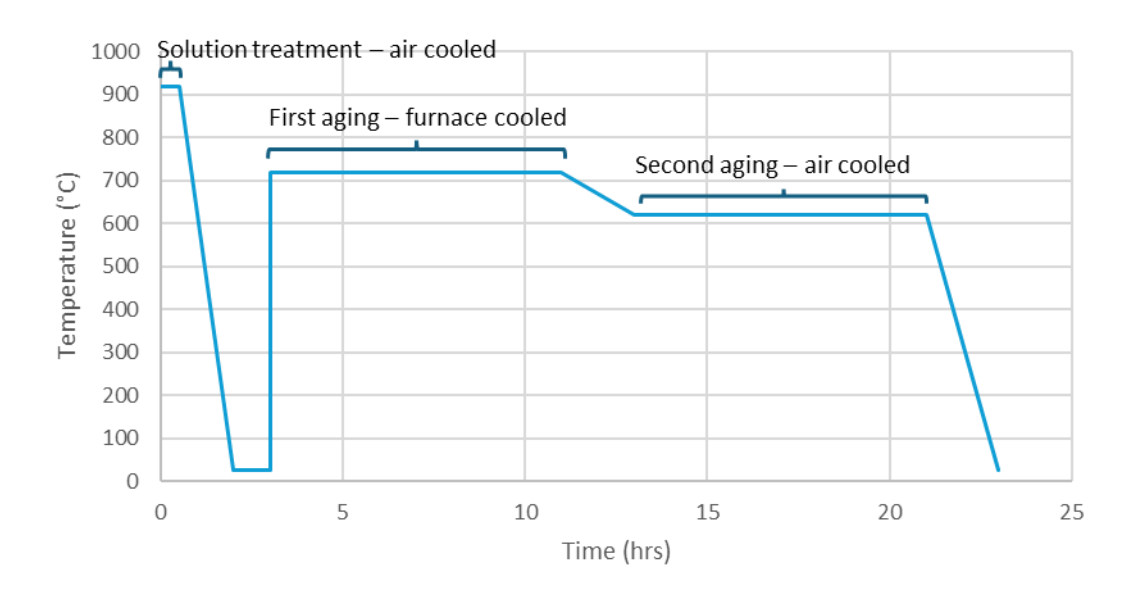


Figure 6-1 Time – temperature chart for heat treatment.

Table 6-3 WAAM process parameters for Inconel 718.

Alloy	CMT	Travel	Wire feed	Standoff	Interpass
	program	speed	speed	distance	temperature
		(mm/s)	(m/min)	(mm)	(°C)
Inconel	CrNi 19 9	15	6.5	10	60
718	CMT928				
Alloy	Step	Current	Voltage	Energy	
	width	(A)	(V)	input	
	(mm)			(kJ/mm)	
Inconel	4	190	20	0.203	
718					

Table 6-4 Composition of Inconel 718 filler wire.

Alloy	С	Si	Ni	Cr	Мо	Fe	Ti	Al	Nb
Inconel	0.04	0.30	52	18	3.1	Bal	0.9	0.20	5.2
718									

The microstructure of Inconel 718 shows major differences compared to alloys in the same family such as Inconel 625 due to the significant iron content [6-11]. The mechanical properties are found to be superior in addition to high performance at elevated temperatures [6-12]. The matrix is primarily the FCC γ phase which is strengthened by γ and γ precipitates in addition to the δ phase and various MC carbides [6-1]. The primary strengthening phase is γ which is metastable, transforming into the stable δ phase following aging or high temperature service [6-6].

The secondary alloying elements in 718 also promote the formation of other phases such as the detrimental Laves phase [6-13]. The microstructure of WAAM produced Inconel 718 will be investigated in this section in a range of heat treatment conditions: as-deposited (AD), solution treated (ST) in addition to an intermediate double aged conditions (A1 and STA). The details of heat treatments are given in Table 6-2 with the TTT diagram shown in Figure 6-2 [14].

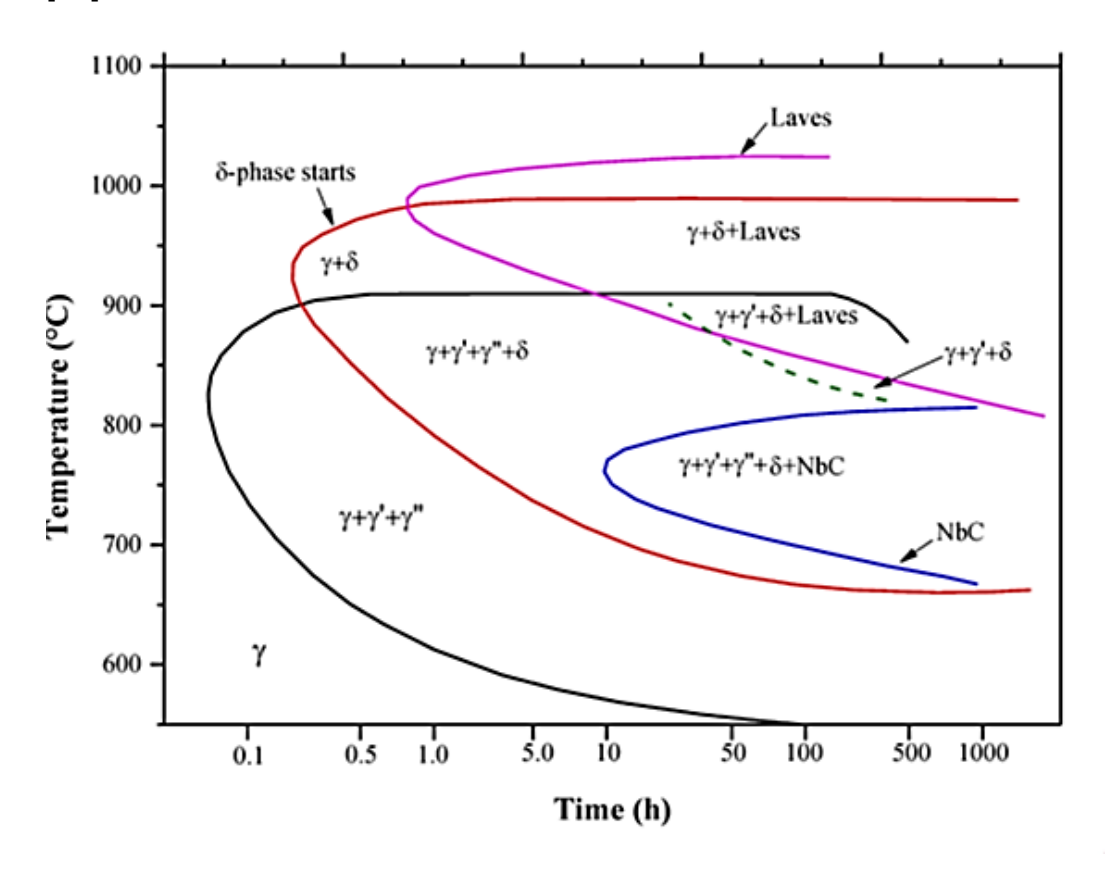


Figure 6-2 Time-Temperature-Transition (TTT) diagram for Inconel 718 [6-14].

As for Inconel 625, the impact of heat treatment on the surface of this alloy has been investigated with the results shown in Figure 6-3. A layer of chromium oxide was found to form to a depth of 1.5µm, while mechanical disturbance to the microstructure was observed to a depth of 8µm caused by surface polishing.

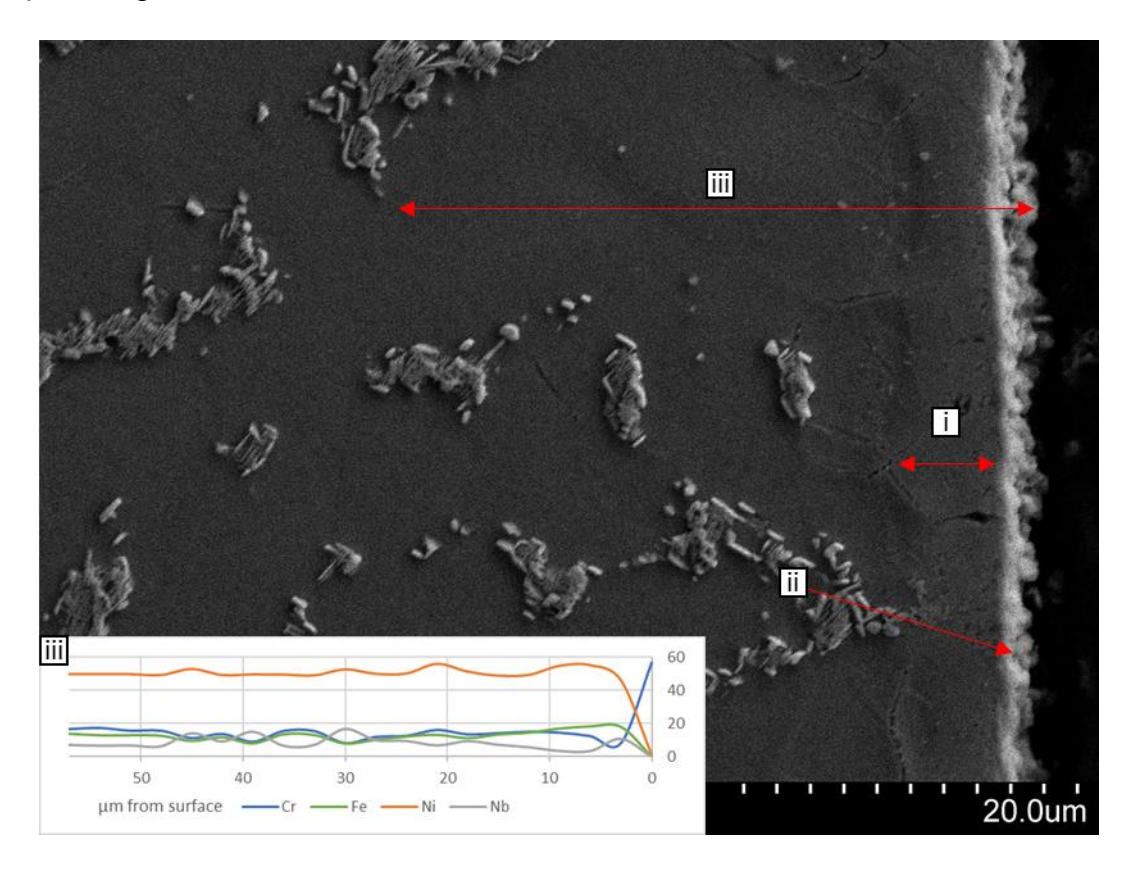


Figure 6-3 SEM imaging of the chromium oxide skin formed through heat treatment of Inconel 718 i) mechanical disturbance region ii) CrO skin iii) EDS scan path.

The deposition of Inconel 718 by the WAAM process leads to a directional columnar dendritic microstructure shown in Figure 6-4, with the dendritic direction following that of the highest thermal gradient. The as-deposited microstructure is dominated by a light matrix and a network of dark precipitates. Under high magnification, as shown in Figure 6-5, these are identified as the detrimental Laves phase and smaller particles of strengthening γ " [6]. This network of Laves phase is directional, following the direction of the thermal gradient during deposition. Other phases noted are the regular, golden shapes of nitrides. In this alloy these typically have the composition of TiN or NbN [6-15].

Following solution treatment, the microstructure evolves. The high temperature of solution treatment results in the Laves phase being partially dissolved, with the acicular δ phase becoming visible at high magnification [6-15]. In addition, regular shaped carbides are observed. The nitrides are not present in this condition, suggesting they are dissolved by solution treatment. It is noted that dendritic regions with a low incidence of δ or Laves phases are caused by a segregation of Nb during solidification [6-16].

Following the aging treatments, the microstructure experiences fewer visible changes, however the Laves phase continues to dissolve while nitrides begin to form, growing in the STA condition. The primary strengthening mechanism is the growth of γ " which is visible at the sub- μ m scale [6-17], which can occur without the hinderance of δ and Laves growth during the double aging process as seen in Figure 6-4.

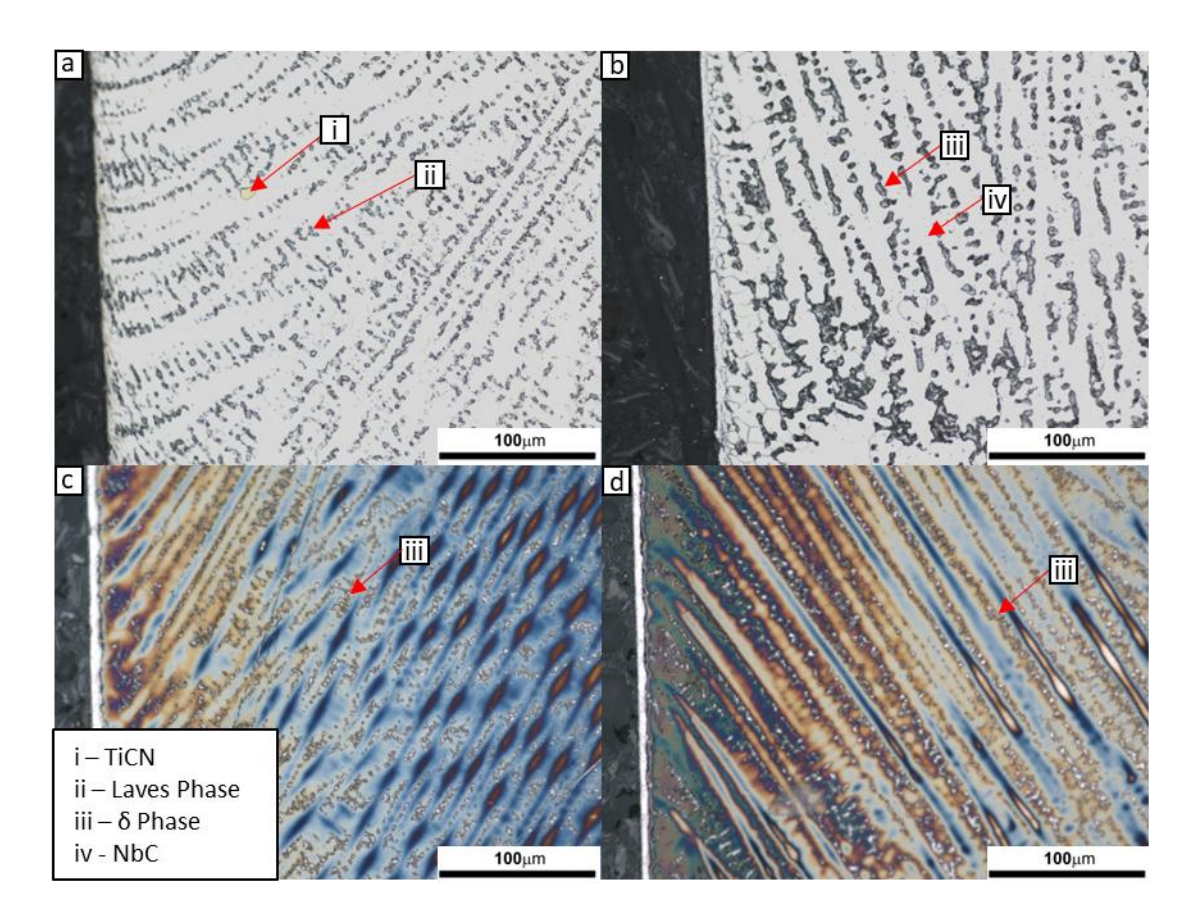


Figure 6-4 Optical micrographs of alloy 718 following each stage of heat treatment: a) as-deposited (AD) b) solution treated (ST) c) intermediate aged (A1) d) double aged (STA).

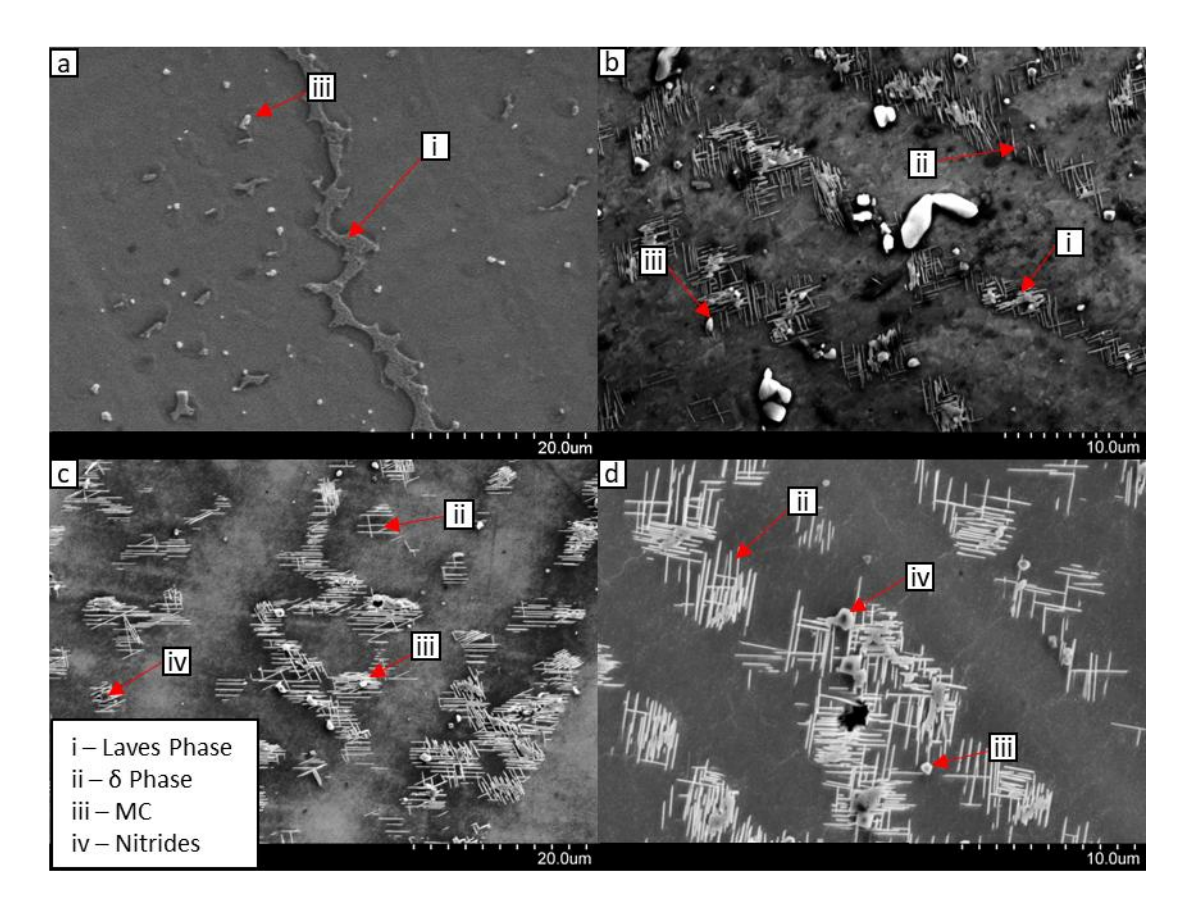


Figure 6-5 SEM micrographs of alloy 718 following each stage of heat treatment: a) as-deposited (AD) b) solution treated (ST) c) intermediate aged (A1) d) double aged (STA).

6.2. Hardness testing

To relate the mechanical properties and microstructure of Inconel 718, microhardness measurements were taken in the heat-treatment states as-deposited, solution treatment, aged and double aged. The results of microhardness testing are shown in Figure 6-6 displaying the statistical variation of the data.

It is noted that solution treatment results in a reduction in hardness and an overall homogenisation of the material [6-18]. When this is followed by aging and double aging treatments, a progressive increase in hardness is observed [6-13].

As has been noted for Inconel 625, the leading contributor to the reduction in hardness following solution treatment is the dissolution of the brittle Laves phase [6-13]. The growth of this phase is promoted by in-situ aging during the WAAM process, so solutionizing the material reverses this process.

Meanwhile, during aging treatments at 720°C and 620°C, the hardness is increased due to the growth of the γ" strengthening phase [6-6]. The hardness values obtained for material in the STA condition meet the minimum value specified in standard ASTM B637 [6-19].

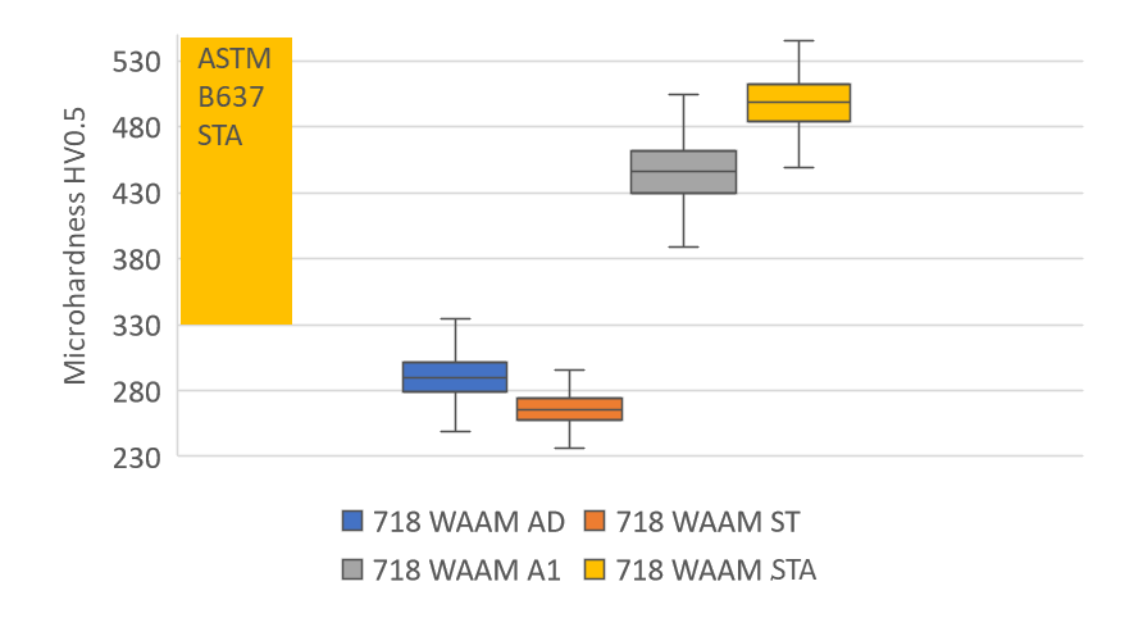


Figure 6-6 Microhardness results for WAAM produced Inconel 718 in different heat treatment conditions compared against standard ASTM B637 [6-19].

6.3. Tensile testing

To establish the mechanical properties of Inconel 718, tensile testing was performed on samples in the typical service condition (STA) [6-16, 6-18]. This testing allowed the yield strength, elongation, and UTS to be determined.

Following testing, the fracture surfaces were examined optically and by SEM to identify the failure mode and aspects of the microstructure correlated with the initiation of failure.

It is noted that much of the strength is derived from the aging heat treatment and the growth of γ " precipitates [6-13]. As can be seen from results from existing literature shown in Figure 6-7, the differences between production method are limited, while significant outliers are identified to be in the asdeposited or solution treated conditions [6-6, 6-16, 6-20, 6-21].

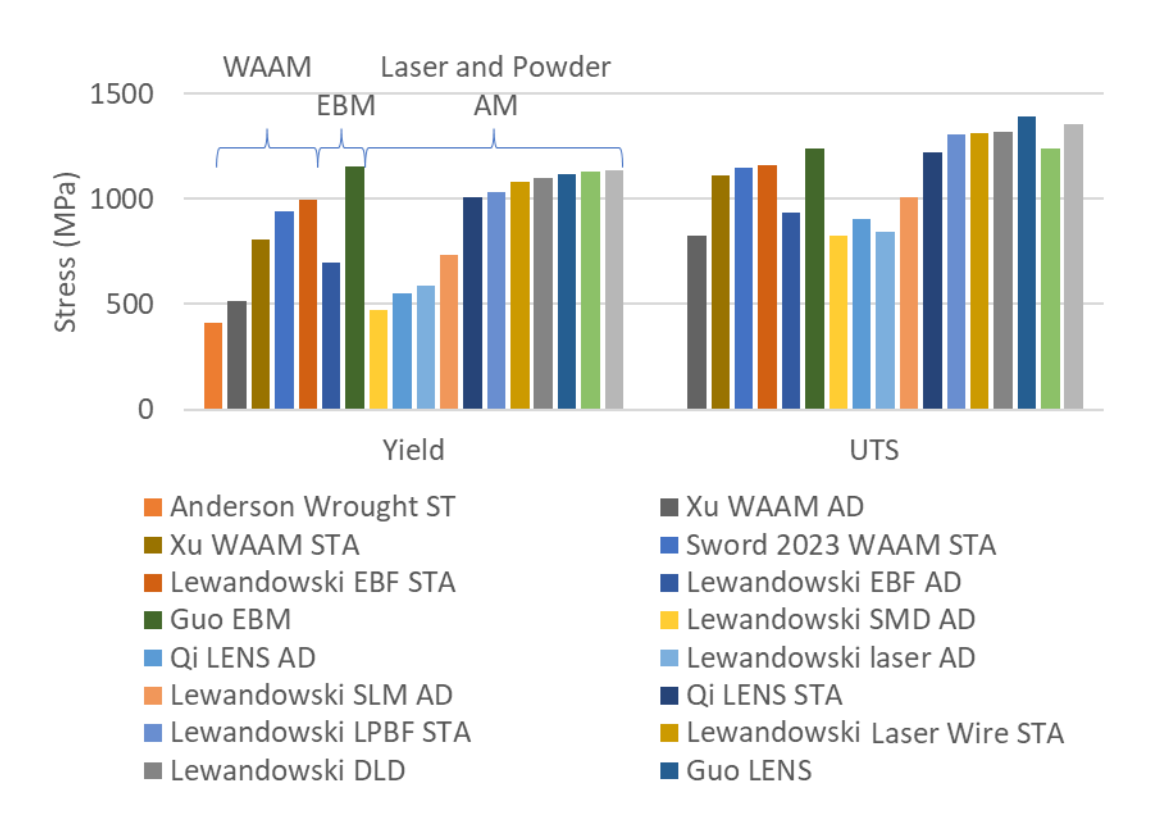


Figure 6-7 Comparison of mechanical properties for the additive manufacturing of Alloy 718 by various methods [6-6, 6-16, 6-17, 6-20 - 6-22].

Samples of WAAM produced Inconel 718 in the double aged condition were subject to tensile testing with the results presented in Figure 6-8. The strength is found to correlate well with the results from Xu et al. [6-20], for WAAM produced alloy in the STA condition, in addition to results from Qi et al. [6-16], for material in the same condition produced through LENS (laser engineered net shape), a laser DED (directed energy deposition) method. It is noted that the powder feedstock methods typically achieve higher strengths due to the smaller and more isotropic grains, with each powder grain being the initiation site for a new grain.

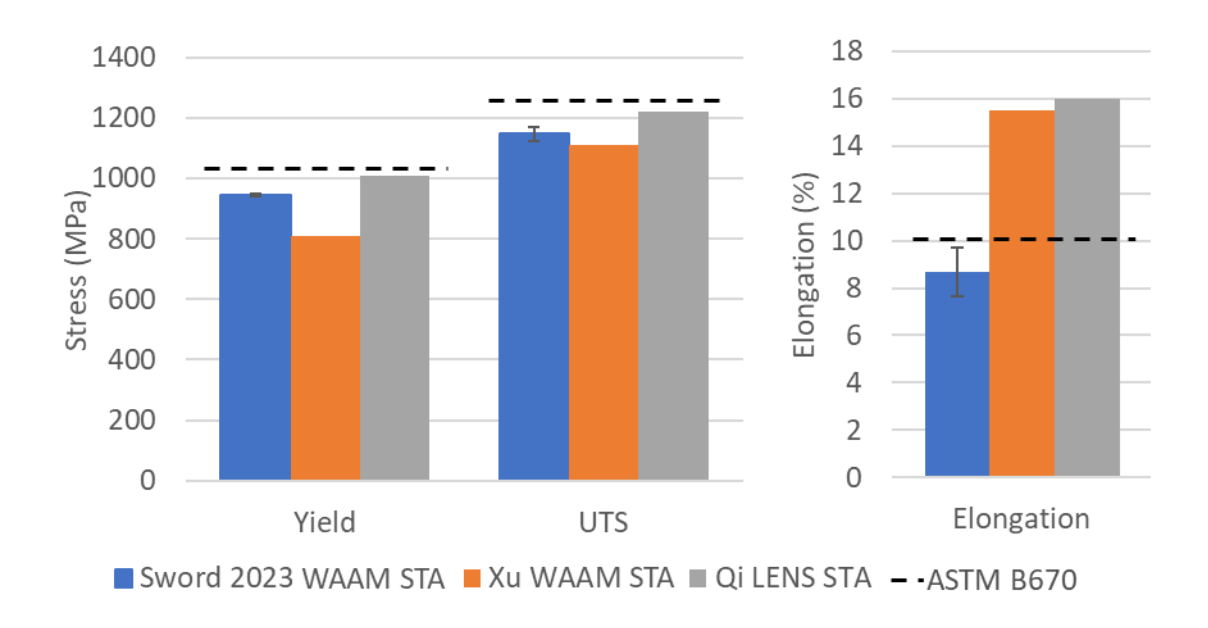


Figure 6-8 Results of tensile testing for WAAM produced, double aged Inconel 718 compared to results from Xu et al. [6-20] and Qi et al. [6-16].

When these results are compared against those from Xu et al. [6-20] it is noted that the improved strength is correlated with a reduction in residual Laves phase following heat treatment, while the reduction in elongation noted when compared to both Xu et al. and Qi et al. [6-16] and is qualitatively associated with reduced dendritic spacing compared to Xu et al. [6-20]. Higher strength achieved by Qi et al using LENS is associated with the use of powder feedstock as previously described.

These results were all found to fall below those specified by ASTM B670 [6-9]. An explanation is the significant development of δ phase compared to the wrought material, known to lead to reduced strength by reducing the Nb available for the formation of strengthening γ " precipitates [6-16].

When the fracture surfaces are observed with electron microscopy, it is noted that features of the fracture surface show similarities to the columnar microstructure shown in Figure 6-4. This effect can be explained by the low ductility observed during tensile testing, specifically following concentrations of the δ phase. Upon closer examination shown in Figure 6-9, microscopic details of the fracture surface also reflect those of δ phase concentrations, displaying dendrites of a form expected for this material [6-23] and at a similar scale to those observed with microscopy.

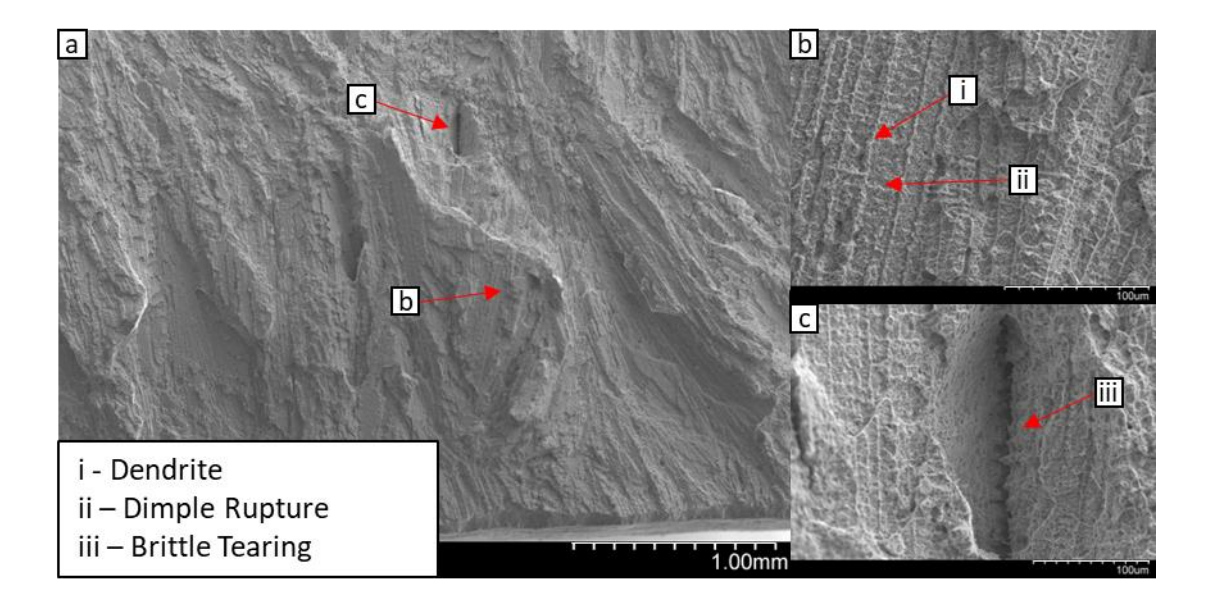


Figure 6-9 SEM fractographs of WAAM produced Inconel 718 following tensile testing.

Additionally, brittle tearing features have been observed on the scale of $100\mu m$, indicating localised regions of high hardness and the retention of small quantities of Laves phase or a concentration of carbides. These results are corroborated by Qi et al. [6-16] on Inconel 718 manufactured using LENS, displaying ductile failure along the dendrites. These results also suggest that carbides and the δ phase are the initiation sites for microvoids during ductile failure.

6.4. Fatigue testing

To assess the response of this material to cyclic loading, a series of fatigue tests have been performed on the WAAM produced, Inconel 718 in the A2 condition. These tests were performed between 90% and 50% of the yield stress of the material with the results plotted on Figure 6-10. The results are compared with existing literature for this material in fatigue [6-14, 6-21, 6-24, 6-25].

This comparison suggests that the results for WAAM are comparable to those obtained for wrought material in the annealed and aged conditions. Meanwhile, the results for as-deposited LPBF [6-24] display a very high fatigue life at the cost of reduced strength, caused by a reduction in strengthening phases (γ ") and higher ductility.

When the fracture surfaces are observed, the crack initiation and growth region is not always obvious. The fast fracture region bears similar features to those noted on tensile samples as shown in Figure 6-9. Representative SEM fractographs are shown in Figure 6-11. In the crack growth region, both cleavage rivers and fatigue striations are noted (Figure 6-11i and ii) while in the fast fracture region, cleavage rivers and interdendritic failure are dominant. In addition, twin boundary failure is also observed. This fracture behaviour has also been identified following slow strain rate testing of this alloy [6-26].

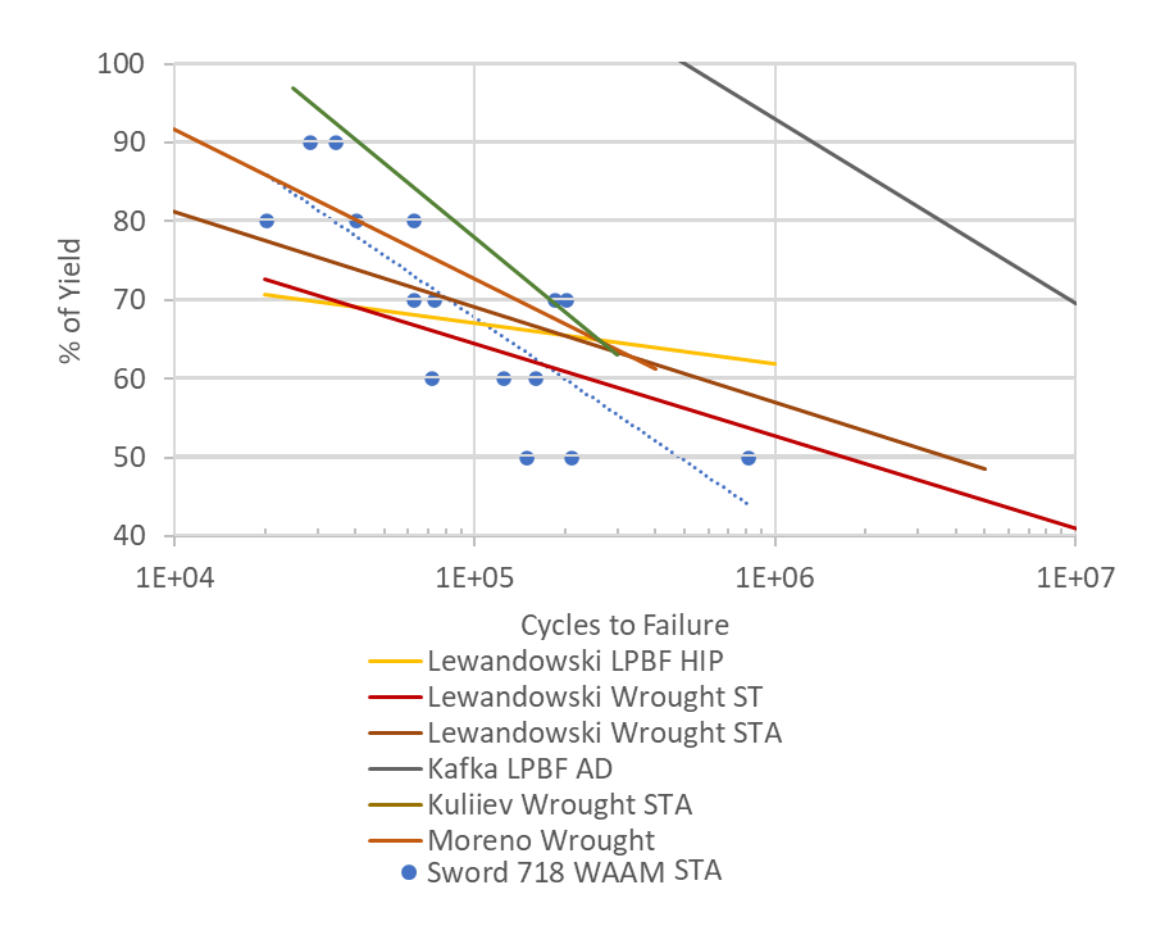


Figure 6-10 Results for fatigue testing of WAAM produced Inconel 718 compared against existing literature [6-14, 6-21, 6-24, 6-25].

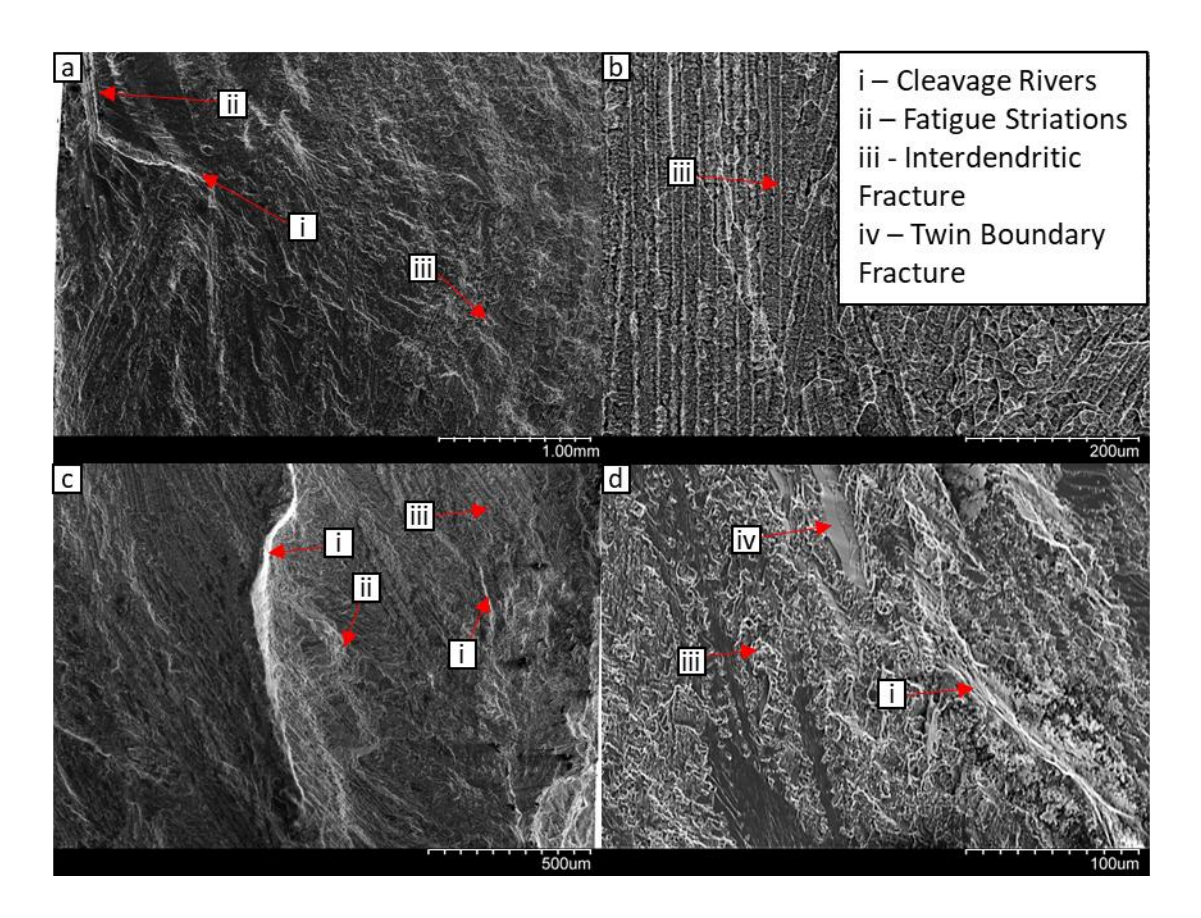


Figure 6-11 SEM fractographs of WAAM produced Inconel 718 following fatigue testing. a) and c) show the crack growth region, while b) and d) show the fast fracture region.

On the fracture surface of one sample shown in Figure 6-12, significant transgranular cracking is identified [6-27] which accelerates the onset of fatigue failure. This sample was tested at 50% of yield strength and the cracking follows the direction of the dendritic microstructure [6-28]. This suggests that these cracks are initiated by localised brittle regions which increase the local stress intensity within the material [6-29]. This effect may be associated with the reduced elongation noted compared to previous studies of tensile properties (Figure 6-7).

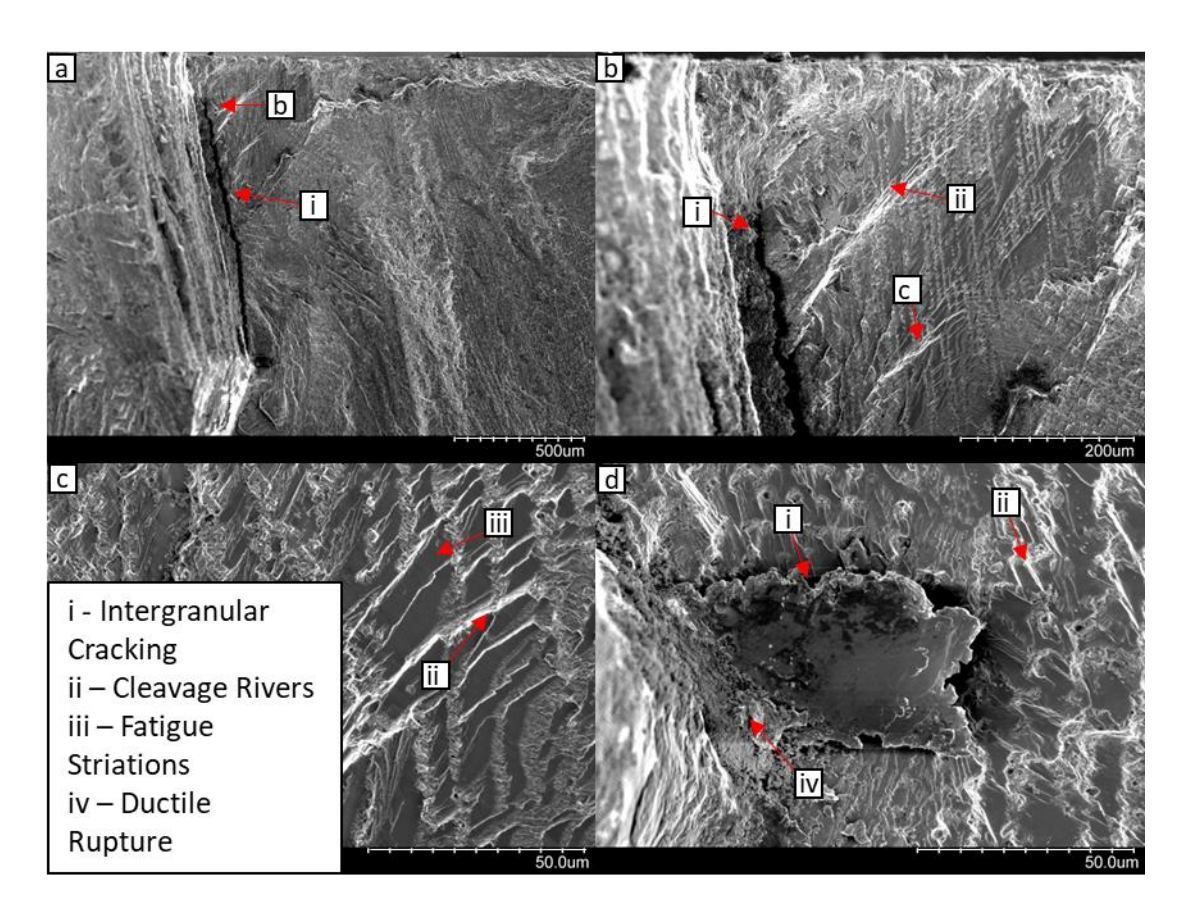


Figure 6-12 SEM fractographs of a sample of Inconel 718 following fatigue testing at 50% of yield for 148,418 cycles. This sample shows significant transgranular cracking.

6.5. Discussion

This chapter has studied Inconel 718 produced using WAAM. Results were obtained for microstructural analysis in addition to hardness, tensile and fatigue testing. These results indicate a similar microstructure to other additive manufacturing methods for this alloy and a hardness within the bounds set out by ASTM standard B637 [6-19]. The results of tensile testing fall below those set out by this standard due to the evolution of the δ phase through in-situ aging during deposition which reduces ductility and strength by reducing the availability of niobium for the formation of the strengthening γ " phase [6-16]. This effect is confirmed by the observation of a dendritic structure in the fracture surfaces following the distribution of the δ phase [6-23].

These results were also compared with existing literature for the same alloy produced using WAAM and LENS by Xu et al. [6-20] and Qi et al. [6-16]. It has been observed that a similar strength was achieved, with Laves phase being observed by Xu accounting for the minor reduction in strength. Furthermore, both of these studies reported higher ductility which is correlated a greater size of the columnar grains.

When compared with previously published data for fatigue testing [6-14, 6-21, 6-24, 6-25], it is noted that the performance is similar to those obtained for LPBF material in the STA condition [6-14], while a steeper gradient is observed when compared to the wrought alloy in both the aged and annealed conditions [6-21]. This difference is likely due to the reduced elongation of the WAAM material caused by the presence of weakening δ phase along the boundaries of columnar grains, making it more susceptible to crack propagation at lower stress ranges.

6.6. References

- [6-1] ASM handbook. Volume 2, Properties and selection: nonferrous alloys and special-purpose materials, 10th edition. ed. Materials Park, OH: Materials Park, OH: ASM International, 1990.
- [6-2] V. Shankar, K. B. S. Rao, and S. L. Mannan, "Microstructure and mechanical properties of Inconel 625 superalloy", *Journal of nuclear materials*, vol. 288, no. 2-3, pp. 222-232, 2001, doi: 10.1016/s0022-3115(00)00723-6.

- [6-3] J. Adamiec, "High temperature corrosion of power boiler components cladded with nickel alloys", *Materials characterization*, vol. 60, no. 10, pp. 1093-1099, 2009, doi: 10.1016/j.matchar.2009.03.017.
- [6-4] A. Bansal, S. Zafar, and Suneet, "Influence of heat treatment on microstructure and mechanical properties of Inconel 625 clad deposited on mild steel", *Indian Journal of Engineering and Materials Sciences*, vol. 24, no. 6, pp. 477-483, 2017.
- [6-5] P. R. Gradl et al., "Additive Manufacturing of Liquid Rocket Engine Combustion Devices: A Summary of Process Developments and Hot-Fire Testing Results", presented at the American Institute of Aeronautics and Astronautics, 2018. doi: 10.2514/6.2018-4625.
- [6-6] M. Anderson et al., "δ Phase precipitation in Inconel 718 and associated mechanical properties", Materials science & engineering. A, Structural materials: properties, microstructure and processing, vol. 679, pp. 48-55, 2017, doi: 10.1016/j.msea.2016.09.114.
- [6-7] K. D. Ramkumar *et al.*, "Investigations on the microstructure, tensile strength and high temperature corrosion behaviour of Inconel 625 and Inconel 718 dissimilar joints", *Journal of manufacturing processes*, vol. 25, pp. 306-322, 2017, doi: 10.1016/j.jmapro.2016.12.018.
- [6-8] G. D. J. Ram et al., "Control of Laves phase in Inconel 718 GTA welds with current pulsing", Science and Technology of Welding and Joining, vol. 9, no. 5, pp. 390-398, 2004, doi: 10.1179/136217104225021788.
- [6-9] ASTM-B670 Standard Specification for Precipitation-Hardening Nickel Alloy (UNS N07718) Plate, Sheet, and Strip for High-Temperature Service, ASTM, 2018.
- [6-10] ASM handbook. Volume 4E, Heat treating of nonferrous alloys. Materials Park, OH: ASM International, 2016.
- [6-11] E. Hosseini and V. A. Popovich, "A review of mechanical properties of additively manufactured Inconel 718", *Additive manufacturing*, vol. 30, p. 100877, 2019, doi: 10.1016/j.addma.2019.100877.
- [6-12] R. C. Reed, *The Superalloys: Fundamentals and Applications*. Cambridge: Cambridge: Cambridge University Press, 2006.
- [6-13] H. Xiao *et al.*, "Laves phase control of Inconel 718 alloy using quasi-continuous-wave laser additive manufacturing", *Materials & design*, vol. 122, pp. 330-339, 2017, doi: 10.1016/j.matdes.2017.03.004.
- [6-14] E. Sadeghi et al., "A state-of-the-art review on fatigue performance of powder bed fusion-built alloy 718", Progress in materials science, vol. 133, p. 101066, 2023, doi: 10.1016/j.pmatsci.2022.101066.
- [6-15] G. K. Sujan et al., "Microstructural characterization and oxidation performance of solution-annealed and precipitation hardened wire-arc additively manufactured Inconel 718 superalloys", Additive Manufacturing, vol. 51, p. 102602, 2022/03/01/ 2022, doi: 10.1016/j.addma.2022.102602.
- [6-16] H. Qi, M. Azer, and A. Ritter, "Studies of Standard Heat Treatment Effects on Microstructure and Mechanical Properties of Laser Net Shape Manufactured Inconel 718", *Metallurgical and materials transactions. A, Physical metallurgy and materials science,* vol. 40, no. 10, pp. 2410-2422, 2009, doi: 10.1007/s11661-009-9949-3.
- [6-17] S. I. Kwon *et al.*, "Characterization of the Microstructures and the Cryogenic Mechanical Properties of Electron Beam Welded Inconel

- 718", *Metallurgical and materials transactions.*, vol. 47, no. 2, pp. 777-787, 2016, doi: 10.1007/s11661-015-3269-6.
- [6-18] D. Zhang et al., "Effect of standard heat treatment on the microstructure and mechanical properties of selective laser melting manufactured Inconel 718 superalloy", Materials science & engineering. A, Structural materials: properties, microstructure and processing, vol. 644, pp. 32-40, 2015, doi: 10.1016/j.msea.2015.06.021.
- [6-19] B637 Standard Specification for Precipitation-Hardening and Cold Worked Nickel Alloy Bars, Forgings, and Forging Stock for Moderate or High Temperature Service, ASTM, 2018.
- [6-20] X. Xu et al., "Investigation of process factors affecting mechanical properties of Inconel 718 superalloy in wire + arc additive manufacture process", Journal of materials processing technology, vol. 265, pp. 201-209, 2019, doi: 10.1016/j.jmatprotec.2018.10.023.
- [6-21] J. J. Lewandowski and M. Seifi, "Metal Additive Manufacturing: A Review of Mechanical Properties", Annual Review of Materials Research, vol. 46, no. 1, pp. 151-186, 2016, doi: 10.1146/annurevmatsci-070115-032024.
- [6-22] N. Guo and M. C. Leu, "Additive manufacturing: technology, applications and research needs", Front. Mech. Eng, vol. 8, no. 3, pp. 215-243, 2013, doi: 10.1007/s11465-013-0248-8.
- [6-23] S. G. K. Manikandan, "Welding the Inconel 718 superalloy: reduction of micro-segregation and laves phases", D. Sivakumar, M. Kamaraj, and Elsevier Eds.: Amsterdam, Netherlands: Elsevier, 2019.
- [6-24] O. L. Kafka et al., "Effects of as-built surface with varying number of contour passes on high-cycle fatigue behavior of additively manufactured nickel alloy 718", *International journal of fatigue*, vol. 176, p. 107872, 2023, doi: 10.1016/j.ijfatigue.2023.107872.
- [6-25] M. Moreno-Rubio et al., "Experimental study on the fretting fatigue of Inconel 718 superalloy", *Tribology international*, vol. 186, p. 108637, 2023, doi: 10.1016/j.engfailanal.2022.106864.
- [6-26] D. Sampath et al., "Hydrogen-Assisted Cracking Behavior of Ni Alloy 718: Microstructure, H Testing Protocol, and Fractography", Metall Mater Trans A, vol. 52, no. 1, pp. 46-64, 2021, doi: 10.1007/s11661-020-06049-9.
- [6-27] Y. Kim and W. Hwang, "High-cycle, low-cycle, extremely low-cycle fatigue and monotonic fracture behaviors of low-carbon steel and its welded joint", *Materials (Basel)*, vol. 12, no. 24, p. 40111, 2019, doi: 10.3390/ma12244111.
- [6-28] X. F. Ma et al., "Fatigue short crack propagation behavior of selective laser melted Inconel 718 alloy by in-situ SEM study: Influence of orientation and temperature", *International journal of fatigue*, vol. 139, p. 105739, 2020, doi: 10.1016/j.ijfatigue.2020.105739.
- [6-29] Q. Wang et al., "Comparison of fatigue crack growth behaviour in electron-beam and laser powder-bed-fusion Inconel 718", Materials Science and Engineering A, vol. 893, p. 146109, 2024, doi: 10.1016/j.msea.2024.146109.

7. Environmental impact analysis

The sustainability of industry has become an increasing priority [7-1] with an emphasis on the reduction of energy consumption and carbon emissions throughout the entire life cycle of a product [7-2]. The production of corrosion resistant alloys, commonly used in industry has a high environmental impact [7-3]. Therefore reduction in their usage through the optimisation of manufacture will result in a reduced environmental impact. A method of quantifying the impact of different manufacturing methods is through a life cycle analysis (LCA) [7-4].

In an LCA, the inputs and outputs of each process throughout the life of a product are recorded. To limit the analysis to solely the impact of manufacturing, the life cycle can be limited to only processes between material extraction and the completion of manufacturing [7-5]. Therefore, the only factors included are material extraction, feedstock preparation, manufacturing processes and post processing such as heat treatment [7-6]. The stages not included by defining such boundaries include commissioning, repair, refurbishment and decommissioning as these will be similar between different manufacturing methods [7-7].

Corrosion resistant alloy components are typically manufactured using machining or forging. These processes involve a high proportion of material waste, and for many metals, the primary energy, associated with material extraction and preparation makes up a significant proportion of the environmental impact of production [7-8]. To reduce the environmental impact of manufacturing these components, novel processes must be considered to reduce material waste. Additive manufacturing processes typically produce components close to their final shape, resulting in limited subtractive manufacturing being required to finish the component to its final dimensions through the removal of small amounts of material [7-9].

The analysis presented in this chapter will consider the environmental impact of manufacturing a turbine impeller from Inconel 625 when WAAM is compared to machining from a solid billet. The method utilised in this analysis is adapted

from previous literature [7-8, 7-10] to determine the energy consumption, equivalent CO₂ emissions and material waste by each process.

7.1. Method

The first stage in determining the environmental impact of WAAM and machining is to identify the material flows throughout the processes in addition to defining the analysis boundary. These material flows are depicted in Figure 7-1 and Figure 7-2 for each manufacturing process.

The scope of this analysis includes all manufacturing techniques and material flows to measure the environmental impact. Production machinery and small consumables such as welding torch contact tips and abrasive grinding disks have not been considered.

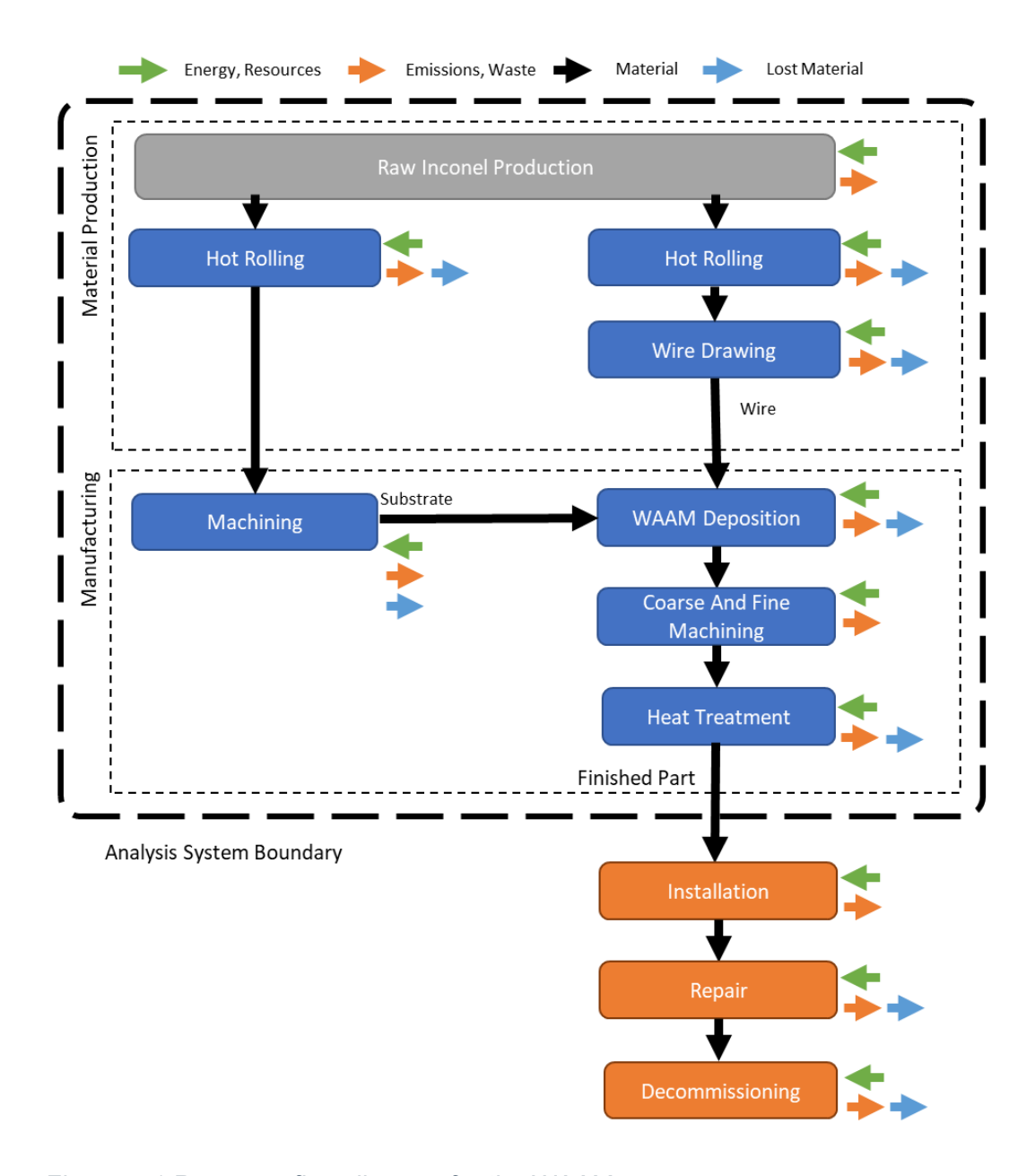


Figure 7-1 Resource flow diagram for the WAAM process.

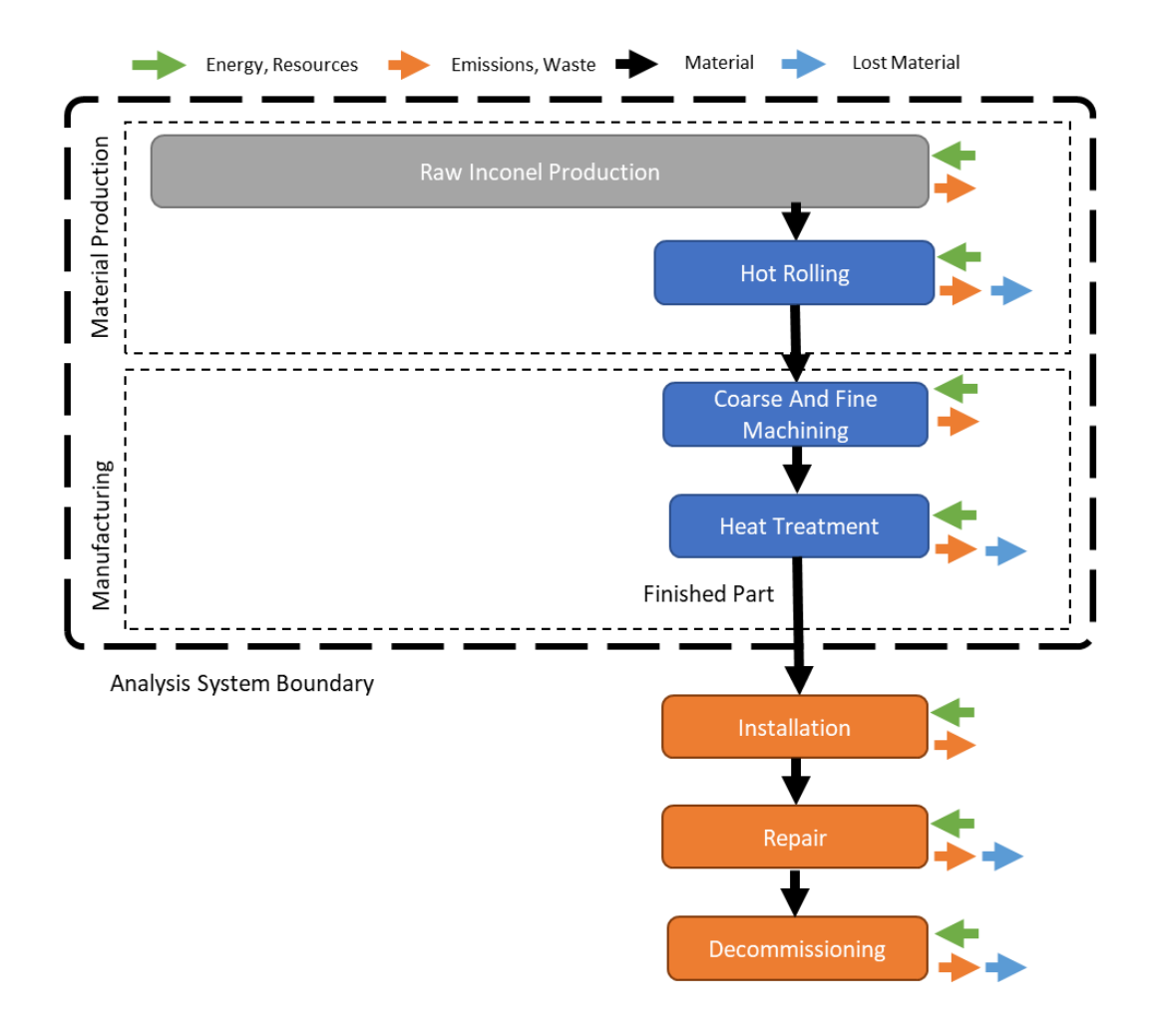


Figure 7-2 Resource flow diagram for the machining process.

7.1.1. Material production and pre-manufacturing

To produce the component, each process requires feedstocks produced by different methods. For example, with the WAAM process, a hot rolled plate and drawn wire are required to produce the substrate and filler wire, while for machining, a hot rolled billet is milled to produce the workpiece.

The rolling and drawing processes result in material loss and incur an environmental impact in primary energy and carbon dioxide emissions. The fraction of lost material and environmental impacts are determined based on existing literature [7-3, 7-10, 7-11].

7.2. WAAM process model

The primary energy required by the WAAM process is determined by breaking down the electrical energy of each aspect of the process, including standby energy of the deposition equipment, arc energy of the cold metal transfer (CMT) deposition equipment, in addition to the primary energy of the shielding gases required. The welding parameters and dwell time between welding passes all have an effect on this primary energy. The energy consumption and carbon emissions of the WAAM process are quantified from Equations 7-1 -7-4 and are adapted from a general assessment of the energy required for WAAM [7-10]. Carbon dioxide emissions for processes which use electrical energy are determined using the carbon emission signature (CES) [7-11], which will be calculated for the global average supply of energy. Western nations typically have a larger proportion of renewable or carbon neutral energy sources, reducing the carbon emissions from the same process.

$$E^{WAAM} = 3.6/\eta \cdot (P_{stb} \cdot t_{stb} + P_{arc} \cdot t_{arc} + dc \cdot P_{heater} \cdot t_{heater})$$

$$+ t_{gas} \sum_{i=1}^{i} E_{gas}^{i} \cdot q_{gas}^{i}$$

$$(7-1)$$

$$SEC = \dot{m}/P_{arc} \tag{7-2}$$

$$CES = \eta(112 \cdot \%_{coal} + 49 \cdot \%_{natural\ gas} + 66 \cdot \%_{fuel\ oil})$$

$$(7-3)$$

$$C = E_n \cdot CES/1000 \tag{7-4}$$

$$E_{e} = P_{f} \sum_{i=1}^{i} dc_{i} \cdot \Delta T_{i} / \dot{T}_{i}$$

$$E_{p} = 3.6 E_{e} / \eta$$
(7-5)
(7-6)

$$E_p = 3.6E_e/\eta \tag{7-6}$$

$$C = E_p \cdot CES/1000 \tag{7-7}$$

 E^{WAAM} Primary energy of the WAAM process (MJ)

 η Energy grid efficiency (0.34 is assumed [11])

 P_{stb} Standby power of the WAAM process cell (robot arm and weld power source) (kW)

 t_{sth} Standby and shutdown time for the WAAM process per component (hr)

SEC Specific energy consumption of the deposition process (kWh/kg)

 m_{wire} mass of wire required to deposit the part (coefficient of 1.02 [7-10] used over deposition mass due to material loss to spatter and wire feed maintenance) (kg)

dc Heater duty cycle, ratio used to determine how much of the deposition time the component heater is running. Set at 0.5 based on production data [7-8].

 P_{heater} Power required to operate the component heater (kW)

 t_{heater} Production time for the component and therefore time the heater is running (hr)

 $E_{\it gas}$ Primary energy of the shielding gas (MJ/I)

t Time the shielding gas is flowing (hr)

 q_{gas} Volumetric flow rate of shielding gas (I/hr)

CES Carbon emission signature (kgCO₂eq/GJ)

C Carbon dioxide emissions (kgCO₂eq)

 E_e Electrical energy used to power the furnace during a heat treatment cycle (kWh)

 E_p Primary energy (MJ)

 P_f Electrical power of the furnace (kW)

 dc_i Duty cycle or ratio of time on to time off during each stage of heat treatment

 ΔT_i Temperature change for each stage of heat treatment (°C)

 \dot{T}_i Temperature ramp rate for each stage of heat treatment (°C/hr)

7.2.1. Machining process model

When a component is machined from solid, a hot-rolled billet with dimensions matching the bounding box of the component is the feedstock for this model. The material flow diagram is shown in Figure 7-3. The machining was conducted in 2 stages, with coarse machining performed to remove material rapidly, but leave the component slightly larger than its final dimensions to allow fine machining to be performed. This fine machining removes material

slowly to reach the specified dimensions and achieve a higher quality surface finish.

7.2.2. Heat treatment model

In the production by WAAM and machining, a heat treatment process was used for stress relief and to develop the microstructure. In the case of the WAAM process, this treatment reduces the residual stresses in WAAM produced Inconel 625 and thus springback during machining, improving the final manufacture tolerances. In addition, an annealing heat treatment process improves the performance of the alloy at elevated temperatures [7-12]. Guidance for the heat treatment processes is given in the ASM handbook for heat treating nickel alloys [7-12].

The energy consumption of a heat treatment is established from the power of the heat treatment furnace, its duty cycle at a range of temperature ramp rates and the time spent at each ramp rate. This is then converted to primary energy consumption and carbon dioxide emissions using Equations 7-5-7-7.

7.2.3. Data gathering

For common processes such as primary production, rolling, drawing and machining; data on primary energy consumption and carbon dioxide emissions has been gathered from Ansys Granta Edupack 2021 R2 [7-3]. Material loss coefficients were also employed for rolling and drawing [7-13]. The primary energy for argon and helium were calculated from the literature [7-14, 7-15].

CES is determined from Equation 7-3, using data from the BP statistical review of world energy [7-16] shown in Table 7-1 giving a global average CES of 1829.4 kgCO₂eg/GJ.

Table 7-1 Percentage of global electrical energy generation by source [7-16].

Supply %	Coal	Natural gas	Fuel oil	Biomass
World	36.5	22.2	3.1	2.7
Supply %	Hydro	Solar	Wind	Nuclear
World	15.3	3.7	6.6	9.9

To assess the environmental impact of heat treatment, data from a bespoke top-hat furnace was collected using integrated thermocouples. These were calibrated by the manufacturer and by monitoring the duty cycle of the heating element over time. This included the temperature ramp rates and the temperature ranges for each ramp rate. The electrical energy input (kWh) was then converted to primary energy consumption (MJ). The carbon dioxide emissions are then calculated using the *CES* in Equation 7-6.

7.3. Case study

To compare the environmental impact of each manufacturing method, a life cycle assessment has been performed for a representative component, manufactured by each method. This component is representative of a turbine impeller used by turbomachinery employed by many industries and often manufactured from Inconel 625 [7-17]. This component incorporates design features that can be manufactured through WAAM and machining [7-18].

The mass of the component at each stage of production was calculated using Solidworks CAD software, with fine machining being assumed to be conducted to remove 2mm of material thickness from all surfaces to reach the specified dimensions.

7.4. Results

The first stage of this LCA is to determine the mass of the component at each stage of production. When combined with process data, this allows the energy consumption and carbon dioxide emissions for each stage to be determined. Combining these contributions gives the total environmental impact for the process which can then be compared directly with other processes.

The mass breakdown for this component, gathered from CAD software is shown in Table 7-2. The process parameters used for WAAM deposition are presented in Table 7-3, allowing for the calculation of environmental impact metrics. Using the data gathered for both WAAM and machining, the primary energy consumption and carbon dioxide emissions to produce an Inconel 625 impeller are tabulated in Table 7-4 and Table 7-5. The results are then presented in Figure 7-4 and Figure 7-5. These results show that for the machined component, the greatest contribution to energy consumption is the primary production of Inconel 625.

Due to the reduction in required material, the contribution of primary production to the WAAM component is dramatically reduced. This causes the heat treatment process to be the greatest proportion of the total energy consumption during WAAM. When the carbon dioxide emissions are compared, the gap is reduced, with emissions being dominated by the equal contribution of heat treatment. This dominance is caused by the significant energy requirements and the conversion factor being based on global averages for carbon emissions for energy production [7-11, 7-16]. This conversion factor is greater than that used by Edupack, so aspects of production calculated using the *CES* conversion are more heavily weighted.

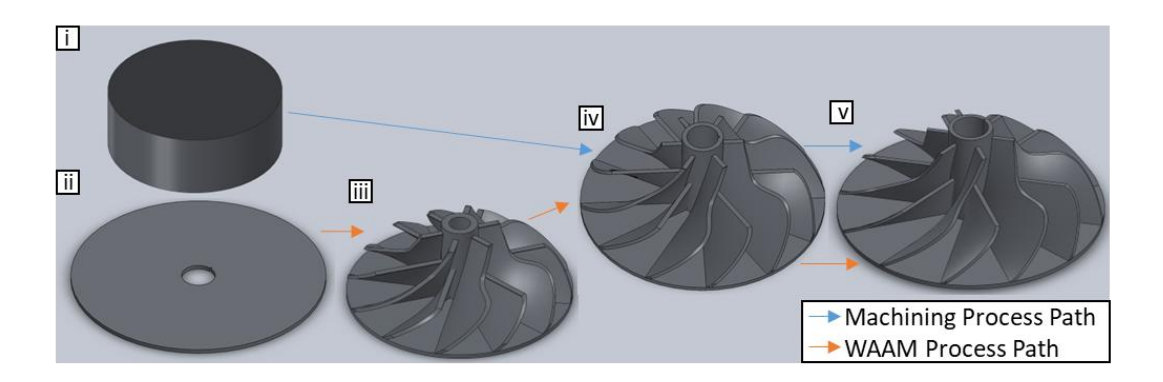


Figure 7-3 Manufacturing stages for life cycle assessment. i) rolled billet for machining ii) substrate for deposition iii) result of WAAM deposition iv) result of coarse machining v) result of fine machining (finished component).

Table 7-2 Mass breakdown for component production by WAAM.

Component mass breakdown (kg)					
Process	WAAM	Machining			
Rolled billet (Substrate)	3.84	73.605			
Deposition	6.763	-			
Coarse machining	-2.969	-65.971			
Fine machining	-0.805	-0.805			
Component total	6.805	6.805			

Table 7-3 Process parameters for WAAM.

WAAM process parameter				
Deposition rate (ideal)	3.74kg/hr			
Arc power	3.0972kW			
Standby power	0.1kW			
Startup time	1			
Arc time	1.85hr			
Gas flow time	1.85hr			
Build time	1.85hr			
Gas flow rate	1320l/hr			

Table 7-4 Energy consumption and carbon dioxide emissions for the component produced by WAAM.

Process	Primary energy	Carbon dioxide	
	(MJ)	(kgCO ₂ eq)	
WAAM idle	1.059	1.936	
WAAM deposition	60.51	110.63	
WAAM shielding gas	2.987	5.461	
WAAM total	64.56	118.03	
Wire primary production	1560.5	103.93	
Substrate primary production	818.5	54.52	
Wire drawing	168.7	12.62	
Substrate rolling	13.82	1.038	
Coarse machining	8.262	0.2188	
Fine machining	4.287	0.322	
Heat treatment	2645.2	4836.1	
Total	5283.8	5126.8	

Table 7-5 Energy consumption and Carbon emissions for the component produced by machining.

Process	Primary energy (MJ)	Carbon dioxide (kgCO ₂ eq)
Billet primary	15336	1021.4
production		
Billet rolling	258.7	19.43
Coarse milling	64.78	4.862
Fine milling	4.287	0.322
Heat treatment	2645.2	4836.1
Total	18244	5877.3

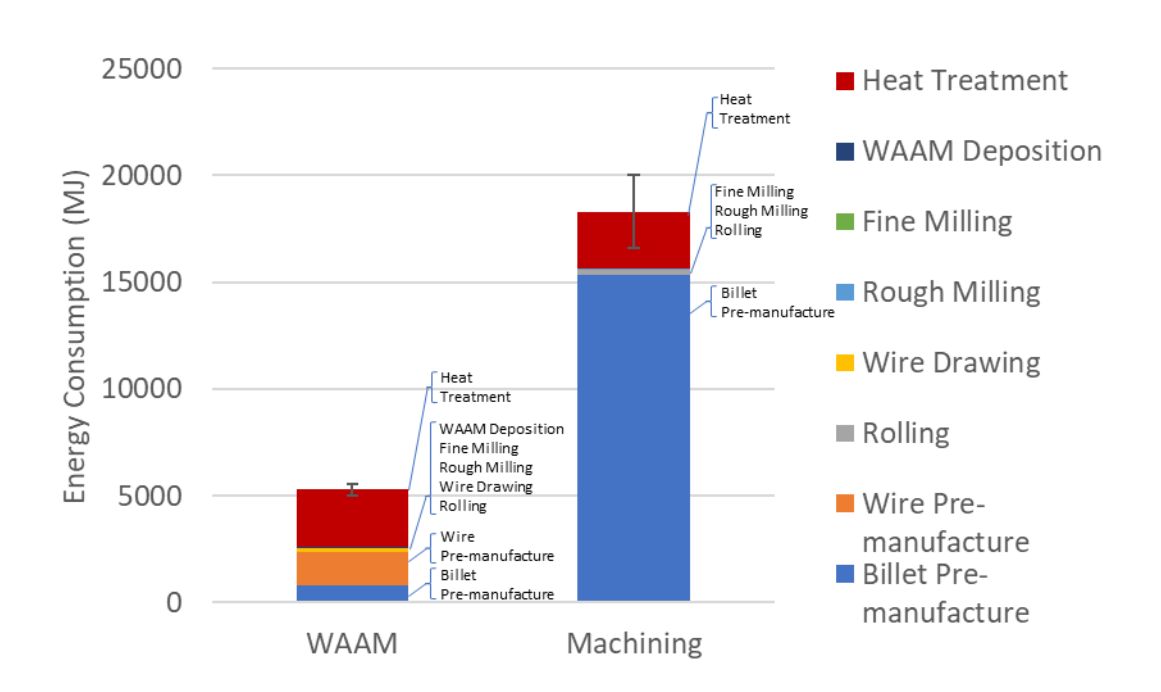


Figure 7-4 Energy consumption required to produce the component.

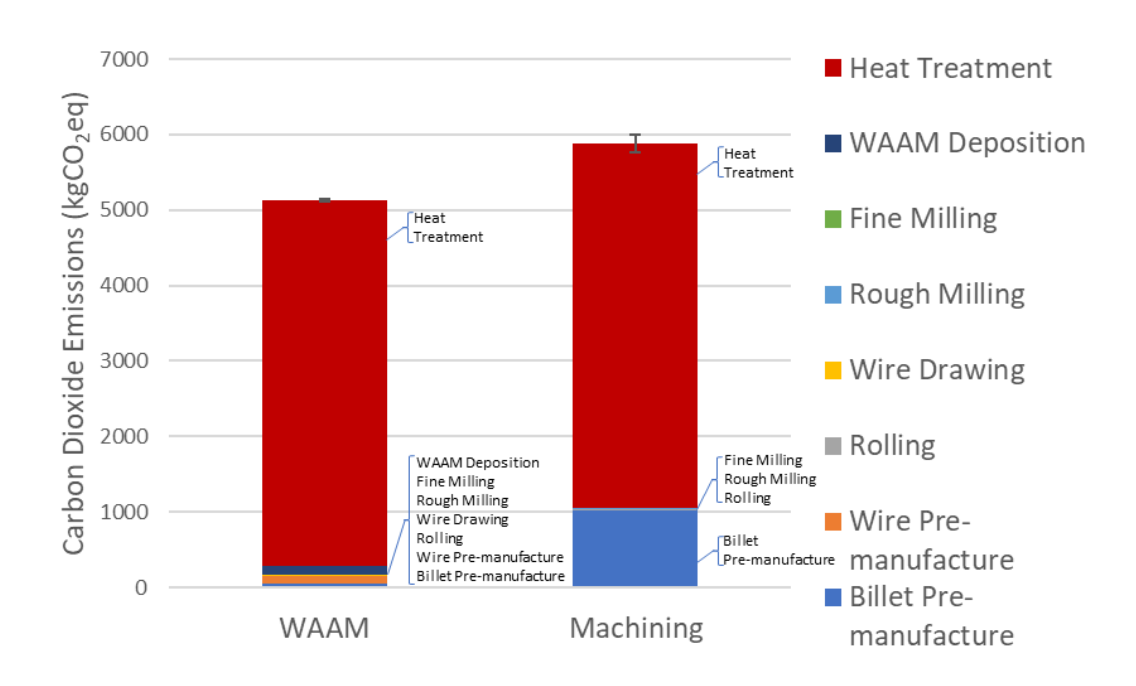


Figure 7-5 CO₂ emissions produced during manufacture of the component.

The results are compared in Table 7-6 using material waste, specific energy consumption and specific carbon dioxide emissions. In Figure 7-6, these metrics are normalised against the results determined for WAAM to provide a direct comparison between the processes. These results show the dramatic difference between the material wasted during WAAM and machining production, and the difference in energy consumption required by both processes. These specific metrics can also be compared to previous data from an LCA of a WAAM produced titanium component [7-8]. In this case, the specific energy consumption and carbon emissions were found to be higher than those reported in the previous study. These increases can be explained by increased arc energy and heat treatment temperature, in addition to the reduced mass of this Inconel component. These led to a reduction in economies of scale for aspects of production which do not scale with mass such as heat treatment.

Table 7-6 Environmental impact metrics and specific impact by process.

	WAAM	Machining
Energy consumption (MJ)	5283.8	18244
Specific energy consumption (MJ/kg)	776.45	2681.0
Carbon emissions (kgCO ₂ eq)	5126.8	5877.3
Specific carbon emissions (kgCO ₂ eq/kg)	753.4	863.7
Material waste (%)	42.80	91.20

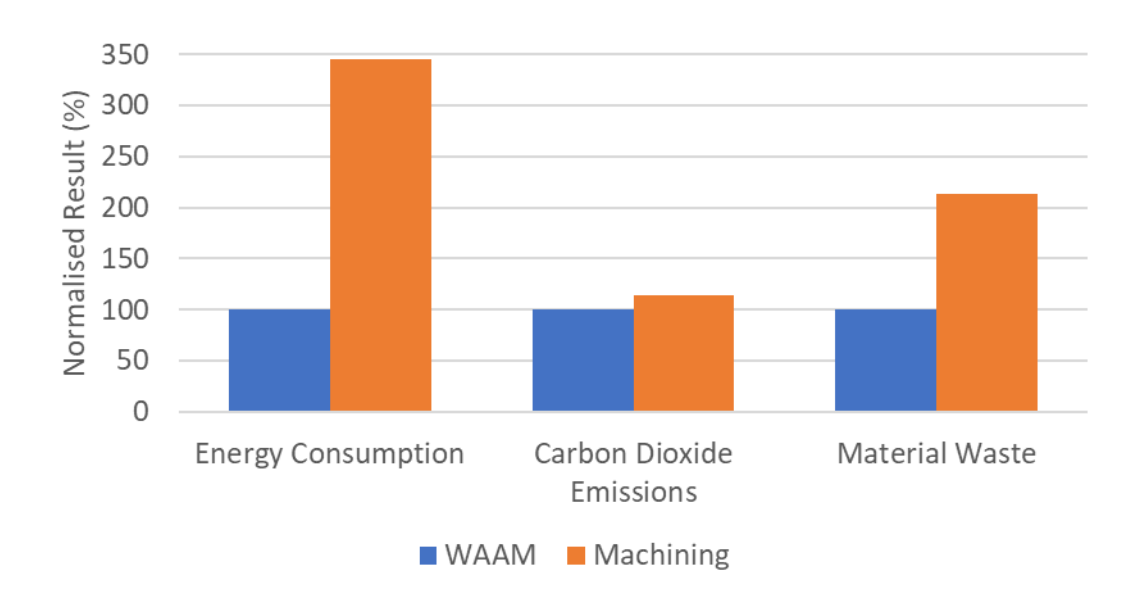


Figure 7-6 Comparison of environmental metrics normalised against the results for WAAM.

7.5. Discussion

This case study details an environmental impact analysis for an impeller manufactured from Inconel 625 using WAAM. The results indicate that WAAM enables a significant reduction in environmental impact using the metrics of energy consumption, carbon dioxide emissions, and material waste. This is primarily due to the decrease in material required for the component when compared to machining from solid. Taking advantage of this primary benefit of WAAM for sustainability results in a threefold reduction in energy consumption and a decrease in material waste from 90% to 40%. The major reduction in environmental impact metrics is associated with the primary energy of production for the alloy, therefore reducing the material requirements significantly reduces the environmental impact of production [7-8].

The value for carbon dioxide emissions is noted to be significantly impacted by the conversion factor (*CES* [7-11]) from electrical energy consumption. This conversion factor is dependent on the proportion of renewable energy sources used during manufacturing. In this study, where carbon emission values were not provided by Edupack, the *CES* conversion factor was calculated using the average result for global energy production based on data from the BP statistical review of world energy 2021 [7-16]. This is a limitation of many environmental impact studies, which combine data from different sources which rely on different assumptions. If the *CES* conversion factor was based on a nation with low fossil fuel usage, it would be expected that the difference between WAAM and machining would increase as the carbon emissions would become less sensitive to the impact of energy consumed during heat treatment.

7.6. References

- [7-1] R. Pang and X. Zhang, "Achieving environmental sustainability in manufacture: A 28-year bibliometric cartography of green manufacturing research," *Journal of cleaner production.*, vol. 233, pp. 84-99, 2019, doi: 10.1016/j.jclepro.2019.05.303.
- [7-2] I. Daniyan, K. Mpofu, K. Bello, and R. Muvunzi, "Life cycle assessment for the milling operation of titanium alloy (Ti6Al4V)," *Procedia CIRP*, vol. 105, pp. 811-816, 2022, doi: 10.1016/j.procir.2022.02.134.
- [7-3] Ansys-Inc, "Granta Edupack 2021 R2," ed, 2021.
- [7-4] J. Shi, J. Hu, M. Ma, and H. Wang, "An environmental impact analysis method of machine-tool cutting units based on LCA," *Journal of engineering, design and technology.*, vol. 19, pp. 1192-1206, 2021, doi: 10.1108/JEDT-06-2020-0247.
- [7-5] A. C. M. Bekker and J. C. Verlinden, "Life cycle assessment of wire + arc additive manufacturing compared to green sand casting and CNC milling in stainless steel," *Journal of cleaner production*, vol. 177, pp. 438-447, 2018/03/10/ 2018, doi: 10.1016/j.jclepro.2017.12.148.
- [7-6] A. R. Catalano, L. Debernardi, R. Balaso, F. Rubbiani, P. C. Priarone, and L. Settineri, "An appraisal of the cradle-to-gate energy demand and carbon footprint of high-speed steel cutting tools," *Procedia CIRP*, vol. 105, pp. 745-750, 2022, doi: 10.1016/j.procir.2022.02.124.
- [7-7] D. D. Tuan and C. Wei, "Cradle-to-gate life cycle assessment of ships: A case study of Panamax bulk carrier," *Proceedings of the institution of mechanical engineers.*, vol. 233, no. 2, pp. 670-683, 2019, doi: 10.1177/1475090218813731.
- [7-8] J. I. Sword, A. Galloway, and A. Toumpis, "An environmental impact comparison between wire + arc additive manufacture and forging for the production of a titanium component," Sustainable Materials and

- *Technologies,* vol. 36, p. e00600, 2023, doi: 10.1016/j.susmat.2023.e00600.
- [7-9] D. Clark, M. R. Bache, and M. T. Whittaker, "Shaped metal deposition of a nickel alloy for aero engine applications," *Journal of materials processing technology,* vol. 203, no. 1, pp. 439-448, 2008, doi: 10.1016/j.jmatprotec.2007.10.051.
- [7-10] P. C. Priarone, G. Campatelli, F. Montevecchi, G. Venturini, and L. Settineri, "A modelling framework for comparing the environmental and economic performance of WAAM-based integrated manufacturing and machining," *CIRP annals manufacturing technology*, vol. 68, no. 1, pp. 37-40, 2019, doi: 10.1016/j.cirp.2019.04.005.
- [7-11] J. Jeswiet and S. Kara, "Carbon emissions and CES™ in manufacturing," *CIRP annals,* vol. 57, no. 1, pp. 17-20, 2008, doi: 10.1016/j.cirp.2008.03.117.
- [7-12] ASM handbook: Induction Heating and Heat Treatment (ProtoView, no. 30). Beaverton: Beaverton: Ringgold, Inc, 2014.
- [7-13] P. C. Priarone, E. Pagone, F. Martina, A. R. Catalano, and L. Settineri, "Multi-criteria environmental and economic impact assessment of wire arc additive manufacturing," *CIRP annals,* vol. 69, no. 1, pp. 37-40, 2020, doi: 10.1016/j.cirp.2020.04.010.
- [7-14] G. Weir and T. Muneer, "Energy and environmental impact analysis of double-glazed windows," *Energy conversion and management*, vol. 39, no. 3, pp. 243-256, 1998, doi: 10.1016/S0196-8904(96)00191-4.
- [7-15] W. Liemberger, M. Miltner, and M. Harasek, "Efficient Extraction of Helium from Natural Gas by Using Hydrogen Extraction Technology," Chemical engineering transactions, vol. 70, pp. 865-870, 07/31 2018, doi: 10.3303/CET1870145.
- [7-16] BP, "Statistical Review of World Energy," 2021.
- [7-17] A. Adiaconitei, I. S. Vintila, R. Mihalache, A. Paraschiv, T. F. Frigioescu, I. F. Popa, and L. Pambaguian, "Manufacturing of Closed Impeller for Mechanically Pump Fluid Loop Systems Using Selective Laser Melting Additive Manufacturing Technology," *Materials.*, vol. 14, p. 5908, 2021, doi: 10.3390/ma14205908.
- [7-18] K. Shi, D. B. Shan, W. C. Xu, and Y. Lu, "Near net shape forming process of a titanium alloy impeller," *Journal of materials processing technology*, vol. 187, pp. 582-585, 2007, doi: 10.1016/j.jmatprotec.2006.11.033.

8. Concluding remarks

This thesis has investigated the WAAM production of the following corrosion resistant alloys (CRA): 15-5PH stainless steel, Inconel 625 and 718. The aims of this thesis were to demonstrate the mechanical properties of these alloys and determine the environmental benefits of a transition from conventional manufacturing to WAAM.

In all of these materials, the developed microstructures were found to differ from their wrought equivalents. Typically, due to the thermal gradients experienced during deposition, a columnar dendritic microstructure developed. In addition, the deposition process caused other detrimental and strengthening phases to form in different proportions to those expected following standard heat treatments for these materials.

It is noted that the process parameters and post weld heat treatment had a significant impact on the mechanical properties which were obtained. Furthermore, it has been shown that WAAM results in a great reduction in energy consumption and material wasted during production. The reduction in carbon emissions has been identified to be strongly dependent on the proportion of fossil fuels used in the generation of electrical energy used in production.

The three alloys investigated, stainless steel 15-5PH, Inconel 625 and Inconel 718 have differing strengthening mechanisms, and as such responded differently to the WAAM process, due to in-situ heating during deposition. 15-5PH was the most sensitive, with in-situ heating causing solutionising of the precipitating elements to different degrees depending on weld heat input. This led to a variation in response to aging heat treatment. Inconel 625 showed the best response to WAAM, as its primary method of strengthening is through solid solution, therefore only a brief solutionising heat treatment was required to return strengthening elements such as molybdenum to the metal matrix. Inconel 718 showed an intermediate sensitivity, as the solutionising treatment was very effective at dissolving the Laves phase and precipitating elements back into the matrix. Reduction in strength compared to wrought material was

identified to be caused by precipitating elements trapped within the acicular δ phase following solutionising, typically located around columnar grains.

Overall, this thesis investigates the effect of the optimisation of process parameters and post weld heat treatment. It is identified that the mechanical properties of corrosion resistant alloys produced through WAAM can be improved to reach those specified for equivalent wrought alloys. In addition, the adoption of this process improves the sustainability of manufacturing components from these alloys through a reduction in material waste.

8.1. WAAM production of 15-5PH

Stainless steel 15-5PH produced using WAAM was compared against the same material in the wrought condition. Analysis was conducted of the microstructure in addition to an assessment of the mechanical properties compared to ASTM standard A693 [8-1]. The WAAM produced material was tested in both the as-deposited and heat treated (H1150) conditions following deposition using two sets of process parameters. These process parameters were selected to tailor the heat input during deposition.

It was determined that material produced using a high heat input deposition and followed by solution treatment H1150 achieved acceptable mechanical properties. This same material, in the as-deposited condition, also demonstrated superior fatigue performance compared to the wrought alloy in the H1025 condition. This data on the wrought alloy was gathered to provide a comparison for the testing of WAAM deposited material.

The results of impact testing demonstrated that aging heat treatment provides a significant improvement in toughness for material produced using both sets of process parameters. In contrast to other chapters, the presentation of impact toughness data within this chapter corresponds with its inclusion within the ASTM standard for this material, while it is not present for Inconel 625 and 718.

Major differences in the microstructure have also been identified, gas porosity is present within the structure of WAAM produced material. In addition, heat

treatment was noted to modify the proportion of δ -ferrite and number of metallic carbides present. These changes in the microstructure were identified to be responsible for changes in mechanical properties. Reductions in δ -ferrite and carbides were responsible for improvements in strength, impact toughness and fatigue strength.

8.2. WAAM production of Inconel 625

The microstructure and mechanical properties of Inconel 625 produced using WAAM were investigated. The microstructure was found to be primarily comprised of columnar dendrites, and in the as-deposited condition, contain the detrimental Laves phase. The properties of this material were enhanced through the application of solution heat treatment which dissolved the Laves phase and developed other strengthening phases. It was determined that the obtained properties in the solution treated condition exceed those specified by the material standard for this alloy in the wrought condition (ASTM B443 [8-2]).

The results for UTS and elongation were also found to exceed those previously published for this combination of material and process [8-3, 8-4]. Differences between these results and those by Tanvir et al. [8-3] are explained by a lower temperature heat treatment being performed by Tanvir, resulting in the precipitation of the δ phase and retention of the Laves phase [8-5], leading to increased hardness and yield strength at the cost of reduced elongation and UTS [8-6].

When the results of fatigue testing are compared against existing literature this material is found to exceed the performance of the wrought alloy [8-7, 8-8] and display comparable results to other AM methods such as LPBF [8-9].

Upon examination of the fracture surfaces following tensile and fatigue testing, it is clear that the material undergoes significant plastic deformation before failure, with slip planes being commonly observed on samples subject to fatigue testing.

8.3. WAAM production of Inconel 718

The microstructure and mechanical properties of Inconel 718 produced using WAAM were investigated. It was found that the prevalence of the δ phase was higher than other manufacturing methods [8-10]. This resulted in a reduction in ductility compared to existing material standards [8-11] and is also reflected in the results for fatigue testing. This is particularly clear in the instances of transgranular cracking identified in limited numbers of tests.

The tensile strength of the material was found to be slightly below that specified for this alloy in the solution treated and aged condition [8-11], however these results are broadly in line with results previously published for Inconel 718 produced by WAAM [8-12] and LENS [8-10].

As-deposited, the microstructure displays dendrites, as commonly observed in WAAM produced material. This dendritic matrix is rich in the Laves phase in addition to carbides of composition TiC and NbC. The solution treatment elimites the detrimental Laves phase, reducing hardness. When this is followed by aging treatments, the growth of strengthening phases such as γ ", carbides and nitrides is promoted, leading to increased strength and hardness [8-10].

The results of fatigue testing indicate that the reduced elongation of the WAAM produced material compared to other methods of manufacture leads to an increased susceptibility to crack propagation at low stress ranges.

8.4. Environmental impact analysis

The environmental impact of manufacturing a turbine impeller from Inconel 625 was compared for WAAM and machining. It was found that the adoption of WAAM leads to a reduction in material waste from 90% to 40% by depositing material only where it is required. In addition, the energy consumption is reduced threefold as less material is required, reducing the primary energy used to produce the component.

The method [8-13] used in this analysis was found to have a significant bias towards the carbon emissions of processes consuming electrical energy due to the carbon emission signature (*CES*) [8-14] conversion factor which has

been used. This suggests that significant reductions can be achieved in industrial sectors through the adoption of renewable sources of electricity, as the consumption of energy for some processes such as heat treatment do not scale with component mass.

8.5. Conclusion summary

Overall, this work has identified a number of challenges related to the production of CRAs deposited using WAAM.

- The difference between wrought and WAAM properties varies depending on the strengthening mechanism of the alloy.
- Solid solution strengthening alloys such as Inconel 625 respond best to WAAM production.
- Precipitation hardening alloys such as 15-5PH stainless steel and Inconel 718 are more sensitive to prior solutionising of the matrix, either through in-situ heating during deposition, or through post weld heat treatment.
- Inter pass temperature and other processing has a significant impact on the resulting mechanical properties, being a method of controlling the growth of columnar grains, which lead to anisotropic properties.
- WAAM can be used to reduce the material waste for complex components, which leads to a reduction in the environmental impact of manufacturing.

8.6. Recommendations for future work

The results presented in this body of research represent a significant contribution to the data on the mechanical properties of corrosion resistant alloys deposited using WAAM. However, this field is not yet fully mature and opportunities for future work have been identified to enhance the adoption of WAAM to produce components from CRAs by industries in the future.

Further to the investigation of precipitation-hardening stainless steel 15 5PH, the mechanical properties do not yet meet the required material

standards (ASTM A693 [8-1]) especially in high strength conditions such as H900 and H1025. As such, further investigations to vary the process parameters and post weld heat treatment (PWHT) are recommended to further optimise the mechanical properties. Interpass treatment such as ultrasonic peening and rolling should be investigated to reduce the size of columnar grains.

- The investigation of the impact of fatigue on WAAM can be enhanced through the gathering of data on corrosion fatigue [8-15, 8-16]. In this regime, the sample is submerged in a corrosive solution during fatigue testing and the growth of fatigue cracks can be accelerated by chemical reactions between the sample and the corrosive solution.
- Furthermore, fatigue testing could be performed to assess the reduction in fatigue performance caused by retaining the as-deposited surface finish, as is experienced by components with internal features such as fluid channels [8-17].
- A development in engineering materials which has been enabled by additive manufacturing includes functionally graded materials (FGM) [8-18] and in situ alloying [8-19]. One possible application of the WAAM process is to produce components combining the fatigue performance and corrosion resistance of Inconel 625 to provide a clad coating for a core of Inconel 718 through WAAM deposition [8-20]. Using in situ alloying techniques, the transition between alloys could be made more gradual, reducing the discontinuity, improving performance [8-21].

8.7. References

- [8-1] A693-16 Standard Specification for Precipitation-Hardening Stainless and Heat-Resisting Steel Plate, Sheet, and Strip, 2016.
- [8-2] ASTM-B443 Standard Specification for Nickel-Chromium-Molybdenum-Columbium Alloy (UNS N06625) and Nickel-Chromium-Molybdenum-Silicon Alloy (UNS N06219) Plate, Sheet, and Strip, ASTM, 2014.
- [8-3] A. N. M. Tanvir et al., "Heat treatment effects on Inconel 625 components fabricated by wire + arc additively manufacturing (WAAM)—part 2: mechanical properties", International journal of advanced manufacturing technology, vol. 110, no. 7-8, pp. 1709-1721, 2020, doi: 10.1007/s00170-020-05980-w.
- [8-4] Y. Wang, C. Xizhang, and S. Chuanchu, "Microstructure and mechanical properties of Inconel 625 fabricated by wire-arc additive manufacturing", *Surface & coatings technology*, vol. 374, pp. 116-123, 2019, doi: 10.1016/j.surfcoat.2019.05.079.
- [8-5] A. N. M. Tanvir *et al.*, "Heat treatment effects on Inconel 625 components fabricated by wire + arc additive manufacturing (WAAM)—part 1: microstructural characterization", *International journal of advanced manufacturing technology*, vol. 103, no. 9, pp. 3785-3798, 2019, doi: 10.1007/s00170-019-03828-6.
- [8-6] J. Mittra *et al.*, "Fracture behavior of Alloy 625 with different precipitate microstructures", *Materials science & engineering. A, Structural materials : properties, microstructure and processing,* vol. 574, pp. 86-93, 2013, doi: 10.1016/j.msea.2013.03.021.
- [8-7] P. W. Trester, J. L. Kaae, and R. Gallix, "Fatigue strength of inconel 625 plate and weldments used in the DIII-D configuration vacuum vessel", Journal of nuclear materials, vol. 133, p. 347, 1985, doi: 10.1016/0022-3115(85)90165-5.
- [8-8] F. G. L. Pereira *et al.*, "Fracture Behavior and Fatigue Performance of Inconel 625", *Materials research*, vol. 21, no. 4, 2018, doi: 10.1590/1980-5373-MR-2017-1089.
- [8-9] N. Martin *et al.*, "Fatigue properties of as-built and heat-treated Inconel 625 obtained by the hybridization of two laser-powder based additive processes", *International journal of fatigue*, vol. 172, p. 107650, 2023, doi: 10.1016/j.ijfatigue.2023.107650.
- [8-10] H. Qi, M. Azer, and A. Ritter, "Studies of Standard Heat Treatment Effects on Microstructure and Mechanical Properties of Laser Net Shape Manufactured Inconel 718", Metallurgical and materials transactions. A, Physical metallurgy and materials science, vol. 40, no. 10, pp. 2410-2422, 2009, doi: 10.1007/s11661-009-9949-3.
- [8-11] B637 Standard Specification for Precipitation-Hardening and Cold Worked Nickel Alloy Bars, Forgings, and Forging Stock for Moderate or High Temperature Service, ASTM, 2018.
- [8-12] X. Xu et al., "Investigation of process factors affecting mechanical properties of Inconel 718 superalloy in wire + arc additive manufacture process", Journal of materials processing technology, vol. 265, pp. 201-209, 2019, doi: 10.1016/j.jmatprotec.2018.10.023.
- [8-13] J. I. Sword, A. Galloway, and A. Toumpis, "An environmental impact comparison between wire + arc additive manufacture and forging for the

- production of a titanium component", *Sustainable Materials and Technologies*, vol. 36, p. e00600, 2023, doi: 10.1016/j.susmat.2023.e00600.
- [8-14] J. Jeswiet and S. Kara, "Carbon emissions and CES™ in manufacturing", *CIRP annals*, vol. 57, no. 1, pp. 17-20, 2008, doi: 10.1016/j.cirp.2008.03.117.
- [8-15] D. Kong *et al.*, "About metastable cellular structure in additively manufactured austenitic stainless steels", *Additive Manufacturing*, vol. 38, p. 101804, 2021/02/01/ 2021, doi: 10.1016/j.addma.2020.101804.
- [8-16] Z. Fu et al., "Hydrogen-assisted fatigue crack propagation behavior of selective laser-melted Inconel 718 alloy", Corrosion science, vol. 227, p. 111745, 2024, doi: 10.1016/j.corsci.2023.111745.
- [8-17] Orbex. "Orbex Commissions Largest Industrial 3D Printer in Europe for Rapid Rocket-Building" https://orbex.space/news/orbex-commissions-largest-industrial-3d-printer-in-europe-for-rapid-rocket-building (accessed 03/09/2021).
- [8-18] T. Abe and H. Sasahara, "Dissimilar metal deposition with a stainless steel and nickel-based alloy using wire and arc-based additive manufacturing", *Precision engineering*, vol. 45, pp. 387-395, 2016, doi: 10.1016/j.precisioneng.2016.03.016.
- [8-19] Z. Yang et al., "Fabrication of multi-element alloys by twin wire arc additive manufacturing combined with in-situ alloying", *Materials research letters*, vol. 8, no. 12, pp. 477-482, 2020, doi: 10.1080/21663831.2020.1809543.
- [8-20] J. Cao, K. Kou, and C. Lam, "Crack propagation analysis of 3D printed functionally graded titanium alloy components", *Theoretical and applied* fracture mechanics., vol. 111, p. 102865, 2021, doi: 10.1016/j.tafmec.2020.102865.
- [8-21] M. S. Domack and J. M. Baughman, "Development of nickel-titanium graded composition components", *Rapid prototyping journal*, vol. 11, no. 1, pp. 41-51, 2005, doi: 10.1108/13552540510573383.

A. Historical Context

This appendix will detail the history of additive manufacturing (AM) and provide context for common forms of metal AM. This will be expanded to provide more detail of recent developments in the field of wire arc additive manufacturing (WAAM). These developments include the cold metal transfer (CMT) and twin wire (T-WAAM) processes.

In addition, a summary of common corrosion resistant alloys (CRAs) and their microstructures will be provided. Furthermore, a brief discussion of fatigue testing and environmental impact analysis is presented.

A.1. Additive manufacturing

The history of additive manufacturing (AM) could be interpreted as going back as far as antiquity, with goods manufactured in ancient Mediterranean civilisations being noted to use coiled pottery [A-1], a form of pottery made using coils of clay pressed together. This process bears similarity to modern extrusion-based manufacturing processes such as FDM (filament deposition modelling).

Several thousands of years later, AM processes have become more advanced. The definition of AM processes is given by BS EN ISO/ASTM 52900-2017 [A-2] and describes a manufacturing process that adds material to form a part, as opposed to subtractive processes such as milling and turning, or formative processes such as forging or bending. This technology sees widespread use in a range of industries and applications; from prototyping and hobbyist 3D printers using plastics [A-3], to laser or arc powered devices used to manufacture metallic components for industries such as aerospace components [A-4] and medical devices [A-5]. In addition, concrete deposition equipment has been proposed for fabricating structures on other worlds [A-6].

A.1.1. Overview of AM processes

Due to the broad definition of AM, a wide variety of processes are included in the field. More specific definitions are often defined by a combination of feedstock material and state, fusion type, and distribution method [A-2]. Various forms of AM processes are shown in Figure A-1.

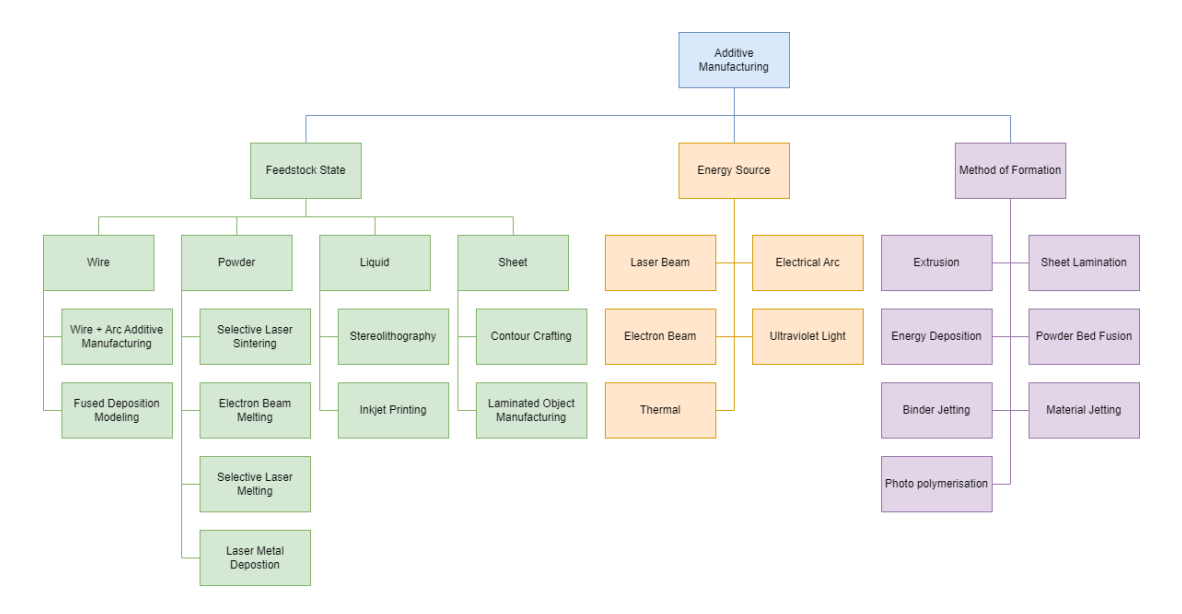


Figure A-1 A taxonomy of additive manufacturing techniques.

Stereolithography is also one of the first commercialized modern AM processes [A-7], it uses UV light to trigger solidification of the polymer feedstock chemically. The component dimension is limited by the build tank which must be filled with liquid polymer [A-8]. Due to the fine resolution possible using an optical process for solidification, nano-scale components can be produced [A-9].

Inkjet printing and contour crafting are typically used in the production of ceramics [A-10] or in the deposition of building materials for large structures. These have uses in applications such as medical tissue engineering or automated construction in harsh environments such as on the moon [A-11].

Applicable to both metals and polymers are powder bed fusion (PBF) processes. This uses either a chemical binder or laser to fuse powder particles together [A-12]. The complete filling of the bed with powder eliminates the need for support structures but does require the inclusion of "drainage" holes for excess powder. The primary drawbacks of PBF methods are the high cost and

low deposition rate [A-13]. The high precision of this method does make it valuable for intricate, small parts with internal features such as fluid channels [A-14].

The most common additive manufacturing method in use today is fused deposition modelling (FDM), widely used by hobbyists [A-15] with a low cost feedstock such as polylactic acid (PLA) [A-16]. This method uses a heated nozzle to melt the filament and deposit it onto a build plate in layers to complete the part. Due to the extrusion of the polymer filament through a nozzle to deposit layers of solid material, it is most similar to coil pottery as discussed at the start of this chapter.

One factor shared between AM technologies is the capability to manufacture complex geometry such as overhangs or internal features. These would be impossible by conventional manufacturing such as casting or machining [A-17]. Additionally, a reduction in material wastage and the elimination of specific tooling required for forging makes these techniques valuable for industry for the reduction of costs and lead times [A-18].

A.1.2. Methods of metal AM for high deposition rate

Powder bed processes are popular for the production of small metallic components by additive manufacturing. This process yields excellent mechanical properties compared with machined or forged equivalents [A-19,A-20] and very high resolution [A-12]. However, these processes exhibit a low deposition rate, typically measured in grams per hour [A-21].

To produce larger scale metallic components for industry, directed energy deposition (DED) processes are typically employed. By using a travelling deposition head incorporating both the energy source and feedstock supply, an increased deposition rate can be achieved. This is typically measured in kg per hour [A-22]. Examples of the energy source include electron beams [A-23], lasers [A-24], as well as electrical [A-25] and plasma arcs [A-26]. Feedstocks are typically in a wire or powder state, with wire-based DED methods being analogous to FDM methods. In both cases, a wire feedstock is fused to the previous layer through the use of a heat source.

A.2. Wire arc additive manufacturing

Within the DED family of processes, wire arc additive manufacturing (WAAM) shows promise for the rapid manufacture of high mass components in industry. This promise is due to a combination of comparable mechanical properties to the wrought alloys [A-27] and relatively low cost due to the use of mature arc welding technology. In addition it is capable of manufacture larger components [A-28] than other methods such as electron beam melting (EBM) which requires a vacuum environment, limiting component size [A-29].

WAAM processes are defined by the use of a wire feedstock and use an arc to fuse the feedstock into the parent material. This arc can be initiated at the feedstock wire, or a tungsten electrode requiring an independent wire feed. Due to the high temperatures involved, a shield of inert gas protects the melt pool from rapid oxidation. This is often a mixture of gasses depending on the material and desired outcomes [A-30].

The drawbacks of WAAM are related to the method by which material is deposited. Compared to laser or electron beams, the electrical arc transfers more energy to the workpiece, over a larger area. As such, the resolution is limited, and the mechanical properties can be reduced due to the heat input. To control this, interpass cooling can be implemented [A-31]. Defects can also be generated during deposition; examples of these include porosity, delamination or cracking. These can be caused by poor quality feedstocks, improper process parameters or the development of residual and thermal stresses [A-32].

A.2.1. Arc sources

There are three primary of arc sources used in WAAM processes. The first is based on GMAW (gas metal arc welding, shown in Figure A-2a) which projects the arc from the feedstock wire. The equipment required for this form of deposition is simple, low cost and can be easily fitted to a robot arm or CNC (computer numerical control) center. Shielding gasses are used to protect the melt pool from oxidation and can improve penetration through increasing the heat transfer to the weld pool [A-33,A-34].

The second is GTAW (gas tungsten arc welding, shown in Figure A-2b) which uses a non-consumable tungsten electrode to direct a more concentrated arc at higher temperature. This produces a melt pool into which the feedstock wire is added. Once again, a shielding gas is used to protect the melt pool, though only inert gasses such as helium and argon are used. The concentrated arc decreases the overall heat addition to the workpiece, typically improving mechanical properties [A-27,A-35].

Finally, PPAD (pulsed plasma arc deposition, shown in Figure A-2c) uses a tungsten electrode to initiate an arc within the nozzle, but this is used to direct a stream of ionized plasma at the workpiece [A-36] which generates a melt pool with a higher energy density and smaller heat affected zone than "free arc" (GMAW and GTAW) deposition, resulting in further improvements in mechanical properties [A-26,A-37].

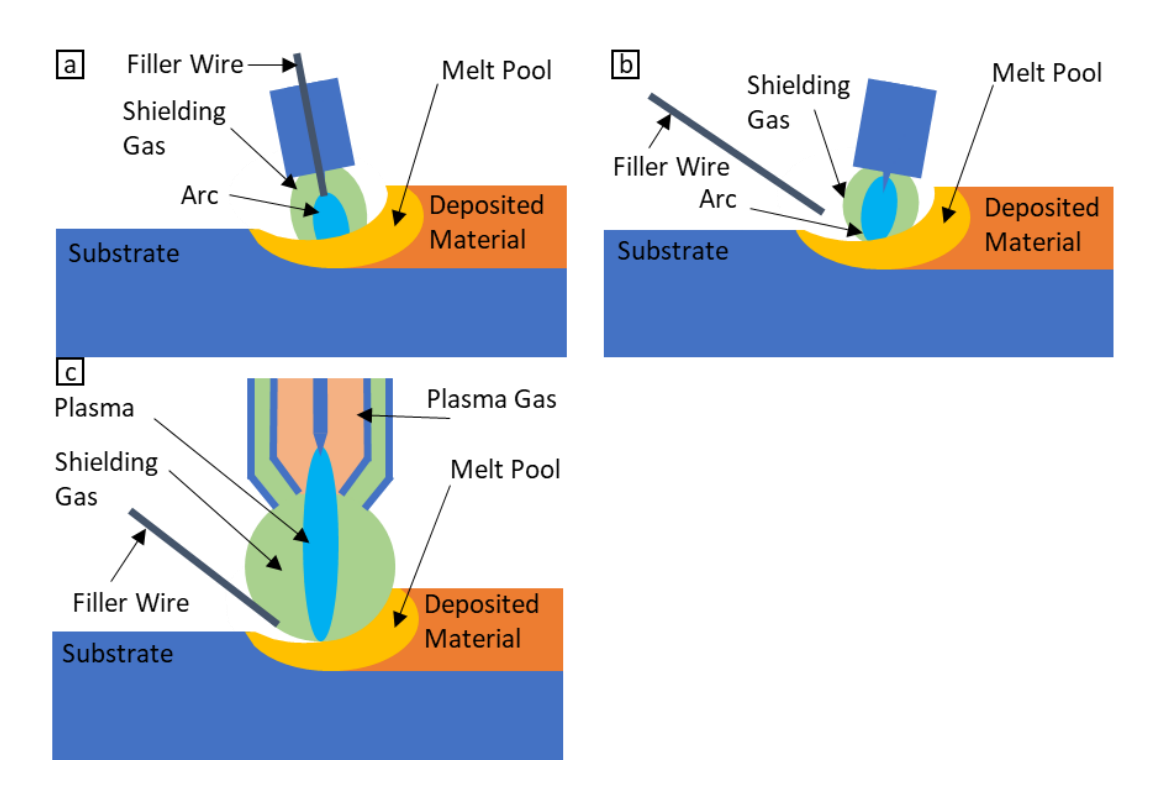


Figure A-2 Forms of arc welding a) gas metal arc welding (GMAW) b) gas tungsten arc welding (GTAW) c) pulsed plasma arc deposition (PPAD)

A.2.2. Cold metal transfer (CMT-WAAM)

CMT (cold metal transfer) is a derivation of GMAW welding, commonly used in WAAM processes to reduce heat input and dilution or join dissimilar metals [A-38,A-39]. CMT achieves a reduction in heat input and improves arc stability through a pulsed arc and retraction of the wire feed with each pulse of the arc. Current and voltage to the arc are controlled through a synergic curve. The process is described as droplet cutting and is achieved through 4 steps:

- 1- The arc melts the tip of the wire electrode.
- 2- The wire feed is extended until the electrode contacts the workpiece, extinguishing the arc.
- 3- Surface tension causes the molten droplet to detach from the wire as it retracts.
- 4- The arc reignites, restarting the cycle [A-40].

A.2.3. Twin wire (T-WAAM)

There is interest in creating functionally graded and intermetallic materials. One means by which this can be achieved is by twin wire WAAM. This uses two independent wire feeds into the same melt pool. By varying the wire feed speeds, alloys of varying composition can be produced [A-27].

A.3. Corrosion resistant alloys

Corrosion resistant alloys (CRAs) are used in applications where extreme environments such high temperature or corrosive atmospheres are likely to be in contact with the metallic components [A-41]. The most commonly used example is stainless steel (iron alloyed with chromium at above 11% [A-42]) which is also used in food processing and medical equipment due to the reduced risk of contamination by corrosion [A-43].

In the oil and gas industry, subsurface and offshore equipment is exposed to a wide range of corrosive agents. These include drilling mud, sour and sweet gas (H₂S and CO₂ respectively) as well as saltwater [A-44]. While stainless steels are often suitable, in some conditions even these alloys will rapidly degrade and nickel-based CRAs are employed such as the Inconel families of alloys [A-45]. The requirements for the material properties of CRAs and when

they should be used are given in the standard API6a CRA for wellhead equipment [A-46].

Other CRAs use a cobalt base such as Stellite 6; these alloys are expensive and are most frequently used as a surface coating to dramatically improve wear resistance. Example uses include heavy gun barrels [A-47], ice axe hammers [A-48] and turbine blades [A-49]. Due to its response to neutron radiation, it is unsuitable for some nuclear reactor designs due to the alloy releasing the radioisotope cobalt-60 from valve faces coated in this alloy [A-50].

A.3.1. Stainless Steels

Stainless steels are a broad family of alloys with a range of compositions and structures, with the most common being austenitic (such as 304 and 316) [A-51]. Other crystal structures such as ferrite and martensite can be achieved through variation in the chemical composition which reduces cost or increases strength respectively [A-42]. More specialised alloys exist such as precipitation-hardening [A-52] and duplex stainless steels [A-53].

Duplex stainless steel is popular in the offshore industry, combining ferritic and austenitic microstructures [A-54]. This enables high corrosion resistance and strength while reducing the usage of nickel, improving cost effectiveness [A-55]. The usage of duplex alloys in harsh environments has led to the development of super-duplex alloys. These are often alloyed with elements such as tungsten or molybdenum for a further increase in strength, but require careful processing [A-56].

Precipitation-hardening (PH) stainless steels have corrosion resistance equivalent to austenitic grades, but through the correct heat treatment can achieve strengths higher than other martensitic grades [A-51]. The hardening effect is achieved through a precipitation process caused by alloying with copper, molybdenum, aluminium or titanium [A-57]. A range of heat treatments are employed for finished components to tailor the strength and impact toughness to the application [A-58]. One of the most commonly used grades is 15-5PH (UNS15500), which is used by the aerospace, marine and energy industries due to its high strength and corrosion resistance [A-59].

A.3.2. Inconel 625

Inconel 625 (also known as ERNiCrMo-3 when used as a welding electrode), is a nickel-based CRA, frequently used in applications such as chemical processing, aerospace and marine engineering due to its excellent strength and resistance to crevice and pitting corrosion [A-60]. Inconel 625 is primarily alloyed with chromium, molybdenum and niobium which improves its strength through the formation of intermetallic phases and precipitates within a Ni-Cr matrix [A-61,A-62]. The microstructure of Inconel 625 is sensitive to heat treatment, with long aging treatments cause an increase in the precipitates produced, while also dissolving some intermetallic phases. The high corrosion resistance provided by the alloy makes it popular as a clad coating for steel components [A-63,A-64].

The commonly referenced phases in Inconel 625 include the metastable strengthening phase, γ " [Ni₃(Nb,AI,Ti)] and the brittle Laves phase [Cr,Mo)]. γ " typically transforms into δ [Ni₃(Nb, Mo)] during prolonged aging treatment or high temperature service. The formation of metallic carbides from the δ phase is also reported in higher temperature regimes. The precipitation of γ " and Ni₂(Cr,Mo) has been found to cause microstrain during high temperature service. This can be eliminated through a repurposing aging treatment at higher temperature to form δ and carbides [A-65]. In cast Inconel 625, the precipitation of δ causes an increase in strength following aging and this effect is more significant at higher concentrations of Nb due to elemental segregation [A-66].

An investigation of the fracture surfaces revealed that aging at too high a temperature creates large δ phase plates which decrease strength. Whereas the growth of γ " phases at lower temperatures cause an increase in strength [A-67]. However, in a study of cast Inconel 625 following long-term aging, higher strength was achieved. This is suggested to be related to the precipitation of the δ phase, increasing brittleness which has been corroborated by results following 10,000hr aging at 700°C [A-66].

The Laves phase is an intermetallic phase of composition [AB₂] [A-68]. In many alloys in which it occurs, this causes a reduction in mechanical properties in

addition to an increase in brittleness [A-69]. In Inconel alloys this takes the form of a dense, Nb rich phase [A-70]. The segregation of this phase on grain boundaries is also found to decrease corrosion resistance [A-35]. Other studies have found that the Laves phase can dissolve upon reheating to form δ [Ni₃(Nb, Mo)], which is corroborated by the findings of reduced hardness in the upper regions of additively manufactured Inconel 625 due to exposure to extended heating during deposition [A-37].

A.3.3. Inconel 718

Inconel 718 is a high strength nickel-based alloy with higher iron content than Inconel 625 in addition to reduced molybdenum and chromium [A-60]. This increase in iron content leads to the ability to perform precipitation hardening while also displaying increased strength and hardness. In addition, this alloy also has high resistance to corrosion and creep as well as excellent weldability [A-71].

The strength of Inconel 718 is derived from the precipitation of γ " particles ([Ni₃Nb] body centred tetragonal structure) within the matrix [A-72]. A δ phase is also identified as a stable transformation product of γ " following overaging. This phase can also be generated directly from the γ matrix during heat treatment [A-73]. It is noted that the heat treatment temperature has a large impact on the hardening of the alloy, with high temperature (975°C) correlated with reductions in hardness due to reduced formation of the intragranular δ phase [A-74]. The common phases are metallic carbides which improve performance, while the Laves phase takes the form of platelets following long duration exposure to high temperature. Akin to the microstructure of Inconel 625, The Laves phase is also found to be detrimental to performance but can be reduced through heat treatment at the cost of promoting grain growth [A-75].

A.4. Fatigue testing

Fatigue testing is a practice of exposing a material to cyclic loading at stresses below its ultimate strength to induce failure after a number of cycles [A-76]. The phenomenon of fatigue was first identified following the failure of a number of train axles [A-77]. This led to the concept of endurance limit by August Wohler in 1870 [A-78]. For a cyclic stress below this value, it was proposed that the lifespan of a component is indefinite. The fatigue of components has led to a number of engineering failures throughout the 20th century with the most notable of these being the catastrophic loss of 3 de Havilland Comet jet airliners in 1954, caused by stress concentration sites in the corners of square openings in their fuselage [A-79]. This series of air disasters was the inspiration for the episode "Operation Crash-Dive" of the 1965 TV series "Thunderbirds" which directly references metal fatigue as a possible cause for the crash of the fictional "Fireflash" aircraft [A-80].

There are a wide range of factors which can impact a fatigue test. These can be broadly divided into two categories: sample factors and test process factors. Examples of sample factors include the geometry of the material to be tested, surface roughness [A-81] and stress concentrators such as notching [A-82]. Test process factors include the amplitude, range and mean of the testing stress [A-83]. In addition, the ratio between maximum and minimum stress and the frequency of cyclic loading can impact the result of fatigue testing [A-84].

A number of systems can be used to determine the fatigue life of components. The two most common are rotating-bending and axial loading. In the former, a sample of cylindrical cross section is subjected to a bending load while rotating. This is analogous to the stress an axle experiences throughout its service life [A-77] with an experienced stress ratio is -1. In axial testing, a universal testing machine is used to apply stress along the length of the sample according to any stress profile the machine is capable of, permitting a range of stress ratios, amplitudes and means. However, frequency is often limited, making such testing time consuming [A-85].

A.5. Environmental impact analysis

A primary area of development in the manufacturing sector is the reduction of environmental impact of the processes used. This can be measured in a number of ways, corresponding to harmful outputs or resources consumed during the manufacture, life and decommissioning of a component or product.

Commonly measured emissions include carbon dioxide (CO₂) and oxides of nitrogen (NO_x), being two prevalent and harmful greenhouse gases [A-86]. Primary energy is also commonly considered, as this accounts for energy lost in thermal or mechanical processes such as turbo-electric electricity generation [A-87]. More detailed metrics include the acidification and toxification potentials of different processes and feedstocks [A-88]. The quantity of material used to produce a component is also considered to assess the efficiency of a production process.

A number of case studies exist, detailing the environmental impact of manufacturing of a given product. These include the investigation of the manufacture of a bulk carrier including shipyard operations [A-89], manufacture of propulsion machinery and sea trials. In addition, an in depth study on each operation performed during the production of high speed steel machine tooling was undertaken [A-90]. Both studies conclude that the extraction and primary production of raw materials is a significant contributor to the environmental impact of these manufacturing processes. A limitation of these studies is the lack of comparison to other processes or materials, to quantify an environmental benefit of a change in design, material or process.

Studies have also been performed on the energy consumption and carbon emissions of WAAM manufacture of steel and aluminium components [A-91,A-92], comparing them with casting and CNC machining. These show a large reduction in energy requirements and carbon emissions. There is also interest in the sustainability of the manufacturing of titanium components [A-93].

A.6. References

- [A-1] C. Knappett, "Tradition and innovation in pottery forming technology: wheel-throwing at Middle Minoan Knossos," *The annual of the British School at Athens.*, vol. 94, pp. 101-129, 1999, doi: 10.1017/S0068245400000538.
- [A-2] BS EN ISO/ASTM 52900:2017 Additive manufacturing General principles — Terminology, BSI, 2017.
- [A-3] M. Mani, A. G. Karthikeyan, K. Kalaiselvan, P. Muthusamy, and P. Muruganandhan, "Optimization of FDM 3-D printer process parameters for surface roughness and mechanical properties using PLA material," *Materials Today: Proceedings*, vol. 66, pp. 1926-1931, 2022, doi: 10.1016/j.matpr.2022.05.422.
- [A-4] E. Hosseini and V. A. Popovich, "A review of mechanical properties of additively manufactured Inconel 718," *Additive manufacturing*, vol. 30, p. 100877, 2019, doi: 10.1016/j.addma.2019.100877.
- [A-5] Z. Yang, Q. Liu, Y. Wang, Z. Ma, and Y. Liu, "Fabrication of multielement alloys by twin wire arc additive manufacturing combined with in-situ alloying," *Materials research letters*, vol. 8, no. 12, pp. 477-482, 2020, doi: 10.1080/21663831.2020.1809543.
- [A-6] M. Troemner, E. Ramyar, R. Marrero, K. Mendu, and G. Cusatis, "Marscrete: A Martian Concrete for Additive Construction Applications Utilizing In Situ Resources," presented at the Earth and Space 2021, 2021.
- [A-7] C. W. Hull, "Apparatus for production of three-dimensional objects by stereolithography," United States, 1984.
- [A-8] C. W. Hull, "On Stereolithography," Virtual and Physical Prototyping, vol. 7, no. 3, pp. 177-177, 2012/09/01 2012, doi: 10.1080/17452759.2012.723409.
- [A-9] J. Z. Manapat, Q. Chen, P. Ye, and R. C. Advincula, "3D Printing of Polymer Nanocomposites via Stereolithography," *Macromolecular materials and engineering*, vol. 302, no. 9, pp. 1600553-n/a, 2017, doi: 10.1002/mame.201600553.
- [A-10] N. Travitzky, A. Bonet, B. Dermeik, T. Fey, I. Filbert-Demut, L. Schlier, T. Schlordt, and P. Greil, "Additive Manufacturing of Ceramic-Based Materials," *Advanced engineering materials*, vol. 16, no. 6, pp. 729-754, 2014, doi: 10.1002/adem.201400097.
- [A-11] B. Khoshnevis, "Automated construction by contour crafting—related robotics and information technologies," *Automation in construction*, vol. 13, no. 1, pp. 5-19, 2004, doi: 10.1016/j.autcon.2003.08.012.
- [12] H. Lee, C. H. J. Lim, M. J. Low, N. Tham, V. M. Murukeshan, and Y.-J. Kim, "Lasers in additive manufacturing: A review," *Int. J. of Precis. Eng. and Manuf.-Green Tech*, vol. 4, no. 3, pp. 307-322, 2017, doi: 10.1007/s40684-017-0037-7.
- [A-13] C. P. Paul, P. Ganesh, S. K. Mishra, P. Bhargava, J. Negi, and A. K. Nath, "Investigating laser rapid manufacturing for Inconel-625 components," *Optics and laser technology*, vol. 39, no. 4, pp. 800-805, 2007, doi: 10.1016/j.optlastec.2006.01.008.
- [A-14] C.-H. Yu, R. L. Peng, V. Luzin, M. Sprengel, M. Calmunger, J.-E. Lundgren, H. Brodin, A. Kromm, and J. Moverare, "Thin-wall effects and

- anisotropic deformation mechanisms of an additively manufactured Nibased superalloy," *Additive manufacturing*, 2020. [Online]. Available: https://doi.org/10.1016/j.addma.2020.101672.
- [A-15] B. Peter, "Particle emissions from fused deposition modeling 3D printers: Evaluation and meta-analysis," *Science of the Total Environment*, vol. 655, pp. 395-407, 2019, doi: 10.1016/j.scitotenv.2018.11.070.
- [A-16] M. Algarni, "The Influence of Raster Angle and Moisture Content on the Mechanical Properties of PLA Parts Produced by Fused Deposition Modeling," *Polymers.*, vol. 13, no. 2, pp. 237-12, 2021, doi: 10.3390/polym13020237.
- [A-17] H. D. Budinoff and S. McMains, "Will it print: a manufacturability toolbox for 3D printing," *International journal on interactive design and manufacturing.*, vol. 15, no. 4, pp. 613-630, 2021, doi: 10.1007/s12008-021-00786-w.
- [A-18] E. Atzeni and A. Salmi, "Economics of additive manufacturing for endusable metal parts," *International journal of advanced manufacturing* technology, vol. 62, no. 9-12, pp. 1147-1155, 2012, doi: 10.1007/s00170-011-3878-1.
- [A-19] S. Li, Q. Wei, Y. Shi, Z. Zhu, and Z. Danqing, "Microstructure Characteristics of Inconel 625 Superalloy Manufactured by Selective Laser Melting," *Journal of Materials Science & Technology*, vol. 31, no. 9, pp. 946-952, 2015, doi: 10.1016/j.jmst.2014.09.020.
- [A-20] J. J. Lewandowski and M. Seifi, "Metal Additive Manufacturing: A Review of Mechanical Properties," Annual Review of Materials Research, vol. 46, no. 1, pp. 151-186, 2016, doi: 10.1146/annurevmatsci-070115-032024.
- [A-21] V. Lunetto, M. Galati, L. Settineri, and L. Iuliano, "Unit process energy consumption analysis and models for Electron Beam Melting (EBM): Effects of process and part designs," *Additive manufacturing.*, vol. 33, p. 101115, 2020, doi: 10.1016/j.addma.2020.101115.
- [A-22] D. Ding, Z. Pan, D. Cuiuri, and H. Li, "Wire-feed additive manufacturing of metal components: technologies, developments and future interests," *Int J Adv Manuf Technol*, vol. 81, no. 1-4, pp. 465-481, 2015, doi: 10.1007/s00170-015-7077-3.
- [A-23] S. S. Al-Bermani, M. L. Blackmore, W. Zhang, and I. Todd, "The Origin of Microstructural Diversity, Texture, and Mechanical Properties in Electron Beam Melted Ti-6Al-4V," *Metall and Mat Trans A*, vol. 41, no. 13, pp. 3422-3434, 2010, doi: 10.1007/s11661-010-0397-x.
- [A-24] P. L. Blackwell, "The mechanical and microstructural characteristics of laser-deposited IN718," *Journal of materials processing technology,* vol. 170, no. 1-2, pp. 240-246, 2005, doi: 10.1016/j.jmatprotec.2005.05.005.
- [A-25] G. Asala, A. K. Khan, J. Andersson, and O. A. Ojo, "Microstructural Analyses of ATI 718Plus® Produced by Wire-ARC Additive Manufacturing Process," *Metall and Mat Trans A*, vol. 48, no. 9, pp. 4211-4228, 2017, doi: 10.1007/s11661-017-4162-2.
- [A-26] F. J. Xu, Y. H. Lv, B. S. Xu, Y. X. Liu, F. Y. Shu, and P. He, "Effect of deposition strategy on the microstructure and mechanical properties of Inconel 625 superalloy fabricated by pulsed plasma arc deposition,"

- *Materials in engineering,* vol. 45, pp. 446-455, 2013, doi: 10.1016/j.matdes.2012.07.013.
- [A-27] Z. Pan, D. Ding, B. Wu, D. Cuiuri, H. Li, and J. Norrish, "Arc Welding Processes for Additive Manufacturing: A Review," in *Transactions on Intelligent Welding Manufacturing*, Singapore, 2018, Pan18: Springer Singapore, in Transactions on Intelligent Welding Manufacturing, pp. 3-24, doi: 10.1007/978-981-10-5355-9
- [A-28] S. Williams, F. Martina, A. C. Addison, J. Ding, G. Pardal, and P. Colegrove, "Wire + Arc Additive Manufacturing," *Materials Science and Technology*, vol. 32, no. 7, pp. 641-647, 2016/05/02 2016, doi: 10.1179/1743284715Y.0000000073.
- [A-29] M. Yao, Z. Yao, X. Tao, and O. Moliar, "Effect of deposition modes on electron beam directed energy deposited Inconel 718," *Materials science and technology,* vol. 36, no. 14, pp. 1556-1565, 2020, doi: 10.1080/02670836.2020.1802838.
- [A-30] A. Galloway, N. McPherson, and A. Gillies, "Helium additions to MIG shielding gas an economic option?," *Welding and Cutting,* vol. 10, no. 2, pp. 118-121, 2011.
- [A-31] B. Wu, D. Ding, Z. Pan, D. Cuiuri, H. Li, J. Han, and Z. Fei, "Effects of heat accumulation on the arc characteristics and metal transfer behavior in Wire Arc Additive Manufacturing of Ti6Al4V," *Journal of* materials processing technology, vol. 250, pp. 304-312, 2017, doi: 10.1016/j.jmatprotec.2017.07.037.
- [A-32] B. Wu, Z. Pan, D. Ding, D. Cuiuri, H. Li, J. Xu, and J. Norrish, "A review of the wire arc additive manufacturing of metals: properties, defects and quality improvement," *Journal of Manufacturing Processes*, vol. 35, pp. 127-139, 2018/10/01/2018, doi: 10.1016/j.jmapro.2018.08.001.
- [A-33] T. Gurcik, "Influence of shielding gas on geometrical quality of WAAM technology," presented at the 28th International Conference on Metallurgy and Materials, 2019.
- [A-34] S. Roy, B. Silwal, A. Nycz, M. Noakes, E. Cakmak, P. Nandwana, and Y. Yamamoto, "Investigating the effect of different shielding gas mixtures on microstructure and mechanical properties of 410 stainless steel fabricated via large scale additive manufacturing," *Additive Manufacturing*, vol. 38, p. 101821, 2021/02/01/ 2021, doi: 10.1016/j.addma.2020.101821.
- [A-35] Y. Wang, C. Xizhang, and S. Chuanchu, "Microstructure and mechanical properties of Inconel 625 fabricated by wire-arc additive manufacturing," *Surface & coatings technology*, vol. 374, pp. 116-123, 2019, doi: 10.1016/j.surfcoat.2019.05.079.
- [A-36] H. Zhang, J. Xu, and G. Wang, "Fundamental study on plasma deposition manufacturing," *Surface & coatings technology,* vol. 171, no. 1-3, pp. 112-118, 2003, doi: 10.1016/S0257-8972(03)00250-0.
- [A-37] F. Xu, Y. Lv, Y. Liu, P. He, B. Xu, and F. Shu, "Microstructural Evolution and Mechanical Properties of Inconel 625 Alloy during Pulsed Plasma Arc Deposition Process," *Journal of Materials Science & Technology*, vol. 29, no. 5, pp. 480-488, 2013, doi: 10.1016/j.jmst.2013.02.010.
- [A-38] B. Cong, R. Ouyang, B. Qi, and J. Ding, "Influence of Cold Metal Transfer Process and Its Heat Input on Weld Bead Geometry and Porosity of Aluminum-Copper Alloy Welds," Rare Metal Materials and

- Engineering, vol. 45, no. 3, pp. 606-611, 2016, doi: 10.1016/S1875-5372(16)30080-7.
- [A-39] K. F. Ayarkwa, S. Williams, and J. Ding, "Investigation of pulse advance cold metal transfer on aluminium wire arc additive manufacturing," *International journal of rapid manufacturing*, vol. 5, 1, pp. 44-57, 2015, doi: 10.1504/IJRAPIDM.2015.073547.
- [A-40] C. G. Pickin, S. W. Williams, and M. Lunt, "Characterisation of the cold metal transfer (CMT) process and its application for low dilution cladding," *Journal of materials processing technology,* vol. 211, no. 3, pp. 496-502, 2011, doi: 10.1016/j.jmatprotec.2010.11.005.
- [A-41] S. Guo, D. Xu, Y. Li, Y. Guo, S. Wang, and D. D. Macdonald, "Corrosion characteristics and mechanisms of typical Ni-based corrosion-resistant alloys in sub- and supercritical water," *The Journal of supercritical fluids*, vol. 170, p. 105138, 2021, doi: 10.1016/j.supflu.2020.105138.
- [A-42] J. R. Davis and A. S. M. I. H. Committee, *Stainless Steels*. ASM International, 1994.
- [A-43] G. L. Winters and M. J. Nutt, "Stainless steels for medical and surgical applications," presented at the Astm International Symposium on Stainless Steels for Medical and Surgical, Applications, West Conshohocken, PA, 2003.
- [A-44] B. D. Craig, "Selection guidelines for corrosion resistant alloys in the oil and gas industry," *Chemical engineering world*, vol. 33, pp. 57-60, 1998.
- [A-45] P. R. Rhodes, "Environment-Assisted Cracking of Corrosion-Resistant Alloys in Oil and Gas Production Environments: A Review," *Corrosion*, vol. 57, no. 11, pp. 923-966, 2001, doi: 10.5006/1.3290320.
- [A-46] API 6a: Specification for Wellhead and Christmas Tree Equipment, 2011.
- [A-47] US-Ordnance. "Stellite." http://www.usord.com/weapons/stellite (accessed 04/04/2020.
- [A-48] R. Fraser, "Final Ascent: The Legend of Hamish MacInnes," ed: BBC, 2020.
- [A-49] M. S. Hasan, A. M. Mazid, and R. Clegg, "The Basics of Stellites in Machining Perspective," *International Journal of Engineering Materials* and Manufacture, vol. 1, no. 2, pp. 35-50, 12/19 2016, doi: 10.26776/ijemm.01.02.2016.01.
- [A-50] L. Zhang, Y. Wang, X. Wang, B. Gao, A. Mi, and Y. Mao, "Study of the Impact of Stellite Material on PWR Co-60 Contamination," presented at the 25th International Conference on Nuclear Engineering, 2017.
- [A-51] ASM handbook. Volume 1, Properties and selection: irons, steels, and high-performance alloys, 10th edition. ed. Materials Park, OH: Materials Park, OH: ASM International, 1990.
- [A-52] L. Couturier, F. De Geuser, M. Descoins, and A. Deschamps, "Evolution of the microstructure of a 15-5PH martensitic stainless steel during precipitation hardening heat treatment," *Materials & Design*, vol. 107, pp. 416-425, 2016/10/05 2016, doi: 10.1016/j.matdes.2016.06.068.
- [A-53] C. Bao and C. Zhang, "Preparation and corrosion resistance properties of duplex stainless steel (00Cr22Ni6MnMoCu)," *Materials Research Express*, vol. 8, no. 12, p. 126501, 2021, doi: 10.1088/2053-1591/ac3bf8.

- [A-54] M. Pohl, O. Storz, and T. Glogowski, "Effect of intermetallic precipitations on the properties of duplex stainless steel," *Materials* characterization, vol. 58, no. 1, pp. 65-71, 2007, doi: 10.1016/j.matchar.2006.03.015.
- [A-55] A. Pramanik, G. Littlefair, and A. K. Basak, "Weldability of Duplex Stainless Steel," *Materials and manufacturing processes*, vol. 30, no. 9, pp. 1053-1068, 2015, doi: 10.1080/10426914.2015.1019126.
- [A-56] S. Hertzman, J. O. Nilsson, R. Jargelius-Pettersson, T. Huhtala, L. Karlsson, M. Nilsson, and A. Wilson, "Microstructure-property relations of Mo- and W-alloyed super duplex stainless steel weld metals," *Materials science and technology*, vol. 13, no. 7, pp. 604-613, 1997.
- [A-57] B. J. A, "Weld microstructure development and properties of precipitation-strengthened martensitic stainless steels," *Welding journal*, vol. 78, no. 8, p. 280, 1999.
- [A-58] J. Niu, B. Cui, H. Jin, J. Yan, W. Meng, C. Min, and D. Xu, "Effect of Post-Weld Aging Temperature on Microstructure and Mechanical Properties of Weld Metal of 15-5 PH Stainless Steel," *Journal of* materials engineering and performance, vol. 29, no. 11, pp. 7026-7033, 2020, doi: 10.1007/s11665-020-05193-y.
- [A-59] M. Abdelshehid, K. Mahmodieh, K. Mori, L. Chen, P. Stoyanov, D. Davlantes, J. Foyos, J. Ogren, R. Clark, and O. S. Es-Said, "On the correlation between fracture toughness and precipitation hardening heat treatments in 15-5PH Stainless Steel," *Engineering failure analysis*, vol. 14, no. 4, pp. 626-631, 2007, doi: 10.1016/j.engfailanal.2006.03.001.
- [A-60] ASM handbook. Volume 2, Properties and selection: nonferrous alloys and special-purpose materials, 10th edition. ed. Materials Park, OH: Materials Park, OH: ASM International, 1990.
- [A-61] E. P. Cardozo, S. Ríos, S. Ganguly, and A. S. C. M. D'Oliveira, "Assessment of the effect of different forms of Inconel 625 alloy feedstock in Plasma Transferred Arc (PTA) additive manufacturing," *Int J Adv Manuf Technol*, vol. 98, no. 5, pp. 1695-1705, 2018, doi: 10.1007/s00170-018-2340-z.
- [A-62] V. Shankar, K. B. S. Rao, and S. L. Mannan, "Microstructure and mechanical properties of Inconel 625 superalloy," *Journal of nuclear materials*, vol. 288, no. 2-3, pp. 222-232, 2001, doi: 10.1016/s0022-3115(00)00723-6.
- [A-63] A. Evangeline and P. Sathiya, "Cold metal arc transfer (CMT) metal deposition of Inconel 625 superalloy on 316L austenitic stainless steel: microstructural evaluation, corrosion and wear resistance properties," *Materials Research Express,* vol. 6, no. 6, p. 066516, 2019, doi: 10.1088/2053-1591/ab0a10.
- [A-64] J. Adamiec, "High temperature corrosion of power boiler components cladded with nickel alloys," *Materials characterization*, vol. 60, no. 10, pp. 1093-1099, 2009, doi: 10.1016/j.matchar.2009.03.017.
- [A-65] S. K. Rai, A. Kumar, V. Shankar, T. Jayakumar, K. B. S. Rao, and B. Raj, "Characterization of microstructures in Inconel 625 using X-ray diffraction peak broadening and lattice parameter measurements," *Scripta materialia*, vol. 51, no. 1, pp. 59-63, 2004, doi: 10.1016/j.scriptamat.2004.03.017.

- [A-66] Y. Mu, C. Wang, W. Zhou, and L. Zhou, "Effect of Nb on delta Phase Precipitation and the Tensile Properties in Cast Alloy IN625," *Metals* (*Basel*), vol. 8, no. 2, p. 86, 2018, doi: 10.3390/met8020086.
- [A-67] J. Mittra, S. Banerjee, R. Tewari, and G. K. Dey, "Fracture behavior of Alloy 625 with different precipitate microstructures," *Materials science* & engineering. A, Structural materials: properties, microstructure and processing, vol. 574, pp. 86-93, 2013, doi: 10.1016/j.msea.2013.03.021.
- [A-68] F. Stein and A. Leineweber, "Laves phases: a review of their functional and structural applications and an improved fundamental understanding of stability and properties," *J Mater Sci*, vol. 56, no. 9, pp. 5321-5427, 2021, doi: 10.1007/s10853-020-05509-2.
- [A-69] N. S. Stoloff, C. T. Liu, and S. C. Deevi, "Emerging applications of intermetallics," *Intermetallics*, vol. 8, no. 9-11, pp. 1313-1320, 2000, doi: 10.1016/S0966-9795(00)00077-7.
- [A-70] J. F. Wang, Q. J. Sun, H. Wang, J. P. Liu, and J. C. Feng, "Effect of location on microstructure and mechanical properties of additive layer manufactured Inconel 625 using gas tungsten arc welding," *Materials* science & engineering. A, Structural materials: properties, microstructure and processing, vol. 676, pp. 395-405, 2016, doi: 10.1016/j.msea.2016.09.015.
- [A-71] H. Zhang, H. Hao, J. Li, X. Zhang, and Y. Liu, "Evaluation on static mechanical stability of wrought Inconel 718 superalloy effect of grain configuration and δ precipitation," *Journal of materials research and technology.*, vol. 24, p. 1776, 2023, doi: 10.1016/j.jmrt.2023.03.123.
- [A-72] J. M. Oblak, D. F. Paulonis, and D. S. Duvall, "Coherency strengthening in Ni base alloys hardened by DO22 γ' precipitates," *Metallurgical transactions*, vol. 5, no. 1, pp. 143-153, 1974/01/01 1974, doi: 10.1007/BF02642938.
- [A-73] S. Azadian, L.-Y. Wei, and R. Warren, "Delta phase precipitation in Inconel 718," *Materials characterization*, vol. 53, no. 1, pp. 7-16, 2004, doi: 10.1016/j.matchar.2004.07.004.
- [A-74] M. Anderson, A. L. Thielin, F. Bridier, P. Bocher, and J. Savoie, "δ Phase precipitation in Inconel 718 and associated mechanical properties," *Materials science & engineering. A, Structural materials :* properties, microstructure and processing, vol. 679, pp. 48-55, 2017, doi: 10.1016/j.msea.2016.09.114.
- [A-75] G. D. J. Ram, A. V. Reddy, K. P. Rao, and G. M. Reddy, "Control of Laves phase in Inconel 718 GTA welds with current pulsing," *Science* and *Technology of Welding and Joining*, vol. 9, no. 5, pp. 390-398, 2004, doi: 10.1179/136217104225021788.
- [A-76] L. Tóth and S. Y. Yarema, "Formation of the science of fatigue of metals. Part 1. 1825–1870," *Materials science.,* vol. 42, no. 5, pp. 673-680, 2006, doi: 10.1007/s11003-006-0132-3.
- [A-77] R. A. Smith and S. Hillmansen, "A brief historical overview of the fatigue of railway axles," *Proceedings of the Institution of Mechanical Engineers.*, vol. 218, no. 4, pp. 267-277, 2004, doi: 10.1243/0954409043125932.
- [A-78] A. Wohler, "On strength tests with iron and steel," *Journal of Construction*, vol. 20, pp. 73-106, 1870.

- [A-79] P. A. Withey, "Fatigue failure of the de Havilland comet I," Engineering failure analysis, vol. 4, no. 2, pp. 147-154, 1997, doi: 10.1016/S1350-6307(97)00005-8.
- [A-80] D. Saunders, "Operation Crash-Dive," in *Thunderbirds*, G. Anderson, Ed., ed. United Kingdom, 1965.
- [A-81] F. Froes and R. Boyer, "Surface Roughness and Fatigue Properties of Selective Laser Melted Ti-6Al-4V Alloy," Elsevier, 2019, sec. Fro19, pp. 1-1.
- [A-82] N. Shamsaei, S. Daniewicz, N. Hrabe, S. Beretta, J. Waller, M. Seifi, F. Berto, A. Fatemi, and S. M. J. Razavi, "Fatigue Assessment of 17-4 PH Stainless Steel Notched Specimens Made by Direct Metal Laser Sintering," *Structural integrity of additive manufactured parts* /, vol. 1620, pp. 415-422, 2020, doi: 10.1520/STP162020180062.
- [A-83] C. K. Lin and C. C. Chu, "Mean stress effects on low-cycle fatigue for a precipitation-hardening martensitic stainless steel in different tempers," Fatigue & fracture of engineering materials & structures, vol. 23, no. 7, pp. 545-553, 2000, doi: 10.1046/j.1460-2695.2000.00324.x.
- [A-84] W. Schneller, M. Leitner, S. Pomberger, F. Grün, S. Leuders, T. Pfeifer, and O. Jantschner, "Fatigue strength assessment of additively manufactured metallic structures considering bulk and surface layer characteristics," *Additive Manufacturing*, vol. 40, p. 101930, 2021/04/01/2021, doi: 10.1016/j.addma.2021.101930.
- [A-85] Y. Lee and M. E. Barkey, "Chapter 4 Stress-Based Uniaxial Fatigue Analysis," in *Metal Fatigue Analysis Handbook*, Y. Lee, M. E. Barkey, and H. Kang Eds. Boston: Butterworth-Heinemann, 2012, sec. Lee12, pp. 115-160.
- [A-86] P. Zhao, J. Post, Z. Wu, W. Du, and Y. Zhang, "Environmental impact analysis of on-demand urban air mobility: A case study of the Tampa Bay Area," *Transportation Research D*, vol. 110, p. 103438, 2022, doi: 10.1016/j.trd.2022.103438.
- [A-87] J. Shi, J. Hu, M. Ma, and H. Wang, "An environmental impact analysis method of machine-tool cutting units based on LCA," *Journal of engineering, design and technology.*, vol. 19, pp. 1192-1206, 2021, doi: 10.1108/JEDT-06-2020-0247.
- [A-88] X. Zhang, Y. Shi, Y. Chen, H. Hu, F. Cheng, R. Li, and Y. Wu, "Ecosystem simulation and environmental impact analysis of transforming microalgae to produce jet fuel," *Journal of cleaner* production., vol. 333, p. 130100, 2022, doi: 10.1016/j.jclepro.2021.130100.
- [A-89] D. D. Tuan and C. Wei, "Cradle-to-gate life cycle assessment of ships: A case study of Panamax bulk carrier," *Proceedings of the institution of mechanical engineers.*, vol. 233, no. 2, pp. 670-683, 2019, doi: 10.1177/1475090218813731.
- [A-90] A. R. Catalano, L. Debernardi, R. Balaso, F. Rubbiani, P. C. Priarone, and L. Settineri, "An appraisal of the cradle-to-gate energy demand and carbon footprint of high-speed steel cutting tools," *Procedia CIRP*, vol. 105, pp. 745-750, 2022, doi: 10.1016/j.procir.2022.02.124.
- [A-91] P. C. Priarone, E. Pagone, F. Martina, A. R. Catalano, and L. Settineri, "Multi-criteria environmental and economic impact assessment of wire

- arc additive manufacturing," *CIRP annals*, vol. 69, no. 1, pp. 37-40, 2020, doi: 10.1016/j.cirp.2020.04.010.
- [A-92] A. C. M. Bekker and J. C. Verlinden, "Life cycle assessment of wire + arc additive manufacturing compared to green sand casting and CNC milling in stainless steel," *Journal of cleaner production,* vol. 177, pp. 438-447, 2018/03/10/ 2018, doi: 10.1016/j.jclepro.2017.12.148.
- [A-93] I. Daniyan, K. Mpofu, K. Bello, and R. Muvunzi, "Life cycle assessment for the milling operation of titanium alloy (Ti6Al4V)," *Procedia CIRP*, vol. 105, pp. 811-816, 2022, doi: 10.1016/j.procir.2022.02.134.

B. Peer Reviewed Journal Articles

J. I. Sword, A. Galloway & A. Toumpis, "An environmental impact comparison between wire + arc additive manufacture and forging for the production of a titanium component." *Sustainable Materials and Technologies*, *36*, e00600, 2023.

https://doi.org/10.1016/j.susmat.2023.e00600

- **J. I. Sword**, A. Galloway & A. Toumpis, "The effect of weld heat input on the microstructure and mechanical properties of wire arc additively manufactured 15-5PH stainless steel." *International Journal of Advanced Manufacturing Technology*, *132*(11-12), 5305–5314, 2024. https://doi.org/10.1007/s00170-024-13674-w
- **J. I. Sword**, A. Galloway & A. Toumpis, "Analysis of Environmental Impact and Mechanical Properties of Inconel 625 Produced Using Wire Arc Additive Manufacturing." *Sustainability*, *16*(10), 4178, 2024. https://doi.org/10.3390/su16104178